

STRUCTURAL AND ELECTROCHEMICAL STUDIES OF THE  
LI-MN-NI-O AND LI-CO-MN-O PSEUDO-TERNARY SYSTEMS

by

Eric McCalla

Submitted in partial fulfillment of the requirements  
for the degree of Doctor of Philosophy

at

Dalhousie University  
Halifax, Nova Scotia  
December 2013

© Copyright by Eric McCalla, 2013

*“A learned blockhead is a greater blockhead than an ignorant one.”*

*- Benjamin Franklin [1]*

*I dedicate this thesis to my mother, Joanne McCalla, who was my first science teacher and helped me become a spectacular blockhead.*

# Table of Contents

<b>List of Tables</b> . . . . .	<b>viii</b>
<b>List of Figures</b> . . . . .	<b>ix</b>
<b>Abstract</b> . . . . .	<b>xvi</b>
<b>List of Symbols and Abbreviations Used</b> . . . . .	<b>xvii</b>
<b>Acknowledgements</b> . . . . .	<b>xix</b>
<b>Chapter 1 Introduction</b> . . . . .	<b>1</b>
1.1 Motivation: Li-Co-Mn-Ni Oxide Materials . . . . .	1
1.2 Layered and Spinel Structures . . . . .	4
1.3 The Li-Co-Mn-O Face of the Pyramid . . . . .	7
1.4 The Li-Mn-Ni-O Face of the Pyramid . . . . .	11
1.4.1 Li-Mn-Ni-O Spinel Solid-Solutions . . . . .	14
1.4.2 Li-Mn-Ni-O Layered Solid-Solutions . . . . .	15
1.4.3 The Co-Existence Region Between the Spinel and Layered Structures . . . . .	18
1.5 Structure of this Thesis . . . . .	21
<b>Chapter 2 Experimental and Theoretical Considerations</b> . . . . .	<b>23</b>
2.1 Sample Preparation . . . . .	23
2.1.1 Synthesis of Combinatorial Samples . . . . .	23
2.1.2 Synthesis of Bulk Samples . . . . .	27
2.2 X-Ray Diffraction . . . . .	28

2.2.1	High Throughput XRD of Combinatorial Samples . . . . .	28
2.2.2	XRD of Bulk Samples . . . . .	29
2.3	Fitting of Combinatorial XRD Patterns . . . . .	30
2.4	Methods to Generate the Phase Diagrams . . . . .	35
2.5	Electrochemical Tests . . . . .	37
2.6	Thermo-Gravimetric Analysis . . . . .	38
2.7	Elemental Analysis . . . . .	38
2.8	Scanning Electron Microscopy . . . . .	39
2.9	Redox Titration . . . . .	39
2.10	X-Ray Absorption Spectroscopy . . . . .	40
2.11	Helium Pycnometry . . . . .	40
2.12	Monte Carlo Simulations . . . . .	42
<b>Chapter 3</b>	<b>Optimization of the Synthesis of Combinatorial Samples</b>	<b>44</b>
3.1	Experimental Design . . . . .	44
3.2	TGA Results for Lithium Loss During Synthesis . . . . .	48
3.3	XRD Results of Lithium Loss . . . . .	50
3.3.1	Combinatorial samples . . . . .	50
3.3.2	Combinatorial Samples During Synthesis . . . . .	54
3.4	Conclusions Regarding Synthesis of Combinatorial Samples . . . . .	61
<b>Chapter 4</b>	<b>Combinatorial Studies in the Li-Co-Mn-O System . . .</b>	<b>63</b>
4.1	Experimental Design . . . . .	63

4.2	Spinel - Layered Co-Existence Region . . . . .	65
4.3	LiCoO <sub>2</sub> - Li <sub>2</sub> MnO <sub>3</sub> . . . . .	68
4.4	Monte Carlo Simulation . . . . .	74
4.5	Conclusions Regarding the Formation of Layered-Layered Composites in the Li-Co-Mn-O System . . . . .	77
<b>Chapter 5 Combinatorial Studies of the Spinel and Rocksalt Re-</b>		
<b>gions in the Li-Mn-Ni-O System . . . . .</b>		<b>79</b>
5.1	Experimental Design . . . . .	79
5.3	Rocksalt Single-Phase Region . . . . .	86
5.4	Mn <sub>2</sub> O <sub>3</sub> - Spinel Co-Existence Region . . . . .	91
5.5	Spinel - Ordered Rocksalt Co-Existence Region . . . . .	96
5.6	Conclusions Regarding Spinel and Rocksalt Li-Mn-Ni Oxides . . . . .	99
<b>Chapter 6 Combinatorial Studies of Compositions Containing Lay-</b>		
<b>ered Phases in the Li-Mn-Ni-O System . . . . .</b>		<b>101</b>
6.1	Experimental Design . . . . .	101
6.2	Single-Phase Layered Region . . . . .	101
6.3	Two-Phase Layered-Spinel Region . . . . .	104
6.4	Two-Phase Layered-Layered Region . . . . .	106
6.5	The R, N, S and M phases . . . . .	108
6.6	Three-Phase Regions, Quenched . . . . .	113
6.7	Three-Phase Regions, Slow Cooled . . . . .	117

6.8	The Upper Boundary of the Layered Region . . . . .	122
6.9	Conclusions Regarding Combinatorial Studies of Li-Mn-Ni-O Materials	123
<b>Chapter 7</b>	<b>Investigations of Bulk Li-Mn-Ni-O Samples to Confirm the Combinatorial Studies . . . . .</b>	<b>126</b>
7.1	Motivation . . . . .	126
7.2	Experimental Design . . . . .	129
7.3	Structural Results . . . . .	129
7.4	Electrochemistry of the R, M and N Phases . . . . .	135
7.5	Conclusions Based on Bulk Li-Mn-Ni-O Samples . . . . .	138
<b>Chapter 8</b>	<b>Layered Materials with Metal Site Vacancies . . . . .</b>	<b>139</b>
8.1	Motivation for the Study of Samples near $\text{Li}_2\text{MnO}_3$ . . . . .	139
8.2	Experimental Design . . . . .	142
8.3	Monte Carlo Results . . . . .	143
8.4	Vacancy Measurements . . . . .	144
8.5	$\text{Li}[\text{Ni}_{1/6}\square_{1/6}\text{Mn}_{2/3}]\text{O}_2$ . . . . .	150
8.6	Conclusions Regarding Metal Site Vacancies in Li-Mn-Ni-O Materials	153
<b>Chapter 9</b>	<b>Materials Near the Layered Boundary . . . . .</b>	<b>155</b>
9.1	Motivation for Studying $\text{LiNi}_{0.5}\text{Mn}_{0.5}\text{O}_2$ . . . . .	155
9.2	Experimental Design . . . . .	158
9.3	Structural Results . . . . .	159

9.4	Monte Carlo Simulation Results . . . . .	163
9.5	Electrochemical Measurements . . . . .	165
9.6	$\text{Li}_{1+x}[\text{Ni}_{0.5}\text{Mn}_{0.5}]_{1-x}\text{O}_2$ Series with $0 \leq x \leq 0.24$ . . . . .	167
9.7	Conclusions Regarding Layered-Layered Nano-Composites . . . . .	171
<b>Chapter 10</b>	<b>Conclusions and Future Works . . . . .</b>	<b>174</b>
10.1	The Li-Co-Mn-Ni-O Pseudo-Quaternary System . . . . .	174
10.2	Resolving Points of Confusion . . . . .	175
10.3	Future Work . . . . .	180
<b>Appendix A</b>	<b>Copyright Agreements . . . . .</b>	<b>183</b>
<b>Bibliography</b>	<b>. . . . .</b>	<b>198</b>

## List of Tables

Table 1.1	The median voltage, specific capacity, crystallographic density and volumetric energy density of some oxide materials. . . . .	2
Table 3.1	$\text{Li}_x\text{Ni}_{2-x}\text{O}_2$ properties obtained by fitting the XRD patterns of the combinatorial samples. . . . .	53
Table 3.2	Average $\text{Li}_2\text{CO}_3$ crystallite size and micro-strain. . . . .	61
Table 5.1	Results for the Rietveld refinement of the sample synthesized at the metal composition: $\text{Li}_{0.25}\text{Mn}_{0.15}\text{Ni}_{0.6}$ in oxygen with regular cooling. . . . .	90
Table 5.2	Output from the Rietveld refinement of the sample synthesized at the metal composition: $\text{Li}_{0.25}\text{Mn}_{0.15}\text{Ni}_{0.6}$ in oxygen with regular cooling. . . . .	90
Table 6.1	The lattice parameters obtained for the single-phase corners of the three-phase regions. . . . .	112
Table 6.2	The coordinates of the four corners of the three-phase regions. . . . .	113
Table 6.3	Rietveld results for bulk samples synthesized at the R, M and N corners. . . . .	114
Table 7.1	Metal molar fractions for samples discussed in the text. . . . .	127
Table 8.1	Metal molar fractions for samples A <sub>8</sub> -D <sub>8</sub> and $\text{Li}_2\text{MnO}_3$ . . . . .	147
Table 8.2	Results for Rietveld refinement, pycnometry, and redox titrations. . . . .	148
Table 9.1	XRD Rietveld refinement and electrochemical results for samples of composition A <sub>9</sub> fit as single-phase layered. . . . .	162
Table 9.2	XRD Rietveld refinement and reversible capacity results for samples along the composition line $\text{Li}_{1+x}(\text{Ni}_{0.5}\text{Mn}_{0.5})_{1-x}\text{O}_2$ . . . . .	171



## List of Figures

Figure 1.1	The Li-Co-Mn-Ni-O pseudo-quaternary system of extreme interest for potential positive electrode materials. . . . .	4
Figure 1.2	Illustrations of layered and spinel structures. . . . .	5
Figure 1.3	The Li-Co-Mn-O pseudo-ternary system with single-phase materials known prior to the combinatorial studies discussed here. . . . .	8
Figure 1.4	Stack of XRD patterns for various values of x along the line from $\text{Li}_2\text{MnO}_3$ to $\text{LiCoO}_2$ reproduced with permission from Ref. [19]. . . . .	9
Figure 1.5	Hexagonal arrays of atoms illustrating the transition metal layer in various materials. . . . .	10
Figure 1.6	TEM images of $\text{Li}_{1.2}\text{Co}_{0.4}\text{Mn}_{0.4}\text{O}_2$ showing the co-existence of layered and monoclinic domains on the nano-scale, reprinted from Ref. [23] with permission from Elsevier. . . . .	12
Figure 1.7	A schematic of layered-layered phase separation with domains of $\text{Li}_2\text{MnO}_3$ and $\text{LiCoO}_2$ , from Ref. [24]. . . . .	12
Figure 1.8	The Li-Mn-Ni oxide pseudo-ternary system with single-phase regions known prior to this thesis. . . . .	13
Figure 1.9	XRD patterns obtained by Lu et al. [46] for samples along the composition line from $\text{Li}_2\text{MnO}_3$ and $\text{LiNi}_{0.5}\text{Mn}_{0.5}\text{O}_4$ . . . . .	16
Figure 1.10	TEM images of $\text{Li}_{1.2}\text{Ni}_{0.2}\text{Mn}_{0.6}\text{O}_2$ : (a) obtained from Jarvis et al. [47] and Lei et al. [45]. . . . .	17
Figure 1.11	TEM images of single-phase $\text{Li}_2\text{MnO}_3$ reprinted from Ref. [48]. . . . .	17
Figure 1.12	XRD patterns reprinted from Ref. [56] with permission from the American Chemical Society. Samples of $\text{LiNi}_{0.5}\text{Mn}_{0.5}\text{O}_2$ were quenched from high temperature before being annealed at the temperatures indicated. . . . .	19
Figure 1.13	XRD patterns obtained for samples along the composition line from $\text{Li}_{1.2}\text{Ni}_{0.2}\text{Mn}_{0.6}\text{O}_2$ to $\text{LiNi}_{0.5}\text{Mn}_{1.5}\text{O}_4$ from Ref. [14]. . . . .	20
Figure 1.14	A partial Li-Mn-Ni-O diagram showing proposed tie-lines between the spinel and layered phases. . . . .	20

Figure 2.1	The PixSis solution-dispensing robot used to make all combinatorial samples in this thesis. . . . .	24
Figure 2.2	Images of the PixSis solution-dispensing robot and a few resulting samples. . . . .	24
Figure 2.3	The Li-Mn-Ni oxide triangle illustrating how samples are synthesized over entire composition range in a ternary system. . . . .	27
Figure 2.4	Example of an XRD pattern obtained with an area detector. . . . .	30
Figure 2.5	Williamson-Hall plot for corundum obtained with the Bruker XRD machine. . . . .	32
Figure 2.6	The fit obtained for an XRD pattern from a combinatorial sample of $\text{LiNiO}_2$ . . . . .	34
Figure 2.7	A section of the Li-Mn-Ni-O phase diagram with proposed tie-lines and a demonstration of using the lever rule. . . . .	36
Figure 2.8	A schematic of the components used in making a typical coin cell for electrochemical testing. . . . .	37
Figure 2.9	XANES spectra published by Myung et al. [65]. . . . .	41
Figure 2.10	An array of atoms illustrating the interactions used in the Monte Carlo simulations . . . . .	41
Figure 3.1	The Li-Mn-Ni oxide pseudo-ternary system showing lithium loss during synthesis of combinatorial samples. . . . .	45
Figure 3.2	XRD scans of $\text{Li}_x\text{Ni}_{2-x}\text{O}_2$ samples at various stages of synthesis. . . . .	46
Figure 3.3	TGA data for samples of $\text{Li}_{0.965}\text{Ni}_{1.035}\text{O}_2$ heated in oxygen, air and argon. . . . .	47
Figure 3.4	TGA results for holds at 600, 700 and 800°C in either oxygen or air. . . . .	50
Figure 3.5	Unit cell volume versus x in $\text{Li}_x\text{Ni}_{2-x}\text{O}_2$ obtained by Goode-nough et al. [72], Li et al. [37], and from the present work. . . . .	51
Figure 3.6	XRD scans of nickel nitrate samples obtained after co-precipitation, drying and heating to various temperatures. . . . .	55
Figure 3.7	Results for XRD peak areas, crystallite size and micro-strain for combinatorial samples of $\text{Li}_x\text{Ni}_{2-x}\text{O}_2$ . . . . .	57

Figure 3.8	Lithium content measured by XRD versus the amount dispensed. . . . .	58
Figure 3.9	Calculated lithium content as a function of temperature. . . .	59
Figure 4.1	The entire Li-Co-Mn oxide Gibbs triangles for samples heated to 800°C in air and quenched, or regular cooled. . . . .	64
Figure 4.2	Stack of XRD patterns with fits and difference plots obtained by heating samples along the line from point A <sub>4</sub> to Li <sub>2</sub> MnO <sub>3</sub> and regular cooling. . . . .	66
Figure 4.3	Stack of XRD patterns for samples lying between LiCoO <sub>2</sub> and point A <sub>4</sub> , as well as results from using the lever rule. . . . .	67
Figure 4.4	Stack of XRD patterns with fits for layered samples made with 15 % excess lithium and heated to 900°C before quenching to room temperature. . . . .	69
Figure 4.5	Hexagonal lattice parameters obtained here by quenching as compared to literature values from Ref. [19]. . . . .	70
Figure 4.6	Calculated crystallite size obtained for samples heated at 800°C, and 900°C. . . . .	71
Figure 4.7	Stack of XRD patterns, along with two-phase fits, of samples made with 15 % excess lithium and heated to 900°C before cooling at a rate of 1°C/min. . . . .	71
Figure 4.8	Hexagonal lattice parameters obtained by heating combinatorial samples to 900°C in air and then either quenching or slow cooling. . . . .	73
Figure 4.9	XRD patterns obtained by regular cooling from 900°C with 15 % excess lithium. . . . .	74
Figure 4.10	Results of the Monte Carlo simulation for the transition metal layer for a sample midway between LiCoO <sub>2</sub> and Li <sub>2</sub> MnO <sub>3</sub> . . . .	76
Figure 5.1	The Li-Mn-Ni-O phase diagram with indicating all compositions synthesized during the combinatorial studies. . . . .	80
Figure 5.2	The complete Li-Mn-Ni-O phase diagram obtained by either quenching or slow cooling from 800°C after heating in oxygen for 3 h. . . . .	81

Figure 5.3	A partial Li-Mn-Ni-O phase diagram obtained in air with regular cooling. . . . .	82
Figure 5.4	The Gibbs triangle with labels used throughout this chapter.	82
Figure 5.5	XRD patterns of a few single-phase Li-Mn-Ni-O spinel structures.	83
Figure 5.6	Partial XRD scans of sample lying in or near the spinel region in the Li-Mn-Ni-O system. . . . .	84
Figure 5.7	Contour plots of the lattice parameter in the cubic spinel region.	85
Figure 5.8	Stack of XRD patterns for single-phase structures obtained by regular cooling in oxygen. . . . .	87
Figure 5.9	The $c/a$ lattice parameter ratio as a function of Li fraction for samples obtained by regular cooling in oxygen. . . . .	88
Figure 5.10	Contour plots of the cubic lattice parameter in the rocksalt region.	92
Figure 5.11	XRD patterns of ordered rocksalt phases obtained in oxygen. .	93
Figure 5.12	A comparison of the angles $\alpha$ and $\alpha_c$ obtained for a point X. .	95
Figure 5.13	The result of using the lever rule in the co-existence regions for samples prepared in oxygen by regular cooling. . . . .	95
Figure 5.14	XRD scans of samples in the co-existence region between the ordered rocksalt structures and the spinel structures along with the corresponding two-phase fits and difference plots. . . . .	97
Figure 5.15	The spinel lattice parameter obtained in the co-existence region between the spinel and ordered rocksalt regions as a function of $\beta$ . . . . .	98
Figure 5.16	The ordered rocksalt lattice parameter obtained in the co-existence region between the spinel and ordered rocksalt regions as a function of $\gamma$ . . . . .	99
Figure 6.1	Metal compositions obtained by atomic absorption for samples prepared by regular cooling or quenching in oxygen. . . . .	102
Figure 6.2	Contour plots of the $a$ and $c$ lattice parameters for regular cooled layered materials made in oxygen. . . . .	103
Figure 6.3	XRD scans of quenched samples in the co-existence region showing both layered and spinel structures near the Li-Mn line. . .	104

Figure 6.4	XRD scans of quenched samples in the layered-layered and layered-spinel co-existence regions. . . . .	105
Figure 6.5	A partial phase diagram indicating compositions used in Figures 6.4, 6.7, 6.10 and 6.11. . . . .	105
Figure 6.6	Lattice parameters obtained in the layered-spinel co-existence region as a function of distance from the S-M line. . . . .	107
Figure 6.7	XRD scans in the two-phase region below the NM line obtained for quenched samples. . . . .	108
Figure 6.8	XRD patterns of the four samples found at the corners of the three-phase regions for samples heated in oxygen and quenched. . . . .	110
Figure 6.9	XRD patterns generated at the four corners of the three-phase regions obtained by quenching and regular cooling. . . . .	111
Figure 6.10	XRD scans of samples in the three-phase regions obtained by quenching. . . . .	115
Figure 6.11	Partial XRD scans of samples in the three-phase regions obtained by quenching. . . . .	115
Figure 6.12	A partial phase diagram focusing on the three-phase regions for quenched samples. . . . .	117
Figure 6.13	XRD scans obtained in oxygen by quenching, regular cooling, and slow cooling. . . . .	119
Figure 6.14	A partial phase diagram with compositions used throughout this chapter. . . . .	119
Figure 6.15	XRD scans of samples in three-phase regions obtained by regular cooling. . . . .	120
Figure 6.16	Partial XRD patterns obtained in the three-phase regions by regular cooling. The labels (a, b, c...) match those used in Figure 6.17. . . . .	120
Figure 6.17	A partial phase diagram showing compositions used in Figures 6.15 and 6.16. . . . .	121
Figure 6.18	SEM images and XRD patterns of both layered and phase separated samples. . . . .	121

Figure 7.1	The pseudo-ternary phase diagrams obtained for the Li-Ni-Mn-O system for combinatorial samples. . . . .	128
Figure 7.2	XRD patterns obtained for sample A <sub>7</sub> heated to 800°C. . . . .	130
Figure 7.3	XRD patterns of samples made at the compositions A <sub>7</sub> ' and B <sub>7</sub> in the Li-Mn-Ni-O system. . . . .	131
Figure 7.4	The single-phase boundaries obtained for combinatorial samples heated in oxygen along with those obtained for bulk samples heated in air. . . . .	133
Figure 7.5	A partial Li-Mn-Ni oxide phase diagram for bulk samples synthesized in air at 900°C. . . . .	134
Figure 7.6	Electrochemical data from half-cells made with the M, N and R materials. . . . .	137
Figure 8.1	The phase diagram for samples made in oxygen and quenched with lines representing constant oxidation number lines. . . . .	140
Figure 8.2	A partial phase diagram for bulk samples quenched from 900°C with compositions indicated for samples discussed in this chapter.	141
Figure 8.3	Monte Carlo results for a sample with Li <sub>0.6</sub> Mn <sub>0.35</sub> Ni <sub>0.05</sub> . . . . .	144
Figure 8.4	XRD scans for samples A <sub>8</sub> - D <sub>8</sub> and for Li <sub>2</sub> MnO <sub>3</sub> . . . . .	146
Figure 8.5	Partial XRD patterns for samples A <sub>8</sub> - D <sub>8</sub> and for Li <sub>2</sub> MnO <sub>3</sub> . . . . .	147
Figure 8.6	Mn K-edge XANES patterns collected for samples showing metal site vacancies. . . . .	149
Figure 8.7	Results of a Monte Carlo simulation for sample D <sub>8</sub> . . . . .	150
Figure 8.8	XRD pattern and Rietveld fit for LiNi <sub>1/6</sub> □ <sub>1/6</sub> Mn <sub>2/3</sub> O <sub>2</sub> . . . . .	152
Figure 8.9	Voltage versus capacity and differential capacity versus voltage plots for LiNi <sub>1/6</sub> □ <sub>1/6</sub> Mn <sub>2/3</sub> O <sub>2</sub> . . . . .	152
Figure 8.10	Capacity versus cycle number for LiNi <sub>1/6</sub> □ <sub>1/6</sub> Mn <sub>2/3</sub> O <sub>2</sub> . . . . .	154
Figure 9.1	Partial phase diagram with contours for the <i>a</i> lattice parameter showing compositions discussed in this chapter. . . . .	156
Figure 9.2	XRD scans of samples with composition A <sub>9</sub> heated at 800°C. . . . .	161

Figure 9.3	Monte Carlo simulation results for the transition metal layer with composition $\text{Ni}_{0.4}\text{Mn}_{0.5}\text{Li}_{0.1}$ and no nickel on the lithium layer. . . . .	163
Figure 9.4	Monte Carlo simulation results of sample $\text{LiNi}_{0.5}\text{Mn}_{0.5}\text{O}_2$ with 10 % nickel on the lithium layer. . . . .	164
Figure 9.5	Capacity versus cycle number for samples with composition $\text{A}_9$ heated to $800^\circ\text{C}$ and $\text{B}_9$ heated to $900^\circ\text{C}$ . . . . .	166
Figure 9.6	Voltage curves and $dQ/dV$ for samples $\text{A}_9$ and $\text{B}_9$ cycled up to 4.4V. . . . .	168
Figure 9.7	Voltage curves and $dQ/dV$ for samples $\text{A}_9$ and $\text{B}_9$ cycled up to 4.8V. . . . .	169
Figure 9.8	Partial XRD patterns for samples $\text{A}_9$ , $\text{B}_9$ and $\text{C}_9$ . . . . .	170
Figure 9.9	Discharge capacity as a function of nominal composition $x$ in $\text{Li}_{1+x}(\text{Ni}_{0.5}\text{Mn}_{0.5})_{1-x}\text{O}_2$ . . . . .	172
Figure 10.1	The Li-Co-Mn-Ni-O pseudo-quaternary system. . . . .	175

## Abstract

The improvement of volumetric energy density remains a key area of research to optimize Li-ion batteries for applications such as extending the range of electric vehicles. There is still improvement to be made in the energy density in the positive electrode materials. The current thesis deals with determining the phase diagrams of the Li-Mn-Ni-O and Li-Co-Mn-O systems in order to better understand the structures and the electrochemistry of these materials. The phase diagrams were made through careful analysis of hundreds of X-ray diffraction patterns taken of milligram-scale combinatorial samples. A number of bulk samples were also investigated.

The Li-Mn-Ni-O system is of particular interest as avoiding cobalt lowers the cost of the material. However, this system is very complex: there are two large solid-solution regions separated by three two-phase regions as well as two three-phase regions. Comparing quenched and slow cooled samples shows that the system transform dramatically when cooled at rates typically used to make commercial materials. The consequences of these results are that much of the system must be avoided in order to guarantee that the materials remain single phase during cooling. This work should therefore impact significantly researchers working on composite electrodes.

Two new structures were found. The first was Li-Ni-Mn oxide rocksalt structures with vacancies and ordering of manganese which were previously mistakenly identified as  $\text{Li}_x\text{Ni}_{2-x}\text{O}_2$ . The other new structure was a layered oxide with metal site vacancies allowing manganese to order on two  $\sqrt{3} \times \sqrt{3}$  superlattices. The electrochemistry of both these materials is presented here.

Finally, the region where layered-layered composites form during cooling has been determined. These materials were long looked for along the composition line from  $\text{Li}_2\text{MnO}_3$  to  $\text{LiNi}_{0.5}\text{Mn}_{0.5}\text{O}_2$  and the most significant consequence of the actual locations of the end-members is that one of the structures contains a high concentration of nickel on the lithium layer. Layered-layered nano-composites formed in this system are therefore not ideal positive electrode materials and it will be demonstrated that single-phase layered materials lead to better electrochemistry.



## List of Symbols and Abbreviations Used

$2\theta$	Scattering angle
$2\theta_k$	Scattering angle for the center of the k-th X-ray diffraction peak
$\alpha, \beta, \gamma$	Angles defined in the Li-Mn-Ni-O Gibbs triangle
$\beta_k$	Integral breadth of the k-th X-ray diffraction peak
$\beta_T$	Constant used to set the temperature scale in Monte Carlo simulations
$\delta$	Ratio of an atom's charge to its oxidation state, used in Monte Carlo simulations
$\epsilon_o$	Permittivity of free space
$\eta$	Lorentzian component in the pseudo-Voigt function
$\lambda$	Wavelength
$\sigma$	Standard deviation
$\mu$	Linear X-ray absorption coefficient
$\sqrt{\langle e \rangle^2}$	Root-mean square micro-strain
AA	Atomic absorption spectroscopy
C	Lorentzian, or Cauchy, function
D	Particle diameter
$F_k$	Sample scattering X-ray diffraction intensity for the k-th peak
FWHM	Full width at half maximum
G	Gaussian function
$H_k$	FWHM of k-th X-ray diffraction peak
ICP	Inductively Coupled Plasma Optical Emission Spectroscopy
$I_k$	Calculated X-ray diffraction intensity for the k-th peak
$I_k^o$	Integrated peak intensity for the k-th X-ray diffraction peak
IRC	Irreversible capacity
$k_B$	Boltzmann constant
L	Average crystallite size
M	XRD machine peak broadening function

JCPDS	Joint Committee on Powder Diffraction Standards
$n_i$	Oxidation state of $i$ -th atom in Monte Carlo simulations
$Ni_{Li}$	Fraction of sites on the lithium layers occupied by nickel
NN	Nearest neighbour
SEM	Scanning Electron Microscopy
T	Temperature
TM	Transition metal
TGA	Thermo-gravimetric Analysis
XRD	X-ray Diffraction
XANES	X-ray Absorption Near-Edge Structure

## Acknowledgements

I would like to thank my supervisor, Dr. Jeff Dahn, for guidance, encouragement and his generous financial support. I have had many interesting and challenging discussions with Dr. Dahn over the last three years and working in his lab has given me access to state of the art research equipment and opportunities to contact world class researchers in industrial and academic fields. I am extremely grateful for the opportunity to have done my doctorate in his research group.

Thanks also go out to the present and former staff in the Department of Physics and Atmospheric Science for their assistance during my time. Thank you to Anne Murphy, Barbara Gauvin, Tanya Timmins, Jennifer Currie and Heather Anne Jennex in the physics office. I would also like to thank Andy George, Kevin Borgel, Dan Chevalier and Simon Trussler for their help and advice.

I would like to thank all members of the Dahnlab over the past few years who have made this time both very enjoyable and sufficiently insane. A number of students were directly involved in this work, including Aaron Rowe, Colby Brown, Cassandra Lowartz, Cody Watson, John Camardese, Paul Duchesne and Ramesh Shunmugasundaram and I would to thank them all for working and arguing with me. I would also like to thank Jennifer Romero, Robbie Sanderson, David Stevens and Trevor Byrne for a lot of help with knowing how to use and fix a variety of equipment. I also thank all the coopians for much needed distractions and useful conversations! Thanks also goes to Laura Downie who ensured I survived the writing of this thesis.

I am, as always, thankful to my family and friends who have supported me throughout.

Halifax, December 2013

Eric McCalla

# Chapter 1

## Introduction

### 1.1 Motivation: Li-Co-Mn-Ni Oxide Materials

Improving the energy density of lithium-ion batteries remains important for a number of applications. In particular, high energy densities are required to extend the range of electric vehicles and minimize the space and mass of the battery pack. In the on-going search for means to increase the energy of Li-ion batteries, the discovery of new positive electrode materials is of critical importance. The positive electrode is synthesized with lithium in it, some of which is removed during charging of the cell along with electrons that travel through the external circuit. The lithium is then re-inserted into the material while the battery is discharged, which is accompanied by electrons traveling through the external circuit to do work. There are many challenges with respect to finding better positive electrode materials, the primary of which are increasing the volumetric energy density, lowering the cost and improving the safety. Though safety is a very important issue with respect to lithium-ion batteries, the focus of this thesis will be to maximize energy while trying to minimize cost.

Table 1.1 shows the volumetric energy density of the most competitive positive electrode materials, calculated from data from Ref. [2]. The most common commercially used positive electrode,  $\text{LiCoO}_2$ , has an energy density of  $3.05 \text{ Wh/cm}^3$  while the material with the highest energy density,  $\text{Li}[\text{Li}_{1/9}\text{Ni}_{1/3}\text{Mn}_{5/9}]\text{O}_2$ , is a lithium-rich layered oxide material that has roughly 25% more energy than  $\text{LiCoO}_2$ . The lithium-rich layered structures are very promising as possible next generation high energy positive electrodes. They exist over wide composition ranges within the Li-Co-Mn-Ni-O system [3, 4] and will be discussed in detail throughout this thesis. Despite the potentially very high energy density, there remains challenges with respect to these materials and this will be discussed throughout the thesis. The primary motivation for studying the Li-Co-Mn-Ni-O system is therefore that many promising materials

Table 1.1: The median voltage, specific capacity, crystallographic density and volumetric energy density of some oxide materials that are either commercially available or promising candidates for next generation Li-ion batteries.

Material	Specific capacity (mAh/g)	Median voltage (V)	Crystallographic density (g/cm <sup>3</sup> )*	Volumetric Energy (Wh/cm <sup>3</sup> )
LiCoO <sub>2</sub>	155	3.9	5.05	3.05
LiNi <sub>1-x-y</sub> Mn <sub>x</sub> Co <sub>y</sub> O <sub>2</sub>	140-180	3.8	4.77 (x=y=1/3)	2.54-3.26
LiMn <sub>2</sub> O <sub>4</sub>	100-120	4.05	4.29	1.74-2.08
Li[Li <sub>1/9</sub> Ni <sub>1/3</sub> Mn <sub>5/9</sub> ]O <sub>2</sub>	240	3.8	4.45	4.06
LiNi <sub>0.5</sub> Mn <sub>1.5</sub> O <sub>4</sub>	130	4.6	4.4	2.63
LiFePO <sub>4</sub>	160	3.45	3.60	1.99
LiNi <sub>0.8</sub> Co <sub>0.15</sub> Al <sub>0.05</sub> O <sub>2</sub>	200	3.73	4.75	3.54

\* The crystallographic densities were obtained from either the JCPDS database or from Refs. [3, 5, 6].

have already been found in this system. For example, all the materials listed in Table 1.1 lie within this system except for the last two, one of which is LiFePO<sub>4</sub> with the lowest energy density of those listed. It must be emphasized here that the primary objective here is maximizing volumetric energy density. For applications where gravimetric energy density and particularly power are more critical materials such as LiFePO<sub>4</sub> are of greater importance. Table 1.1 therefore demonstrates why looking for materials with maximum energy in the Li-Co-Mn-Ni-O system is warranted for applications where the objective is to maximize energy within a limited volume. A particular effort must be made to minimize the cobalt content to lower the cost of the material.

Much work has already been performed on materials in the Li-Co-Mn-Ni-O system as potential positive electrode materials. Typical studies map out composition lines and, as a result, a number of useful single phase systems were discovered such as Li<sub>1+x</sub>Mn<sub>2-x</sub>O<sub>4</sub> [7-9] and Li[Ni<sub>x</sub>Mn<sub>x</sub>Co<sub>1-2x</sub>]O<sub>2</sub> [6, 10]. The current project is limited to two subsets of this system: Li-Mn-Ni-O and Li-Co-Mn-O. The objective is to map these two systems out in their entirety which has never been done before. Carey and Dahn demonstrated that a combinatorial solution-based approach can be used

to synthesize oxide materials by making Li-Ni-Mn-O spinel materials [11]. The main goal of this thesis is to adapt this method for use over the two systems of interest.

Each of the Li-Mn-Ni-O and Li-Co-Mn-O systems can be viewed as Gibbs triangles, though this implies plotting compositions based on metallic fractions only. As such, these systems will be referred to as “pseudo-ternary” because the oxygen content of the samples was not controlled and reached equilibrium concentrations as the samples were synthesized. However, non-quenched samples only reached near-equilibrium since the oxygen content for slow cooled samples is affected by the kinetics during cooling. Given that phase transformations occur during cooling [12], as will be discussed extensively throughout the thesis, the pseudo-ternary phase diagrams presented here are in fact phase stabilities, or meta-stabilities in the case of the slow cooled system where equilibrium conditions are never reached [13]. The phase diagrams typically shown for such systems prior to this work are far from complete with no studies looking at the materials over all composition ranges. This has severely limited the extent to which single-phase regions have been explored and has made studies of composite electrodes particularly difficult since the phases involved in the co-existence regions have not been precisely determined [14, 15]. This thesis is therefore part of a project that has as ultimate goal to examine the entire Li-Co-Mn-Ni oxide pseudo-quaternary phase diagram and should be of significant interest to the Li-ion research community. Figure 1.1 shows the Gibbs pyramid representing the pseudo-quaternary system. The Li-Co-Mn and the Li-Ni-Mn oxide systems studied here are faces on the pyramid. Some of the results from this project for quenched samples have been included in Figure 1.1.

The rest of this introduction deals primarily with the state of knowledge prior to the current project, with a particular emphasis on points of confusion in the literature where the phase diagrams developed here allow for a better understanding of previously published results. Throughout the introduction, these points of confusion will be numbered in bold roman numerals, i.e. **I**, **II**, **III**..., and these will be re-visited in the Conclusions and Future Works chapter.

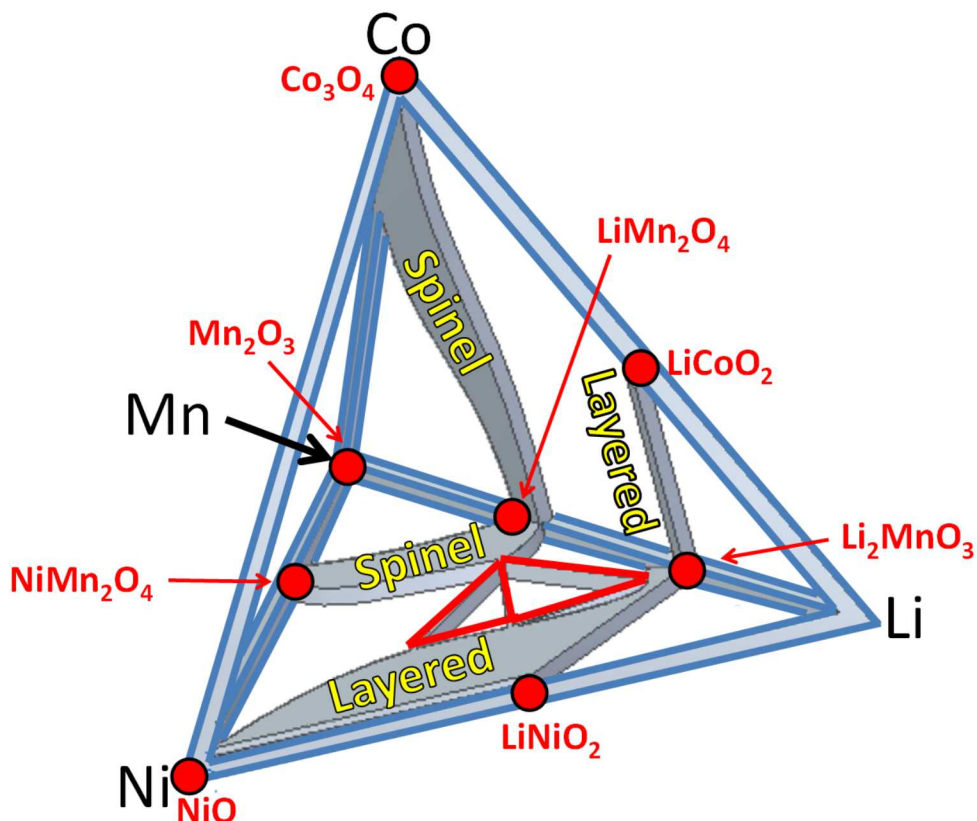


Figure 1.1: The Li-Co-Mn-Ni-O pseudo-quaternary system of extreme interest for potential positive electrode materials. The blue lines indicate the axes, while the red dots represent a few of the single-phase materials known prior to the current study. The single-phase regions along the Li-Co-Mn and Li-Mn-Ni faces are shown and are the results of this project for samples quenched from 800°C and the red lines bound three-phase regions.

## 1.2 Layered and Spinel Structures

Both faces of interest in Figure 1.1 contain two large single-phase regions of high promise as potential positive electrode materials: the layered and spinel phases. There are materials with either of these structures that are commercially relevant and each will be discussed in depth in this thesis. The layered materials can be viewed as ordered rocksalt structures with parallel sheets of atoms where each sheet is made up of hexagonal arrays. These layers alternate following the pattern: lithium, oxygen, transition metal (TM), oxygen, lithium... All lithium atoms are in octahedral sites

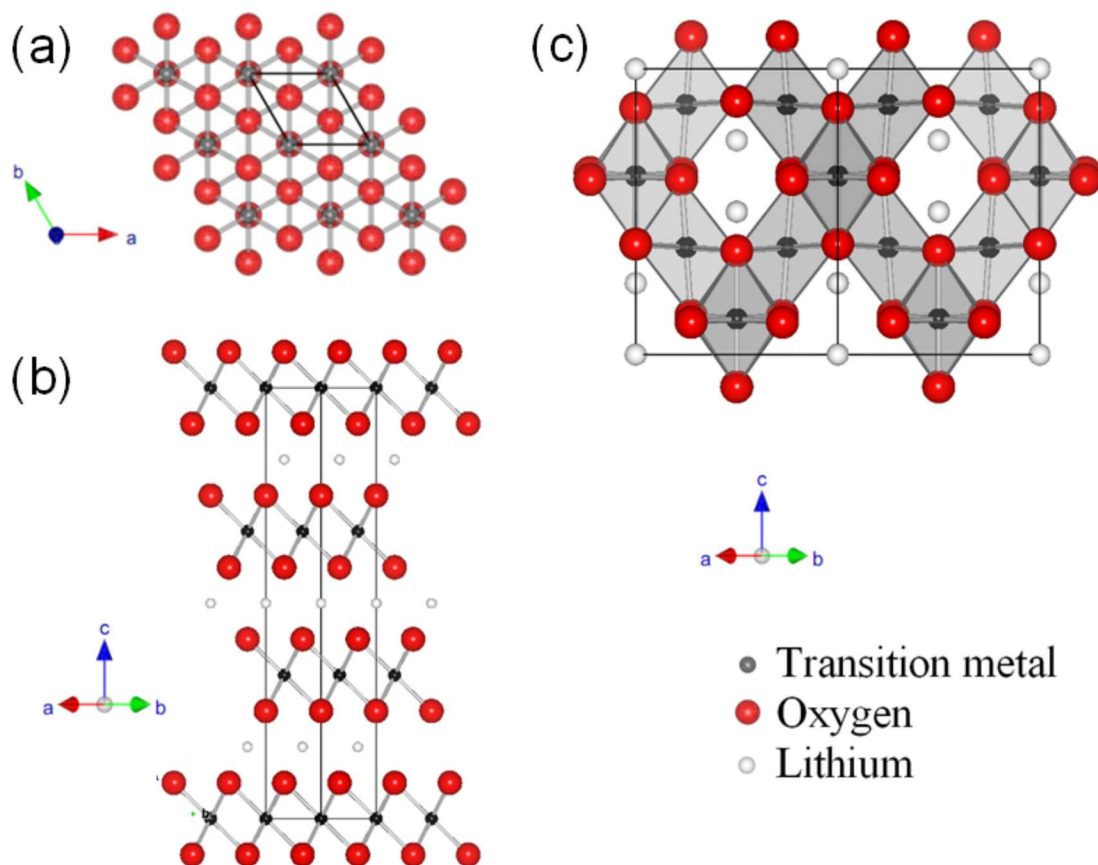


Figure 1.2: Structure of a layered lithium metal oxide along the 001 projection (a) and the 110 projection (b). (c) Structure of a cubic spinel along the 110 projection showing the lithium atoms in the tunnels. The bonds between transition metal atoms and oxygen atoms are shown as well as the edges of the unit cell. The octahedra shown in (c) have a transition metal atom at the center and six oxygen atoms at the corners.

in these structures (6 nearest neighbour oxygens forming an octahedron). Figure 1.2 shows the structures of the layered and spinel phases. Examples of layered metal oxides that are currently used commercially are:  $\text{Li}[\text{Co}]\text{O}_2$  and  $\text{Li}[\text{Ni}_{1/3}\text{Mn}_{1/3}\text{Co}_{1/3}]\text{O}_2$  where the square brackets represent the transition metal layer [2]. This notation will be used throughout this thesis in situations where it is useful to distinguish between the lithium layers and the TM layers. Barring any vacancies or other defects, these materials have a one-to-one oxygen-to-metal ratio. It is important to notice that this



idealized structure changes considerably as compositions are altered, e.g. some nickel is often present in the lithium layer and lithium can be found in the TM layer [3].

Charging a lithium-ion cell with a positive electrode having a layered oxide structure removes lithium by way of two different mechanisms. The first is de-intercalation of lithium wherein the oxidation number of one of the transition metals increases in order to maintain an overall zero oxidation number in the electrode material. The second mechanism is less well understood and takes place around 4.5 V in materials with excess lithium and results in some lithium remaining after all transition metal atoms have been oxidized [3]. This capacity near 4.5 V, referred to here as the “high voltage plateau”, is accompanied with a phase transformation [16, 17] and may also involve the production of oxygen gas [18]. The amount of oxygen loss may depend on the stoichiometry of the starting material [16]. Although some electrochemical studies are included in this thesis, the primary focus will be the structures of the starting materials such that an in-depth description of the electrochemical behaviour of these materials will not be included in this introduction. It is sufficient to point out that lithium can be removed from the layered materials by way of 2-D transport along the hexagonal planes.

Figure 1.2 (c) shows that the spinel structures have lithium atoms aligned in rows within the cubic lattice. Here, every lithium atom is in a tetrahedral site, surrounded by four nearest neighbour oxygens. In spinel structures, the oxygen content is higher than for layered materials as there are four oxygen atoms per three metal atoms. This higher oxygen content in the spinels will be significant in discussing how the boundaries of the single-phase regions move under various synthesis conditions. Charging of a cell made with a spinel positive electrode involves one dimensional lithium-ion transport through the 3-D network of tunnels and proceeds by the de-intercalation mechanism described for the layered structures [2].

While no attempt has been made to precisely work out electronic structures of the layered and spinel materials, simple models considering the oxidation state of each metallic atom can be very useful in predicting the possible mechanisms taking place during cycling. To illustrate the importance of the oxidation states of the starting materials, consider  $\text{LiMn}_2\text{O}_4$ . The initial average oxidation number of the manganese

is 3.5+ such that all the lithium can be removed while the manganese transitions to the 4+ state. However, it is possible to synthesize  $\text{Li}_{1+x}\text{Mn}_{2-x}\text{O}_4$  materials with more lithium, up to a maximum of  $\text{Li}_{4/3}\text{Mn}_{5/3}\text{O}_4$  [8,9]. In this material, all manganese is in the 4+ state such that no redox transition is possible and thus no lithium can be removed in the potential window typically used (below 5.0 V vs  $\text{Li}^+/\text{Li}$ ). This illustrates how very simple models can be useful. This approach will be used throughout this thesis to discuss the electronic structures of the metals in these complex structures as they undergo changes during electrochemical cycling.

### 1.3 The Li-Co-Mn-O Face of the Pyramid

Figure 1.3 shows the single-phase structures known in the Li-Co-Mn-O system prior to the current work. To demonstrate how these Gibbs triangles are constructed, consider the sample  $\text{LiCo}_{2/3}\text{Mn}_{4/3}\text{O}_4$  that has metallic fractions  $\text{Li}_{1/3}\text{Co}_{2/9}\text{Mn}_{4/9}$  and is therefore plotted at the point  $(\text{Li}, \text{Co}, \text{Mn}) = (0.333, 0.222, 0.444)$ . The tick marks on all ternary diagrams are slanted to make the values of the three axes more apparent. Only the metal atoms obey the rules of a Gibbs triangle and the three axes are therefore the metal atomic fractions with  $\text{Li} + \text{Co} + \text{Mn} = 1$  for all points. The labels at the three corners only show the phases present at the corners. Also, since the cobalt content can be calculated as  $1 - \text{Li} - \text{Mn}$ , all points will be shown as  $(\text{Li}, \text{Mn})$ , such that  $(0.333, 0.444)$  refers to  $\text{LiCo}_{2/3}\text{Mn}_{4/3}\text{O}_4$ ,  $(0.333, 0.666)$  refers to  $\text{Li}_2\text{MnO}_3$  and  $(0.5, 0)$  refers to  $\text{LiCoO}_2$ . It is worth noting that since the oxygen content varies through the triangle, this pseudo-ternary diagram represents a non-planar surface in the Li-Mn-Ni-O quaternary system. As such, the oxygen content at any point is not only a function of the position within the triangle but also depends on the synthesis conditions. The atmosphere and temperature profiles used during heating are particularly important.

Figure 1.3 also shows that only a few spinel structures were known in this triangle prior to this research [20–22]. However, the fact that the cobalt corner takes a cubic spinel structure,  $\text{Co}_3\text{O}_4$ , and the placement of the other single-phase spinel materials, suggests that there may be a large spinel region spanning from  $\text{LiMn}_2\text{O}_4$  to  $\text{Co}_3\text{O}_4$ .

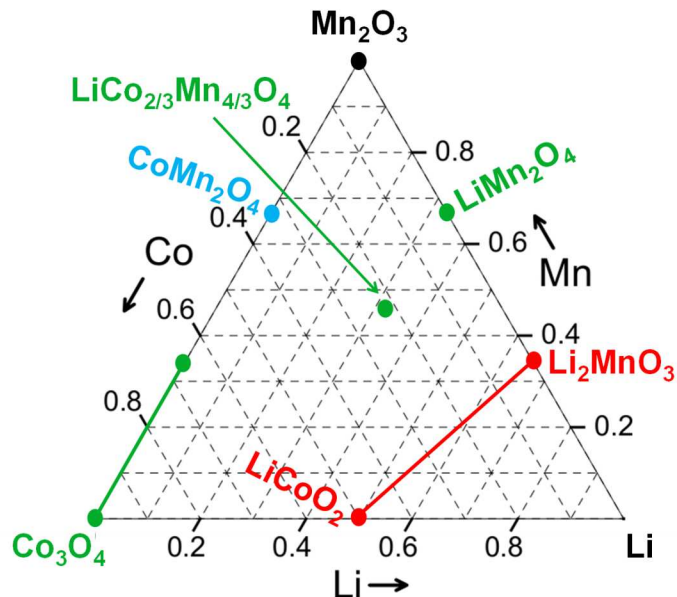


Figure 1.3: The Li-Co-Mn-O pseudo-ternary system with single-phase materials known prior to the combinatorial studies discussed here. The red symbols indicate layered oxides while the green and blue are cubic and tetragonal spinels, respectively, and the black circle represents bixbyite  $\text{Mn}_2\text{O}_3$ . The lithium corner is labeled as Li as no stable solid phases are seen here as lithium is gradually lost during synthesis.

The layered structures in the Li-Co-Mn oxide system have been studied extensively along the composition line  $\text{Li}[\text{Li}_{(1-x)/3}\text{Co}_x\text{Mn}_{(2-2x)/3}]\text{O}_2$ ;  $0 \leq x \leq 1$ , which joins  $\text{LiCoO}_2$  to  $\text{Li}_2\text{MnO}_3$  [19, 23, 24]. Figure 1.4 shows X-ray diffraction (XRD) patterns along this composition line reported by Kim et al. [19]. The XRD pattern for  $\text{LiCoO}_2$  can be attributed to the layered structure described in the previous section where nearly every site on the TM layer is occupied by cobalt. All scattering peaks can be indexed to the R-3m space group, which has a hexagonal lattice with every unit cell being made up of three TM layers and three lithium layers (this stacking is referred to as O3-type and is illustrated in Figure 1.2 (b)). Figure 1.5 shows two possible arrangements of atoms on TM layers. The first, shown in (a), assumes random occupation of all sites as would be obtained for  $\text{LiCoO}_2$ . For  $\text{Li}_2\text{MnO}_3$ , however, there are extra peaks seen in the scattering angle range  $20\text{-}30^\circ$  which can be attributed to ordering on the TM layer [25]. Figure 1.5 (b) shows such an ordered layer where the red atoms represent lithium while the blue atoms represent manganese. The red

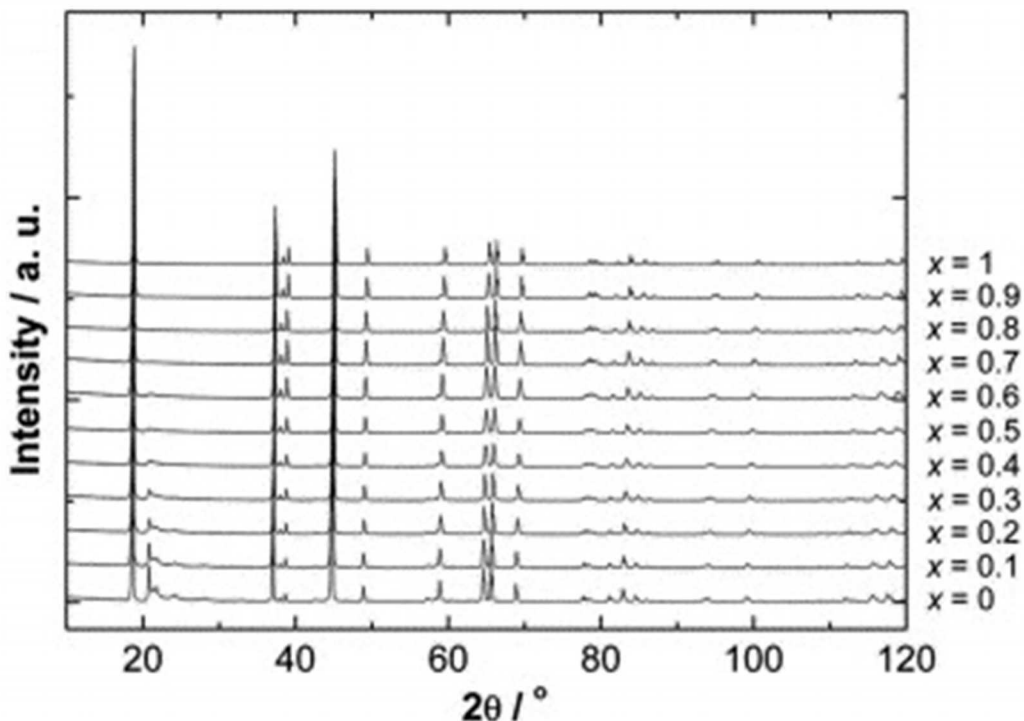


Figure 1.4: Stack of XRD patterns for various values of  $x$  along the line from  $\text{Li}_2\text{MnO}_3$  ( $x = 0$ ) to  $\text{LiCoO}_2$  ( $x = 1$ ) reprinted from Ref. [19] with permission from Elsevier. Vertical offsets applied for clarity, as is the practice throughout this thesis.

atoms all lie on a lattice that is  $\sqrt{3}$  times larger in each direction than the hexagonal lattice shown in (a). As such, this ordered lattice will be referred to as a  $\sqrt{3} \times \sqrt{3}$  superlattice. The ordering on the TM layer is typically accompanied by a distortion in the stacking of the layers such that the structure can no longer be described as a hexagonal lattice, but instead a monoclinic unit cell is required. Typically, the  $C2/m$  space group is used to describe these structures. However, the monoclinic distortions in the lattice for  $\text{Li}_2\text{MnO}_3$  are relatively small and require long annealing times at high temperature to develop extended long range order [25]. These distortions can best be seen in a peak splitting in the (104) hexagonal peak near  $45^\circ$  in the XRD patterns, which is replaced by the (-202) and (131) peaks in the monoclinic structure. Some of the XRD patterns obtained in this thesis were refined for both space groups in order to determine where monoclinic distortions became significant.

There is no consensus in the literature as to whether the line from  $\text{LiCoO}_2$  to

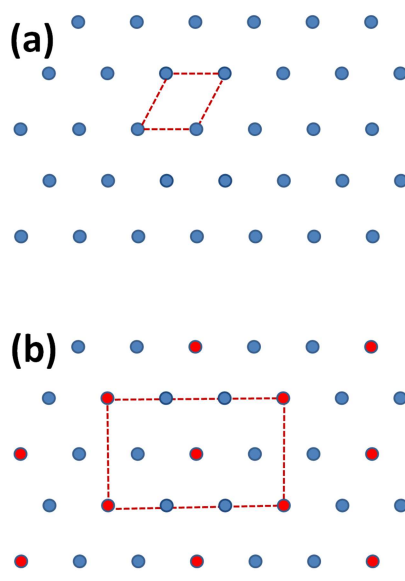


Figure 1.5: (a) A hexagonal array of atoms as seen in layered Li-Mn-Ni oxides as would be obtained for a disordered transition metal layer where every site is randomly occupied by Ni, Mn and/or Li. The red dashed lines indicate the unit cell. (b) A transition metal layer showing ordering where one third of the sites are red (e.g. lithium in  $\text{Li}_2\text{MnO}_3$ ) and the other two thirds are blue (e.g. manganese in  $\text{Li}_2\text{MnO}_3$ ). The red dashed lines show the monoclinic unit cell necessary to describe the structure.

$\text{Li}_2\text{MnO}_3$  forms a solid solution [19] or if there is phase separation taking place on the nanometer length scale [24]. Kim et al. found that the XRD patterns were consistent with a solid solution with peaks indexing to either a hexagonal space group, R-3m (over the entire composition range), or to the ordering peaks in the C2/m space group, which increased in intensity as the  $\text{Li}_2\text{MnO}_3$  endpoint was approached. However, careful examination of the published XRD patterns from Kim et al. (Figure 1.4) shows that the peaks at high scattering angles broaden near the center of the line (near  $x = 0.4$  to  $0.6$ ). This broadening could either be due to a reduction in crystallite size [26] or to the co-existence of two closely related structures. One objective of this project is to determine the actual source of the peak broadening and to develop tools to help distinguish these two situations as this occurs repeatedly in these systems I.

In contrast to the solid-solution model, studies by Wen et al. [23] and Bareño et al. [24] show transmission electron microscopy (TEM) and X-ray absorption near edge structure (XANES) data suggesting layered-layered phase separation takes place

on the 2-10 nm length scale for a sample made at 900°C with composition  $x = 0.4$ . This sample lies in the region where peak broadening can be seen in the XRD data published by Kim et al. [19]. Figure 1.6 shows TEM data demonstrating that two different domains, separated by dashed lines, exist. The domains made up of rows of pairs of atoms are attributed to  $\text{Li}_2\text{MnO}_3$  where only the 2/3 of sites occupied by manganese appear in the image. Figure 1.7 shows the outcome of a simple model used to illustrate the phase separation on the TM layer. The model was made by Bareño [24] assuming the composite material was made up of domains of pure  $\text{LiCoO}_2$  (Co on TM layer) and  $\text{Li}_2\text{MnO}_3$  ( $\text{Mn}_{2/3}\text{Li}_{1/3}$  on the TM layer). For both of these phases, the lithium layer is filled solely with lithium atoms such that the phase separation does not affect the lithium layer. However, on the transition metal layer the result yields nano-scale domains of each phase. An important question to be answered is whether or not the presence of these nano-scale domains can be detected in the XRD patterns. This depends greatly on the difference in lattice parameters between the two phases (if they are sufficiently different, the phase separation should at the very least result in severe peak broadening). Since TEM data cannot be used to determine the compositions of each phase present, it will be important to determine whether or not phase separation does occur over the entire  $\text{LiCoO}_2$  -  $\text{Li}_2\text{MnO}_3$  composition line. Chapter 4 of this thesis will deal with this region of the Gibbs triangle and will help determine over which composition ranges the phase separation actually occurs and which conditions give rise to the co-existence **II**.

#### 1.4 The Li-Mn-Ni-O Face of the Pyramid

Figure 1.8 (a) shows the Li-Mn-Ni-O pseudo-ternary phase diagram with single-phase regions that had already been studied extensively before this project. Again, as in the Li-Co-Mn system, points in the Gibbs triangles will be denoted by two coordinates: (Li, Mn). Here, the nickel metal content is  $1 - \text{Li} - \text{Mn}$ . It warrants pointing out that computational combinatorial science has already been invaluable in screening for potential electrode materials [27–29]. However, Figure 1.8 (b) shows that the public materials database [30] is currently limited to the binaries at the outer edges of the triangle and no solid solution regions extending into the triangle have yet been

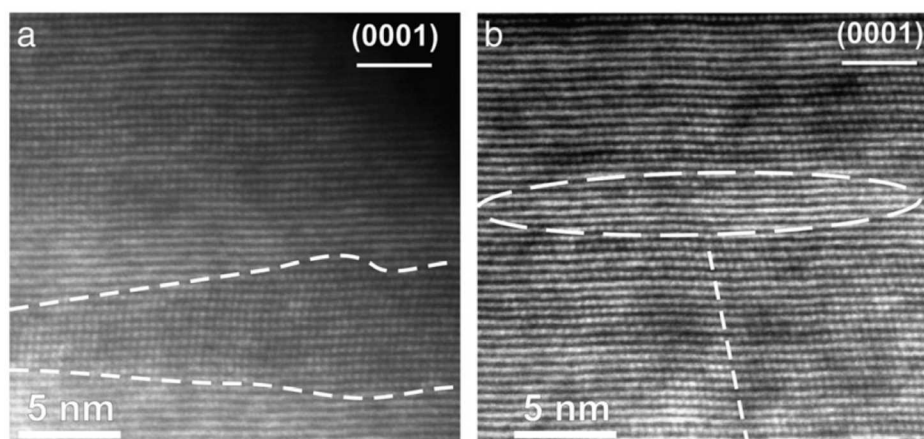


Figure 1.6: TEM images of  $\text{Li}_{1.2}\text{Co}_{0.4}\text{Mn}_{0.4}\text{O}_2$  showing the co-existence of layered and monoclinic domains on the nano-scale, reprinted from Ref. [23] with permission from Elsevier.

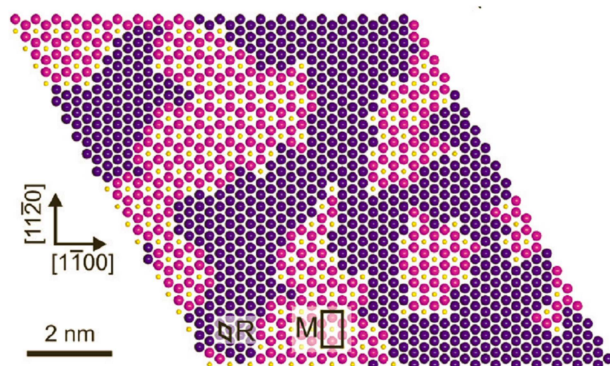


Figure 1.7: A schematic of layered-layered phase separation with domains of  $\text{Li}_2\text{MnO}_3$  and  $\text{LiCoO}_2$ , reprinted from Ref. [24] with permission from the American Chemical Society. Lithium atoms are yellow, while manganese atoms are purple and cobalt atoms are blue.

identified by such methods. Therefore, a large amount of work must yet be done before computations can fill in the system with the accuracy required, particularly in the co-existence regions where identifying what phases co-exist is particularly computationally demanding. As such, an experimental approach is used here and this system has been mapped out in its entirety by making samples at over 300 different compositions.

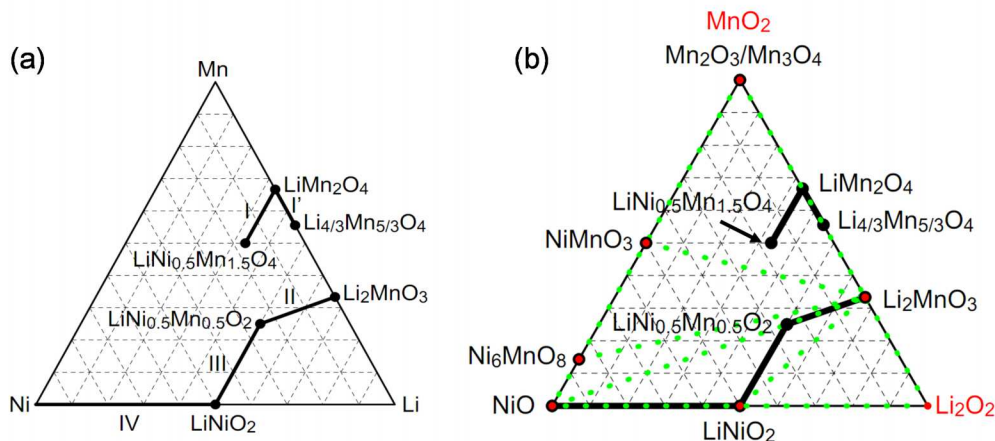


Figure 1.8: (a) The Li-Mn-Ni oxide pseudo-ternary system where the corners refer to the metals used during sample preparation and oxygen content varies throughout the triangle. The bold lines represent lithium-containing single-phase regions. Spinel samples are along line I:  $\text{LiNi}_x\text{Mn}_{2-x}\text{O}_4$  with  $0 \leq x \leq 0.5$ . Samples along the line labeled I' are spinel at lower temperatures but phase separate at the higher temperatures dealt with here. The other lines are rocksalt structures. Line II is layered  $\text{Li}[\text{Li}_{(1-2x)/3}\text{Ni}_x\text{Mn}_{(2-x)/3}]\text{O}_2$ ;  $0 \leq x \leq 0.5$ , III is  $\text{Li}[\text{Ni}_{1-x}\text{Mn}_x]\text{O}_2$ ;  $0 \leq x \leq 0.5$  and IV is  $\text{Li}_x\text{Ni}_{2-x}\text{O}_2$ ;  $0 \leq x \leq 1$ . (b) The same diagram with single-phase samples predicted by the public materials database [30] in green dotted lines are tie-lines at the edges of three-phase regions.

Carey and Dahn [11] successfully used a combinatorial robot to synthesize  $\text{LiNi}_x\text{Mn}_{2-x}\text{O}_4$  spinel samples (line I in Figure 1.8) by carbonate co-precipitation of microliter mixtures of lithium, manganese and nickel nitrates followed by heating to  $800^\circ\text{C}$  in air. It is therefore tempting to apply this method to all samples throughout the triangle. However, there is a significant challenge: certain regions show extreme lithium loss during synthesis such that certain sections of the triangle cannot be synthesized even at  $700^\circ\text{C}$  in air. In the literature, this loss is either viewed as  $\text{Li}_2\text{O}$  evaporation [31] or the formation of lithium peroxide vapour [32].  $\text{LiNiO}_2$  has a low lithium binding energy and so it shows some of the highest losses; typically 5% in bulk samples synthesized by solid-state reactions and heated in air [33,34]. The small combinatorial samples result in far greater losses due to the larger surface area to volume ratios, while the  $\text{LiNi}_x\text{Mn}_{2-x}\text{O}_4$  spinel samples showed virtually no lithium loss [11] due to the larger lithium binding energy. Thus, before studying the entire system in Figure



1.8, the lithium loss in the lithium nickel oxide samples must be minimized. This will be explored in Chapter 3 and will help resolve whether lithium is lost as lithium oxide or peroxide **III**.

Once again, the key structures for lithium-ion batteries in the Li-Mn-Ni-O diagram are either spinel or layered. Line I represents spinel samples with composition  $\text{LiNi}_x\text{Mn}_{2-x}\text{O}_4$  with  $0 \leq x \leq 0.5$  [7,35], while samples along line I' are spinel at lower temperatures [8,9]. The other lines are layered structures: line II is the lithium-rich layered line  $\text{Li}[\text{Li}_{(1-2x)/3}\text{Ni}_x\text{Mn}_{(2-x)/3}]\text{O}_2$ ;  $0 \leq x \leq 0.5$  [3], III is  $\text{Li}[\text{Ni}_{1-x}\text{Mn}_x]\text{O}_2$ ;  $0 \leq x \leq 0.5$  [36] and IV is  $\text{Li}_x\text{Ni}_{2-x}\text{O}_2$ ;  $0 \leq x \leq 1$  [37]. Another composition line in the triangle that has previously been studied in detail is the  $\text{Li}_x\text{Ni}_{2-x}\text{O}_2$  line from  $x = 0$  to 1 (from the Ni corner to  $\text{LiNiO}_2$ ). For  $x < 0.62$ , samples are cubic rocksalt where the metal atoms occupy a face-centered cubic lattice and every metal site is randomly occupied. Though these materials are not interesting as positive electrodes they warrant study because they often appear as contaminants in the synthesis of either spinel materials or layered-spinel composites as discussed below. Above  $x = 0.62$ , the structures are hexagonal with the lithium and nickel preferentially ordering on alternating layers as illustrated in Figure 1.2 (a) [37]. The transition at  $x = 0.62$  can be identified by fitting the XRD patterns as hexagonal and plotting the  $c/a$  lattice parameter ratio versus  $x$ . Extrapolating to the point where the ratio reaches  $\sqrt{24}$ , the expected value for a cubic structure [37] gives the position of the phase transition. This method will be used in Chapter 5.

#### 1.4.1 Li-Mn-Ni-O Spinel Solid-Solutions

The spinel solid solution (line I in Figure 1.8) has been thoroughly studied. The nickel-rich endpoint,  $\text{LiNi}_{0.5}\text{Mn}_{1.5}\text{O}_4$ , is single-phase when prepared in oxygen but shows a contaminant rocksalt phase when heated in air [35]. More recently, Ma et al. attributed the contaminant to  $\text{Ni}_6\text{MnO}_8$  [38] while Cabana obtained a cubic lattice parameter of 4.15 Å leaving the stoichiometry of the contaminant phase undetermined [39]. This confusion about the actual composition of this contaminant will be resolved here by mapping out the entire spinel-rocksalt co-existence region carefully **IV**.

It is also important to be mindful that  $\text{LiNi}_{0.5}\text{Mn}_{1.5}\text{O}_4$  spinel can sustain oxygen

vacancies at high temperature and that oxygen returns into the sample during slow cooling [40, 41]. Compositions of  $\text{LiNi}_{0.5}\text{Mn}_{1.5}\text{O}_{4-\delta}$  with  $\delta = 0.1$  were obtained at temperatures at or above  $750^\circ\text{C}$  [42]. However, it is hard to distinguish this from phase separation with the formation of the rocksalt phase since both occur simultaneously in air and both result in an increase in the lattice parameter as well as a mass decrease due to oxygen loss. The observations in Chapter 5 comparing quenched and slower cooled samples over wide composition ranges helps distinguish these two forms of oxygen loss **V**.

#### 1.4.2 Li-Mn-Ni-O Layered Solid-Solutions

As previously mentioned, the lithium-rich layered oxide structures have alternating lithium and transition metal hexagonal layers, with some excess lithium on the TM layers. Figure 1.9 and Ref. [3] show that when synthesized in air these structures form a solid-solution along the whole composition line at or above  $800^\circ\text{C}$  according to the XRD patterns [3]. Once again, although the structures in the layered region are all O3-type, they are not all described by the same space group. For example,  $\text{Li}_2\text{MnO}_3$  takes a monoclinic structure best described by the C2/m structure while  $\text{LiNi}_{0.5}\text{Mn}_{0.5}\text{O}_2$  takes an R-3m hexagonal structure with random occupation on the TM layer [43]. One important point of conflict in the literature is whether or not the Li-rich line forms a solid solution. Some argue that the superlattice peaks seen in the XRD patterns of samples where the lithium content on the TM layer is not  $1/3$  is an indication of local phase separation into  $\text{Li}_2\text{MnO}_3$  and  $\text{LiNi}_{0.5}\text{Mn}_{0.5}\text{O}_2$  domains on the nanometer length scale [44, 45]. Lu et al., however, suggested that the weak ordering peaks can be attributed to ordering of lithium and manganese on the transition metal layers with nickel randomly occupying the remaining sites [46].

Figure 1.10 shows how Lei et al. [45] used TEM data to support the claim that this phase separation occurs in  $\text{Li}_{1.2}\text{Ni}_{0.2}\text{Mn}_{0.6}\text{O}_2$  while Jarvis et al. [47] presented TEM data supporting that this same structure is made up of a single phase. Figure 1.11 shows TEM images of single-phase  $\text{Li}_2\text{MnO}_3$  with domains of perfect O3 stacking with the ordering expected for this material. However, there are significant concentrations of stacking faults which seem to occur on roughly the same scale as the new phase

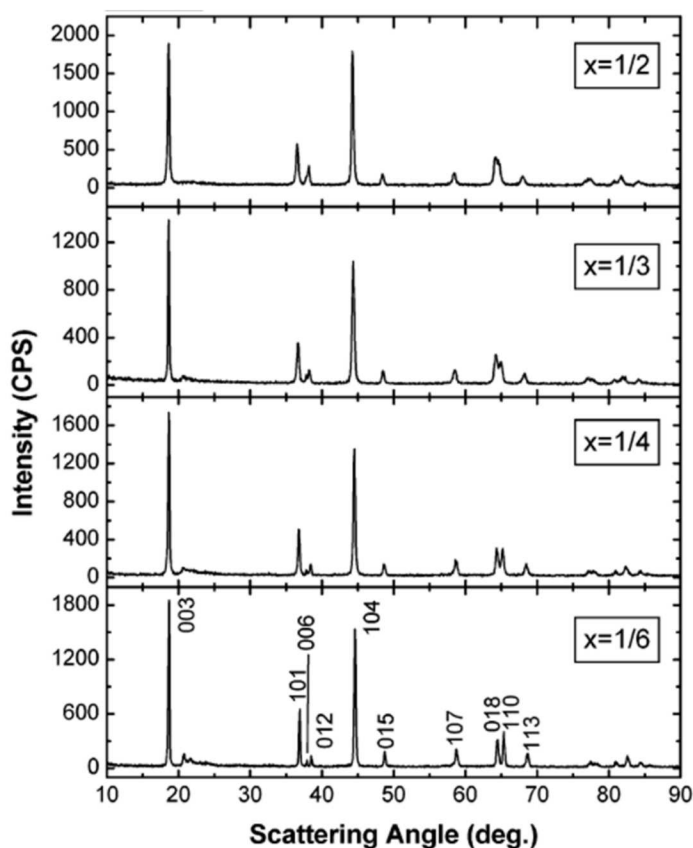


Figure 1.9: XRD patterns, reprinted from Ref. [46] with permission from the American Chemical Society, for samples along the composition line from  $\text{Li}_2\text{MnO}_3$  ( $x=0$ ) and  $\text{LiNi}_{0.5}\text{Mn}_{0.5}\text{O}_4$  ( $x=0.5$ ). Peaks are indexed according to the R-3m space group for hexagonal structures.

identified by Lei et al. in Figure 1.10 (b). Clearly, TEM studies of these materials remain inconclusive as to whether or not short range phase separation occurs. The phase diagrams obtained here offer significant insight into the compositions at which layered-layered phase separation might occur and under which conditions. This work therefore helps resolve this issue **VI**.

Recent work, again on the lithium-rich layered oxide  $\text{Li}_{1.2}\text{Ni}_{0.2}\text{Mn}_{0.6}\text{O}_2$ , has suggested that as much as 25 % of the manganese is in the 3+ oxidation state based primarily on the fact that the magnetic moment was lower than that expected if all manganese is in the 4+ state [49]. This result is unexpected since research shows that manganese is typically synthesized in the 4+ state in the lithium-rich layered

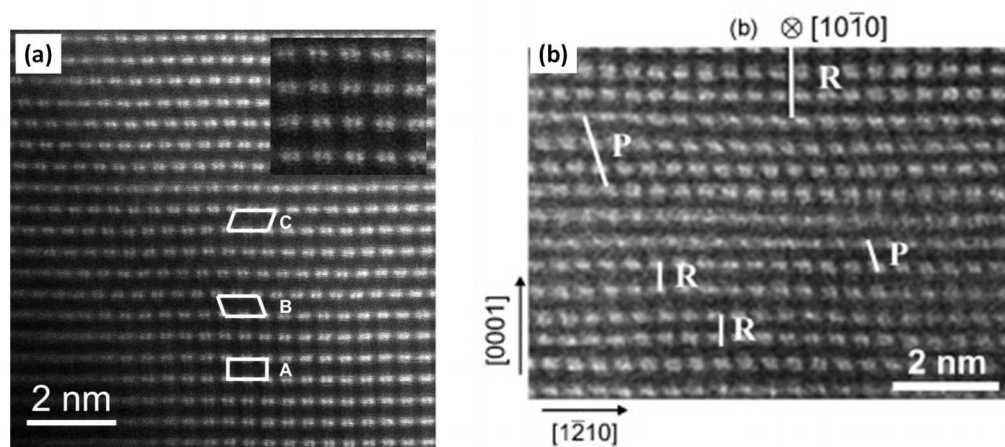


Figure 1.10: TEM images of  $\text{Li}_{1.2}\text{Ni}_{0.2}\text{Mn}_{0.6}\text{O}_2$ : (a) reprinted from Jarvis et al., Ref. [47], with permission from the American chemical society. (b) reprinted from Lei et al., Ref. [45], with permission from Elsevier.

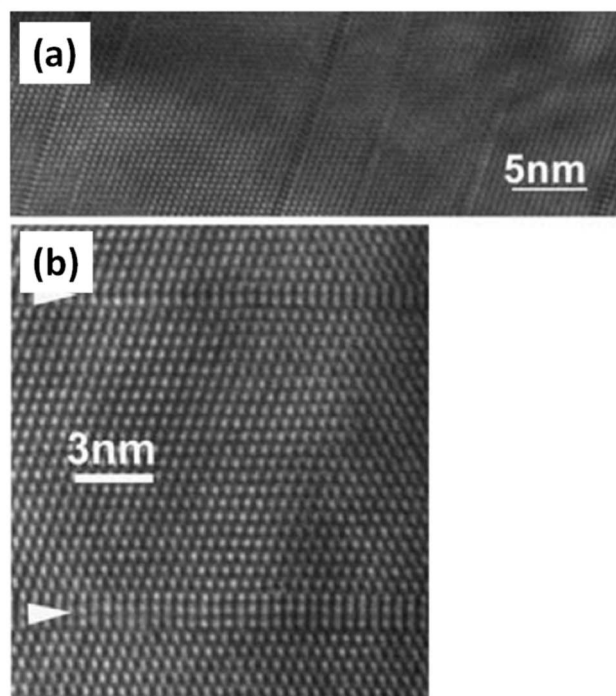


Figure 1.11: TEM images of single-phase  $\text{Li}_2\text{MnO}_3$ , reprinted from Ref. [48] with permission from Springer, showing ordered domains with stacking faults (one of which is indicated by the white arrow).

oxides [50, 51]. A better understanding of these layered structures, as determined in Chapter 8, will help explain these discrepancies **VII**.

The final source of confusion in the literature relating to the lithium-rich structures involves the use of excess lithium during synthesis. As discussed here, the samples lose some lithium during synthesis and so it has become common practice to make lithium-rich layered oxides with a small amount of excess lithium (e.g. 5%) and to assume the excess burns off during heating [52, 53]. It will be shown here that this is not always the case and some of this excess lithium can be tolerated in the structures such that they may lie below line II in Figure 1.8. Lattice parameter contour plots prove invaluable in determining the actual compositions of such published samples and this will help explain why materials seemingly synthesized at the same composition have very different electrochemistry (e.g.  $\text{LiNi}_{0.5}\text{Mn}_{0.5}\text{O}_2$  [3, 53, 54]) **VIII**.

### 1.4.3 The Co-Existence Region Between the Spinel and Layered Structures

There are a few particularly strange results in the literature for samples made at the composition of  $\text{LiNi}_{0.5}\text{Mn}_{0.5}\text{O}_2$ . The first is that the XRD peaks of  $\text{LiNi}_{0.5}\text{Mn}_{0.5}\text{O}_2$  are very broad when synthesized in oxygen at 800°C. This broadening of the peaks was interpreted by Jo et al. [55] as being due to small crystallite sizes of about 14 nm. However, this is a small value for a sample made at these temperatures and so it is important to consider the possibility that this broadening is due to multiple phases with slightly different lattice parameters. By looking at samples over wide composition ranges and various synthesis conditions it is possible to distinguish between these two possibilities and so one objective of this thesis is to better understand the observations of Jo et al [55] **IX**. Figure 1.12 shows an even more peculiar observation made in a sample of  $\text{LiNi}_{0.5}\text{Mn}_{0.5}\text{O}_2$  by Hinuma et al. [56]. This sample, made by ion-exchange and heating to 1000°C (pristine), showed a strange phase transformation when annealed at 600°C. The extra peaks found after annealing were not identified and the sample returned to its single-phase layered structure when annealed at 1000°C and quenched back to room temperature. This dramatic change between high and medium temperature behaviour was seen repeatedly during the current study when

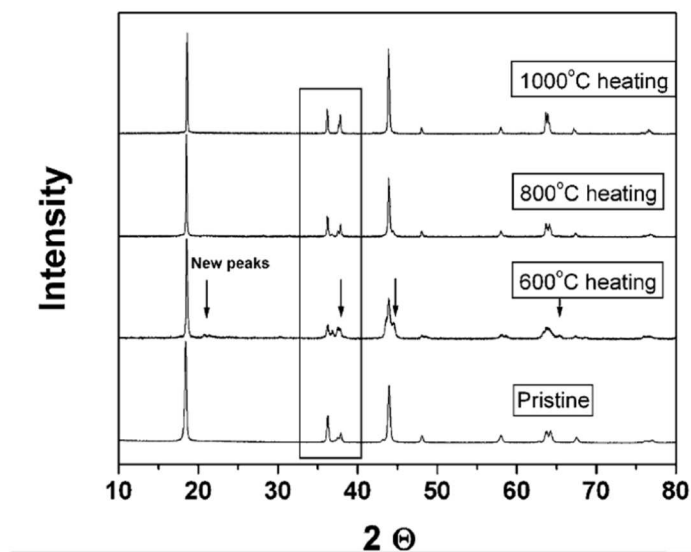


Figure 1.12: XRD patterns reprinted from Ref. [56] with permission from the American Chemical Society. Samples of  $\text{LiNi}_{0.5}\text{Mn}_{0.5}\text{O}_2$  were quenched from high temperature before being annealed at the temperatures indicated.

comparing quenched samples to those obtained by slow cooling. Thus, another objective of this study is to explain the results seen by Hinuma et al. [56] **X**.

Finally, another significant motivation for this research is the recent interest in composite electrodes combining spinel and layered structures in the Li-Mn-Ni-O system [14,15,57,58]. In such studies, the samples are assumed to be made up of phases along lines I and II in Figure 1.8, with the occasional presence of rocksalt contamination (this turns out to be the same rocksalt contaminant as seen in the spinel samples and will be identified in Chapter 5). Figure 1.13 shows the XRD patterns obtained by Cabana et al. [14]. The results clearly show spinel and layered co-existence. However, without clearly knowing the boundaries of the single-phase regions, nor the direction of tie-lines (co-existence regions where all samples along the line are made up of the two phases at the endpoints), it is impossible to determine the composition of each phase and interpreting electrochemical data becomes extremely difficult. Figure 1.14 shows a partial phase diagram with a few proposed tie-lines. This diagram does not hold up well, it is included here for illustrative purposes only. The red dashed lines indicate tie-lines. The line joining  $\text{Li}_{1.2}\text{Ni}_{0.2}\text{Mn}_{0.6}\text{O}_2$  to  $\text{LiNi}_{0.5}\text{Mn}_{1.5}\text{O}_4$  is the tie-line

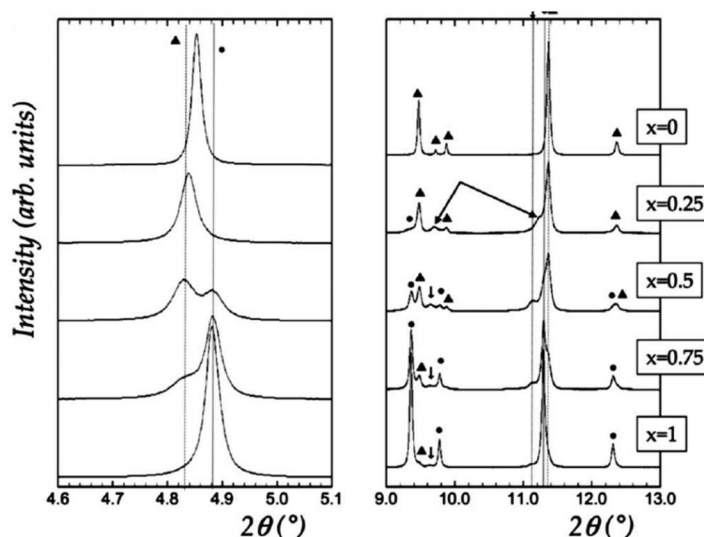


Figure 1.13: XRD patterns obtained at a synchrotron, reprinted from Ref. [14] with permission from the Electrochemical Society. Samples lie along the composition line from  $\text{Li}_{1.2}\text{Ni}_{0.2}\text{Mn}_{0.6}\text{O}_2$  ( $x=0$ ) to  $\text{LiNi}_{0.5}\text{Mn}_{1.5}\text{O}_4$  ( $x=1$ ). The triangles indicate peaks that index to a layered material, while the circles represent peaks from a spinel material and the arrows indicate a rocksalt contaminant.

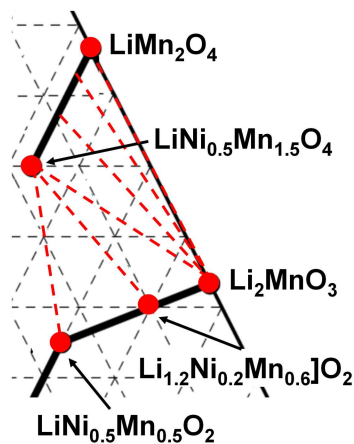


Figure 1.14: A partial Li-Mn-Ni-O diagram showing the spinel and layered phases known prior to this work (solid lines). The red dashed lines indicate tie-lines one might expect assuming a two-phase region exists. These tie-lines are refined considerably during this study and are used here only for illustration.

assumed to exist by Belharouak et al. and other groups [14, 15, 57, 58]. However, this tie-line is not accurate as the layered end of the tie-line lies above line II in Figure 1.8 as will be demonstrated in Chapter 6. Thus, another objective here is to help clarify

what phases are actually present in this particularly complex section of the phase diagram **XI**. The current project will precisely determine the nature of the whole co-existence region between the layered and spinel phases which should be of benefit to any researcher studying layered-spinel composite electrodes in this composition space. It is also important to keep in mind that all samples are in equilibrium with oxygen gas such that a sample containing  $N$  solid phases is in fact made up of  $N+1$  phases. Throughout this thesis, the number of phases present will always refer to the number of solid phases only.

## 1.5 Structure of this Thesis

Chapter 2 will introduce all experimental and theoretical methods used throughout this thesis, as well as discuss analysis techniques developed for this project. Chapter 3 focuses on optimizing the synthesis method used to make the combinatorial samples. This was done in order to minimize lithium loss such that significant knowledge about the mechanisms involved in this loss are included in this chapter. Chapter 4 presents results from a combinatorial structural study looking at the Li-Co-Mn-Ni-O system and emphasis is placed on phase transformations taking place in the layered structures when slow cooled. Chapters 5 and 6 present the large amount of evidence supporting the Li-Mn-Ni-O phase diagrams. Chapter 5 presents the spinel and rock-salt structures as well as the co-existence regions between them. This information is required before considering the complex behaviours of samples containing layered phases which are of highest interest to the Li-ion research community. Nonetheless, the information gained about the spinel and rocksalt structures is of value in its own right as spinel materials are currently being used commercially and rocksalt contaminants are often seen in materials made in this system. Chapter 6 focuses on regions of the triangle where layered phases are present, which includes the single-phase region, three two-phase regions and two three-phase regions. This complex system also transforms during slow cooling and evidence for this is included. Chapter 7 demonstrates how the Li-Mn-Ni-O phase diagrams generated in the combinatorial studies can easily be adapted for bulk samples made in air. Chapter 8 provides a detailed study of a new class of layered structures in the Li-Mn-Ni-O triangle where a significant



concentration of metal site vacancies are found. Chapter 9 examines materials very near the layered boundary in the region near  $\text{LiNi}_{0.5}\text{Mn}_{0.5}\text{O}_2$ . Phase separation into layered-layered nano-composites is shown to result in poor electrochemistry. Finally, Chapter 10 summarizes the work presented here, addresses the points of confusion outlined throughout this introduction and makes suggestions as to future work to be done based on the results from this thesis.

## Chapter 2

### Experimental and Theoretical Considerations

#### 2.1 Sample Preparation

##### 2.1.1 Synthesis of Combinatorial Samples

The method used to synthesize hundreds of samples across the pseudo-ternary systems was to make combinatorial arrays of milligram-scale oxides. Throughout this section, the method used to make samples in the Li-Mn-Ni-O system will be described. The only variation needed to make samples in the Li-Co-Mn-O system is to replace the nickel starting solution with a cobalt solution (both were nitrates in these studies). This method, developed by Carey and Dahn [11], was closely based on that typically used for large scale samples made in a tank reactor. Carey [11] mixed a total of 10  $\mu\text{L}$  of roughly 2 M lithium nitrate (Aldrich, 98 %), manganese nitrate (Sigma-Aldrich, 97 %) and nickel nitrate (Sigma-Aldrich, 97 %) using a Cartesian Pixsys solution-processing robot shown in Figure 2.1. Figure 2.2 (a) shows how these solutions were dispensed onto an alumina plate (Pi-Kem, 96 %) coated with stearic acid (Aldrich, 96 %) which served to bead the solutions. Carey then added ammonium bicarbonate (Alfa Aesar, 98 %) in excess to cause co-precipitation of Li, Mn and Ni carbonates. After drying at 55°C, the sample was made up of the mixed carbonate and any other products of the reaction (in Chapter 3, this will be shown to be primarily ammonium carbonate). Carey then heated the samples to 800°C for 3 h in air to form the oxides. Silicon (100) wafers were then covered in a tacky mixture of Trilene-65 (a polymer mixture made by Lion Copolymer) and cyclohexane. The wafer was placed over the alumina plates and flipped in order to transfer the samples onto the silicon wafer. The final products were shown to be the expected spinel oxides by XRD.

By contrast, for bulk samples a precursor is made over the course of several hours by mixing manganese and nickel solutions in a tank reactor in the presence of a

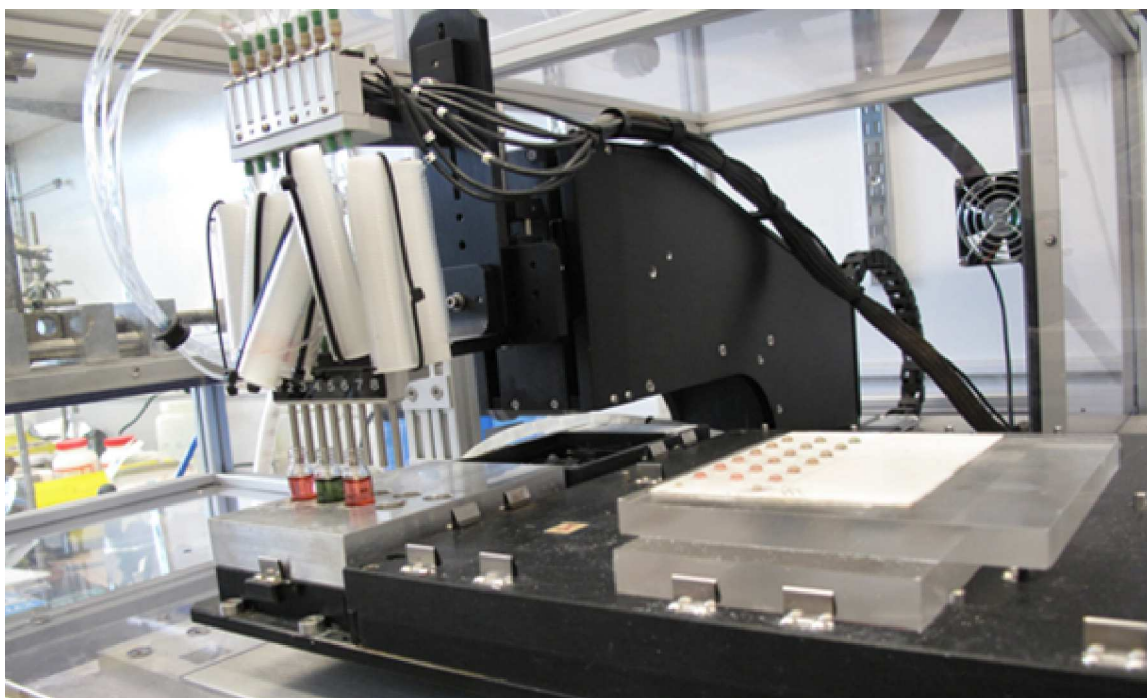


Figure 2.1: The PixSis solution-dispensing robot used to make all combinatorial samples in this thesis. The three ceramic tips are pulling solutions from the vials in preparation for a dispense onto the partially filled alumina plate.

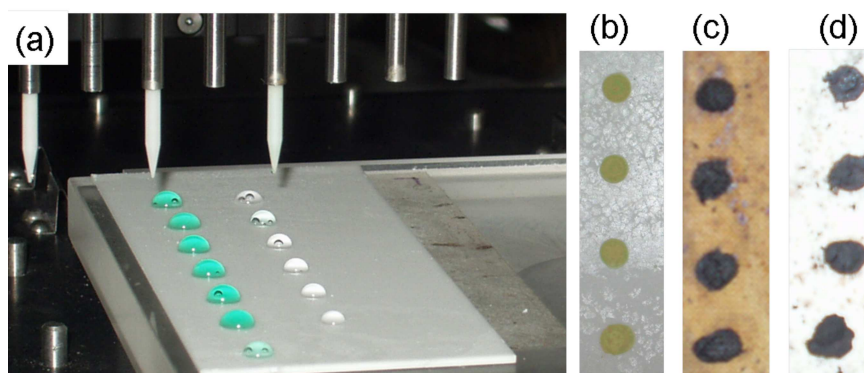


Figure 2.2: (a) The PixSis solution-dispensing robot making samples with lithium and nickel. Spinel samples at various stages of synthesis: (b) after drying overnight, (c) after heating to 300°C and (d) after heating to 800°C in oxygen.

precipitator such as ammonium bicarbonate or ammonium hydroxide. The results of this co-precipitation reaction, after rinsing, is a mixed manganese-nickel compound

(either hydroxide or carbonate) which is then mixed with a lithium salt (typically  $\text{Li}_2\text{CO}_3$  or  $\text{LiOH}$ ) and heated to high temperature to make the oxide material. The main differences between the combinatorial approach and the tank reactor method are that in the combinatorial approach all three metals are mixed at the same time, the co-precipitation reaction times are short, there is stearic acid present and the samples are not rinsed after the co-precipitation. The main consequence of the short reaction times is that particles are smaller than those seen typically for bulk samples, especially with the short 3 h heating times. This can be seen by examining the crystallite size in Chapter 3 and in the SEM images in Chapter 6. The fact that particles are small may allow phase separation to occur more rapidly in these samples, thereby confirming the changes seen in the combinatorial samples also occur in bulk samples is critical and is dealt with in Chapter 7. The main consequence of having stearic acid present is that there are contaminants in the samples, though some contaminants are also due to not rinsing the samples after the co-precipitation reaction, and all were found to disappear during synthesis. Figure 2.2 (b)-(d) shows the samples at various stages of heating. After drying at  $55^\circ\text{C}$ , the stearic acid can be seen on the substrate, while at  $300^\circ\text{C}$  decomposition of the stearic acid has begun. The fact that the substrate appears clean after heating to  $800^\circ\text{C}$  shows that decomposition of the stearic acid does reach completion. There is no evidence that the contaminants during heating affect the final products. Nor is there any evidence of there being consequences to mixing all three metals in one step, but again it is important to confirm that the tank reactor method gives comparable results to those obtained for the combinatorial samples, and so bulk and combinatorial samples will be compared throughout this thesis.

Chapter 3 shows the results of testing a number of variables in order to optimize the combinatorial synthesis method to minimize lithium loss. These variables were: the substrate used (alumina, alumina coated with  $\text{LiAlO}_2$ , and magnesia), the precipitator used (ammonium bicarbonate or ammonium hydroxide), the atmosphere used during heating (air or pure oxygen), the amount of solutions dispensed (10 or 20  $\mu\text{L}$ ) and the temperature at which the samples are heated (200, 300, 400...  $1000^\circ\text{C}$ ). The

sources of all chemicals were the same as those listed above, and ammonium hydroxide was obtained from Fisher while magnesia plates were obtained from Ceramatec. All substrates were first coated with stearic acid. The best combination obtained in that study was used throughout the rest of the thesis and proceeds as follows. Each combinatorial sample, with a mass of approximately 2 mg, was made by dispensing a total of 20  $\mu\text{L}$  of 1.78 M solutions with the solution-processing robot. The concentrations were measured to within 2 % using atomic absorption as described later in this chapter. The three solutions were lithium, manganese and nickel nitrates, and the amounts of each were varied in order to map out the Gibbs triangle. The substrate used during heating was alumina. After dispensing the nitrates, 23  $\mu\text{L}$  of 2 M ammonium bicarbonate was added, thereby ensuring that it was in excess for all samples. The samples were then dried overnight at 55°C before being heated for 3 hours at 800°C. Some samples were heated in air in a box furnace while others were heated in a tube furnace under a flow of at least 30 mL/min of oxygen. Four cooling rates were used. The first involved turning off the power to the furnace which will be referred to as regular cooling. At high temperatures this resulted in an approximate cooling rate of 8°C/min and an overall rate of about 5°C/min. This cooling method is comparable to that used in the making of commercial electrodes. The second cooling method was to quench the samples by transferring the alumina plate from the furnace onto a steel slab as quickly as possible. A Mastercraft infrared temperature sensor was used to determine that the quenched samples reached 100°C within 1 min after removal from the furnace. This corresponds to a cooling rate of roughly 10°C/sec. A second quenching method was used wherein samples were transferred into liquid nitrogen. This cooling occurs on the order of a few seconds such that a cooling rate of about 100°C/sec was obtained. The final cooling rate, used occasionally, was to cool the samples at a controlled rate of 1°C/min and will be referred to as slow cooling.

Figure 2.3 illustrates the methodology involved in making samples throughout the Li-Ni-Mn Gibbs triangle. Samples were made at every intersection point of the dashed lines, which resulted in 66 different compositions within the triangle. This was accomplished by making three plates, each holding a 6 x 6 array of samples. The plates were first cut in half in order to fit into the tube furnace. The three

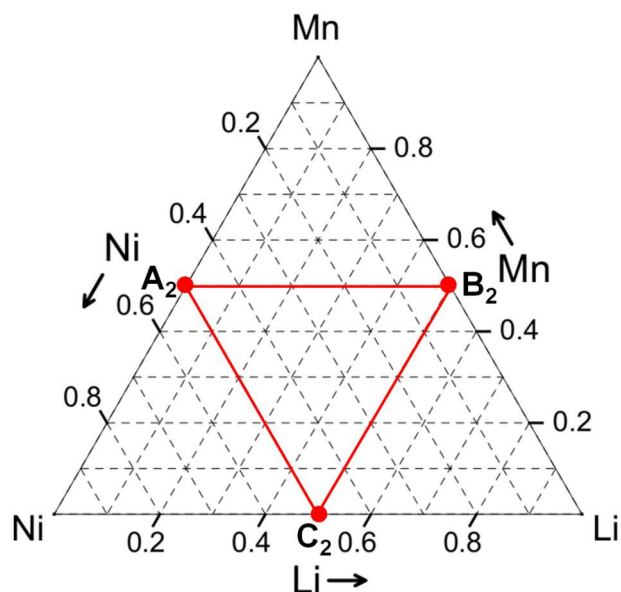


Figure 2.3: The Li-Mn-Ni oxide triangle illustrating how samples are synthesized over entire composition range in a ternary system.

arrays corresponded to samples within each of the three parallelograms shown in Figure 2.3:  $\text{NiA}_2\text{B}_2\text{C}_2$ ,  $\text{LiC}_2\text{A}_2\text{B}_2$ , and  $\text{MnB}_2\text{C}_2\text{A}_2$ . This gave 21 compositions that were repeated on each of the three plates which served as a reproducibility check. Thus, this method results in a total of 108 samples made at 66 compositions. For each system this mapping was done first. Then, as required, arrays were made over narrower ranges in order to zoom in on compositions of interest. In all cases, there were some duplicate samples to confirm reproducibility (usually duplicating a few samples from the original 66).

### 2.1.2 Synthesis of Bulk Samples

Three different synthesis methods were used to make bulk samples. The simplest was to use a solid-state reaction such as that used in Chapter 3 to make  $\text{LiNiO}_2$ . This involved grinding  $\text{NiO}_{(s)}$  (Nova Met, 98 %) with  $\text{LiOH}_{(s)}$  (Sigma-Aldrich, 98 %) and heating to high temperature in air. The second bulk synthesis method mimicked the combinatorial method on a larger scale. This involved mL-scale (usually a total of about 20-40 mL) mixtures of lithium, manganese and nickel nitrates (from the

same sources as in the combinatorial synthesis). Excess ammonium bicarbonate was then added to the mixtures in a beaker and stirred for a few minutes. After drying overnight at 55°C the samples were heated to 400°C for about 30 minutes to drive off the ammonium carbonate and any other products of the reaction. The samples were then ground and heated for 5 h in air or a flow of oxygen, and either quenched, regular cooled or slow cooled. The resulting samples had masses of approximately 1-2 g. This method will be referred to as the “one-pot” synthesis and was used to determine the impact of the high surface area to volume ratio in the combinatorial samples.

To ensure that the results obtained both by the combinatorial method and the one-pot synthesis are significant for other synthesis routes, bulk samples were also made using a tank reactor as described in Ref. [59]. These samples were made by Aaron Rowe and his contributions to this project will be pointed out explicitly throughout this thesis. A continuously stirred tank reactor was used to make mixed manganese-nickel hydroxide precursors. The metal precursor solutions were made using  $\text{NiSO}_4 \cdot 6\text{H}_2\text{O}$  and  $\text{MnSO}_4 \cdot \text{H}_2\text{O}$  (both 99 % from Aldrich Chemical Co) in such a way that a variety of nickel to manganese ratios were obtained. The tank reactor was used to mix  $\text{NH}_4\text{OH}$  with the metal sulfate solutions at a constant pH of 10.3 throughout the 10 h reaction under a flow of nitrogen. The precursor was then rinsed with distilled water and dried at 140°C before being mixed with varying amounts of  $\text{Li}_2\text{CO}_3$  to yield the desired stoichiometry. These mixtures were heated to 900°C for 10 h in a box furnace and then either quenched to room temperature between two copper plates or cooled at a slower controlled rate of 5°C/min (which is comparable to the regular cooling rate used for the combinatorial samples and will be referred to as such).

## 2.2 X-Ray Diffraction

### 2.2.1 High Throughput XRD of Combinatorial Samples

Due to the large number of combinatorial samples, a Bruker D8 Discover X-Ray system was used to characterize the vast majority of the combinatorial samples. All

X-ray diffractometers used during this project use Cu-K $\alpha$  radiation. The Bruker system has a collimated 0.5 mm wide beam, a Göbel mirror and an area detector. Each scan was made up of three frames with a 30 % overlap and each frame is obtained by counting for 300 s. Figure 2.4 shows typical results after stitching the frames together as well as the outcome of integrating along the arcs. This gave a scattering angle range of 15-70° and required approximately 15 minutes per sample. The Bruker D8 diffractometer is equipped with a sample translation stage that allows motion in the x, y and z directions such that the scattering patterns from samples in the combinatorial arrays were automatically measured in sequence. As described previously, the samples were first transferred onto a silicon (100) single crystal which served as a zero-background holder during the XRD scans as long as the Bragg condition for the Si(400) peak was avoided. Although the peak positions determined using the Bruker diffractometer were extremely accurate, the scattered intensities were affected by the stitching of frames and the integration along arcs. As such, Rietveld refinement generally failed for scans produced in this way. The next section describes the diffractometers used when Rietveld refinement was essential.

### 2.2.2 XRD of Bulk Samples

The X-ray scattering patterns from bulk samples as well as from a few combinatorial samples were collected using either a JD-2000 diffractometer or a Siemens D-5000 diffractometer. Both are equipped with a Cu-target X-ray tube and a diffracted beam monochromator, though the D-5000 also has a Soller slit to minimize out-of-plane scattering. These scans could be fit accurately using Rietveld refinement to obtain values for lattice parameters as well as site occupations. Rietveld refinement was performed on single-phase samples only using the software Rietica. The information required was the space group and site occupations, though the occupations were often left as variables in the refinements. The function used for the peak shape was pseudo-Voigt (described in the next section). The primary outputs of the refinements were lattice parameters, site occupations, fitted peak widths and fit quality parameters such as the Bragg factor. In order to account for the average vibrations of the atoms, an overall thermal parameter was allowed to be refined.



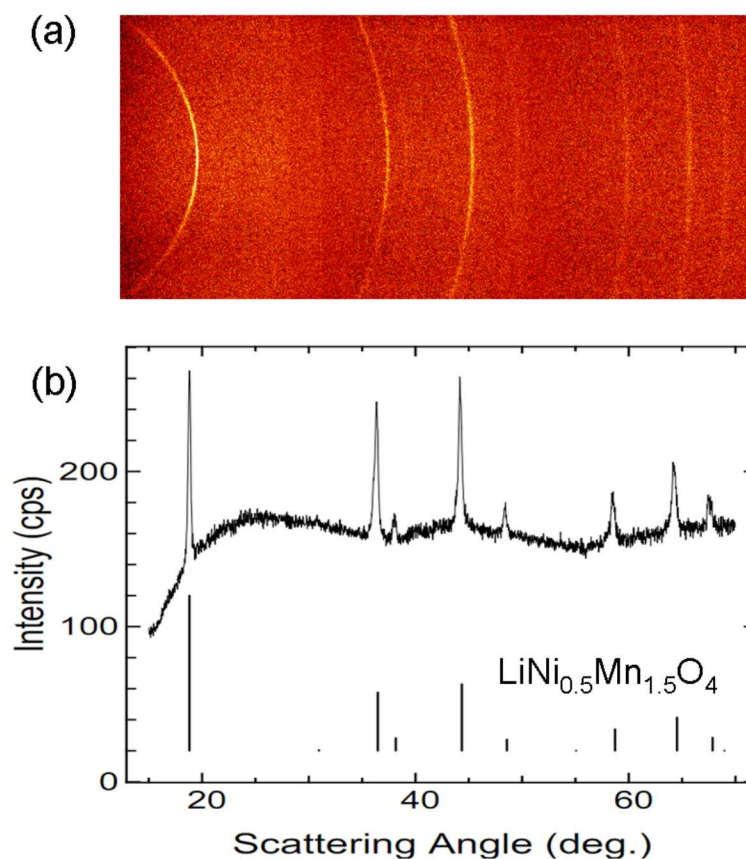


Figure 2.4: (a) The XRD image obtained after stitching three frames together for a spinel sample. (b) The result of integrating along the arcs while the vertical lines correspond to  $\text{LiNi}_{0.5}\text{Mn}_{1.5}\text{O}_4$  spinel (JCPDS #80-2162).

### 2.3 Fitting of Combinatorial XRD Patterns

Several challenges present themselves with respect to the analysis of XRD data obtained from the high-throughput Bruker machine. The peak intensities are distorted such that Rietveld refinement fails. Carey extracted precise lattice parameters by fitting the top of peaks only [11]. However, this is not feasible when there are multiple phases present for which overlapping peaks result in shifts in apparent peak positions and only using peaks that have no overlap would result in poor precision. To overcome this, an in-house software was written in Yorick to fit the entire scans using a non-linear least squares fitting algorithm [60]. Fitting the entire patterns had

the added benefit of extracting peak width information that was used to calculate crystallite sizes and strains.

Using a degree six polynomial to describe the background was found to converge very slowly. This was resolved by using a cubic function and two broad asymmetric Gaussians centered near 20 and 45° to describe the background. This procedure was found to work well for all samples, including spinel samples where manganese fluorescence gives rise to a complicated background when the three frames are stitched together as shown in Figure 2.4 (b).

In the program, each experimental peak was described by the convolution of the sample scattering with the machine broadening as outlined by Warren [61]:

$$I_k(2\theta) = \int F_k(2\theta - z)M(z)dz \quad (2.1)$$

where  $2\theta$  is the scattering angle,  $F_k$  is the sample scattering due to the  $k$ -th peak, and  $M$  is the machine broadening normalized to have an area of unity. The integration over  $z$ , the scattering angle of the machine broadening, was done numerically. The sample scattering was described with a pseudo-Voigt function:

$$F_k(2\theta) = I_k^\circ [\eta C(2\theta, 2\theta_k, H_k) + (1 - \eta)G(2\theta, 2\theta_k, H_k)] \quad (2.2)$$

where  $I_k^\circ$  is the integrated peak intensity of the  $k$ -th peak,  $H_k$  is the full width at half maximum (FWHM),  $2\theta_k$  is the position of the center of the peak,  $\eta$  is the Lorentzian component and is kept constant for all scattering angles, and  $C$  and  $G$  are the Lorentzian and Gaussian functions, respectively, each normalized to have an area of unity. The peak intensities were fitting parameters, thereby avoiding problems with distortions due to the stitching of frames. The position of each peak was calculated from the  $h$ ,  $k$ , and  $l$  values given in the Joint Committee on Powder Diffraction Standards (JCPDS) database and from the adjustable lattice parameters. The  $K\alpha_1$  and  $K\alpha_2$  peaks were included in a 2:1 ratio in the calculation in order to fit the high angle peaks accurately.

The machine broadening function,  $M$ , was determined by measuring the scattering from corundum (NIST standard 1976a) the expected scattering from which is given in JCPDS #46-1212. The scan was fit using pseudo-Voigt functions with  $\eta = 0.5$  and letting the FWHM of each peak,  $H(\theta)$ , be a fitting parameter. Although corundum is

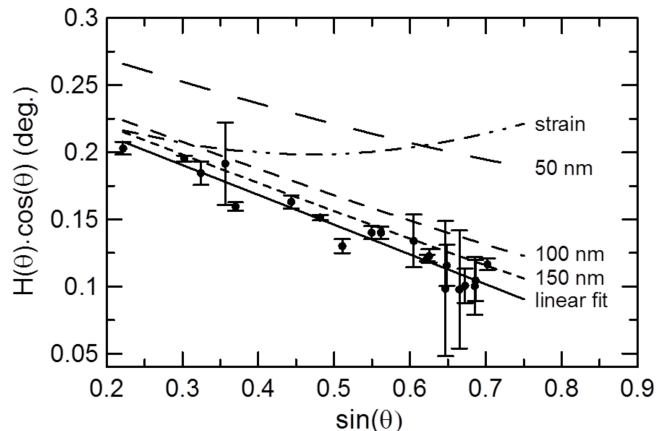


Figure 2.5: Williamson-Hall plot for corundum obtained with the Bruker XRD machine with a beam spot of 0.5 mm. The solid line is a linear fit and is used to define the machine broadening. Dashed lines are obtained assuming peaks are Gaussian and using the Scherrer equation to describe the size broadening. The dotted-dashed line is obtained similarly, assuming an infinite crystallite with a strain of  $1.0 \times 10^{-3}$ .

not commonly used as a standard for machine broadening, it is sufficient to describe the extensive broadening obtained with the 0.5 mm wide beam. This was determined by measuring the scattering from a silicon wafer which was ground. The results gave peak widths comparable to those obtained with the corundum, however the five peaks showed far more scatter such that corundum proved to be the better standard. Figure 2.5 shows that the resulting peak widths can be described by the Williamson-Hall expression:  $H(\theta) \cdot \cos\theta = A + B \sin\theta$ , where  $A$  and  $B$  are constants. The slope,  $B$ , is negative because the scattering volume decreases for frames with higher incident angles and there is no analyzer monochromator. There is also evidence of slight plateaus in the Williamson-Hall plot corresponding to the stitching of frames, but this problem is minimized by the 30 % overlap, and the linear fit does describe the data well over the scattering angle range 15-70° used throughout this project.

In order to extract values for crystallite size and micro-strain, the integral breadth method outlined by Klug and Alexander was used [26]. This involved assuming that the size contribution was Lorentzian and describing the strain broadening with a Gaussian function. The integral breadth of the  $k$ -th peak was obtained by dividing

the area of the pseudo-Voigt function by its height, which yields:

$$\beta_k = H_k/\alpha \quad (2.3)$$

where

$$\alpha = 2[\eta/\pi + (1 - \eta)\sqrt{(\ln 2/\pi)}]. \quad (2.4)$$

Utilizing the quadratic approximation [26, 62] and solving for the full width at half maximum gives:

$$H_k = \frac{\alpha}{2} \left[ \frac{K\lambda}{L\cos\theta} + \sqrt{\left(\frac{K\lambda}{L\cos\theta}\right)^2 + 64e^2\tan^2\theta} \right] \quad (2.5)$$

where  $L$  is the average crystallite size, the root-mean-square micro-strain is  $\sqrt{\langle e^2 \rangle} = e/1.25$ , and the usual approximation of  $K = 1$  was made. The quadratic approximation is generally considered to give values for size and strain that are close to those obtained by Fourier methods without requiring extensive computations [62]. The micro-strain includes all contributions due to non-uniform lattice distortions, dislocations, stacking faults, and local structural defects such as vacancies and interstitial atoms. In the case of  $\text{Li}_x\text{Ni}_{2-x}\text{O}_2$ , fluctuations in lithium content within a grain have been observed in the early phases of synthesis in samples with lower lithium content ( $x < 0.6$ ) [63]. A non-homogeneous lithium distribution within grains would result in lattice distortions thereby contributing to the strain. As a result, the strain parameter is of particular interest during synthesis of the samples and is therefore followed closely in Chapter 3.

In order to estimate the minimum crystallite size that can be resolved with the combinatorial X-ray machine, the broadening of the machine peaks due to crystallites of various sizes was calculated by using the Scherrer equation and assuming the peaks were Gaussian to minimize the broadening. A similar calculation was made for strain, assuming crystallites of infinite size. Figure 2.5 shows the results of these calculations and shows that the Bruker XRD system resolves crystallite sizes precisely up to 100 nm; however, above this point, machine broadening begins to dominate and any size greater than 150 nm cannot be determined. For larger crystallites, it would be necessary to use a smaller beam spot (0.3 mm or even 0.1 mm are commonly used),

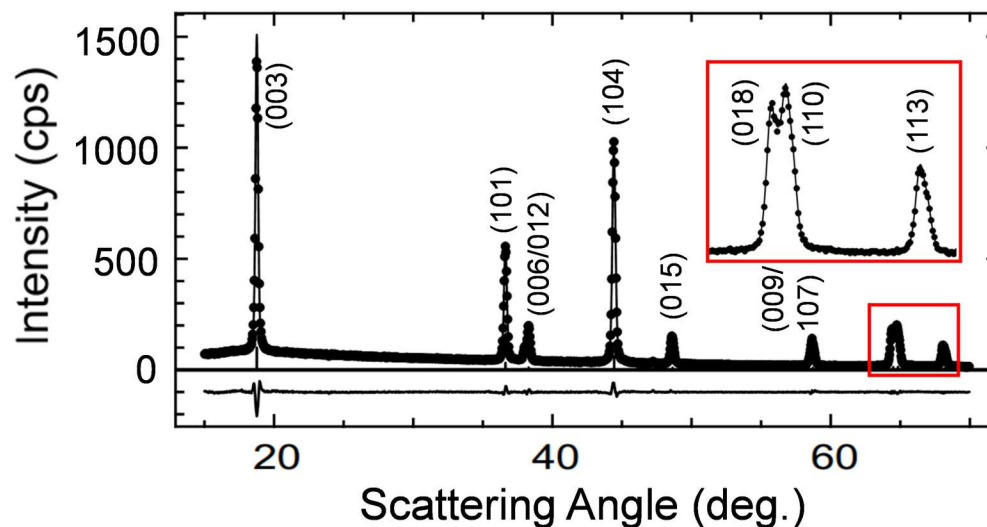


Figure 2.6: The fit obtained for a combinatorial sample of  $\text{LiNiO}_2$ . This reflects the quality of fit typically obtained for XRD scans of the combinatorial samples taken with the Bruker diffractometer. For clarity, only every third data point is included as closed circles while the result of the fit is shown as a solid line and the difference plot is shown below.

but this was avoided here since it would have greatly increased the required count time. Figure 2.5 also shows that a strain value of  $1 \times 10^{-3}$  can be readily resolved. Any strain value below  $0.1 \times 10^{-3}$  was considered too small to be measured accurately.

Figure 2.6 shows a typical scan obtained for a combinatorial lithium nickel oxide sample measured with the Bruker machine along with the fit produced by the in-house software. The peaks fitted the experimental data extremely well such that the lattice parameters and the size/strain values extracted from the fitting routine were well constrained. For clarity, all XRD patterns shown throughout the rest of this thesis have the fitted background subtracted from the experimental patterns. This allows for easy comparison of many samples stacked in the same plot.

The program was written to be able to fit multi-phase samples. The calculated pattern was therefore a linear combination of the functions representing each of the single-phases. Thus, the fitting of multi-phase scans generated lattice parameters and integrated peak areas for each phase. The size and/or strain was examined in Chapters 3 and 4 only. For all other combinatorial results, phase compositions

(obtained from the calculated peak areas) and lattice parameters were extracted. As shown in the next section, this information is sufficient to generate precise phase diagrams.

## 2.4 Methods to Generate the Phase Diagrams

The information extracted from the XRD scans are: phase types (layered, spinel, rocksalt...), lattice parameters, and the peak areas of each peak for all phases present. These are sufficient to determine the boundaries of the single-phase regions and the nature of the co-existence regions. Figure 2.7 (a) shows the proposed tie-lines lying between the spinel and layered regions in the Li-Mn-Ni-O system as discussed in the introduction. This will be used here to illustrate how the XRD patterns could be used to confirm that the proposed diagram was correct. Firstly, all XRD patterns obtained would have to be visually consistent with the phase diagram. This simply means that no signs of a second phase existed in scans of samples in the single-phase region, and no samples lying in the co-existence regions appeared single-phase (as will be shown in Chapters 5 and 6, this proposed phase diagram fails on both counts). However, visual inspection of XRD scans was insufficient to precisely identify the boundaries of the single-phase region. The next step was to carefully examine the values of the lattice parameters obtained in the co-existence region and to compare them to those found for single-phase samples. In the proposed phase diagram, tie-lines fan out from  $\text{Li}_2\text{MnO}_3$  up to an angle of about  $\alpha = 70^\circ$ . This implies that up to this angle the value of the layered lattice parameters in the two-phase samples should be equal to those of  $\text{Li}_2\text{MnO}_3$ . Figure 2.7 (b) illustrates the expected plot of the  $c$  lattice parameter as a function of  $\alpha$  based on the proposed tie-lines. Since  $c = 14.23 \text{ \AA}$  for  $\text{Li}_2\text{MnO}_3$  when fitted as a hexagonal structure, as shown in Chapter 6, such a graph would confirm that the tie-lines fan-out from  $\text{Li}_2\text{MnO}_3$ . Plots of this type were extremely useful in demonstrating the directions of tie-lines in the Li-Mn-Ni-O system and were used throughout this thesis. In three-phase regions, there is no variation in the phases present; only the amount of each phase varies. As such, the fitted lattice parameters should remain constant throughout the three-phase region.

In order to work out the boundaries of the single-phase regions, the lever rule was

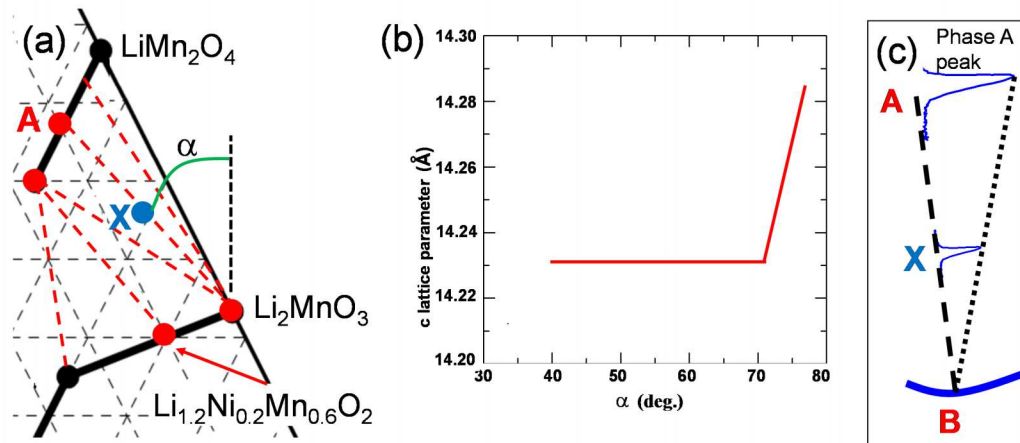


Figure 2.7: (a) A section of the Li-Ni-Mn-O phase diagram showing previously known single-phase regions. Red dashed lines represent proposed tie-lines. (b) An illustration of how lattice parameter values can be used to determine the direction of tie-lines in two-phase regions. (c) A schematic of using the lever rule in a two-phase region to determine the location of a point B on the boundary of the single-phase region (e.g. if (a) is correct point B should be  $\text{Li}_2\text{MnO}_3$ ).

used. Figure 2.7 (c) illustrates the use of the lever rule for sample X lying on a tie-line between phases A and B. Extrapolating to where the integrated peak intensity of the phase A peaks would be zero yields point B. If the proposed phase diagram is correct, point B would coincide with  $\text{Li}_2\text{MnO}_3$ . In practice the distance from A to B was calculated using the mathematical form of the lever rule which states that the fraction of phase A is equal to  $d(X,B)/d(A,B)$ . This allows for the calculation of the position of point B, which can then be compared to the position of  $\text{Li}_2\text{MnO}_3$ . This same method was used to determine the positions of the corners of three-phase regions as will be demonstrated in Chapter 6. It should be noted that micro-absorption effects were not taken into account in the calculations. This is justified for the combinatorial samples with small particle sizes, as will be demonstrated in Section 5.4. Therefore, even without Rietveld refinement, the XRD patterns can be used to identify the boundaries of single-phase regions, the direction of tie-lines in two-phase regions and the extent of three-phase regions. The large number of scans in the single-phase regions also provided lattice parameters over wide composition ranges which were expressed as contour plots in Chapters 5, 6 and 7. These contour plots should be of considerable use to researchers working in these systems.

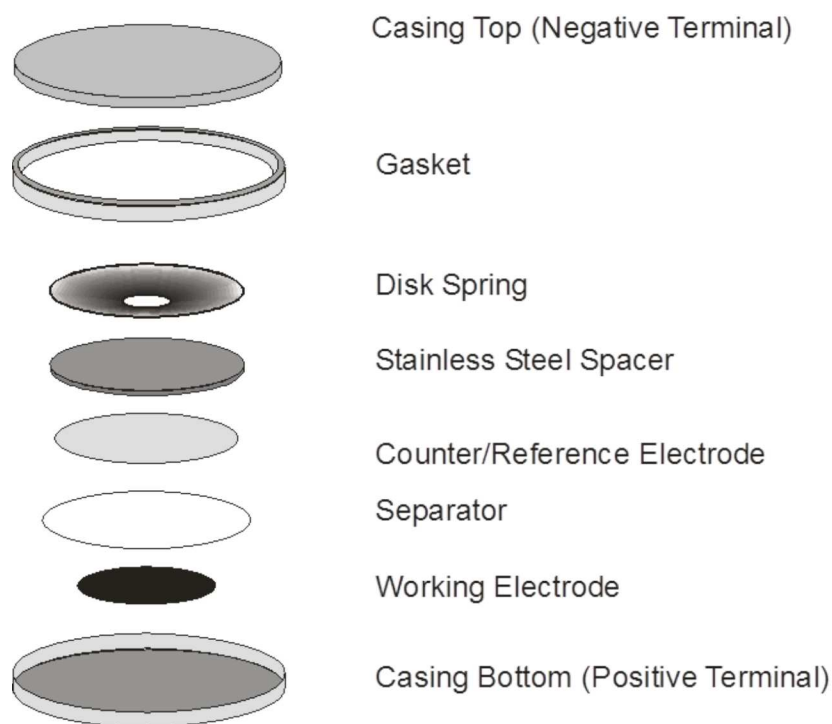


Figure 2.8: A schematic of the components used in making a typical coin cell for electrochemical testing.

## 2.5 Electrochemical Tests

Coin cells were made from a few bulk samples in order to determine the electrochemical performance of materials of interest. Figure 2.8 shows the parts involved in assembling a standard coin cell. Electrochemical tests were carried out using a standard 2325 coin cell with the positive electrode being cycled against a lithium counter electrode (Chemetall Foote Corp.). The electrolyte used was 1 M  $\text{LiPF}_6$  in 1:2 ethylene carbonate:diethyl carbonate (Novolyte Corp., now part of BASF). The positive electrodes contained 5 % polyvinylidene-fluoride binder (Kynar 301P, Elf Atochem) and 5 % carbon black (TIMCAL). Two identical cells were typically made. The details of the coin cell design are included in Ref. [64]. The cycling conditions varied from experiment to experiment and will be stated explicitly in the results sections.



## 2.6 Thermo-Gravimetric Analysis

As a consequence of the high surface area to volume ratio, the combinatorial samples were very sensitive to surface reactions. The mass changes resulting from these reactions were studied using a thermo-gravimetric analyzer (TGA). The TGA was useful in the study of lithium loss during synthesis as will be discussed in Chapter 3. A typical TGA run involved heating approximately 10 mg of sample in a small alumina cup in a TA Instruments SDT-Q600 TGA under a gas flow of 50 mL/min. These samples were approximately five times larger than those made by the solution-dispensing robot and so the TGA results can be considered to be an ideal limit for the behaviour of the combinatorial samples (i.e. the combinatorial samples would lose slightly more lithium than those heated in the TGA). The lithium loss experiments were repeated in flows of argon, air and oxygen in order to identify the role played by the atmosphere.

## 2.7 Elemental Analysis

With lithium being lost during heating of the combinatorial samples in certain regions of the Li-Mn-Ni Gibbs triangle, the composition of a sample is not necessarily the same before and after heating. As such, either atomic absorption (AA) or inductively coupled plasma optical emission spectroscopy (ICP) have been used as elemental analysis in order to determine the actual compositions of samples. To do this for combinatorial samples, the samples were transferred into 2 mL vials with the use of a transfer plate that clamps the substrate to the vials thereby preventing mixing of neighbouring samples. To each vial, approximately 0.5 mL of a solution of 25 % nitric acid and 75 % hydrochloric acid was added to dissolve the samples. The solutions were then analyzed by Dan Chevalier (Minerals Engineering Centre, Dalhousie University) to give the concentrations of nickel, lithium and manganese accurate to 5 % for the small samples. The same method was used for bulk samples though slightly more powder was used to improve the precision of the measurements. For the starting solutions used with the solution-processing robot, AA measurements were repeated three times such that the uncertainty was 2 %.

## 2.8 Scanning Electron Microscopy

Scanning electron microscopy (SEM) allows the viewing of particles as small as 50 nm in length. As will be discussed in the next chapter, the crystallites made in combinatorial samples heated to 800°C typically fall in this range such that the SEM was useful in order to get a better idea of whether or not phase separation had occurred. To this end, a few samples were imaged by Ramesh Shunmugasundaram using a Hitachi S-4700 field emission scanning electron microscope with an accelerating voltage of 10 kV and an emission current of 15  $\mu$ A.

## 2.9 Redox Titration

As mentioned in the introduction, the oxidation states of the transition metals in the electrode material have a large effect on the electrochemistry. It proved useful to use redox titrations in order to determine the average oxidation state of the nickel and manganese for the materials discussed in Chapter 8. This involved two redox titrations, both using potassium permanganate. The first involved adding the potassium permanganate to the samples (both dissolved in acid) in order to determine the total amount of manganese present. The second titration involved first mixing the dissolved sample with ferrous ammonium sulfate in order to reduce nickel and manganese to the 2+ oxidation state while oxidizing some iron to 3+. The subsequent titration with potassium permanganate then reduced iron back to 2+. The two measurements allowed the determination of the average manganese oxidation state (assuming all nickel was in the 2+ state). As such, a result for the manganese oxidation state greater than 4.0 would imply some  $\text{Ni}^{3+}$  was present. It is important to notice that this method cannot distinguish between a  $\text{Ni}^{2+}$ - $\text{Mn}^{4+}$  pair and a  $\text{Ni}^{3+}$ - $\text{Mn}^{3+}$  pair since this approach essentially counts the number of oxidation states above 2+. To make the distinction between these two combinations, manganese X-ray absorption spectra were taken as described in the next section. The titrations were performed by Oliver Schilling of Erachem Comilog.

## 2.10 X-Ray Absorption Spectroscopy

The X-ray absorption spectra of materials are sensitive to both the local and long range electronic structure of the material. Fitting the spectra is rather complex, but information about the oxidation state of each metal can be extracted relatively easily by comparison with known reference materials. Comparing two spectra of materials with similar structures means that the differences seen are primarily due to the electronic configuration of the atom in question.

Figure 2.9 shows the X-ray absorption near-edge structure (XANES) spectra for manganese-containing samples near the Mn K-edge (obtained by exciting 1s electrons) published by Myung et al. [65]. The position of the main absorption edge, marked for each spectrum with a red arrow, is sensitive to the oxidation state of the manganese atoms. Thus, the two reference materials ( $\text{Li}_2\text{MnO}_3$  for 4+ and  $\text{LiMnO}_2$  for 3+) were used by Myung to determine that the manganese atoms in the  $\text{LiNi}_{0.5}\text{Mn}_{0.5}\text{O}_4$  sample were in the 4+ state. This simple analysis will be used in Chapter 8 to determine the oxidation state of the manganese atoms. The XANES spectra were collected by Paul Duchesne on the PNC-CAT beamline 20-BM at the Advanced Photon Source of Argonne National Labs. Incident X-rays were made monochromatic using a silicon (111) double-crystal system employing platinum mirrors for harmonic rejection. The samples were all measured in transmission mode at room temperature using ionization chamber detectors.

## 2.11 Helium Pycnometry

Some of the materials studied in this thesis showed oxygen non-stoichiometry (either oxygen or metal vacancies). Precise density measurements were used to identify the concentrations of such vacancies. This required knowing the metallic compositions from ICP and the volume of the unit cell from XRD. A Micromeritics AccuPyc II 1340 Helium Pycnometer was used to measure the true volume of the samples. The pycnometer works by pressurizing an empty reference chamber and measuring this pressure before opening a valve between the reference and sample chambers and re-measuring the pressure again. Since the volumes of the empty chambers are known,

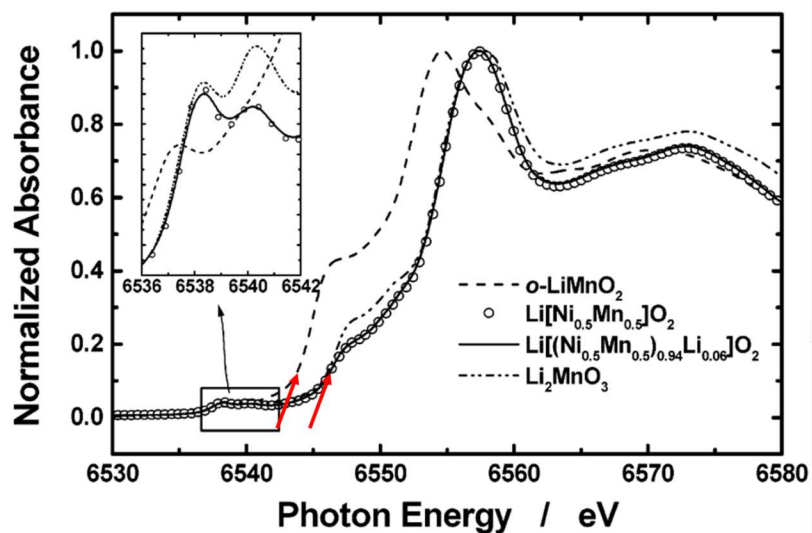


Figure 2.9: XANES spectra reproduced from Ref. [65] with permission from the American Chemical Society. The red arrows mark the rough positions of the main absorption edges.

Boyles' law was used to calculate the volume of the sample. A high precision scale was used to measure the mass of the sample. Multiple measurements with the pycnometer were used in order to calculate a statistical uncertainty. This approach was used in Chapters 6 and 8.

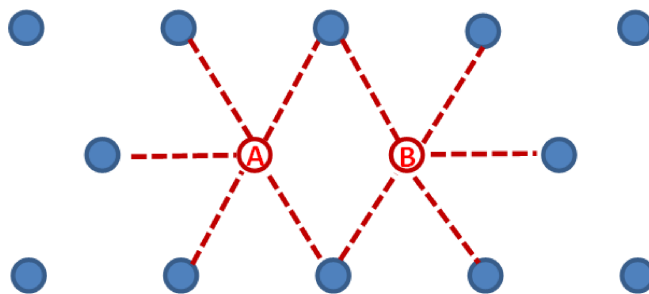


Figure 2.10: An array of atoms illustrating the interactions used in the Monte Carlo simulations (red lines) when calculating the probability of accepting a move wherein atoms A and B are interchanged.

## 2.12 Monte Carlo Simulations

As has been discussed, a significant portion of this thesis deals with phase transformations taking place during slow cooling. A Monte Carlo simulation was used to examine the changes that take place on the metal atom layers in the layered oxide materials during slow cooling. This was used on three occasions, in Chapters 4, 8 and 9. In each case, a 50 x 50 hexagonal array was made with compositions matching the stoichiometry on the TM layer determined experimentally. The initial array was made assuming random occupation of all sites such that the starting configuration corresponded to infinite temperature where entropy wins out entirely over internal energy. For all simulations, the potential used for the energy of the system was the coulombic potential for nearest neighbour (NN) interactions only and periodic boundary conditions were used. The effective charge of each atom was assumed to be proportional to its oxidation number. The simulation involved evaluating whether randomly chosen nearest neighbours might exchange position. Figure 2.10 shows the interactions involved in calculating the change in energy between the original configuration and the proposed one obtained by switching the atoms A and B. The effective charge of the  $i$ -th atom is  $\delta \cdot n_i$  with  $n_i$  being the oxidation number of atom  $i$  in the original structure and  $n'_i$  that of the atom in the structure after the proposed change. The change in energy due to such a move is:

$$\frac{\Delta E}{k_B T} = \beta_T \left( \sum_{i,j}^{NN} n'_i n'_j - \sum_{i,j}^{NN} n_i n_j \right) \quad (2.6)$$

where  $k_B$  is the Boltzmann constant,  $T$  is temperature,  $\beta_T = \delta^2 / (4\pi\epsilon_o k_B T \cdot a)$ ,  $\epsilon_o$  is the permittivity of free space, and  $a$  is the in-plane lattice parameter. In this model, it was assumed that all nearest neighbours were separated by a distance  $a$ . The Metropolis rate equation [66] was used such that the probability of accepting a move is 1 if  $\Delta E < 0$  and  $e^{-\Delta E/k_B T}$  if  $\Delta E > 0$ . The simulation was run for increasing values of  $\beta_T$  (0.5, 1, 1.5 ... 5) in order to simulate slow cooling. At each temperature, 10000 Monte Carlo steps were performed (2500 attempted moves constituted a Monte Carlo step).

The third use of this simulation, discussed in Chapter 9, involved a situation where the lithium layer was not entirely filled with lithium. As such, interactions between

the lithium and TM layers had to be taken into account. Again, only the six NN out-of-plane interactions were considered (three from the plane above, three from the plane below). The out-of-plane nearest neighbour lies  $c/6$  away in the out-of-plane direction and  $a/\sqrt{3}$  away in the in-plane direction such that the distance between out-of-plane nearest-neighbours is roughly 1.004 times larger than for in-plane neighbours based on  $a = 2.90 \text{ \AA}$  and  $c = 14.30 \text{ \AA}$  as obtained in Chapter 9. Thus, the in-plane and out-of-plane nearest neighbours are nearly equidistant and this correction was included in the calculations.

## Chapter 3

### Optimization of the Synthesis of Combinatorial Samples

Data in this chapter are reprinted from Ref. [67] with permission from Elsevier.

#### 3.1 Experimental Design

Though combinatorial samples were synthesized along each of the single-phase regions I, II, III and IV shown in Figure 3.1, only the  $\text{Li}_x\text{Ni}_{2-x}\text{O}_2$  samples (line IV) are reported here in order to describe the mechanisms for lithium loss in the small samples. The methods used to make the samples were closely based on the synthesis done by Carey [11], but several variables were controlled in order to find the conditions that minimize the lithium loss. These included the choice of substrate, the chemical used to cause precipitation (called “precipitator” here), the heating temperature, and the atmosphere during heating.

Three substrates were tested:  $\text{Al}_2\text{O}_3$ ,  $\text{MgO}$ , and  $\text{Al}_2\text{O}_3$  treated with  $\text{LiOH}$ . The main concern with respect to alumina is that it reacts with lithium carbonate to form  $\text{LiAlO}_2$ , a process which has been observed to go to completion at  $700^\circ\text{C}$  [68]. Magnesia shows no such reaction, but it is hygroscopic and porous, thereby requiring large quantities of stearic acid to prevent the water in the solutions from entering the substrate before the co-precipitation reaction takes place. The  $\text{LiOH}$  treatments were done by spraying 3 M  $\text{LiOH}$  onto the surface, drying at  $55^\circ\text{C}$  and then heating to  $900^\circ\text{C}$  for an hour in a box furnace. This was repeated three times. Figure 3.2 (d) shows that after the treatments the substrate had a layer of  $\text{LiAlO}_2$  (JCPDS #73-1338) on the surface. A fourth treatment typically resulted in cracking and flaking of this layer.

The primary objective here was to synthesize  $\text{LiNiO}_2$  at  $800^\circ\text{C}$ , the temperature required to make the spinel samples in the Li-Mn-Ni-O system. Since stearic acid has been found to react with lithium to form lithium stearate [69, 70], this chapter also

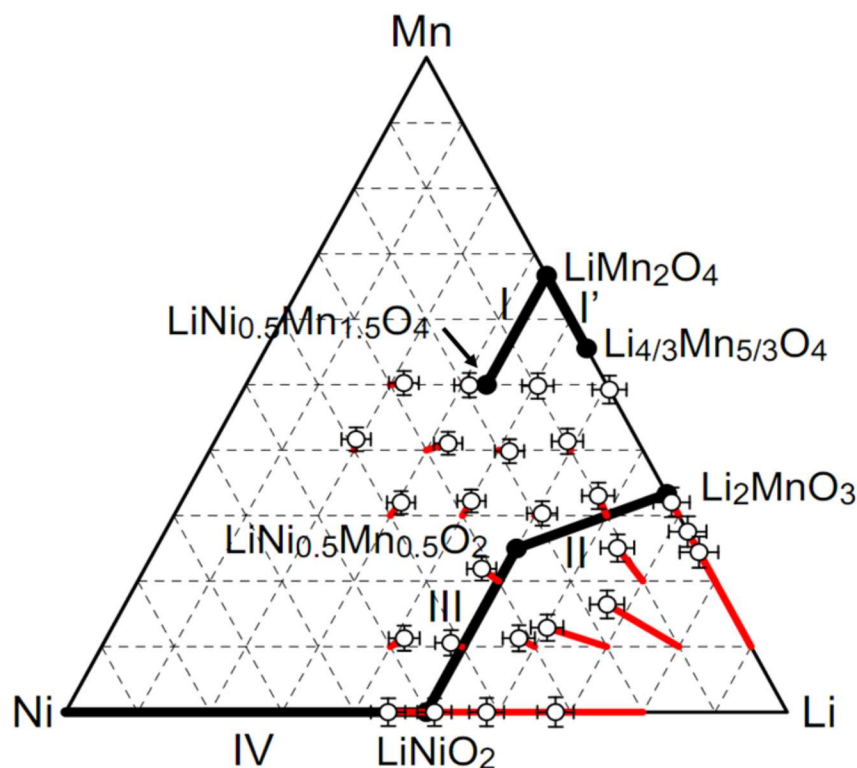


Figure 3.1: The Li-Mn-Ni oxide pseudo-ternary system where the corners refer to the metals used during sample preparation and oxygen content varies throughout the triangle. The bold lines represent lithium containing single-phase regions known prior to the current project. The open data points represent combinatorial samples prepared at 800°C in oxygen. The compositions were determined by atomic absorption, and the lines leading to each point begin at the as-dispersed compositions; if no line is present the point lies directly above its dispensed composition.

deals with identifying the role of stearic acid in the samples, especially on magnesia where more was required. The precipitators tested were ammonium bicarbonate and ammonium hydroxide, these being the two most commonly used to synthesize metal carbonates or hydroxides from solution. The atmospheres used were either air in a box furnace or oxygen flowing in a tube furnace. The heating temperature was varied over the range 200-900°C to track changes during synthesis. The amount of lithium dispensed was also varied to test the extent to which excess lithium could be used to compensate for the lithium loss.

For the thermo-gravimetric measurements, a bulk  $\text{LiNiO}_2$  sample of approximately 3.5 g was made by the solid-state reaction of lithium hydroxide (5 % excess) with nickel



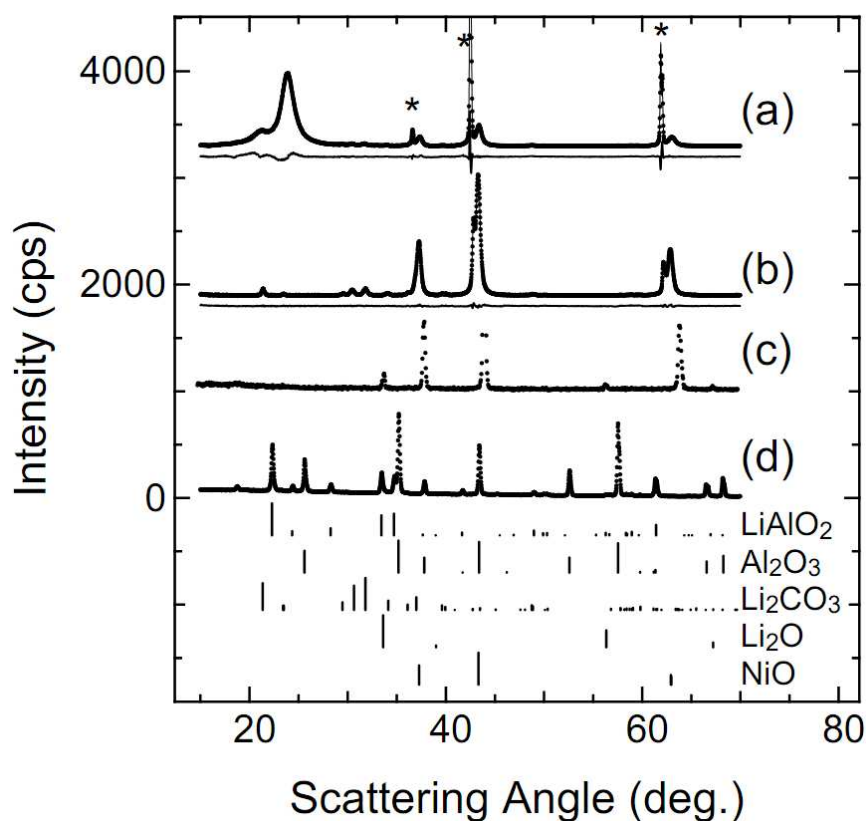


Figure 3.2: (a) XRD scan of a  $\text{Li}_x\text{Ni}_{2-x}\text{O}_2$  sample with  $x = 1$  as-dispersed with ammonium bicarbonate precipitator, after heating to  $400^\circ\text{C}$  in oxygen. The data are shown with the fit and the difference plot immediately below. The position of the sharp MgO peaks are indicated by \*. (b) Sample with  $x = 1$  as dispersed with hydroxide precipitator after heating to  $400^\circ\text{C}$  in air; with fit and difference plot. (c) The bulk sample ( $x = 0.965$ ) after heating in the TGA in a flow of argon. (d)  $\text{Al}_2\text{O}_3$  substrate after three treatments with LiOH. Vertical lines indicate peaks from the JCPDS database.

oxide as described in Section 2.1.2. The mixture was placed in an alumina boat and heated to  $750^\circ\text{C}$  for 10 hours in air. For each TGA run 11-13 mg were heated in a TA Instruments SDT-Q600 thermo-gravimetric analyzer (TGA) under a gas flow of 50 mL/min. The experiment was repeated in argon, air and oxygen. Figure 3.3 shows the temperature profile used. Samples were also heated at a rate of  $20^\circ\text{C}/\text{min}$  to either 600, 700 or  $800^\circ\text{C}$  and held there for several hours in either a flow of oxygen or air. This was done in order to estimate the expected lithium loss during the three hours of heating used to synthesize the combinatorial samples.

Combinatorial samples with a mass of less than 1 mg were made by dispensing a

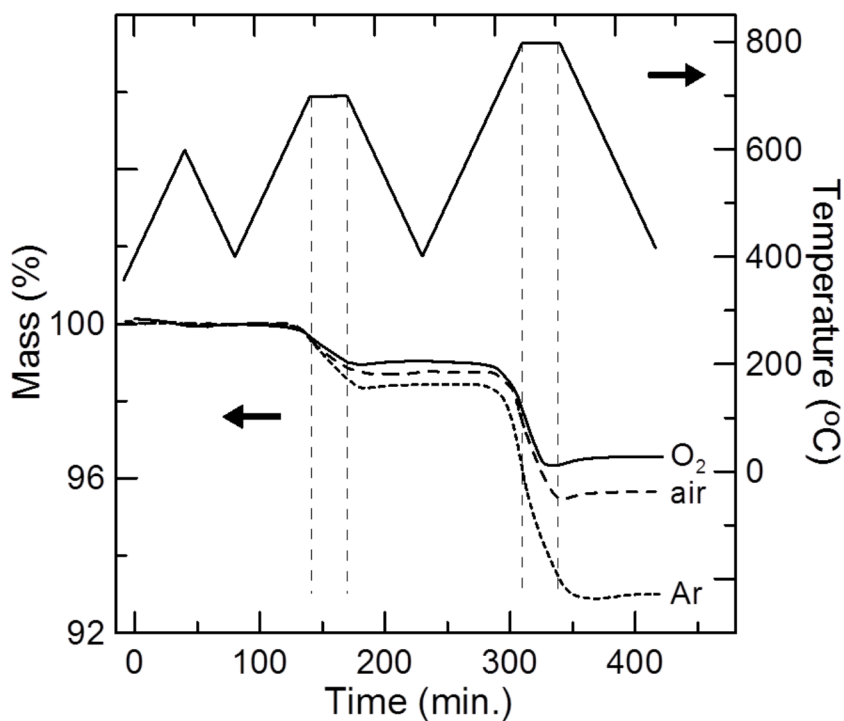


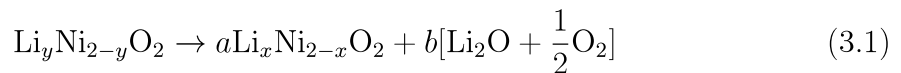
Figure 3.3: TGA data for samples of  $\text{Li}_{0.965}\text{Ni}_{1.035}\text{O}_2$  heated in oxygen (solid line), air (dashed line) and argon (short dashed line). A gas flow of 50 mL/min was used in each case. The vertical dashed lines mark the start and end of the temperature holds.

total of 10  $\mu\text{L}$  of 1.78 M solutions with a Cartesian Pixsys solution-processing robot (described in Section 2.1.1). To see the effect of sample size, a few were made by dispensing a total of 20  $\mu\text{L}$ . The amounts of lithium and nickel nitrate dispensed were varied in order to make  $\text{Li}_x\text{Ni}_{2-x}\text{O}_2$  with  $x = 0, 0.8, 0.9, 1, 1.1$  and 1.2 if there was no lithium loss (this is referred to as “x as-dispensed”). Samples with  $x = 1.2$  ( $\text{Li}_{1.2}\text{Ni}_{0.8}\text{O}_2$ ) therefore represent a 50 % lithium excess compared to nickel content with respect to  $x = 1$ .

It was also important to determine whether or not the method developed here results in small lithium loss throughout the entire Gibbs triangle. To do this, a number of 20  $\mu\text{L}$  combinatorial samples containing varying amounts of lithium, nickel and manganese were prepared by heating at 800°C for 3 hours in flowing oxygen. The samples were then dissolved in concentrated acid and the resulting compositions were determined with atomic absorption spectroscopy.

### 3.2 TGA Results for Lithium Loss During Synthesis

The bulk sample was characterized using a JD-2000 diffractometer and Rietveld refinement to determine that it was single-phase  $\text{Li}_x\text{Ni}_{2-x}\text{O}_2$  with  $x = 0.965$ . Figure 3.2 (c) shows the XRD scan of this sample after being heated to  $900^\circ\text{C}$  in argon in the TGA. The scan contains two phases:  $\text{Li}_x\text{Ni}_{2-x}\text{O}_2$  with  $x < 0.62$ , and  $\text{Li}_2\text{O}$  (JCPDS #77-2144). Lithium oxide is therefore one product of the thermal decomposition of lithium nickel oxide and balancing the equation with oxygen yields:



where  $a = (2 - y)/(2 - x)$ ,  $b = (y - x)/(2 - x)$  and  $y > x$ . This reaction was first proposed by Antolini while studying the thermal decomposition of lithium nickel oxide,  $\text{Li}_y\text{Ni}_{2-y}\text{O}_2$ , with an initial lithium content of  $y < 0.6$  using thermo-gravimetric analysis at temperatures of  $900^\circ\text{C}$  and higher [71].

In order to confirm Eq. 3.1 and to verify that both lithium oxide and oxygen are lost, the x-ray scattering from certain samples was measured after the TGA runs used to produce Figure 3.3. The sample that was heated in air initially had a mass of 11.66 mg and 0.70 mg was lost during the TGA measurements. Equation 3.1 and the assumption that both  $\text{O}_2$  and  $\text{Li}_2\text{O}$  are lost were used to determine that the final state corresponded to  $x = 0.828$ . XRD with the JD-2000 diffractometer analyzed with Rietveld refinement yielded  $x = 0.839$ . Similarly, the sample heated in oxygen had a lithium content of  $x = 0.887$  according to XRD in good agreement with 0.870 obtained from Eq. 3.1.

Furthermore, Sata found that lithium oxide then reacts with oxygen according to:  $2\text{Li}_2\text{O}_{(s)} + \text{O}_{2(g)} \rightarrow 2\text{Li}_2\text{O}_{2(g)}$  [32]. Thus, the means for lithium loss during synthesis of the combinatorial samples may be due to the production of lithium oxide which is then converted to lithium peroxide vapour. The fact that solid  $\text{Li}_2\text{O}$  was only seen in the XRD scans after heating in argon is consistent with the loss of lithium arising from the reaction of lithium oxide with oxygen identified by Sata [32]. Since lithium oxide does not decompose or evaporate at these temperatures and the TGA data are consistent with losing both oxygen and lithium oxide, the decomposition of lithium nickel oxide followed by the formation of lithium peroxide vapour was therefore the

likeliest source of lithium loss in the bulk samples.

Figure 3.3 shows the mass loss of samples heated in argon, air and oxygen. Clearly, the reaction for lithium loss was slowed by oxygen. Furthermore, the sample heated in argon showed continued mass loss during cooling after the hold at 800°C while the samples heated in oxygen and air showed no such loss and perhaps even a small mass increase during the initial stages of cooling. This effect suggests that oxygen re-entered the sample during cooling in order to counter a deficiency which emerged during heating and only samples in argon continued to lose mass.

Figure 3.4 shows the lithium content in the samples held at a constant temperature in either oxygen or air. The lithium content is calculated using Eq. 3.1 with  $y = 0.965$  and assuming that both lithium oxide and oxygen are lost. Since this does not take into account the oxygen deficiency suggested by Figure 3.3, the calculated  $x$ -value represents a lower limit on the actual lithium content. The samples heated at 800°C clearly showed two regimes as described by Antolini [71]. His data showed similar results and he attributed the rapid initial lithium loss to the reaction being limited by diffusion along grain boundaries. Next, the rate diminished and this was consistent with the lithium loss being limited by diffusion within grains. The first 50 minutes seen here at 800°C in Figure 3.3 were consistent with the more rapid loss attributed to the reaction being limited by diffusion along grain boundaries, while after this point the grain surfaces were depleted sufficiently so that the limiting step was diffusion within grains. During the first step the differences between the behaviours in the two gases was slight. In contrast, at 700°C a single regime was seen. At this temperature, the change of rate occurred after approximately 4.5 hours and so the lithium loss was roughly proportional to time at this temperature during the 3 h heating of the combinatorial samples. It is also significant that the lithium loss over 3 hours in oxygen was only about 15 % lower than in air. Similarly, only one regime was seen at 600°C and the mass loss was quite small, particularly in oxygen.

Figure 3.4 suggests that a sample with an initial value of  $y = 1$  should end up with a lithium content of approximately  $x = 0.94$  after heating for 3 hours at 700°C in air. Similarly, a sample with  $y = 1$  heated at 800°C in oxygen should have a final  $x$  value of about 0.90. Combinatorial samples were typically less than 1 mg in mass such

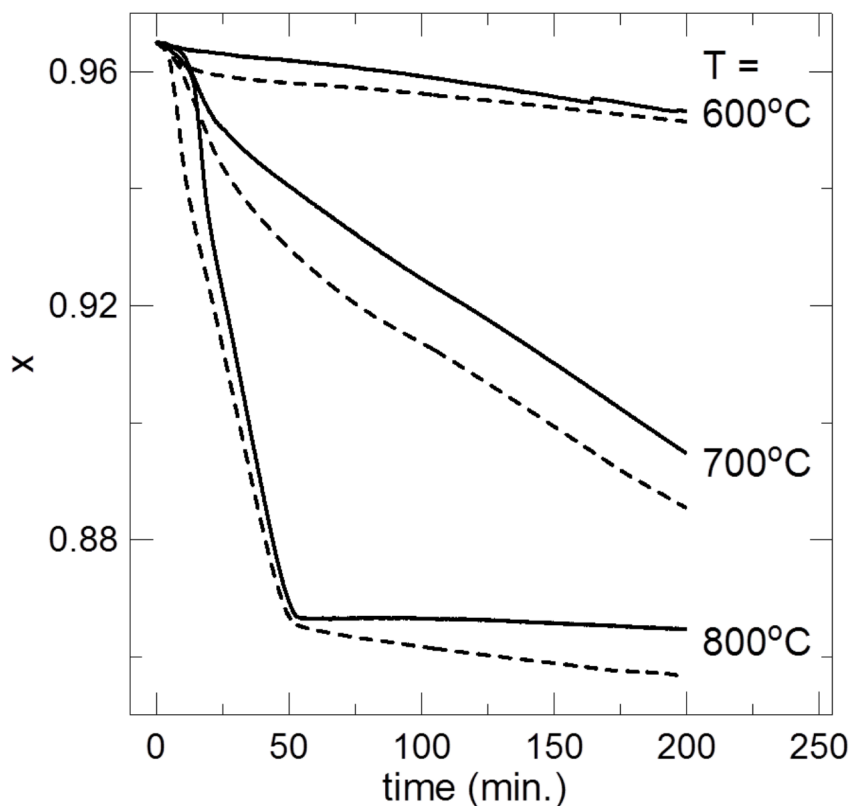


Figure 3.4: TGA results for holds at 600, 700 and 800°C in either oxygen (solid lines) or air (dashed lines). The samples were heated at 20°C/min and  $t = 0$  min represents the moment when the temperature first reached its intended value. The lithium content was calculated from the mass loss using Eq. 3.1 assuming that both lithium oxide and oxygen are lost.

that a larger lithium loss was expected for these samples, but the value of 0.90 can be considered an ideal objective for the combinatorial samples. This data therefore clearly shows that excess lithium is required to synthesize combinatorial samples of  $\text{LiNiO}_2$  at 800°C.

### 3.3 XRD Results of Lithium Loss

#### 3.3.1 Combinatorial samples

Accurate values for the lithium content of the samples after heating were obtained from the lattice parameters. The  $\text{Li}_x\text{Ni}_{2-x}\text{O}_2$  structures are cubic up to  $x = 0.62$  but it has been shown that the entire range of samples from  $x = 0$  to 1 can be described with

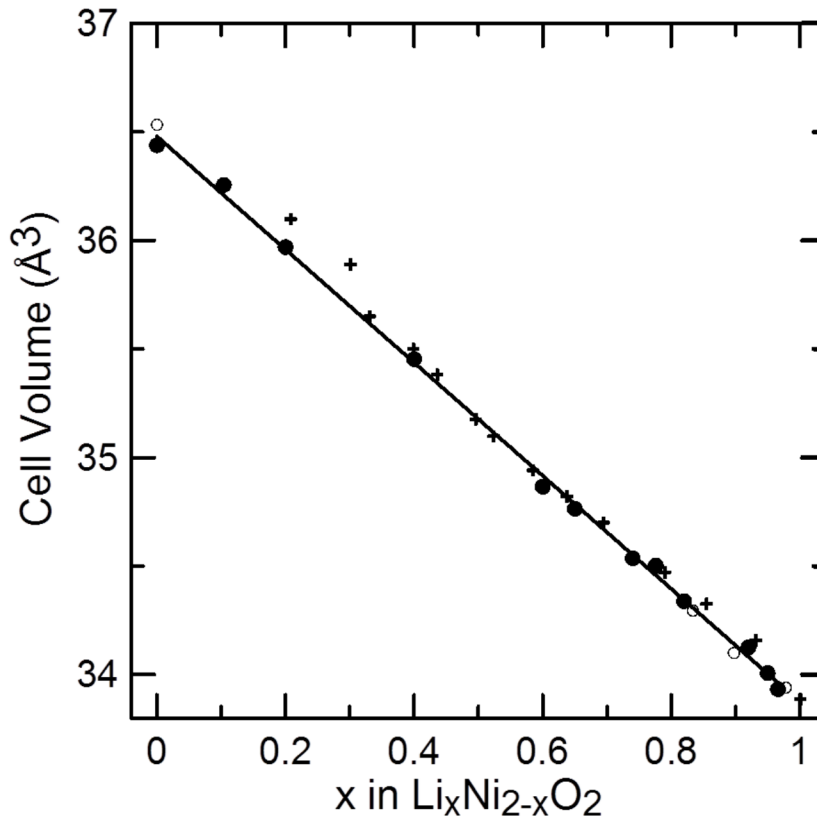


Figure 3.5: Unit cell volume versus  $x$  in  $\text{Li}_x\text{Ni}_{2-x}\text{O}_2$  obtained by Goodenough et al. [72] (closed circles), Li et al. [37] (crosses), and from the present work scanned on the JD-2000 and analyzed with Rietveld refinement (open circles). The unit cell volume is per  $\text{Li}_x\text{Ni}_{2-x}\text{O}_2$  formula unit.

a hexagonal structure using peak indexing according to  $\text{LiNiO}_2$ , JCPDS #89-3601 [33, 37, 72]. Figure 3.5 shows the cell volume as a function of  $x$  as measured by Li [37] and Goodenough [72]. Samples measured with the JD-2000 were also included in the graph since the lattice parameters and lithium content were independent fitting parameters in the Rietveld refinement. The data are linear over the entire compositional range and well defined by  $V = 36.479 - 2.6048x$  which is a fit to the Goodenough data only.

Table 3.1 shows the values for  $x$ , size and strain obtained for a wide variety of combinatorial samples prepared as described in Section 2.1.1. The samples measured on both the JD-2000 and the Bruker show that using the unit cell volume to calculate  $x$  gives the same value as obtained by Rietveld refinement within 0.02. Furthermore, the four combinatorial samples that were prepared in oxygen and fit with Rietveld

refinement showed that the maximum amount of nickel on the lithium layers was  $4.4 \pm 2.1$  % more than that expected for a perfectly ordered structure at  $800^\circ\text{C}$  and  $3.5 \pm 1.6$  % at  $700^\circ\text{C}$ . Although these values are slightly higher than the value of 2.1 % obtained by Li et.al. [37], it can be concluded that the amount of nickel disorder on the lithium layers in the combinatorial samples was not greatly different from that seen in bulk samples. Also, the Bragg R-factors obtained for the combinatorial samples ranged over 2.2 - 3.5 %, compared to 2.3 - 3.4 % for Li et.al. showing that high quality fits were generated by the refinement. When heated in air, the lithium loss is extreme: 47 % on alumina at  $700^\circ\text{C}$ . This is reduced to approximately 32 % by using either magnesia or alumina treated with lithium hydroxide. The poor performance of the alumina substrate implies that it reacted with the lithium in the samples to form  $\text{LiAlO}_2$ . However, even the samples with 50 % excess lithium on magnesia had a low lithium content ( $x = 0.769$ ) at  $700^\circ\text{C}$  showing that excess lithium is not sufficient to synthesize  $\text{LiNiO}_2$  in air and that the lithium loss is far greater than the 6 % expected from the TGA data.

Oxygen played a dramatic role in reducing the lithium loss. The best result at  $700^\circ\text{C}$  without using excess lithium was  $x = 0.923$  ( $< 8$  % Li loss) obtained on alumina treated with LiOH, though this is quite close to the value of  $x = 0.906$  obtained on alumina. The reduction of lithium loss in oxygen as compared to air was far greater than the 15 % difference seen in the TGA results. These observations suggest that the thermal decomposition of lithium nickel oxide is not the only mechanism for lithium loss in these samples. Additionally, the substrate had little effect on the lithium content when heated in oxygen, showing that the reaction between alumina and lithium was suppressed.

The results were somewhat erratic on  $\text{LiAlO}_2$  which may be due to inconsistencies in the thickness of the LiOH layers. The sample with  $x = 0$  as-dispensed was used to see if the  $\text{LiAlO}_2$  layer gave some lithium to the samples. The results of  $x = 0.06$  and 0.05 show that a small amount of lithium was transferred to the nickel oxide but this is not considered to be a significant factor.

The result of  $x = 0.910$  obtained on alumina at  $800^\circ\text{C}$  in oxygen without excess lithium shows that the lithium loss under these conditions was comparable to the

Table 3.1:  $\text{Li}_x\text{Ni}_{2-x}\text{O}_2$  properties obtained by fitting the XRD patterns of the combinatorial samples. All samples were prepared by heating for 3 h in a flow of approximately 30 mL/min of oxygen gas or in air in a box furnace. The uncertainty values shown are the maximum for the entries in each column. Size is shown for the samples made at 700°C only.

Substrate	Precipitator	Gas flow	x initial	x calculated		size (nm)	strain ( $\times 10^{-3}$ )	
				( $\pm 0.036$ ) <sup>‡</sup>			$\pm 0.004 \times 10^{-3}$	
				700°C	800°C	( $\pm 20\%$ )	700°C	800°C
$\text{Al}_2\text{O}_3$	$\text{CO}_3^{2-}$	Air	1.0	0.527	0.529*	37	0.078	0.019
$\text{LiAlO}_2$	$\text{CO}_3^{2-}$	Air	1.0		0.687*	71*		0.287
$\text{MgO}$	$\text{CO}_3^{2-}$	Air	1.0	0.681		55	0.278	
			1.0	0.878		54	0.388	
				0.898 <sup>†</sup>	0.834 <sup>†</sup>			
$\text{MgO}$	$\text{CO}_3^{2-}$	$\text{O}_2$	1.09	0.967		89	0.319	
				0.977 <sup>†</sup>	0.914 <sup>†</sup>			
			1.2	0.994		73	0.176	
			0.9	0.796		61	0.384	
$\text{MgO}$	$\text{OH}^-$	$\text{O}_2$	1.0	0.886		66	0.379	
			1.2	0.987		117	0.174	
			0.8	0.704	0.650	40	0.207	0.293
$\text{Al}_2\text{O}_3$	$\text{OH}^-$	$\text{O}_2$	1.0	0.906	0.910	57	0.655	0.118
			1.2	1.01	0.952	133	0.104	0.111
			0.0	0.065	0.052	134	0.077	0.055
$\text{LiAlO}_2$	$\text{OH}^-$	$\text{O}_2$	1.0	0.923	0.828	—**	0.196	0.032
			1.2	0.938	0.829	111	0.149	0.011

\* Data collected at 750°C by Graham Carey.

\*\* Size values greater than 150 nm are omitted as the size broadening is indistinguishable from the XRD machine peak broadening.

<sup>†</sup> Scanned on the JD-2000 diffractometer; fit with Rietveld refinement using the Rietica software.

<sup>‡</sup> The uncertainty on x was reduced to 0.006 for  $x > 0.7$ .



ideal situation found with the TGA where a value of  $x = 0.90$  was predicted. Also, the results of  $x = 0.952$  obtained under the same conditions with 50 % excess lithium shows that samples of  $\text{Li}_x\text{Ni}_{2-x}\text{O}_2$  can be synthesized over nearly the whole  $x$ -range under the same conditions as required to prepare the spinel samples. Though a sample with  $x = 1$  was not made, the objective of finding the conditions that minimize the lithium loss was reached and  $x = 0.95$  is comparable to that obtained for bulk samples heated in air. Figure 3.1 shows that samples synthesized throughout the Gibbs triangle under these conditions result in little lithium loss. The only exceptions are samples near the lithium corner where large losses occurred because  $\text{Li}_2\text{O}$  cannot exist in atmospheres containing oxygen as previously discussed.

### 3.3.2 Combinatorial Samples During Synthesis

To determine the cause of the extra lithium loss in air that was not accounted for by the thermal decomposition of  $\text{LiNiO}_2$  and to better understand how the combinatorial samples were synthesized, a number of samples were prepared and measured with the Bruker diffractometer after heating to various temperatures. Combinatorial samples were dispensed on magnesia, dried at  $55^\circ\text{C}$  and the XRD spectra were measured directly on the substrate. Figure 3.6 shows the results for two samples prepared from nickel nitrate only. There were a number of phases present in these scans with the strongest peaks being from ammonium nitrate (JCPDS #83-0520), which arose as a product of the reaction between the metal nitrates and the precipitator. The samples were then heated for three hours at  $200^\circ\text{C}$  and scanned again. As expected, the ammonium nitrate decomposed at this temperature [73], and the peaks due to this phase were not seen beyond this point. The heating step was then repeated at 300, 400...  $900^\circ\text{C}$  and the scattering from each of the samples was measured after each heating step. Figure 3.6 shows that the  $x = 0$  samples contained NiO only (JCPDS #47-1049) after being heated at  $300^\circ\text{C}$  such that all contaminants are eliminated at this temperature.

Magnesia was selected for this part of the study because it only has three X-ray peaks in the range over which scans were taken. These peaks were fit to and subtracted from the patterns. In practice, the MgO peaks (JCPDS #45-0946) were

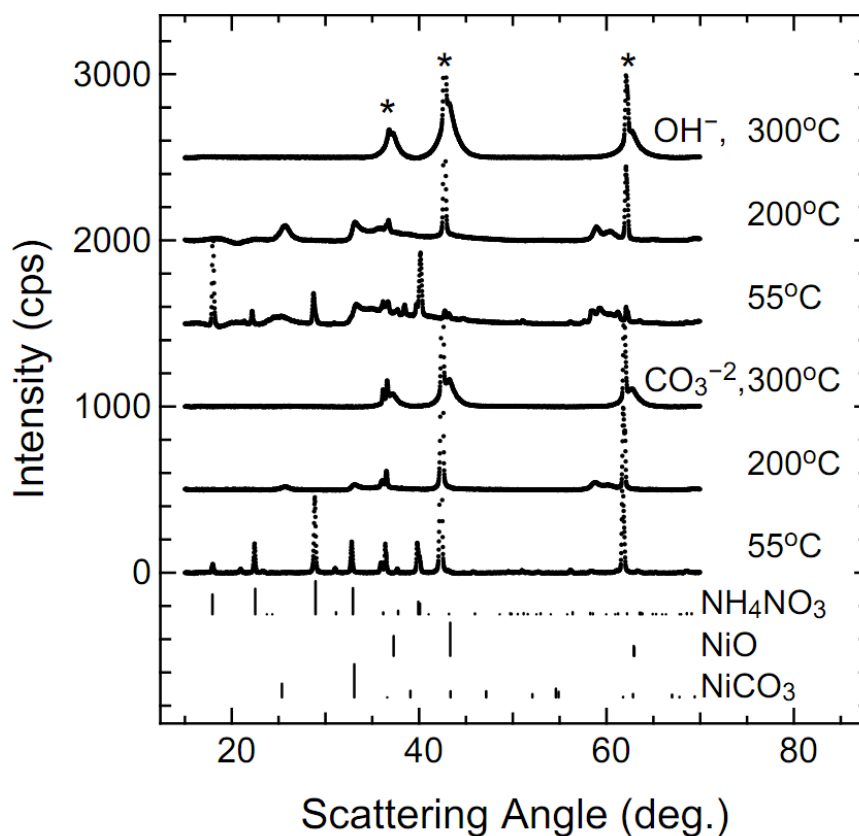


Figure 3.6: XRD scans of nickel nitrate samples obtained after co-precipitation, drying and heating to various temperatures. The MgO peaks were truncated at 500 cps and \* indicates their positions. For ease of viewing, a polynomial background was fit and subtracted from each scan. The vertical lines indicate peak positions and relative intensities from the JCPDS database.

shifted from their expected positions because the X-ray machine was aligned to the top of the samples such that the substrate had a vertical misalignment of up to 1 mm. This misalignment varied from sample to sample such that an independent zero in scattering angle was needed for these peaks.

Some samples studied in this way were prepared with the bicarbonate precipitator heated in oxygen, while others were prepared from ammonium hydroxide heated in air. In order to help distinguish the effect of the precipitator from the atmosphere, samples prepared with ammonium hydroxide and heated in oxygen were measured after heating to 600, 700, 800 and 900°C only. Figures 3.2 (a) and (b) show XRD scans obtained by this approach, along with the fits and difference plots. The lithium

hydroxide converted to lithium carbonate, and this occurred readily at 300°C while the stearic acid decomposed. Even the smaller amounts of stearic acid used on alumina (approximately 1.5 mg/cm<sup>2</sup>) were sufficient to produce enough carbon dioxide to react with all the lithium in the combinatorial samples. Thus, the synthesis of lithium nickel oxide in the combinatorial samples involved the reaction of lithium carbonate with nickel oxide regardless of the precipitator used. The fitting of the XRD scans therefore required three phases: lithium carbonate (JCPDS #80-1307), lithium nickel oxide and magnesium oxide.

Figure 3.2 (a) shows that the scattering from samples prepared with ammonium bicarbonate contained a large peak near 23.5°. The position of this peak varied from sample to sample, following the magnesia peaks showing that it can be attributed to the surface of the substrate. Lala et al. [69] found that lithium stearate has a large peak near 24° and a smaller peak above 40°. Since the peak near 24° was only seen in samples with lithium, it was most likely lithium stearate, though there may have been some nickel stearate as well since it also has peaks in this range [74]. The peak was fit using a pseudo-Voigt function. Figure 3.7 shows that the stearate peak grew as the samples were heated, especially during the stearic acid decomposition. The peak disappeared after heating at 600°C in most samples, consistent with the fact that lithium stearate converts to lithium carbonate at 522°C [69]. The lithium stearate on the substrate surface results in a lithium deficiency in the sample during heating that could affect the final lithium content of the samples. The stearate peak was never seen when ammonium hydroxide was used as the precipitator. It is also possible that some lithium stearate decomposition also contributed to the lithium loss.

Figure 3.8 shows that at 400°C the amount of lithium in the lithium nickel oxide structure was constant regardless of the amounts dispensed. At this temperature, the amount of lithium carbonate co-existing with the structure was proportional to the amount of lithium dispensed. Since the excess lithium found in the  $x = 1.1$  and  $1.2$  samples did not react into the nickel oxide structure, the lithium nickel oxide synthesis was limited by the slow rate of reaction between lithium carbonate and the rocksalt structure at low temperatures.

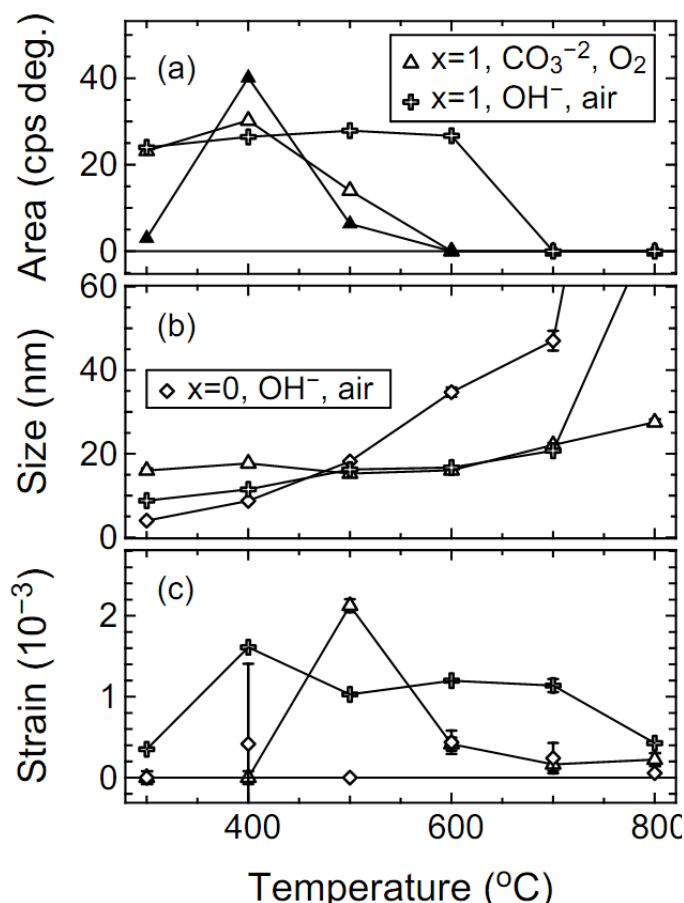


Figure 3.7: (a) Peak areas as a function of temperature. Open symbols are for the  $\text{Li}_2\text{CO}_3$  (002) peak. The closed triangles represent the large stearate peak (divided by 30) obtained with ammonium bicarbonate and heated in air. (b)  $\text{Li}_x\text{Ni}_{2-x}\text{O}_2$  crystallite size and (c) strain as a function of temperature. Error bars smaller than the symbols were omitted.

Figure 3.9 shows the calculated value of  $x$  for samples with  $x = 0$  and 1 as-dispersed as a function of the heating temperature. Samples with  $x = 0.8, 0.9, 1.1$  and  $1.2$  showed the same trends as the  $x = 1$  sample; they were excluded for clarity. The amount of lithium in the rocksalt structure stays low in air with the only significant increase taking place at  $700^\circ\text{C}$  where  $x = 0.32$ . This behaviour is in sharp contrast to that seen in the spinel  $\text{LiMn}_2\text{O}_4$  samples where lithium mixes in readily at  $250^\circ\text{C}$  [70]. Figure 3.7 (a) shows that lithium carbonate co-existed with lithium nickel oxide up to  $600^\circ\text{C}$  in air. Since lithium carbonate decomposes spontaneously at  $640^\circ\text{C}$  [75], there was no temperature in air at which lithium carbonate reacted

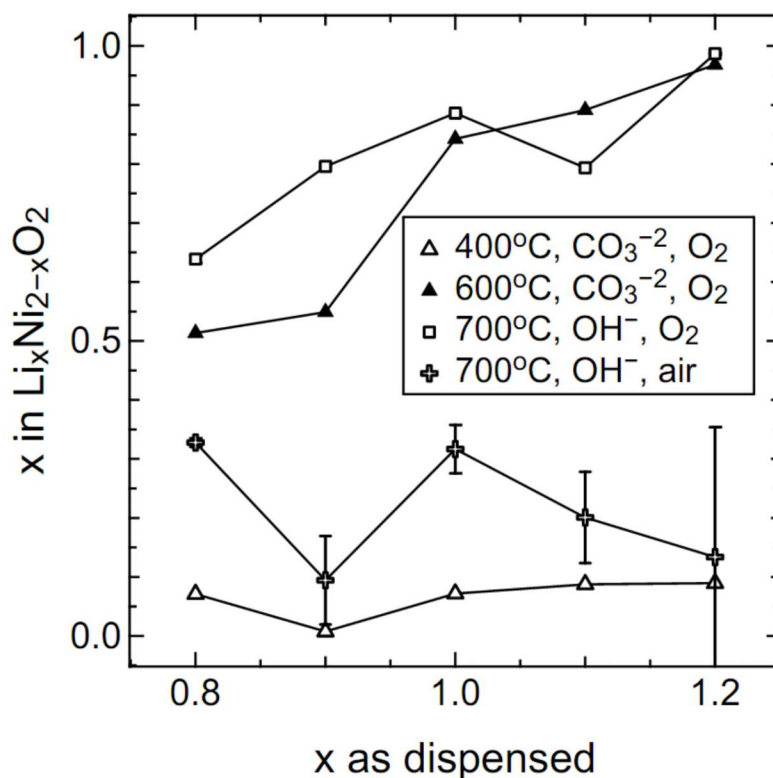


Figure 3.8: Lithium content measured by XRD versus the amount dispensed.

rapidly with nickel oxide and lithium carbonate did not decompose. Both reactions occurring simultaneously above 640°C keeps the lithium content low throughout the experiment. The lithium loss in these samples is therefore attributed primarily to the slow reaction rate for the formation of  $\text{LiNiO}_2$  and is not the result of the thermal decomposition of lithium nickel oxide. In a flow of oxygen, lithium carbonate was not present after heating at 600°C and the lithium content jumped to  $x = 0.85$  at this point. This shows that the reaction between lithium carbonate and the NiO structure:



is significantly slower in air and occurs readily at 600°C in oxygen. This temperature is important because lithium carbonate does not yet decompose. Thus, the second mechanism for lithium loss in the combinatorial samples is the thermal decomposition of lithium carbonate. The fact that the substrate has little effect on the lithium content of the samples in oxygen implies that lithium already in the  $\text{Li}_x\text{Ni}_{2-x}\text{O}_2$

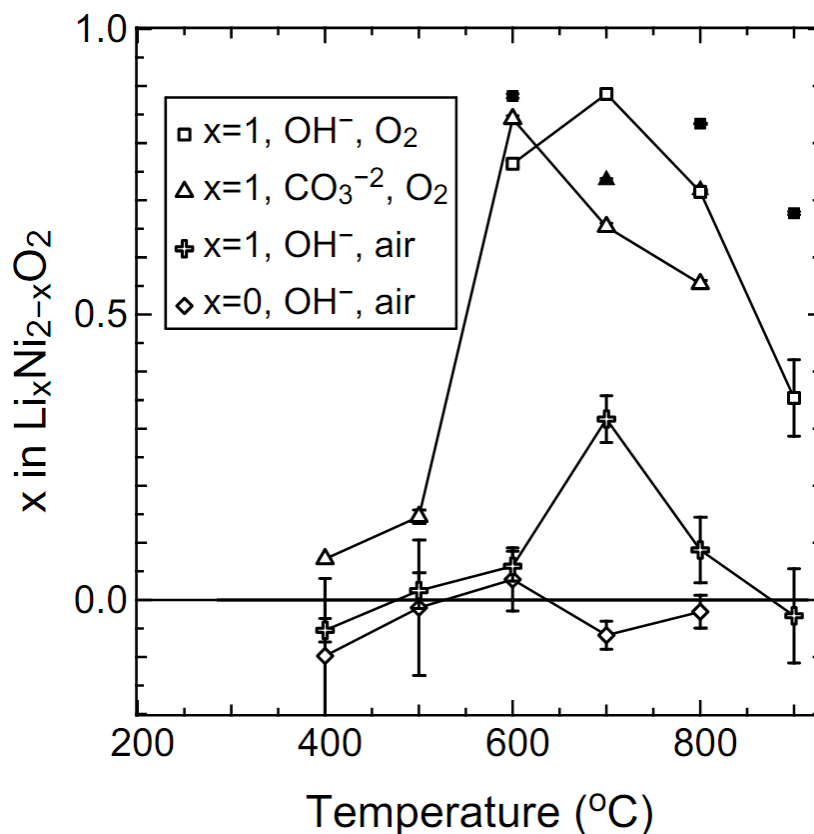


Figure 3.9: Calculated lithium content as a function of temperature. Closed symbols indicate samples made by dispensing 20  $\mu\text{L}$  of solution as compared to 10  $\mu\text{L}$  for the open symbols.

structure does not react with alumina. It is therefore the accelerated formation of lithium nickel oxide that resulted in the suppression of the formation of  $\text{LiAlO}_2$  for samples heated on alumina in oxygen.

In order to determine why the formation of lithium nickel oxide is hindered in air, 10  $\mu\text{L}$  combinatorial samples with  $x = 1$  as-dispensed were prepared and heated for 3 hours at 600°C. Three were heated in a tube furnace in a flow of 5.5 %  $\text{O}_2$ , 94.5 %  $\text{N}_2$  and XRD showed that the lithium content in these samples was  $x = 0.91 \pm 0.03$ . When pure oxygen was used the result was  $x = 0.95 \pm 0.01$  such that the amount of oxygen played a small role here implying that it must have been constituents other than oxygen and nitrogen that primarily hindered the synthesis of  $\text{LiNiO}_2$  when heated in air. Other samples were heated in a tube furnace without the caps on the ends of the tube thereby allowing the escape of carbon dioxide produced

during the decomposition of the stearic acid. The XRD scans of these samples showed that lithium carbonate was still present and the lithium content in the lithium nickel oxide structures was  $x = 0.68 \pm 0.02$ . In a closed box furnace, the result was  $x = 0.59 \pm 0.02$  and lithium carbonate was also evident in the scans. This shows that the presence of carbon dioxide slowed down the reaction between lithium carbonate and nickel oxide as one would expect since it is a product of the synthesis. However, venting the excess carbon dioxide had a relatively small effect on the lithium content of the samples, suggesting that another gas such as water vapour may also play a role here. Samples made with double the volume of solution (solid symbols in Figure 3.9) have higher lithium content after heating, with this effect being more pronounced at higher temperatures. These observations reinforce how sensitive these samples were to surface area. Larger dispense volumes do provide another means to reduce the lithium loss, but  $20 \mu\text{L}$  is the practical limit for samples made with the solution-dispensing robot.

Another means of reducing the lithium loss was found by first heating the samples to  $600^\circ\text{C}$  before heating to the desired temperature. To illustrate this,  $20 \mu\text{L}$  samples of the  $x = 1.2$  as-dispensed compositions were prepared by heating at  $850^\circ\text{C}$  for 3 hours in oxygen. The resulting XRD scan showed  $x = 0.83$  while repeating the process with the addition of a 3 hour heating step at  $600^\circ\text{C}$  before heating to  $850^\circ\text{C}$  gave a lithium content of 0.88. Though this effect may be diminished at  $800^\circ\text{C}$ , there should still be some benefit to heating at  $600^\circ\text{C}$  in order to ensure that as much lithium as possible enters the nickel oxide structure at a temperature where the thermal decomposition reaction is slow and lithium carbonate does not decompose.

The values for crystallite size and strain of lithium carbonate were found to be very stable over the temperature range in which it was present. Table 3.2 shows the average values obtained in either air or oxygen. The lithium carbonate crystallites were larger and more strained when the sample was prepared in air and this effect was enhanced if the carbonate precipitator was used. Using the carbonate precipitator in air resulted in crystallites that were considerably larger than the rocksalt structure with which it was reacting (Figure 3.7 (b)). Furthermore, the lithium carbonate crystallites were small with little strain when heated in oxygen.

Table 3.2: Average  $\text{Li}_2\text{CO}_3$  crystallite size and micro-strain. Values were stable over the heating temperature range in which lithium carbonate is present. The uncertainty is half the range in the values.

Precipitator	Atmosphere	Size (nm)	Strain ( $10^{-3}$ )	Temperature ( $^{\circ}\text{C}$ )
$\text{OH}^-$	Air	$22 \pm 1$	$0.14 \pm 0.04$	300, 400, 500, 600
$\text{CO}_3^{2-}$	Air	$51 \pm 4$	$0.30 \pm 0.01$	400 (2 samples)
$\text{CO}_3^{2-}$	$\text{O}_2$	$13 \pm 4$	0.0*	300, 400, 500

\* The fitting software converged to a strain of 0 which indicates that the machine broadening dominated.

Figure 3.7 (b) shows that nickel oxide crystallites grew steadily over the entire temperature range and the strain stayed small. By contrast, when lithium was present, crystallites remained small until all the lithium was done reacting. Figure 3.7 (c) shows that in oxygen, the strain increased dramatically while the lithium entered the structure (500 - 700 $^{\circ}\text{C}$ ) indicative of an increase in the number of defects as well as variations in lithium content within each crystallite [63]. In air, the results were similar with the crystallites only growing rapidly once most of the lithium was reacted. The higher strain was also present over a greater temperature range. Figure 3.7 (c) suggests that heating to 800 $^{\circ}\text{C}$  ensures that the crystallites obtained are relatively homogeneous and have few defects.

### 3.4 Conclusions Regarding Synthesis of Combinatorial Samples

Mechanisms for lithium loss during and after the formation of combinatorial samples of lithium nickel oxide were identified. During synthesis in air, the main source of lithium loss was the decomposition of lithium carbonate that failed to react with the nickel oxide structure. The fact that the formation of  $\text{LiNiO}_2$  was hindered significantly in air was attributed to the presence of constituents in air other than oxygen and nitrogen, the likeliest candidates being carbon dioxide and water vapour. The second mechanism for lithium loss was the thermal decomposition of  $\text{Li}_x\text{Ni}_{2-x}\text{O}_2$ . TGA was used to confirm that both lithium oxide and oxygen were lost when the



samples were heated in either air or oxygen. In both cases, the loss of lithium from the samples was attributed to the conversion of lithium oxide to lithium peroxide vapour. Synthesizing the samples in dry, carbon dioxide free air would therefore result in lithium content very close to that seen in oxygen, the only difference being attributed to a slight increase in the rate of decomposition of lithium nickel oxide as seen in the TGA. Combinatorial samples of  $\text{Li}_x\text{Ni}_{2-x}\text{O}_2$  cannot be made with  $x > 0.77$  at  $700^\circ\text{C}$  in air. In a flow of oxygen, excess lithium was used to react a sufficient amount of lithium into the material to form  $\text{Li}_{0.95}\text{Ni}_{1.05}\text{O}_2$  at  $800^\circ\text{C}$  on an alumina substrate. These conditions allow the simultaneous synthesis of the layered and spinel structures in the Li-Mn-Ni-O system.

Alumina, the least desirable substrate in air, performed comparably to the others in oxygen. Magnesia required large amounts of stearic acid in order to bead the solutions and the subsequent decomposition of the stearic acid was found to interfere with the samples. The third substrate tested was alumina treated with lithium hydroxide and it was difficult to treat it uniformly enough to get consistent results. The substrate selected for further combinatorial studies was therefore alumina in a flow of oxygen. Two precipitators were tested: ammonium bicarbonate and ammonium hydroxide. Little difference can be found in the lithium content of the final samples, but only the carbonate precipitator resulted in the formation of lithium stearate on the surface of the substrate.

The map of lithium loss in Figure 3.1 shows that samples can be prepared throughout the Gibbs triangle with the exception of samples near the Li corner where the formation of lithium peroxide vapour prevents co-existence with lithium oxide. Consequently, the issue of lithium loss in the Li-Mn-Ni oxide pseudo-ternary system is manageable with the methodology developed here and used throughout the rest of this thesis for combinatorial synthesis. All other Li-Mn-Ni-O samples were therefore heated at  $800^\circ\text{C}$  for 3 h in oxygen. Various cooling rates were used, but the heating rate was always  $5^\circ\text{C}/\text{min}$ . The only variation for Li-Co-Mn-O materials was that they were heated in air in a box furnace since it was found that lithium loss was much smaller for these samples as discussed in the next chapter.

## Chapter 4

### Combinatorial Studies in the Li-Co-Mn-O System

Data in this chapter are reprinted from Ref. [76] with permission from the American Chemical Society.

#### 4.1 Experimental Design

Figure 4.1 shows the results of the current project for the Li-Co-Mn oxide pseudo-ternary system obtained in air at 800°C. The two single-phase regions that lie solely on the Co-Mn line are a tetragonal spinel phase (including  $\text{CoMn}_2\text{O}_4$ ) and a bixbyite phase (including  $\text{Mn}_2\text{O}_3$ ). Once again, there are two solid solution regions of significance to the Li-ion research community: the cubic spinel and layered regions. The co-existence region between them is relatively simple with two-phase co-existence only. The layered single-phase region and the co-existence between the layered structures and  $\text{Co}_3\text{O}_4$  are the focus of this chapter. The entire spinel region was also determined [77]. Much of the work for the spinel region was done by Colby Brown and evidence for this will be part of his Master's thesis.

Each combinatorial sample, with an approximate mass of 2 mg, was made using the method described in Section 2.1.1. Samples were made for 11 compositions evenly spaced along each of the three lines:  $\text{LiCoO}_2$  -  $\text{Li}_2\text{MnO}_3$ ,  $\text{LiCoO}_2$  - sample  $A_4$ , and  $\text{Li}_2\text{MnO}_3$  - sample  $A_4$  (using the labels in Figure 4.1). In this system, lithium loss is less severe than in the case of the Li-Mn-Ni-O layered materials such that 3 hours heating in air ( $P_{\text{O}_2} = 0.21$  atm) was possible. In the vast majority of studies found in the literature, the samples were made by cooling from high temperature at roughly 5 - 10°C/min, e.g. [19] and [24]. However, the cooling rate can have a significant impact on the phases obtained, so one important feature of the current study was to vary the cooling rate to see the effect on the layered region. The objective was to understand how and at which compositions the layered-layered nano-composites form in order to

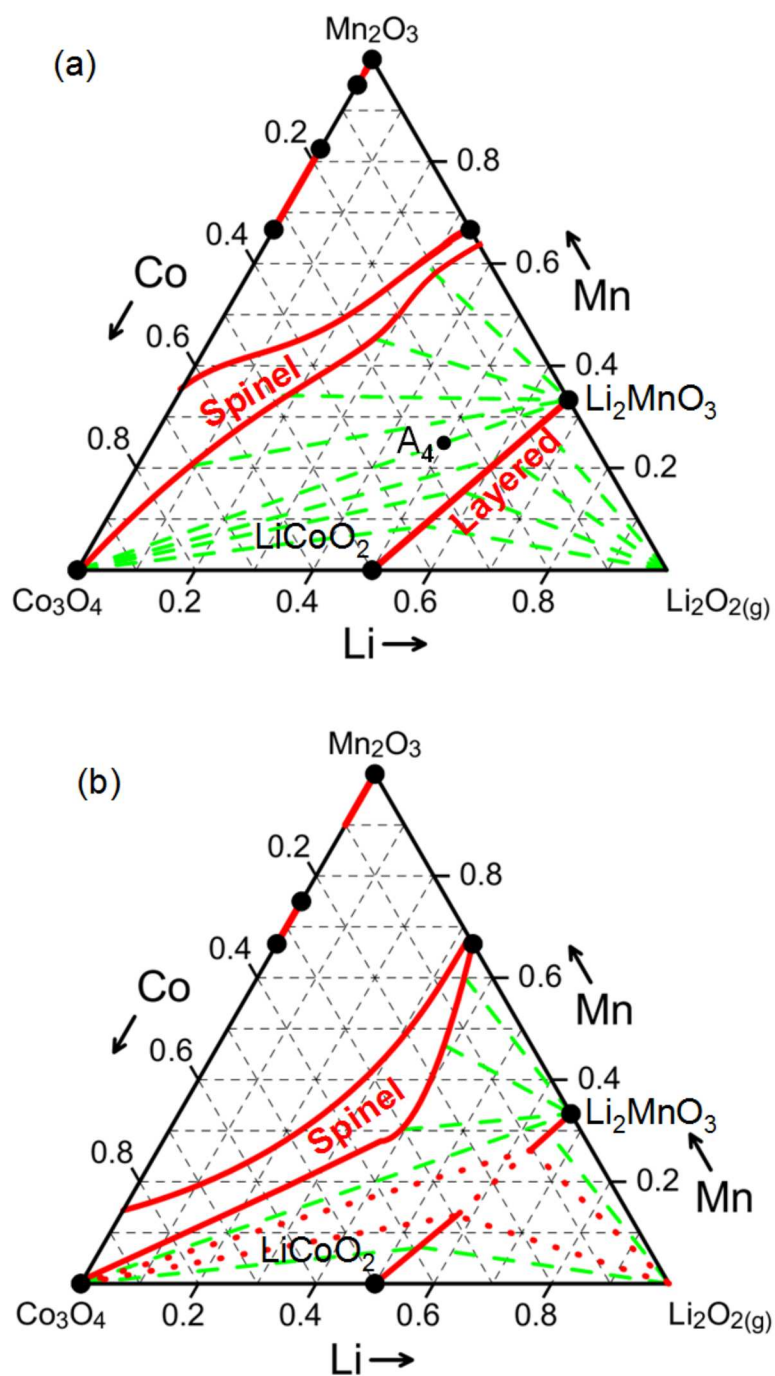


Figure 4.1: The entire Gibbs triangles for samples heated to  $800^\circ\text{C}$  in air and quenched (a), or regular cooled (b). Sample  $A_4$  is at the composition  $\text{Li}_{0.5}\text{Mn}_{0.25}\text{Co}_{0.25}$  and is referred to throughout the text. Green dashed lines are tie-lines, solid red lines are boundaries to single-phase regions while red dotted lines are tie-lines bounding three-phase regions.

determine if the phase diagrams produced with combinatorial samples can be used to predict nano-composite formation. Three cooling rates (quenched, regular cooling and slow cooling) were therefore used.

It was found that lithium loss occurred in all samples at 900°C when non-quenched, as well as in a few samples heated to 800°C when slow cooled. This loss resulted in samples lying in the spinel-layered co-existence region (Figure 4.1) such that  $\text{Co}_3\text{O}_4$  peaks could be seen in the XRD patterns. In order to compensate for this, samples were made along the  $\text{LiCoO}_2$  -  $\text{Li}_2\text{MnO}_3$  line with 15 % excess lithium. As will be discussed in the results sections below, this eliminated all spinel peaks and the resulting oxides fell on the desired composition line. There was also no evidence of excess  $\text{Li}_2\text{CO}_3$  remaining after synthesis which is another possible product formed when excess lithium does not evaporate as  $\text{Li}_2\text{O}_2$ .

After heating, the samples were characterized using a Bruker D8 Discover X-ray diffractometer. The software written in-house (Section 2.3) was used to fit entire X-ray patterns in order to extract lattice parameters and phase compositions. In order to help determine whether the peak broadening seen is consistent with crystallite size effects, the peaks were first corrected for machine broadening and then crystallite size was calculated assuming no micro-strain.

In order to better understand the changes taking place during cooling, the Monte Carlo simulation described in Section 2.12 was used with the composition lying midway between  $\text{LiCoO}_2$  and  $\text{Li}_2\text{MnO}_3$ , i.e.  $x = 0.5$  in  $\text{Li}[\text{Li}_{(1-x)/3}\text{Co}_x\text{Mn}_{(2-2x)/3}]\text{O}_2$ . The transition metal layer was made up of 50 % cobalt atoms, 33.3 % manganese and 16.7 % lithium, with only lithium on the lithium layers.

## 4.2 Spinel - Layered Co-Existence Region

Figure 4.2 shows a stack of XRD scans taken for 11 samples evenly spaced along the line from  $\text{Li}_2\text{MnO}_3$  to sample  $A_4$  after heating to 800°C for 3 h and regular cooling. The scans show two phases:  $\text{Li}_2\text{MnO}_3$  and  $\text{Co}_3\text{O}_4$ . The peaks at 19.05, 59.5 and 65.2° (all indexed to the spinel phase) show most clearly the disappearance of  $\text{Co}_3\text{O}_4$  for compositions approaching  $\text{Li}_2\text{MnO}_3$ . Figure 4.3 (a) shows a few XRD scans of materials along the line from  $\text{LiCoO}_2$  to point  $A_4$ . Again, co-existence between a

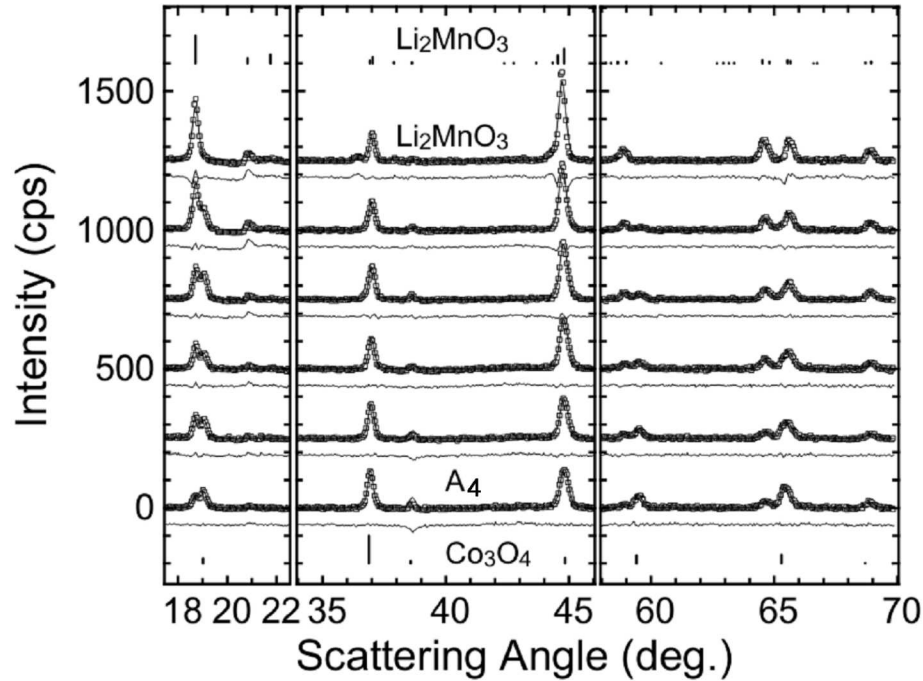


Figure 4.2: Stack of XRD patterns with fits and difference plots obtained by heating to 800°C and regular cooling. The vertical lines indicate peaks from the JCPDS database, reference #84-1634 for  $\text{Li}_2\text{MnO}_3$  and #74-1656 for  $\text{Co}_3\text{O}_4$ . The unlabeled scans between  $\text{A}_4$  and  $\text{Li}_2\text{MnO}_3$  are evenly spaced in composition between the two end-members. For clarity, only every third data point is plotted.

layered phase and  $\text{Co}_3\text{O}_4$  can clearly be seen, though the layered peaks shift to lower angle as the composition moves towards point  $\text{A}_4$ . This is consistent with the tie-lines shown in Figure 4.1 (a) which fan out from the cobalt corner such that the lattice parameters of the layered phase increase as the average composition moves from  $\text{LiCoO}_2$  to  $\text{A}_4$  while the spinel lattice parameter remains that of  $\text{Co}_3\text{O}_4$ .

The two-phase scans were fit and this resulted in 20 values of the cubic lattice parameter for the spinel phase for samples along either the  $\text{LiCoO}_2$  -  $\text{A}_4$  or  $\text{A}_4$  -  $\text{Li}_2\text{MnO}_3$  lines. The average value was  $a = 8.065 \pm 0.002 \text{ \AA}$ , with a standard deviation of  $0.010 \text{ \AA}$  and is in agreement with the literature value of  $a = 8.065 \text{ \AA}$  (JCPDS #74-1656) for  $\text{Co}_3\text{O}_4$ . In contrast, the same 20 compositions, made by quenching from 800°C, resulted in an average value of  $a = 8.0761 \pm 0.0005 \text{ \AA}$  with a standard deviation of  $0.002 \text{ \AA}$ . A combinatorial sample made at the cobalt corner by quenching had a

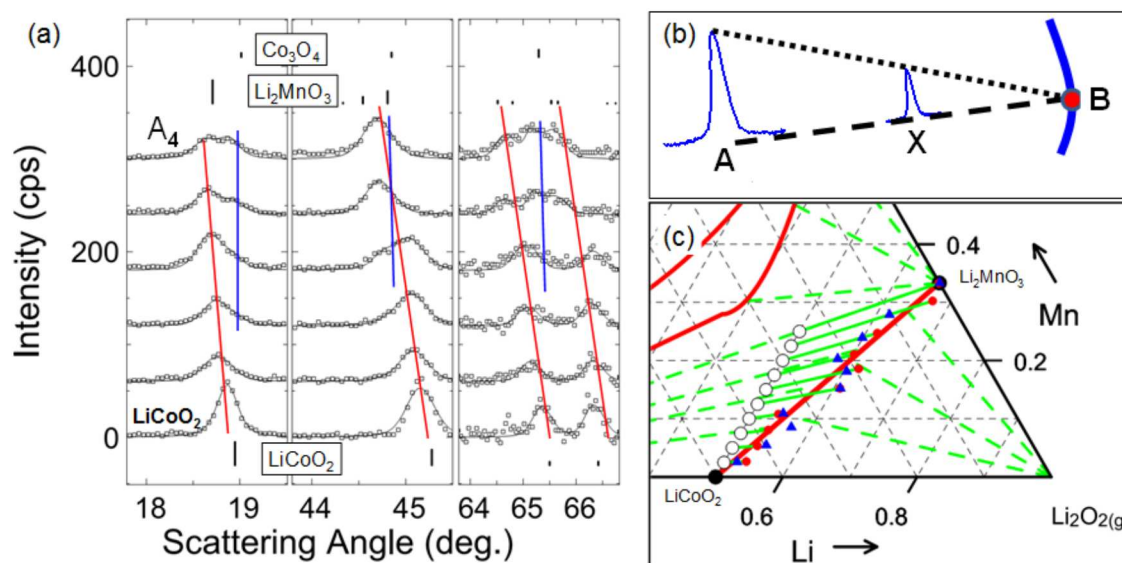


Figure 4.3: (a) Stack of XRD patterns for samples lying between LiCoO<sub>2</sub> and point A<sub>4</sub> obtained by heating to 800°C and regular cooling. The red lines indicate the layered peaks while the blue lines represent the positions of the Co<sub>3</sub>O<sub>4</sub> peaks. The vertical lines for LiCoO<sub>2</sub> are from JCPDS #50-0653. (b) A schematic representation of using the lever rule with a peak of phase A (Co<sub>3</sub>O<sub>4</sub> here). The sample X lies in the co-existence region such that extrapolating to where the area of the phase A peak is zero gives a point B on the boundary of the layered region. (c) The results of using the lever rule for samples along the line from A<sub>4</sub> to LiCoO<sub>2</sub>, represented by the open circles (these represent point X in (b)). The red circles (point B in (b)) are the resulting points on the boundary of the layered region for samples made at 800°C and cooled at the regular rate, while the blue triangles were obtained from quenched samples.

lattice parameter of  $8.084 \pm 0.002$  Å, which is in good agreement with the average value obtained in the co-existence region. The larger lattice parameter obtained by quenching is consistent with oxygen vacancies appearing in the spinel structures at high temperature; a result that was also seen in the spinel structures in the Li-Mn-Ni-O system in Chapter 5. Furthermore, the agreement between the average spinel lattice parameter and that of Co<sub>3</sub>O<sub>4</sub> shows that the tie-lines fan-out from the Co corner up to the tie-line connecting Co<sub>3</sub>O<sub>4</sub> to Li<sub>2</sub>MnO<sub>3</sub> as shown in Figure 4.1.

In order to determine whether the layered single-phase region is truly a line with no width, the lever rule was used for samples synthesized along the composition line LiCoO<sub>2</sub> - sample A<sub>4</sub>. Figure 4.3 (b) illustrates the use of the lever rule for a

sample, X, containing two phases that lie on a tie-line between points A ( $\text{Co}_3\text{O}_4$  in this case) and B (the layered structure in this example). The fraction of each phase was determined from the XRD fits by dividing the integrated peak area of the largest peak of each phase by the corresponding value for the single-phase sample lying on the same tie-line. The phase fractions were then normalized to add up to unity. The lever rule, described in Section 2.4, was used to determine the position of points on the end of the tie-line. Figure 4.3 (c) shows the lever rule results for both quenched and regular cooled samples heated at  $800^\circ\text{C}$ . Within the fluctuations resulting from the experimental methods used, the single-phase layered region is a single line in the Gibbs triangle. This line corresponds to all cobalt atoms being in the 3+ oxidation state while all manganese atoms are in the 4+ state. Generally, Co cannot be oxidized beyond 3+, nor Mn above 4+, under the synthesis conditions used here. The one known exception is that  $\text{Li}_{1+x}\text{Co}_{1-x}\text{O}_2$  can be synthesized with  $x = 0.06$  in oxygen [78]. Therefore there may be a small width to the layered region near  $\text{LiCoO}_2$  but no evidence for this was seen in the current data.

### 4.3 $\text{LiCoO}_2$ - $\text{Li}_2\text{MnO}_3$

Figure 4.4 shows expanded regions of the XRD patterns obtained along the  $\text{LiCoO}_2$  -  $\text{Li}_2\text{MnO}_3$  line by heating to  $900^\circ\text{C}$  and quenching. The scans were consistent with a solid solution over the entire range with no evidence of peak broadening. Similar patterns were obtained by quenching from  $800^\circ\text{C}$  and again samples appeared single-phase. Figure 4.5 shows that the resulting fitted lattice parameters are in good agreement with published values from Kim et al. [19] shown in the introduction. In fact, the  $a$  lattice parameter follows a straight line over the entire composition range for the samples quenched from  $900^\circ\text{C}$ , while the literature values flatten out for  $x > 0.5$ . Kim's data obtained by regular cooling from  $950^\circ\text{C}$  more closely resemble the results for quenching from  $800^\circ\text{C}$ . The values for  $\text{LiCoO}_2$  ( $x = 1$ ) are also very close to the JCPDS values of  $a = 2.815 \text{ \AA}$  and  $c = 14.049 \text{ \AA}$ , while the values obtained at the other endpoint,  $a = 2.845 \text{ \AA}$  and  $c = 14.23 \text{ \AA}$ , are consistent with  $\text{Li}_2\text{MnO}_3$  when described with a hexagonal lattice.

Figure 4.6 shows calculated crystallite size assuming no micro-strain such that the

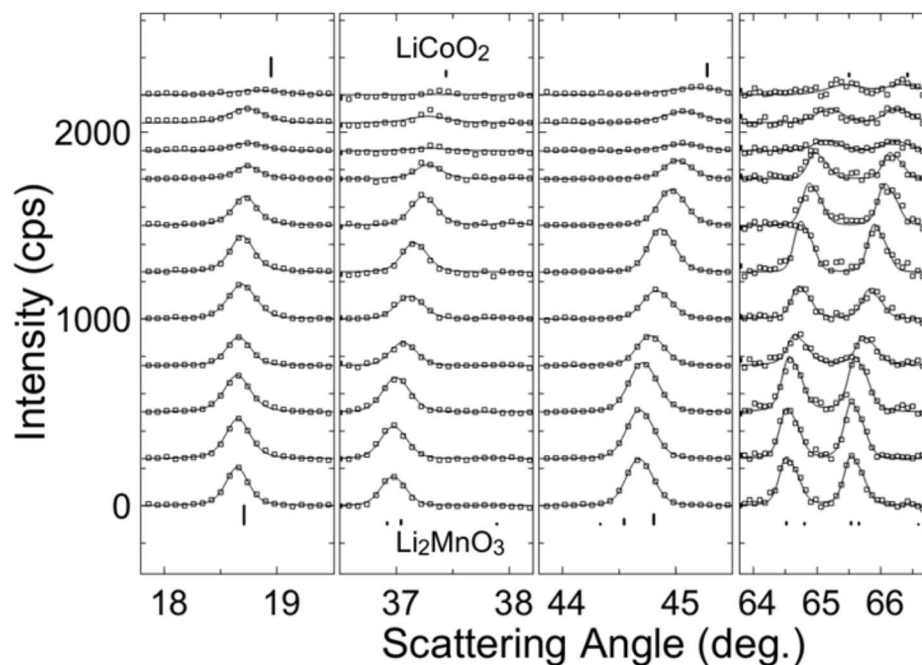


Figure 4.4: Stack of XRD patterns with fits for samples made with 15 % excess lithium and heated to 900°C before quenching to room temperature. For clarity, the second frame (36-38°) has scattering intensities scaled by a factor of two, while the fourth frame (64-67°) has a different x-scale and intensities scaled by a factor of five. This same scaling method is used for Figures 4.7 and 4.9.

size parameter was sensitive to any source of peak broadening. All composition lines had duplicates at  $x = 0.5$  (if they cannot be distinguished, they are overlapping), such that these reflect the fluctuations in the size values resulting from the small combinatorial samples. The results for quenched samples, both at 800 and 900°C, show that the size stays roughly linear over the entire composition range except for a sharp increase for  $\text{Li}_2\text{MnO}_3$  in the data at 800°C. This implies that at high temperature there is no reduction in crystallite size near the center of the composition line. Ergo, since the high angle peak broadening observed in Kim's data [19] is not seen in any of the quenched samples, it must come about during slower cooling.

Figure 4.7 shows the resulting XRD patterns when samples are slow cooled (1°C/min) from 900°C. Near each endpoint (i.e. for  $x < 0.3$  and  $x > 0.7$ ) the scans appear single-phase with the expected shifts in peak position with composition. However, as suggested by the red and blue lines, there is phase separation near the center



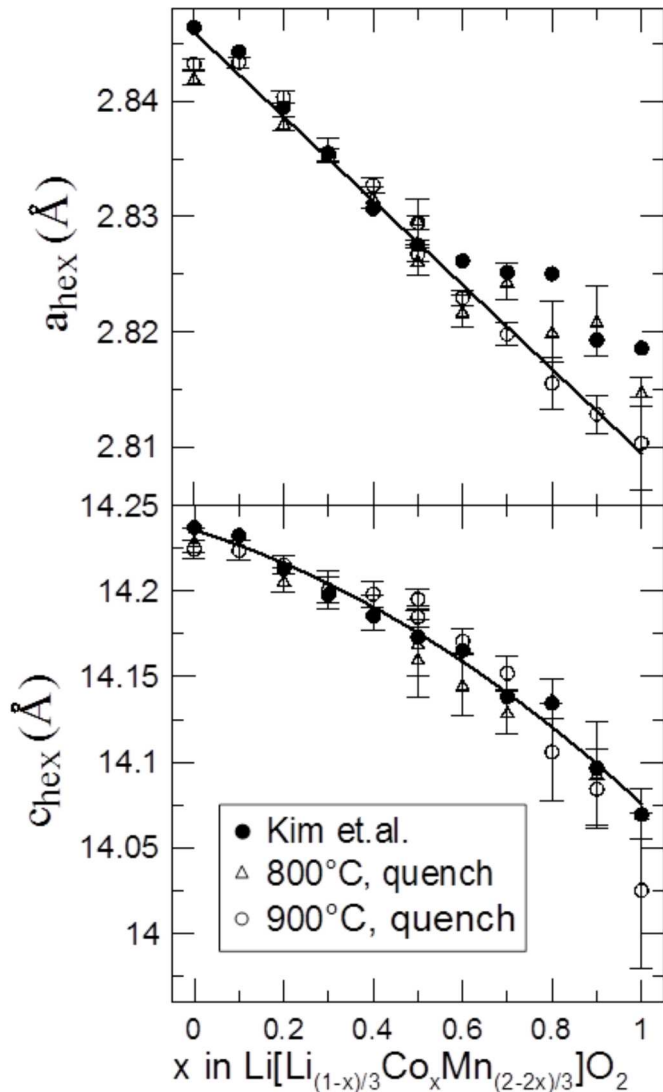


Figure 4.5: Hexagonal lattice parameters obtained by quenching combinatorial samples compared to literature values from Ref. [19]. The lines are guides for the eye.

of the composition line and all peaks are consistent with two layered structures roughly corresponding to the scans at  $x = 0.2$  and  $0.7$ . In order to confirm that lithium loss is not resulting in phase separation here, the region near  $19.06^\circ$ , where a  $\text{Co}_3\text{O}_4$  peak (JCPDS #74-1656) would appear, was examined. No  $\text{Co}_3\text{O}_4$  peaks were present, showing that lithium loss during synthesis was limited to eliminating the excess lithium. Similar peak splitting was observed by Sun et.al. [79] but was interpreted as peak splitting due to monoclinic distortions. Tracking these peaks

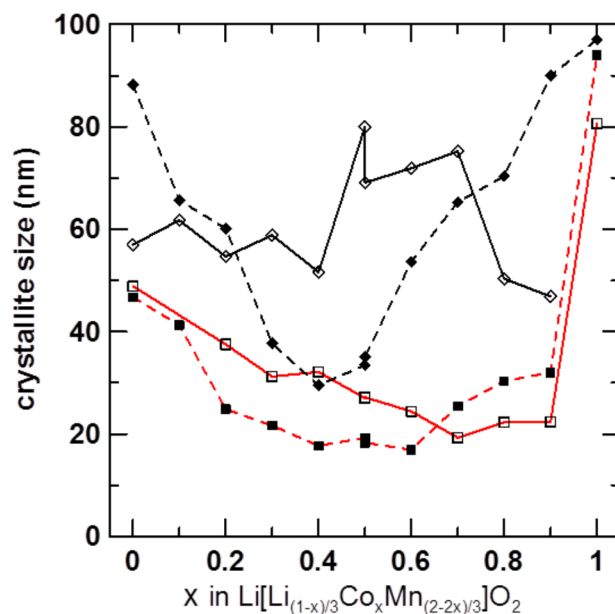


Figure 4.6: Calculated crystallite size obtained for samples heated at 800°C (squares/red lines), and 900°C (diamonds/black lines). Open symbols/solid lines represent samples cooled by quenching, while closed symbols/dashed lines are for regular cooling.

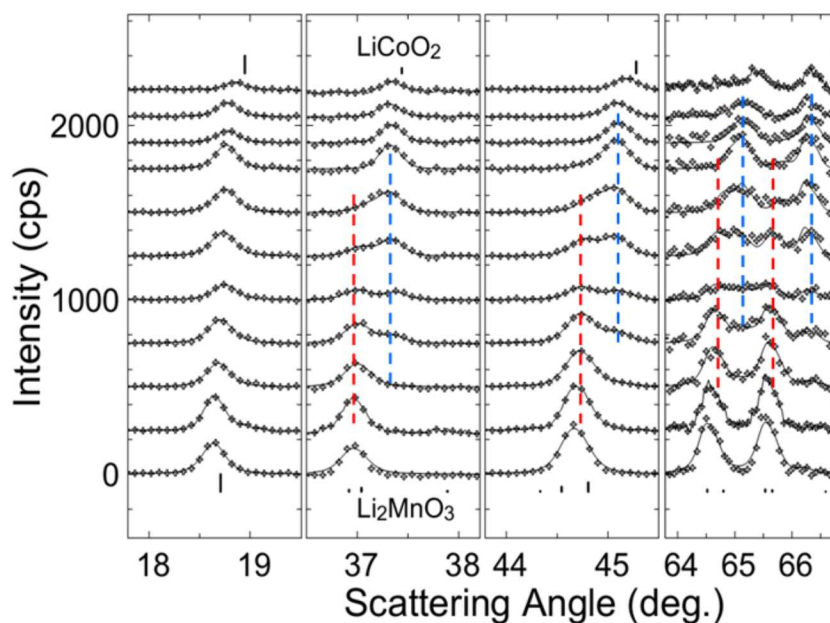


Figure 4.7: Stack of XRD patterns, along with two-phase fits, of samples made with 15 % excess lithium and heated to 900°C before cooling at a rate of 1°C/min. The red and blue dashed lines are guides to the eye in the samples showing two layered structures co-existing.

through the entire composition line as shown in Figure 4.7 clearly shows that the peak splitting is in fact due to co-existence between two layered phases. Figure 4.8 shows the fitted lattice parameters for samples prepared at 900°C. Once again the quenched samples show a single phase only and the lattice parameters progress with composition as expected from literature. The values obtained by slow cooling show that at both ends there are solid solution regions but near the middle there are two layered phases corresponding roughly to  $x = 0.2$  and  $0.8$ . This confirms that a tie-line exists near the center of the composition line for non-quenched samples. For samples that were slow cooled after heating to 800°C, the same signs of phase separation were seen: there was extreme peak broadening near the center of the composition line and two samples showed clear peak splitting.

The clear phase separation seen during slow cooling was not seen when regular cooling was used. Figure 4.9 shows the XRD patterns obtained by regular cooling from 900°C. Excess lithium was used during synthesis because, without excess lithium, two of the twelve samples showed the  $\text{Co}_3\text{O}_4$  peak at  $19.06^\circ$ . The scans show that the peaks broaden near the center of the composition range consistent with data from Kim et al. [19]. For example, the peak near  $45^\circ$  had a peak width (full width at half maximum) of about  $0.26^\circ$  for samples at either endpoint, but that peak broadened to about  $0.41^\circ$  at  $x = 0.4$ . To quantify this effect and correct for machine broadening, crystallite sizes were once again calculated. Figure 4.6 shows that near each endpoint, crystallite growth continued during regular cooling as one would expect for single-phase materials due to longer time spent at high temperature. In the center of the composition line the apparent crystallite size diminished. For the samples made at 900°C this dip corresponds to where phase separation was seen upon slow cooling ( $1^\circ\text{C}/\text{min}$ ) such that the peak broadening seen in the regular cooled samples can be attributed to the onset of phase separation. The same decrease in apparent crystallite size near the center of the line was seen at 800°C when regular cooled samples were compared to quenched ones, though the change is more subtle. Thus, it can be concluded that regular cooling from 800°C results in phase separation over the range  $x = 0.2$  to  $0.6$ , though this may take place over relatively short length scales such that partial XRD peak splitting results in an apparent peak broadening. This phase

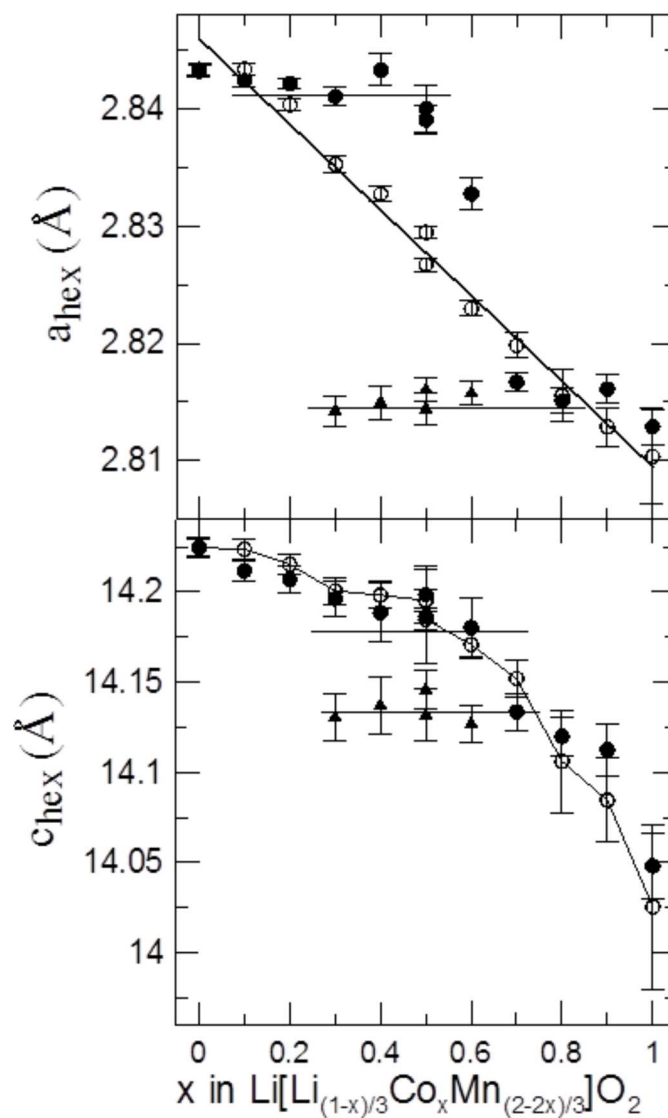


Figure 4.8: Hexagonal lattice parameters obtained by heating combinatorial samples to 900°C in air and then either quenching (open symbols) or slow cooling (closed symbols). All slow cooled samples were fit as two layered structures (near the end-points, however, one phase always had negligible intensity and so only a single lattice parameter is included for those compositions).

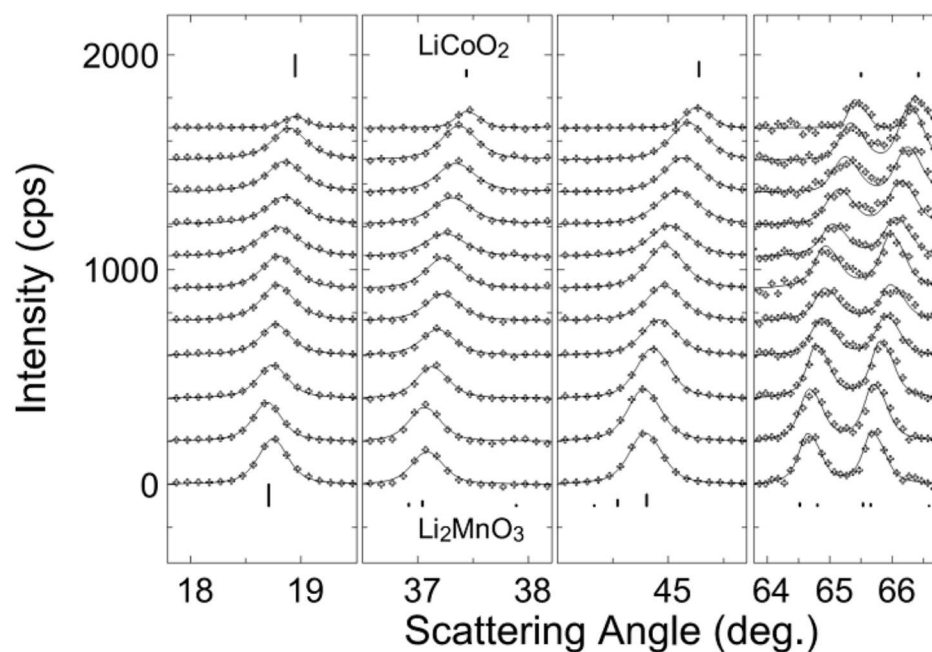


Figure 4.9: XRD patterns obtained by regular cooling from 900°C with 15 % excess lithium. All fits were made assuming a single layered phase.

separation along the layered line gives rise to the three-phase regions shown in Figure 4.1 (b).

As mentioned in the introduction, it is of high interest to have a better understanding of how and at which compositions layered-layered nano-composites might form in oxide systems. Here, layered-layered phase separation was found to occur on the line between  $\text{LiCoO}_2$  and  $\text{Li}_2\text{MnO}_3$  but the composites were not made up of pure  $\text{LiCoO}_2$  and  $\text{Li}_2\text{MnO}_3$  as suggested by others [24]. The two phases present contained roughly 20 % disorder wherein one endpoint ( $x = 0.2$ ) corresponded to 80 %  $\text{Mn}_2\text{Li}$  and 20 % Co on the transition metal (TM) layer, while the other endpoint ( $x = 0.8$ ) was made up of 80 % Co and 20 %  $\text{Mn}_2\text{Li}$ .

#### 4.4 Monte Carlo Simulation

Figure 4.10 shows results of the Monte Carlo simulation of the material at the center of the layered line. The starting structure shows random occupation of all sites on the hexagonal lattice and therefore represents the product of an instantaneous quench

from extremely high temperature. In the simulation, the temperature scale is set by the variable  $\beta_T$  defined in Section 2.12. The result for  $\beta_T = 1$  corresponds to an intermediate temperature. Figure 4.10 (b) shows signs of phase separation with each domain having some disorder with cobalt present in the  $\text{Mn}_2\text{Li}$ -rich domains and both lithium and manganese in the cobalt-rich domains. This picture illustrates well what was seen experimentally where the layered-layered composites were found to be made up of structures with  $x = 0.2$  and  $0.8$ . As such,  $\beta_T = 1$  in the simulation would appear to correspond to a temperature where phase separation took place, below  $800^\circ\text{C}$ . Though not shown, these disordered domains were also found for  $\beta_T = 1.5$  and  $2.0$  demonstrating that these domains minimize the free energy over a range of temperatures during cooling. Furthermore,  $\beta_T = 5$  corresponds to  $1/5$  of the temperature at  $\beta_T = 1$  and can therefore be considered to be below room temperature. Figure 4.10 (c) shows nearly complete phase separation takes place at this lower temperature and only trace amounts of cobalt can be seen in the  $\text{Mn}_2\text{Li}$  domains and these regions are bounded by pure cobalt domains. This picture is very similar to the model made by Bareño [24]. Since this equilibrium state was not seen experimentally here, it can be concluded that slow kinetics must take over at some point during cooling preventing the system from reaching the low energy state. In terms of the simulation, one would need to consider the activation energy involved in switching two neighbouring atoms in order to simulate the “freezing” of the structure during cooling.

In order to confirm that equilibrium was reached in Figure 4.10 (b), the simulation was repeated keeping  $\beta_T$  fixed at 1 for 100,000 Monte Carlo steps (i.e. 10 times as many as during the simulated slow cool). Figure 4.10 (d) shows the results of this simulated anneal and confirms that equilibrium was reached in (b) such that the disorder in the two domains cannot be eliminated at this temperature. The domains may also be slightly larger after the anneal: the small cobalt-rich domains in (b) appear to be replaced by a few larger ones in (d). However, the relatively small array makes it unwise to make such generalizations.

The results from the Monte Carlo simulation suggest that  $\beta_T = 1$  corresponds roughly to 900 K (i.e. near to but below  $800^\circ\text{C}$ ). This implies that the Li - Li nearest

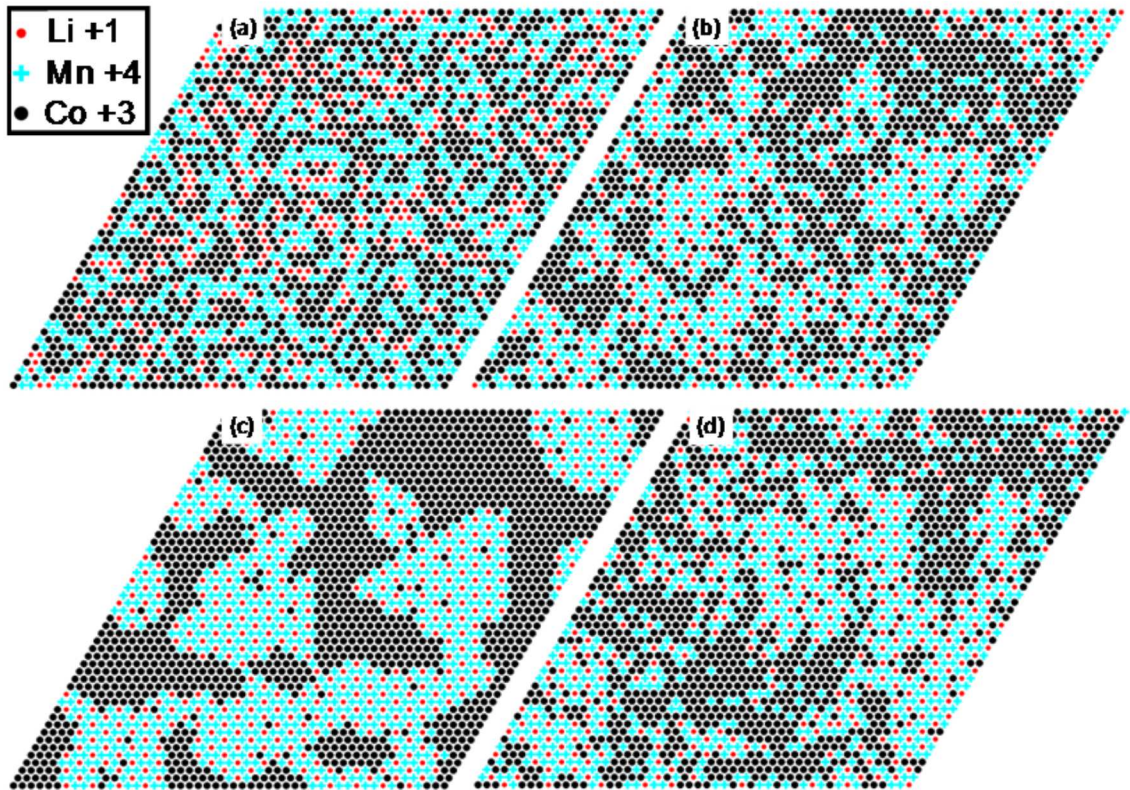


Figure 4.10: Results of the Monte Carlo simulation for the transition metal layer with  $x = 0.5$  in  $\text{Li}[\text{Li}_{(1-x)/3}\text{Co}_x\text{Mn}_{(2-2x)/3}]\text{O}_2$  such that 50 % of the atoms are cobalt, 33.3 % are manganese and 16.7 % are lithium. Results for the simulated slow cool (10000 Monte Carlo steps at each temperature) are: (a) Random occupation of sites (equivalent to  $\beta_T = 0$ , or infinite temperature), (b)  $\beta_T = 1$ , and (c)  $\beta_T = 5$ . (d) The result of the simulated anneal at  $\beta_T = 1$  (100000 Monte Carlo steps).

neighbour (NN) interaction is  $\beta_T k_B T = 78$  meV. Published ab initio calculations in  $\text{LiCoO}_2$  obtain values of 29 meV as the effective cluster interaction for NN Li-Li clusters, while 7 and 6 meV are obtained for next NN and next next NN, respectively [80]. The interaction energy obtained here is larger; this can be partially attributed to the fact that the only interaction used here is for nearest neighbours. Furthermore, this result implies that a relatively strong interaction was required in order to obtain the phase separation seen during cooling in the current study. One more consequence of this result is that  $\delta$ , the effective charge fraction of the metal atoms, has a value of 12 % of that expected from the oxidation number. This low value shows that the nearest neighbour interactions are much weaker than that expected from coulombic

interactions assuming all metal-oxygen bonds are purely ionic. It should also be stressed that strain within the lattice was neglected in the simulation (all nearest neighbours were exactly one lattice parameter away from each other). The unit cell volume of  $\text{LiCoO}_2$  and  $\text{Li}_2\text{MnO}_3$  differ by 3.4 % while those for  $x = 0.2$  and  $0.8$  differ by only 1.3 % (using lattice parameters from Ref. [19]). Phase separating over the entire composition line might require fracturing the crystallites, which may be the reason why the endpoints found experimentally were nearer to the center of the line.

#### 4.5 Conclusions Regarding the Formation of Layered-Layered Composites in the Li-Co-Mn-O System

The layered single-phase region in the Li-Co-Mn oxide pseudo-ternary system was explored by a solution-based combinatorial approach. The results showed that the layered region is a single composition line corresponding to cobalt being constrained to the 3+ oxidation state only. This composition line, joining  $\text{LiCoO}_2$  to  $\text{Li}_2\text{MnO}_3$ , was a solid solution over its entire length when samples were quenched from either 800 or 900°C. Upon slow cooling, the structures phase separated near the center of the line with the maximum phase separation occurring over the range  $x = 0.2$  to  $0.8$  in  $\text{Li}[\text{Li}_{(1-x)/3}\text{Co}_x\text{Mn}_{(2-2x)/3}]\text{O}_2$  when samples were cooled from 900°C at a rate of 1°C/min. These endpoints correspond to Co and  $\text{Mn}_2\text{Li}$  domains with approximately 20 % disorder on the transition metal layers. Such disorder was also found over a range of temperatures during cooling using a Monte Carlo simulation.

The phase separation upon slow cooling helps explain results from previous studies [19] performed with an intermediate cooling rate where peak broadening seen in the XRD patterns can now be attributed to phase separation on the 2 - 10 nm length scale with both domains lying on the same lattice as shown in Ref. [23]. The results here show that the nano-scale phase separation occurs when the system has insufficient time to make large scale crystallites of each phase, and the unit cells are close enough in size that the lattice does not fracture upon phase separation. It was also demonstrated that this partial phase separation can be detected by way of careful peak width analysis in the XRD patterns. As such, nano-domain composites can be



expected when samples are regular cooled at composition points on the phase diagram that are single-phase when quenched and show layered-layered phase separation when slow cooled. This conditon will be used in Chapter 9 to determine the location of nano-composites in the Li-Ni-Mn oxide system where there continues to be considerable debate regarding the structures of the Li-rich layered materials [3,44–47].

## Chapter 5

# Combinatorial Studies of the Spinel and Rocksalt Regions in the Li-Mn-Ni-O System

Data in this chapter are reprinted from Ref. [81] with permission from Elsevier.

### 5.1 Experimental Design

In order to map out the entire Li-Mn-Ni-O system, combinatorial samples were made at over 300 different compositions using the method described in Section 2.1.1. Figure 5.1 shows these compositions. Due to the large amount of data used in producing the phase diagrams, the supporting evidence is split between two chapters. Figure 5.2 shows the phase diagrams obtained in oxygen. In this chapter, evidence for the spinel and rocksalt phases will be presented. The two-phase regions between  $\text{Mn}_2\text{O}_3$  and the spinel structures as well as between the spinel and rocksalt materials will also be examined here.

In the lithium loss study described in Chapter 3, two different precipitators were used to cause co-precipitation of the Li, Mn and Ni mixed nitrate solutions: ammonium bicarbonate and ammonium hydroxide. Although ammonium bicarbonate precipitates all three metals and the hydroxide only precipitates the Mn and Ni atoms, no significant differences were obtained by using either precipitator in the lithium loss study, nor in this study. As such, no distinctions will be made in this chapter between the two precipitators, as in all cases the phases obtained were identical suggesting that ionic transport at high temperature overcomes any lithium inhomogeneity in the starting material.

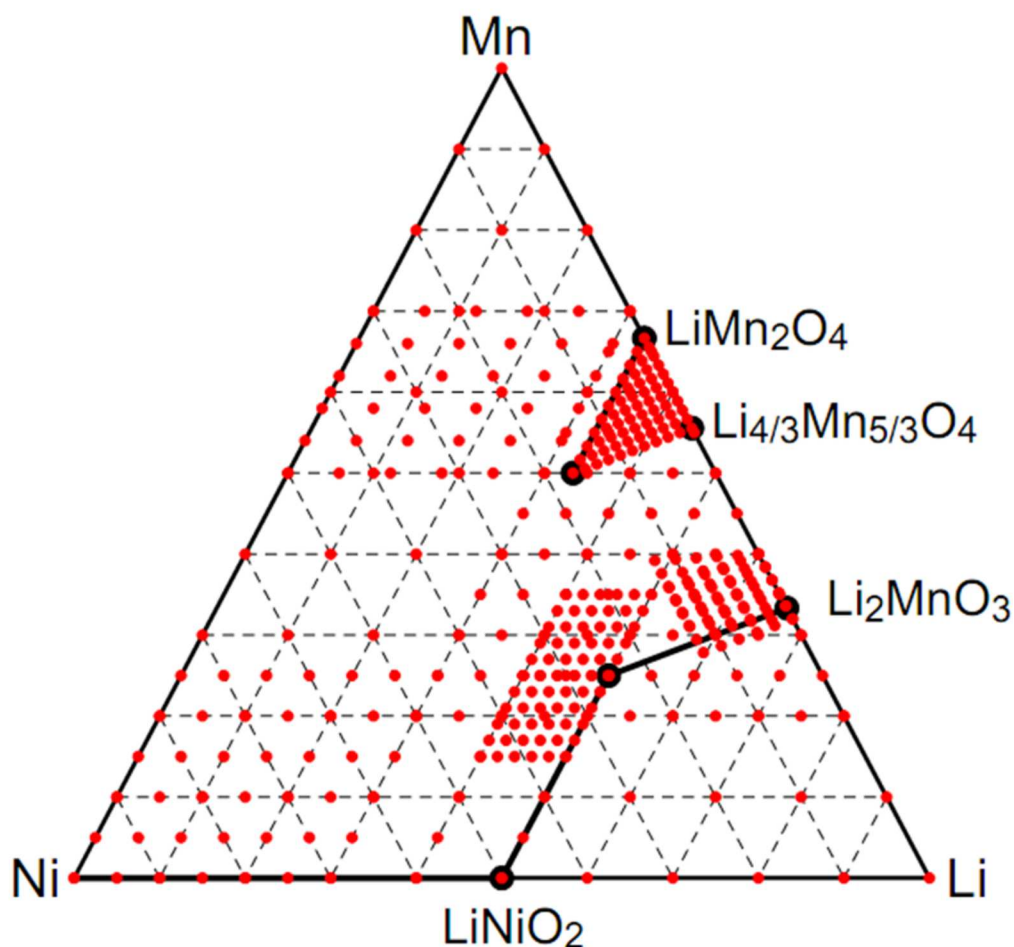


Figure 5.1: The phase diagram with red points indicating all compositions synthesized during the combinatorial studies for regular cooled samples heated in oxygen. Quenched samples were also made at these compositions, with minor variations. The axes are Li, Mn, and Ni metal molar fractions.

800°C in air with regular cooling.

Figure 5.4 shows labels used throughout the results section.  $A_5$ - $F_5$  are specific compositions, while  $\alpha$ ,  $\beta$ , and  $\gamma$  are angles formed by points in the co-existence regions. Figures 5.5 and 5.6 (left) show XRD patterns of samples in the spinel region that are evenly spaced between points  $E_5$  and  $F_5$  in Figure 5.4. The shifting of the (400) spinel Bragg peak near 44° indicates a solid solution. The (220) peak, near 30° in Figure 5.5, increases in intensity as the composition approaches the Ni-Mn line moving from  $E_5$  to  $F_5$  in Figure 5.4. Due to the importance of the spinel samples as

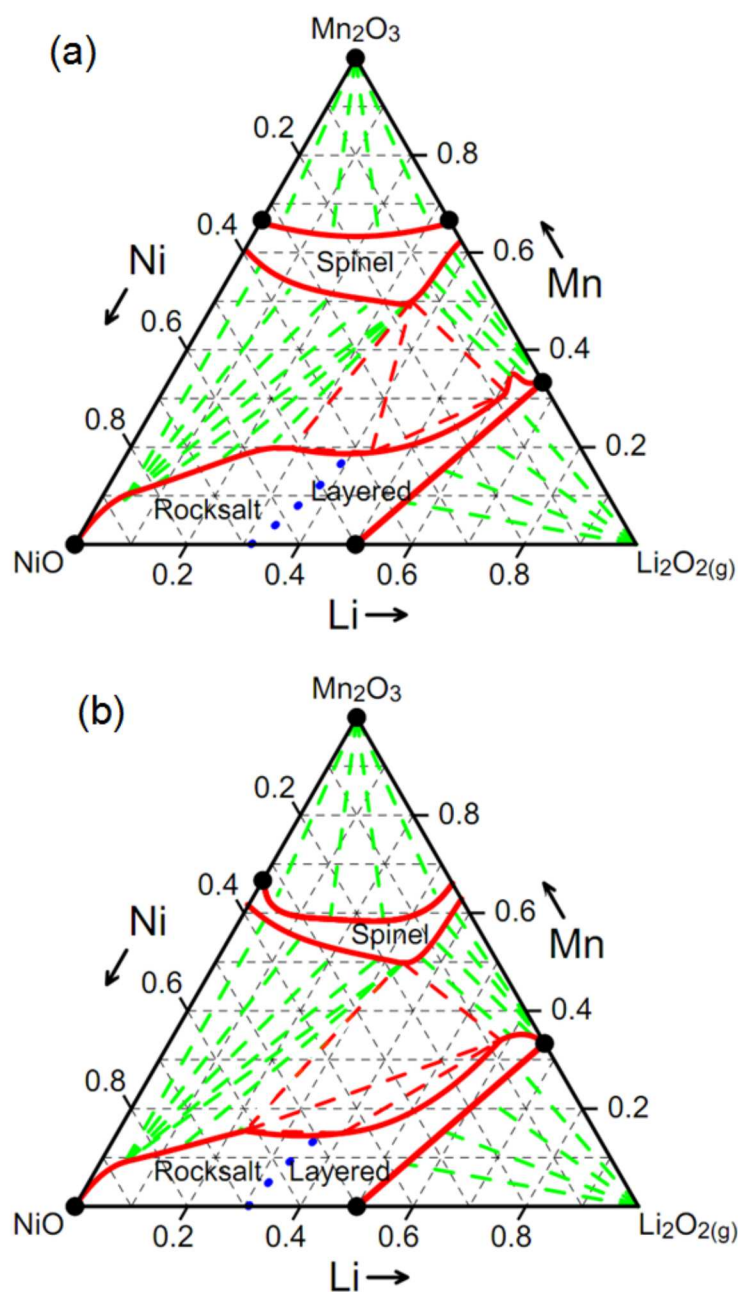


Figure 5.2: (a) The complete phase diagram obtained by quenching from 800°C after heating in oxygen for 3 h. The red lines are boundaries to the single-phase regions, green dashed lines are tie-lines while red dashed lines are tie-lines at the outer edges of the three-phase regions. The blue dotted line represents a phase transition from the cubic rocksalt to the layered rocksalt structures. (b) The phase diagram for samples heated in flowing oxygen obtained by regular cooling from 800°C.

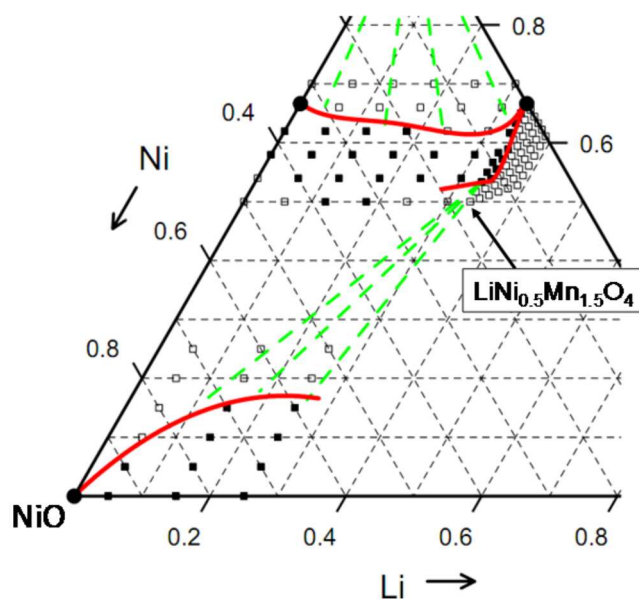


Figure 5.3: A partial phase diagram obtained in air with regular cooling. Regions showing severe lithium loss were avoided. Filled points represent single-phase samples while empty ones showed co-existence of multiple phases.

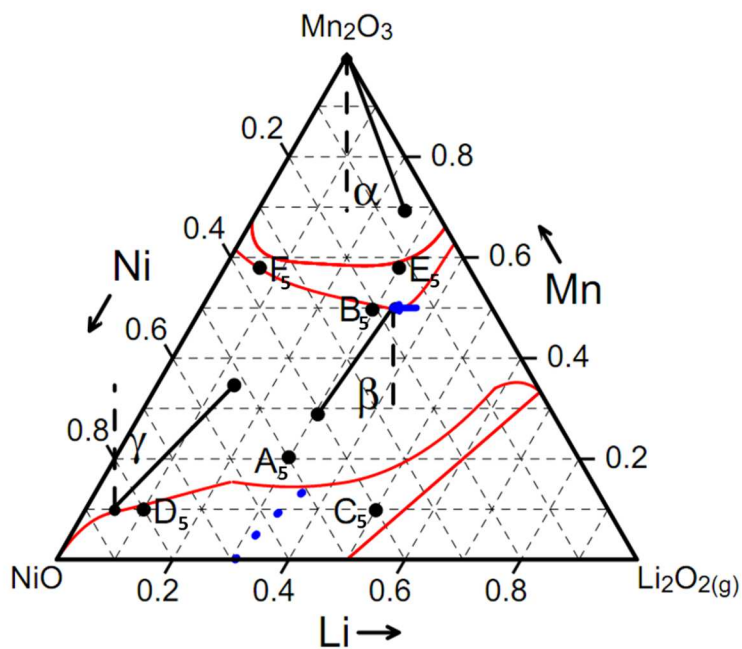


Figure 5.4: The Gibbs triangle with labels used throughout this chapter.

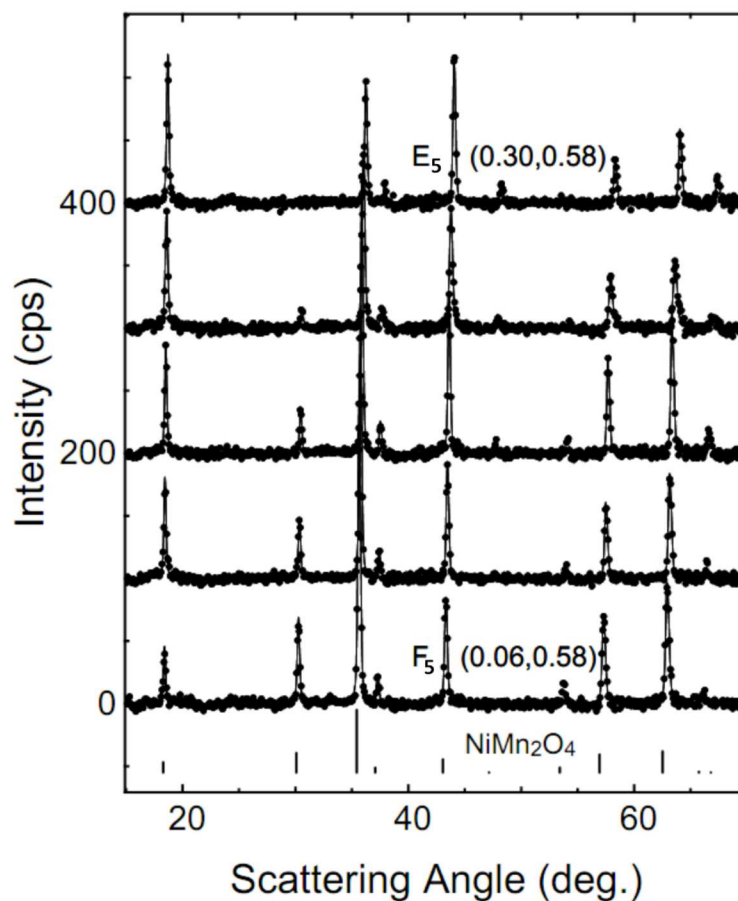


Figure 5.5: XRD patterns of a few single-phase spinel structures. Samples  $E_5$  and  $F_5$  are labeled in Figure 5.4. The database peaks shown are for spinel  $NiMn_2O_4$ , from JCPDS #84-0542. For clarity, only every third data point is shown.

potential electrode materials, a large number of samples were made in the triangle joining  $LiMn_2O_4$ ,  $LiNi_{0.5}Mn_{1.5}O_4$  and  $Li_{4/3}Mn_{5/3}O_4$ . The samples made in this region of the phase diagram can be seen as a triangle of densely packed points in Figure 5.1 (a). The XRD scans from these samples made it possible to visually determine where the spinel single phase region ends. Figure 5.6 (right) shows a stack of XRD patterns of samples along the blue arrow in Figure 5.4. These samples lie on either side of the boundary of the spinel region and the disappearance of the layered (104) peak is used to identify the position of the boundary. Although determining the exact point where the layered peak disappears is difficult, this example illustrates that the error in this method is no more than 0.01 in lithium content (i.e. an error of no more than

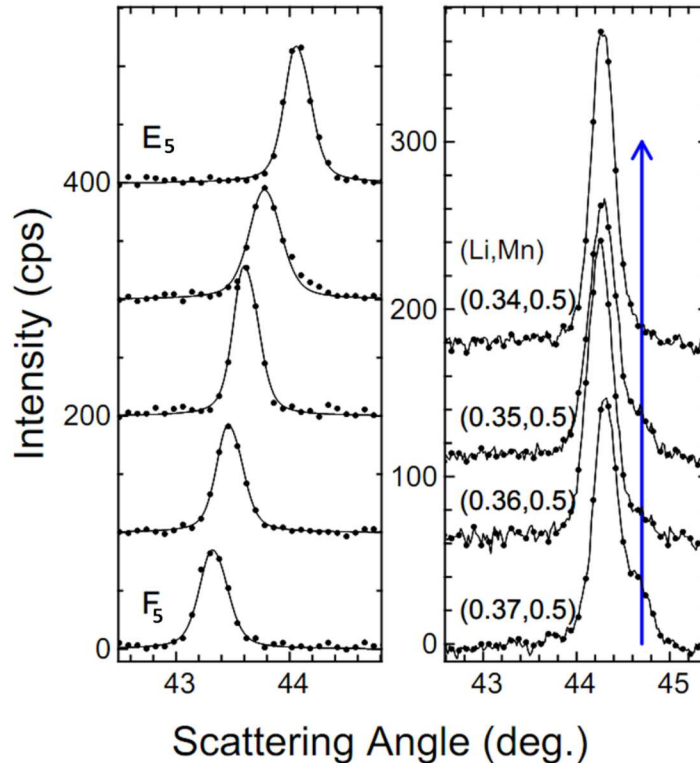


Figure 5.6: Left: XRD patterns obtained for single-phase spinel structures. Points  $E_5$  and  $F_5$  are labeled in Figure 5.4. Right: XRD patterns near the boundary of the spinel region; the blue arrow matches that shown in Figure 5.4 and indicates the position of the layered (104) peak here. The other peak is the spinel (400).

one scan in the stack).

Figure 5.7 shows contour plots obtained for the spinel lattice parameter throughout the single-phase region. The lattice constants were obtained by whole pattern fitting with the in-house software mentioned in Section 2.3. Here, this meant at least eight peaks were used to refine the lattice parameters. The contours extend beyond the single-phase boundary for clarity in labeling but have no meaning outside the boundaries. Samples synthesized by regular cooling, be it in oxygen or air, show lattice parameters as expected from Zhong et. al. for the stoichiometric spinel line  $\text{LiNi}_x\text{Mn}_{2-x}\text{O}_4$ ;  $x \leq 0.5$  [35]. The consistency between the lattice parameters obtained in air and oxygen when regular cooled extends to the rest of the solid solution region. However, in oxygen, the lower boundary has moved down. This implies that

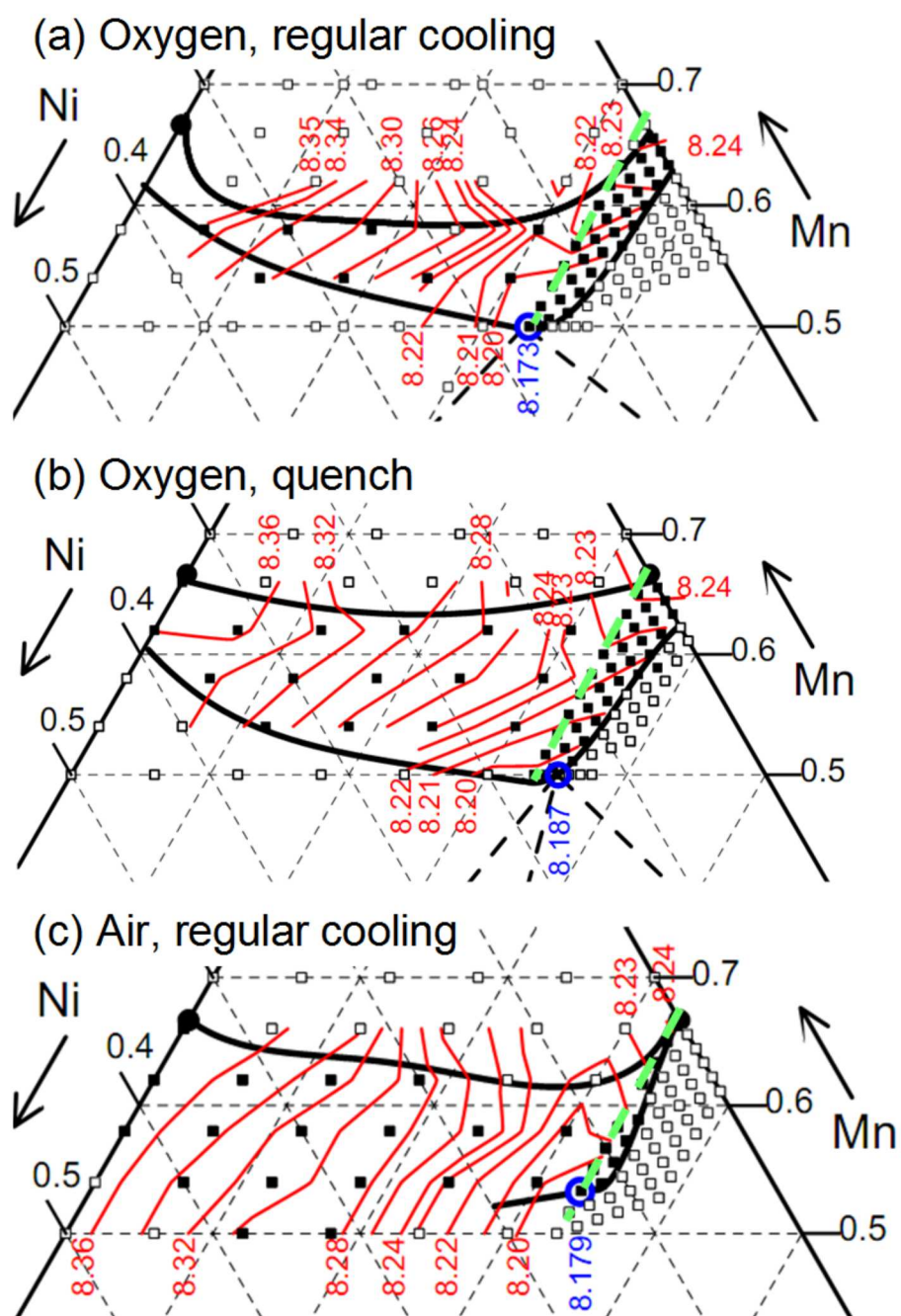


Figure 5.7: Contour plots of the lattice parameter in the cubic spinel region. Filled points indicate single-phase samples while open symbols are used to denote coexistence of multiple phases. The green dashed line represents the stoichiometric spinel composition line:  $\text{LiNi}_x\text{Mn}_{2-x}\text{O}_4$ ;  $x \leq 0.5$ .



the spinel region is favoured over the layered materials as oxygen partial pressure increases. This can be attributed to the higher oxygen content in the spinel structures as discussed in the introduction (Section 1.4.1). The cooling rate seems to have no effect on the position of this lower boundary in oxygen even though the minimum lattice parameter near  $\text{LiNi}_{0.5}\text{Mn}_{1.5}\text{O}_4$  increases from 8.173 (regular cooling) to 8.187 Å (quenching). Since this increase is not associated with any phase separation, it can be attributed to oxygen deficiencies arising during heating at 800°C and then being relieved by oxygen returning into the sample during regular cooling, as observed by Ma [38].

Figure 5.7 also shows that excess lithium can be added to the stoichiometric spinel samples. The stoichiometric  $\text{LiNi}_x\text{Mn}_{2-x}\text{O}_4$  line was included in Figure 5.7 as a green dashed line. The lower boundary of the single-phase spinel region lies to the right and below the green dashed line, corresponding to an excess of lithium. This effect was more significant in oxygen but even in air at 800°C a small amount of excess lithium can be added to the spinel structures containing nickel. Therefore, some spinel-layered tie-lines terminate at points slightly below the  $\text{LiNi}_x\text{Mn}_{2-x}\text{O}_4$  line.

The contour plots also show that the upper spinel phase boundary moves up significantly at high temperature. This can be interpreted as oxygen loss since co-existence with  $\text{Mn}_2\text{O}_3$  requires a higher oxygen content per metal atom (3:2) than that of a single-phase spinel sample (4:3). The fact that the upper boundary is also higher for samples made in air is consistent with this interpretation: the lower oxygen content favours spinel structures over manganese oxide. The motion of the boundaries can therefore be explained using Le Chatelier's principle and the fact that at high temperature oxygen gas is produced giving rise to high entropy.

### 5.3 Rocksalt Single-Phase Region

Figure 5.8 shows XRD patterns obtained along the  $C_5 - D_5$  line in Figure 5.4. The right panel showing the region near 44° suggests a solid-solution. For the samples with 0.4 or 0.5 lithium fraction, all peaks index to the layered structure of  $\text{LiNiO}_2$  (JCPDS #89-3601). For lower lithium content, the structures become cubic and will be discussed in more detail below.

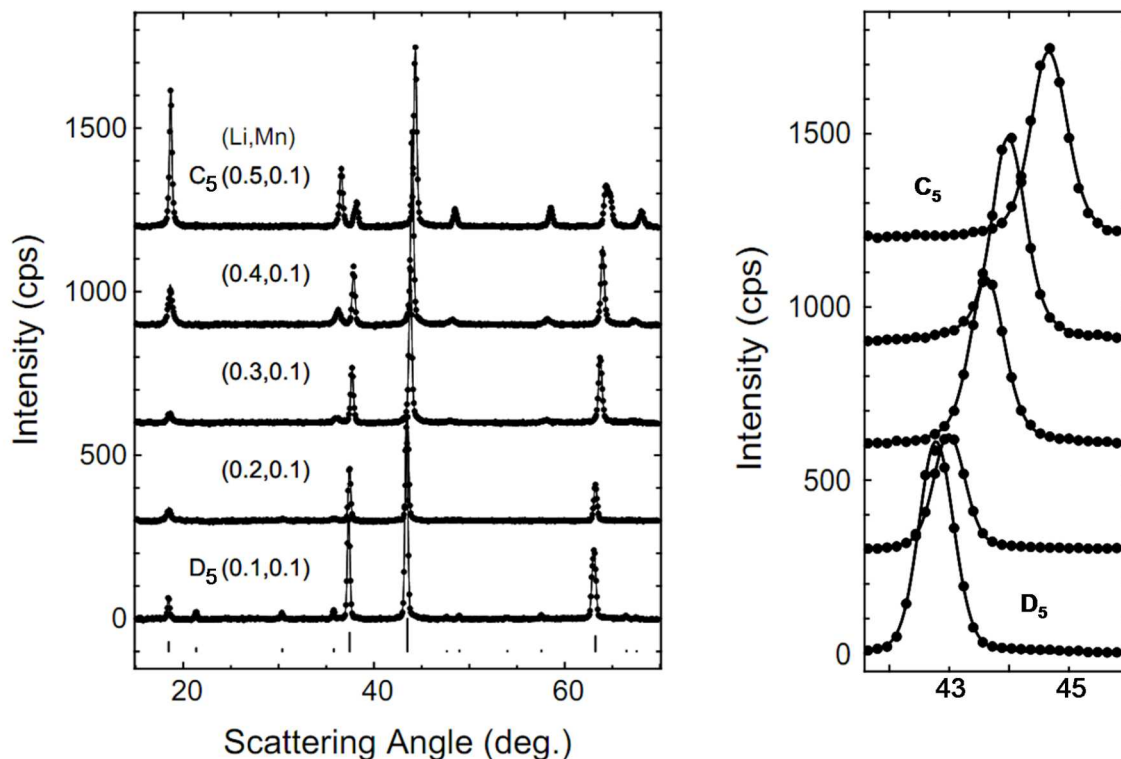


Figure 5.8: Left: stack of XRD patterns for single-phase structures obtained by regular cooling in oxygen. Right: the same scans in the region near  $44^\circ$ . The vertical lines in the left panel are for  $\text{Ni}_6\text{MnO}_8$  from JCPDS reference #89-4619.  $\text{C}_5$  and  $\text{D}_5$  refer to compositions defined in Figure 5.4.

The location of the phase transition from the cubic to hexagonal layered structures was obtained by fitting all samples as layered and then using the  $c/a$  ratio as discussed in Section 1.4. Figure 5.9 shows the  $c/a$  ratio as a function of lithium content along three lines with various manganese contents. In a cubic structure,  $c/a = \sqrt{24}$  such that extrapolating to this value gives the composition where the structures convert from a cubic to a hexagonal structure. Li et al. found that this transition occurs at a lithium content of 0.31 along the Li-Ni line [37]. The blue dotted lines in Figures 5.2, 5.4 and 5.10 show the position of the phase transition obtained by using the four points generated by this method.

The three largest peaks seen in the XRD scan of sample  $\text{D}_5$  in Figure 5.8 can be indexed to  $\text{Li}_x\text{Ni}_{1-x}\text{O}$ ;  $x < 0.31$ , a cubic rocksalt material. However, there are extra peaks present which match up well with the XRD scattering for  $\text{Ni}_6\text{MnO}_8$ . Therefore,

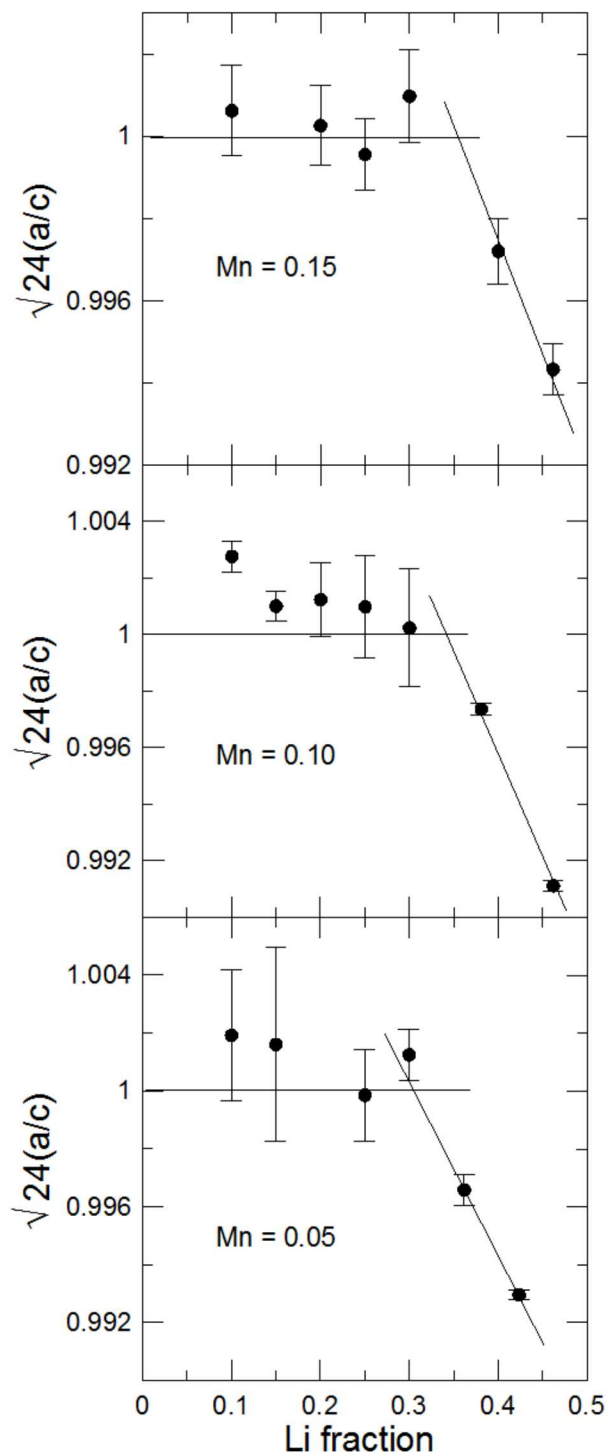


Figure 5.9: The  $c/a$  lattice parameter ratio as a function of Li fraction for three different manganese fractions obtained by regular cooling in oxygen and fitting the XRD patterns as hexagonal structures.

sample  $D_5$  shows extra ordering peaks as compared to those expected for rocksalt.  $Ni_6MnO_8$  and  $Mg_6MnO_8$  are isostructural. Kasper and Prener [82] determined that  $Mg_6MnO_8$  takes the  $Fm\bar{3}m$  space group with the following sites:

- 4a sites occupied by Mn at (0, 0, 0)
- 4b sites at (0.5, 0.5, 0.5) are vacant
- 8c oxygen sites at (0.25, 0.25, 0.25)
- 24d sites occupied by Ni at (0, 0.25, 0.25)
- 24e oxygen sites at (x, 0, 0)

To better understand the structure of samples such as  $D_5$  in Figure 5.8, a regular cooled combinatorial sample synthesized under oxygen at  $(Li, Mn) = (0.25, 0.15)$  was scanned using the JD-2000 diffractometer and the pattern was fit using Rietveld refinement. The refinement allowed for manganese and nickel on the 4a sites, all three metals on the 24d sites, and both lithium and nickel on the 4b sites. A key variable tested was the occupation of the 4b sites which are vacant in  $Ni_6MnO_8$ . Table 5.1 shows the results for the quality parameters obtained as the 4b occupation changes. Decreasing the occupation below 60 % gave increasingly poorer fits. The best result was obtained with 30 % of the 4b sites vacant. However, it is important to notice that the weak scattering from lithium atoms makes it difficult to distinguish them from vacancies and so the minimum seen in the quality parameters is shallow. Nonetheless, it is clear that the 4b sites are partially vacant. At this composition, if nickel is in the 2+ state and manganese in the 4+ state, we would expect approximately 19.5 % vacancies on the 4b sites such that the composition would be  $Li_{0.244}Mn_{0.146}Ni_{0.585}O$ . This is a likely structure, but more study is required to clearly distinguish the lithium atoms from vacancies.

Table 5.2 shows the refinement results obtained when 30 % of the 4b sites are left vacant. The 4a sites being completely occupied by manganese means that Mn orders on a  $2 \times 2 \times 2$  rocksalt cubic lattice making up one eighth of the metal atoms. The 4b sites form another  $2 \times 2 \times 2$  lattice and here lithium orders, with no nickel. This structure will be referred to as ordered rocksalt throughout this thesis. The lattice

Table 5.1: Results for the Rietveld refinement of the sample synthesized at the metal composition:  $\text{Li}_{0.25}\text{Mn}_{0.15}\text{Ni}_{0.6}$  in oxygen with regular cooling.

4b site occupation	$R_B$ (%)	$R_P$ (%)	$R_{WP}$ (%)
100 %	2.76	14.01	19.17
90 %	2.13	13.92	19.09
80 %	1.39	13.84	19.06
70 %	1.18	13.83	19.06
60 %	1.43	13.89	19.07

Table 5.2: Output from the Rietveld refinement of the sample synthesized at the metal composition:  $\text{Li}_{0.25}\text{Mn}_{0.15}\text{Ni}_{0.6}$  in oxygen with regular cooling.

Lattice parameter	
$a = 8.304(1) \text{ \AA}$	
Site occupancies	
4a:	4.0 Mn
4b :	2.8 Li
	1.2 $\square$
8c:	8 O
24d:	4.9 Li
	0.62 Mn
	18.48 Ni
24e:	24 O
	(0.2344,0,0)
$R_B = 1.18 \%$	

parameter value of  $8.304 \text{ \AA}$  for the  $2 \times 2 \times 2$  lattice is in excellent agreement with the value of  $4.15 \text{ \AA}$  obtained by Cabana et al. [39] for the rocksalt lattice confirming that the material found here is the contaminant phase often found when making the spinel and layered-spinel materials discussed in Section 1.4.

Figure 5.10 shows the contour plots obtained for the cubic lattice parameter in the rocksalt region of the triangle. As a confirmation that these contours are accurate, the value of  $8.33 \text{ \AA}$  obtained for the contour line through  $\text{Li}_{0.1}\text{Ni}_{0.9}$  in air can be compared to the value of  $8.3278 \text{ \AA}$  obtained for  $\text{Li}_{0.104}\text{Ni}_{0.896}\text{O}$  from JCPDS #89-3605 (the lattice parameter was doubled to compare it with the unit cell of the ordered rocksalt).

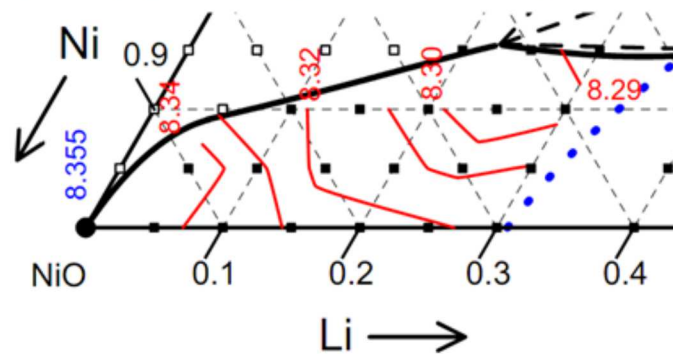
Along the boundary of the single-phase region, the lattice parameter decreased as the lithium content increased as expected. However, the behaviour along constant lithium lines was more complex. For example, along the line with 0.2 lithium content in the samples synthesized by quenching, the lattice parameter first increased as more manganese was added and then after the kink near  $\text{Mn} = 0.1$  the lattice parameter decreased. Figure 5.11 shows the ordering peaks obtained for samples in this region. In the quenched sample at (0.2, 0.1) there was the first sign of the ordering peaks and so the onset of ordering might be associated with the decrease in lattice parameter. The kink in the contour plot may therefore indicate the location of the order-disorder transition between the rocksalt and ordered rocksalt structures. By contrast, in the regular cooled samples, the ordering peaks were sharp at (0.2, 0.1) and there was even a trace of the peak at  $18.5^\circ$  in the sample at (0.2, 0.05). Here, the contour plot in Figure 5.10 (a) shows that the lattice parameter decreases steadily as manganese was added, again suggesting a correlation between ordered rocksalt formation and the decrease in lattice parameter. This decrease may therefore be attributed to the ordering of manganese on the cubic lattice resulting in a more efficient packing and thus a decrease in lattice parameter. No transition between the rocksalt and ordered rocksalt was shown on the phase diagrams here, but these preliminary results suggest that there exists an order-disorder transition and that it is sensitive to synthesis conditions. Finding the maximum in lattice parameter as a function of manganese content with a greater number of samples in this region might be one way to determine the position of this phase transition.

Under the conditions used here,  $\text{Ni}_6\text{MnO}_8$  was present in XRD scans along the Ni-Mn line near the Ni corner showing that it was stable at  $800^\circ\text{C}$  in oxygen. Along the rest of this line, a combination of spinel structures and  $\text{NiMnO}_3$  were found. However, no lithium containing samples were found to co-exist with these structures so they are of little interest in the context of Li-ion battery research.

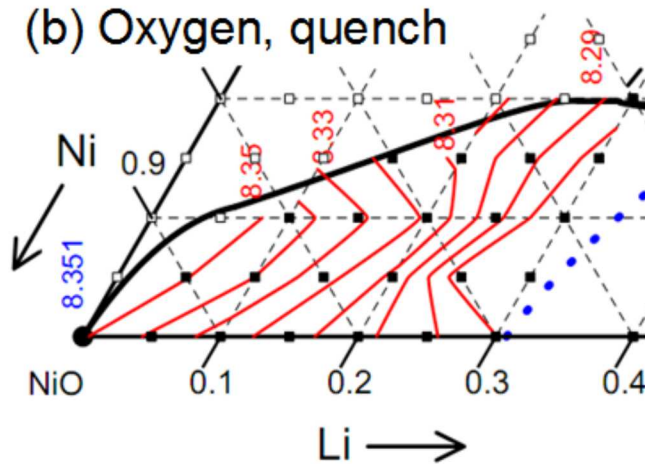
#### 5.4 $\text{Mn}_2\text{O}_3$ - Spinel Co-Existence Region

In the manganese oxide - spinel co-existence region at the top of the triangle, XRD scans from 22 samples were fit. The fits were made using the in-house software.

(a) Oxygen, regular cooling



(b) Oxygen, quench



(c) Air, regular cooling

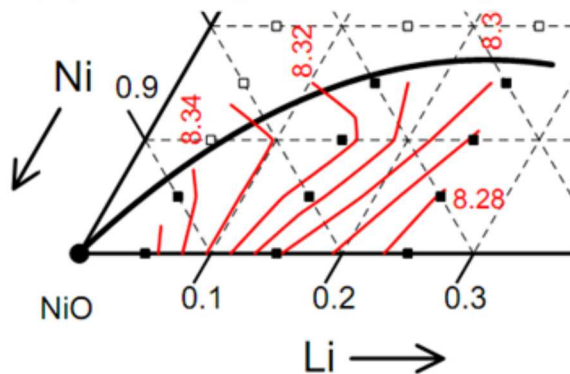


Figure 5.10: Contour plots of the cubic lattice parameter in the rocksalt region. Open symbols show phase separation while the closed symbols represent single-phase samples.

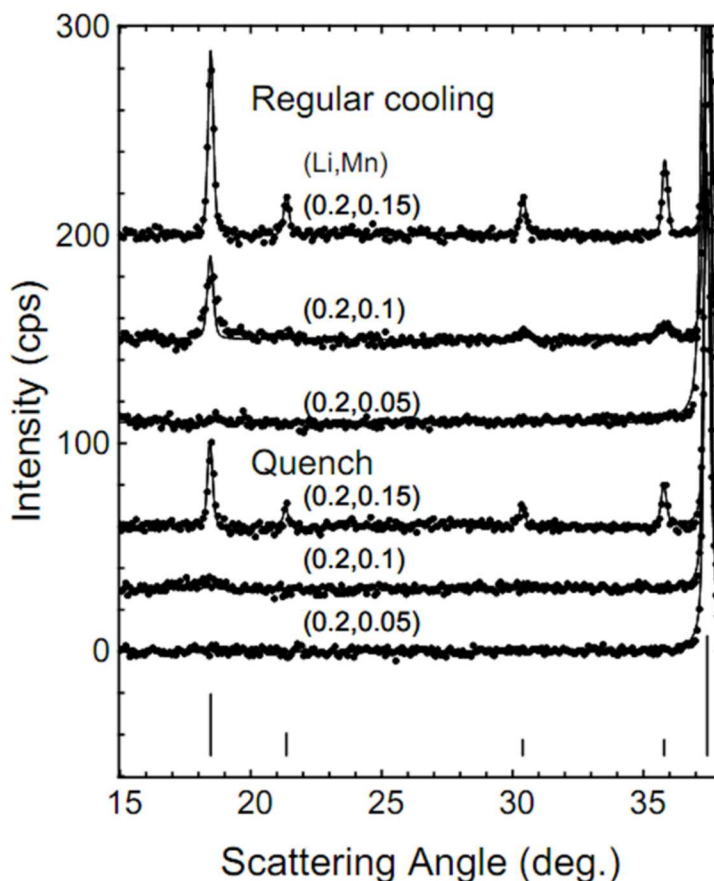


Figure 5.11: Ordered rocksalt phases obtained in oxygen along the line  $\text{Li} = 0.2$ . Ordering is more pronounced in the slower cooled samples. The expected peaks for  $\text{Ni}_6\text{MnO}_8$  (JCPDS #89-4619) are shown as vertical lines. The coordinates are (Li, Mn).

The two-phase fitting was performed by keeping the peak width parameters constant at the values obtained for single-phase samples; thereby ensuring that the fitting algorithm did not broaden peaks instead of fitting them with overlapping peaks from two or more different phases. The resulting  $\text{Mn}_2\text{O}_3$  cubic lattice parameters had an average value of  $9.406 \pm 0.002 \text{ \AA}$  and the standard deviation was  $0.011 \text{ \AA}$ . The lattice parameter obtained for the sample synthesized at the Mn corner was  $9.409 \pm 0.001 \text{ \AA}$  in excellent agreement with the value of  $9.4091 \text{ \AA}$  given in the JCPDS entry #41-1442 for  $\text{Mn}_2\text{O}_3$ . This result shows that the lattice parameters obtained in the co-existence regions were precise, though the noise on any given measurement was significant and



statistics over multiple samples were required. The standard deviation is 0.12 % of the lattice parameter and this value will be used in this chapter and the next as the benchmark to identify a phase from which tie-lines fan out.

In this co-existence region, the tie-lines were easy to determine since they must fan out from the manganese oxide corner. However, it was important to establish that the lattice parameters obtained in co-existence regions were sufficient to determine directions of tie-lines. Figure 5.12 defines the angle  $\alpha$  formed by a point in the co-existence region. For any given point, the spinel lattice parameter obtained in the two-phase fit can be used to find a corresponding point on the upper boundary of the spinel line with the same lattice parameter (i.e. this sample corresponds to the end of the tie-line). This point can then be used to define a theoretical tie-line forming angle  $\alpha_c$ . Figure 5.12 (left) demonstrates this using the point (0.30, 0.66) which had two-phases present in the XRD and the spinel lattice parameter was  $8.225 \pm 0.003 \text{ \AA}$ . The contour plots from Figure 5.7 were used in Figure 5.12 to illustrate the calculation of  $\alpha_c$  (in practice, the contour plots were not used, instead the values were obtained by extrapolating between the known data points). Ideally,  $\alpha = \alpha_c$  for all points in the co-existence region. Figure 5.12 (right) shows the plot of  $\alpha_c$  vs  $\alpha$  obtained for samples heated in oxygen with regular cooling. Since calculating  $\alpha_c$  involved extrapolating the spinel lattice parameters along the boundary of the single-phase region the results were not perfect and the linear fit crosses slightly below the origin. Nonetheless, when a linear fit is forced through the origin, the result is  $\alpha_c = 1.0006\alpha$  with an R-value of 0.9952 ( $R = 1$  for a perfect linear fit). This result shows that with a sufficient number of samples in a co-existence region, the lattice parameters can be used to determine the tie-lines.

The position and shape of the upper boundary of the spinel region was determined using the lever rule. This method was discussed in Section 2.4, where a sample X made up of phases A and B was used to calculate the composition of phase B if the composition of phase A was known. In this chapter, point A was always at a composition from which tie-lines fanned out, e.g.  $\text{Mn}_2\text{O}_3$  here, and the generated points, B, lie on the boundary of a single-phase region, e.g. upper spinel boundary here. Best results were obtained by using points in the co-existence regions that

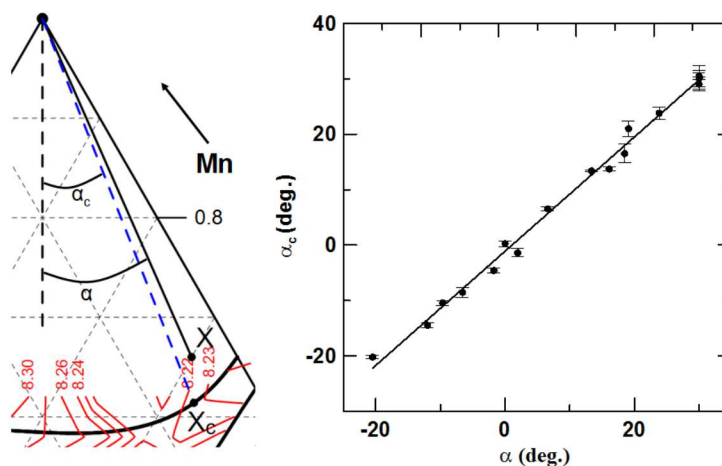


Figure 5.12: Left: A comparison of the angles  $\alpha$  and  $\alpha_c$  obtained for a point X, (0.30, 0.66). The spinel lattice parameter at point X was  $8.225 \pm 0.003 \text{ \AA}$  such that extrapolation between lattice parameters along the boundary defines point  $X_c$ . Right:  $\alpha_c$  as a function of  $\alpha$  for samples throughout the co-existence region. The line,  $\alpha_c = 1.03\alpha - 1.2$ , is a linear fit to the data.

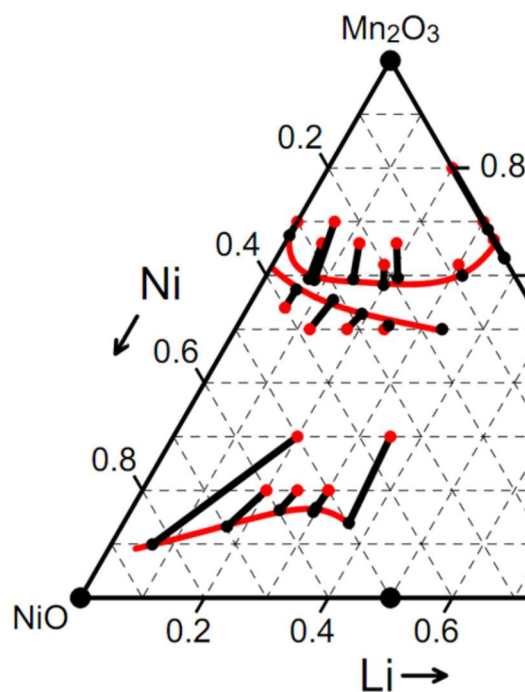


Figure 5.13: The result of using the lever rule in the co-existence regions for samples prepared in oxygen by regular cooling. Red points represent the compositions of the samples in the two-phase region while the black points are the results of the lever rule calculations.

were relatively close to the boundary being identified thereby limiting the uncertainty resulting from the calculation. No corrections were made for micro-absorption effects. Brindley suggested that this is justified for samples if  $\mu D < 0.01$  for each phase present, where  $\mu$  is the linear absorption coefficient and  $D$  is the diameter of the corresponding particles [83]. Only a few samples were examined by SEM (shown in Chapter 6) but typical particle sizes were found to be in the 50-150 nm range. For  $\text{LiNi}_{0.5}\text{Mn}_{1.5}\text{O}_4$ , the absorption coefficient is about  $570 \text{ cm}^{-1}$  such that  $\mu D = 0.0086$  for 150 nm particles which explains why using the lever rule without the Brindley correction worked well.

Figure 5.13 (left) shows the boundaries obtained by the lever rule for samples heated in oxygen with regular cooling. The boundaries were in excellent agreement with the visual identification of phases shown in Figure 5.7 (a). The same method was used to generate the boundaries for the quenched samples as well as those heated in air and again the agreement with visually determined phases was good. The upper boundary of the spinel phase is shown in Figures 5.2, 5.3 and 5.7.

## 5.5 Spinel - Ordered Rocksalt Co-Existence Region

Figure 5.14 shows XRD scans in the co-existence region between the spinel and ordered rocksalt regions. The spinel peaks clearly diminished and were replaced by the ordered rocksalt peaks consistent with a two-phase regime. The fits shown in Figure 5.14 show good agreement with the data and no peaks are unaccounted for.

Figure 5.15 shows the spinel lattice parameter obtained in the co-existence region by regular cooling in oxygen as a function of the angle  $\beta$  defined in Figure 5.4. Up to  $\beta = 55^\circ$ , the spinel lattice parameter remains constant and the 13 scans in this region have an average lattice parameter of  $8.1722 \pm 0.0005 \text{ \AA}$  with a standard deviation of  $0.0019 \text{ \AA}$  which corresponds to 0.02 % of the lattice parameter. The average lattice parameter is therefore consistent with tie-lines fanning out from a single point. Furthermore, the value of the average lattice parameter is very close to  $8.173 \pm 0.001 \text{ \AA}$ , the lattice parameter obtained for  $\text{LiNi}_{0.5}\text{Mn}_{1.5}\text{O}_4$ , as shown in the contour plot of figure 5.7 (a). The tie-lines were therefore drawn fanning out from this point up to a maximum angle of  $\beta = 55^\circ$ .

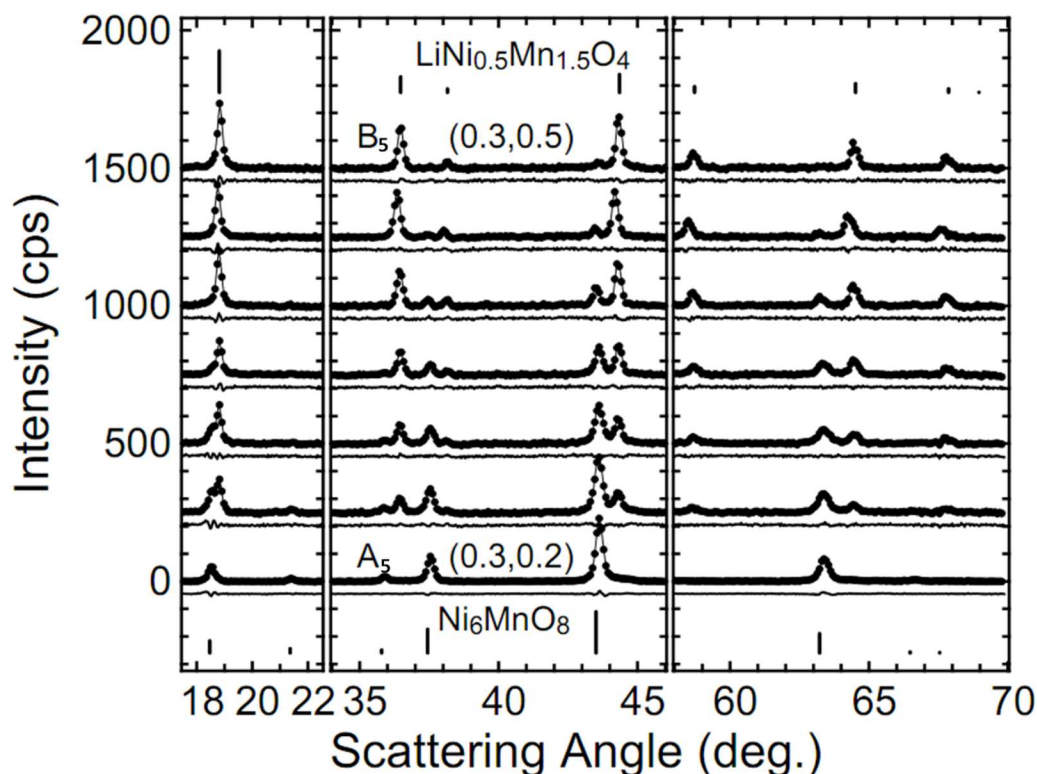


Figure 5.14: XRD scans of samples in the co-existence region between the ordered rocksalt structures and the spinel structures along with the corresponding two-phase fits and the difference plots below each scan. The expected peaks for  $\text{LiNi}_{0.5}\text{Mn}_{1.5}\text{O}_4$  are from JCPDS #80-2162. Samples  $A_5$  and  $B_5$  are labeled in Figure 5.4 and the other samples are evenly spaced between  $A_5$  and  $B_5$ .

By contrast, in air  $\text{LiNi}_{0.5}\text{Mn}_{1.5}\text{O}_4$  is not single-phase but shows a small amount of a second phase as discussed in Section 1.4.1. The tie-line drawn at the composition of  $\text{LiNi}_{0.5}\text{Mn}_{1.5}\text{O}_4$  in Figure 5.3 shows that the spinel structure is co-existing with an ordered rocksalt structure quite close in composition to the one analyzed by Rietveld refinement in Section 5.3. This phase has previously been referred to as  $\text{Li}_x\text{Ni}_{1-x}\text{O}$  rocksalt [35]. Recognizing that the end of the tie-line is higher up in the triangle than previously suspected has consequences when one attempts to work out the stoichiometry of the spinel sample based on the amount of oxygen lost during synthesis.

The lever rule, described in Section 2.4, was used with  $\text{LiNi}_{0.5}\text{Mn}_{1.5}\text{O}_4$  as the pivot point (point A in Figure 5.13, right) in order to identify the upper boundary

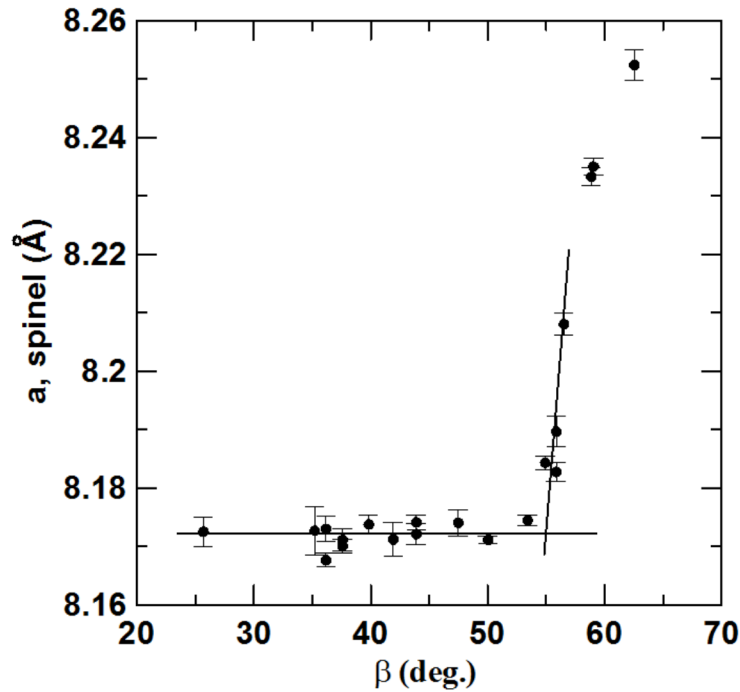


Figure 5.15: The spinel lattice parameter obtained in the co-existence region between the spinel and ordered rocksalt regions as a function of  $\beta$ .

of the ordered rocksalt region. Figure 5.13 (left) shows the points used to define this boundary. Figure 5.10 shows that once again the boundaries obtained with the lever rule agree with the phases determined by visual inspection of the XRD scans. Although the point (0.45, 0.3) lies in the three-phase region of the regular-cooled triangle, it is close enough to the edge of the region that it appears two-phase and provides a useful point to obtain the correct curvature of the boundary of the rocksalt solid solution region.

The position of the boundary at  $\beta = 55^\circ$  is at (0.05, 0.09), the point used in Figure 5.4 to define the angle  $\gamma$ . Figure 5.16 shows the ordered rocksalt lattice parameter as a function of  $\gamma$ . Here, the lattice parameter is constant with a value of  $8.320 \pm 0.001$  Å up to a maximum angle of approximately  $54^\circ$ . This is close to the value of  $8.328 \pm 0.001$  Å obtained for the sample at (0.05, 0.10) but this still represents the greatest discrepancy seen along tie-lines in this study. Should this region become of greater interest, it may be necessary to explore this boundary more closely. Nonetheless, the data suggests that the tie-lines fan-out from a point near (0.05, 0.09) up to  $\gamma =$

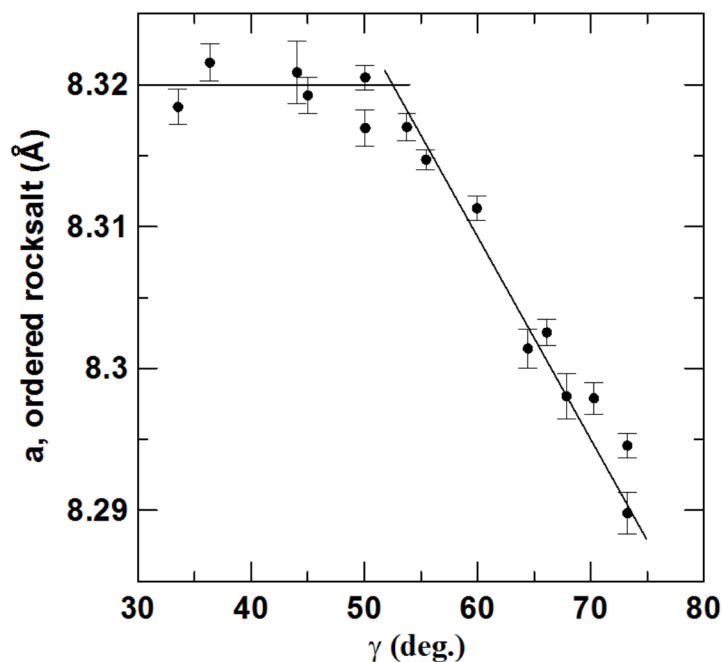


Figure 5.16: The ordered rocksalt lattice parameter obtained in the co-existence region between the spinel and ordered rocksalt regions as a function of  $\gamma$ .

54 or 55° beyond which the samples were in the region where tie-lines fan out from  $\text{LiNi}_{0.5}\text{Mn}_{1.5}\text{O}_4$  (i.e.  $\beta < 55^\circ$ ). All tie-lines in the region between the spinel and ordered rocksalt phases were therefore identified and included in Figure 5.2.

The lever rule was then used with the point (0.05, 0.09) as the pivot in order to determine the lower spinel boundary to the left of  $\text{LiNi}_{0.5}\text{Mn}_{1.5}\text{O}_4$ . This was only done for samples heated in oxygen and in both of these phase diagrams this boundary matched up very well with the phases determined by visually examining the XRD scans as well as joining nicely with the boundary determined in the region to the right of  $\text{LiNi}_{0.5}\text{Mn}_{1.5}\text{O}_4$ . In air, insufficient data was collected to use the lever rule in this region and so the lower spinel boundary in Figure 5.3 is left incomplete.

## 5.6 Conclusions Regarding Spinel and Rocksalt Li-Mn-Ni Oxides

The entire spinel and rocksalt solid-solution regions of the Li-Mn-Ni oxide pseudo-ternary system were determined at 800°C when regular cooled in air and when quenched or regular cooled in oxygen. All samples discussed here either contained one

or two phases; and no evidence for non-equilibrium behaviour was seen. Two-phase fits in the co-existence regions were used to determine lattice parameters to allow the drawing of tie-lines. The lever rule was used to determine the boundaries and showed excellent agreement with visually identified phases. Milligram-scale combinatorial samples can therefore be used to obtain a high degree of precision in the mapping of pseudo-ternary phase diagrams.

The spinel samples near  $\text{LiNi}_{0.5}\text{Mn}_{1.5}\text{O}_4$  quenched in oxygen showed oxygen vacancies. It is likely that samples quenched in air with a lower oxygen partial pressure also have vacancies. Since oxygen vacancy formation occurs simultaneously as an oxygen loss resulting in an upwards motion of the lower spinel boundary, it is important to recognize that both these effects are present in samples synthesized in air and are difficult to differentiate. However, it has not yet been determined whether or not bulk samples also show these deficiencies; it is possible that oxygen loss is significantly more prominent in the combinatorial samples due to the large surface area to volume ratios.

Comparing Figures 5.2 and 5.3 shows the motion of single-phase boundaries with synthesis conditions. Generally, the single-phase regions are much larger than previously known and increase in size with temperature (i.e. quenched) and they are also larger when prepared in air. The ordered rocksalt boundary is higher in air than it is in oxygen. In air, the lower oxygen partial pressure favours structures with lower metal oxidation numbers (i.e. lower oxygen content) such that the boundary of the rocksalt and layered regions are expected to move upwards, particularly when quenched. The resulting lattice parameter contour plots show that the spinel samples made in oxygen have oxygen site vacancies which are relieved during regular cooling.

The structure of the cubic rocksalt materials is more complex than previously suspected. The refinement of the XRD patterns showed ordering of lithium, manganese and metal site vacancies on the cubic lattice, and the extent of this ordering increased during regular cooling.

## Chapter 6

# Combinatorial Studies of Compositions Containing Layered Phases in the Li-Mn-Ni-O System

Data in this chapter are reprinted from Ref. [13] with permission from the American Chemical Society.

### 6.1 Experimental Design

This chapter deals with the remainder of the Li-Mn-Ni-O phase diagram obtained with combinatorial samples. The experimental design is the same as that described in Chapter 5. The objective here is to show supporting evidence for the rest of the phase diagrams shown in Figure 5.2.

A few combinatorial samples were imaged by SEM as described in Section 2.8. Bulk samples with key compositions were also synthesized using the “one-pot” method outlined in Section 2.1.2. The helium pycnometer was used to obtain accurate density measurements of an ordered rocksalt sample to calculate the concentration of vacancies present in the structure as described in Section 2.11.

### 6.2 Single-Phase Layered Region

Once again, one challenge with the combinatorial synthesis of samples in the layered region of the triangle is that the samples lose lithium during heating. Figure 6.1 (a) shows the phase diagram with points resulting from using atomic absorption to determine the composition of the samples after heating. All points included here are within error bars from the as-dispensed composition. Other samples were synthesized by the same method and characterized by XRD in order to determine the phases present. The boundary line from  $\text{LiNiO}_2$  to  $\text{Li}_2\text{MnO}_3$  is drawn as a straight line as this seems to agree with the data available but more samples are required to confirm



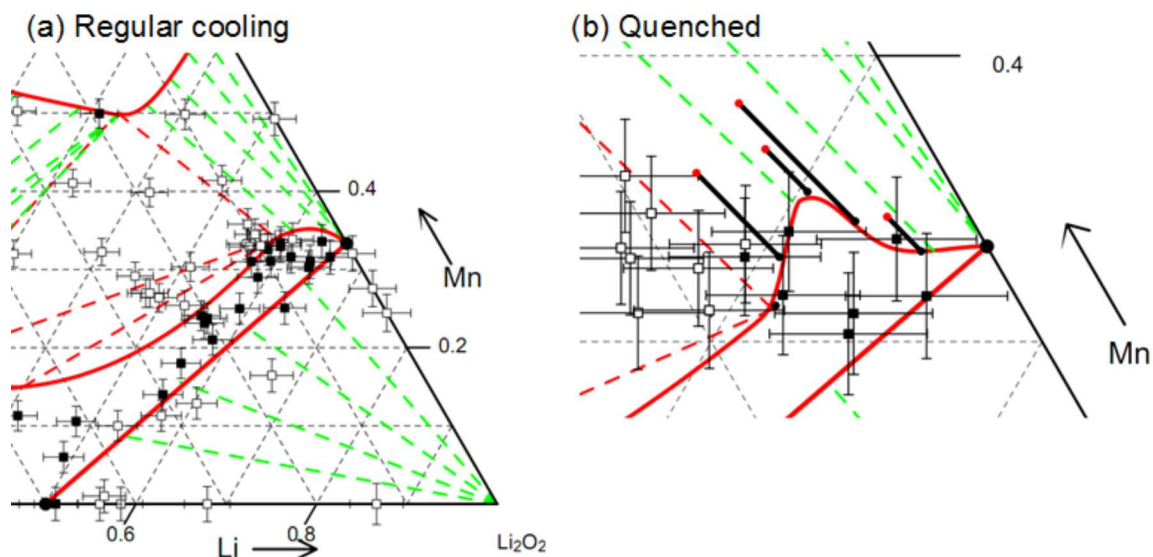


Figure 6.1: (a) Metal compositions obtained by atomic absorption for samples prepared by regular cooling in oxygen. The open-symbols indicate multiple phases in the XRD patterns while the closed symbols indicate single-phase scans. (b) A portion of the phase diagram obtained in oxygen by quenching. The compositions are assumed to be identical to those determined by atomic absorption for samples prepared by regular cooling. The red points are two-phase samples connected to the point obtained by the lever rule to generate the edge of the layered region.

this. The upper boundary of the layered region was determined as described in Section 6.8 and was in good agreement with the samples shown in Figure 6.1 (a).

Figure 6.2 shows contour plots for both the  $a$  and  $c$  lattice parameters when the structures in the layered region are fit using peak indexing according to a lithium-rich layered material,  $\text{Li}_{1.15}(\text{Mn}_x\text{Ni}_{1-x})_{0.85}\text{O}_2$  (JCPDS #52-0457) [84]. In the region near the Li-Mn line, the addition of lithium results in a significant reduction in the  $c$  axis but very little change in the  $a$  lattice parameter. Since this is part of the lithium-rich region, this increase in lithium content is likely to result in an increase in the amount of lithium in the transition metal layer such that the hexagonal layers stack tighter while the spacing within the layers is mainly unaffected. The  $a$  and  $c$  values obtained for  $\text{Li}_x\text{Ni}_{2-x}\text{O}_2$  near  $x = 1$  are in good agreement with Li et.al. [37]

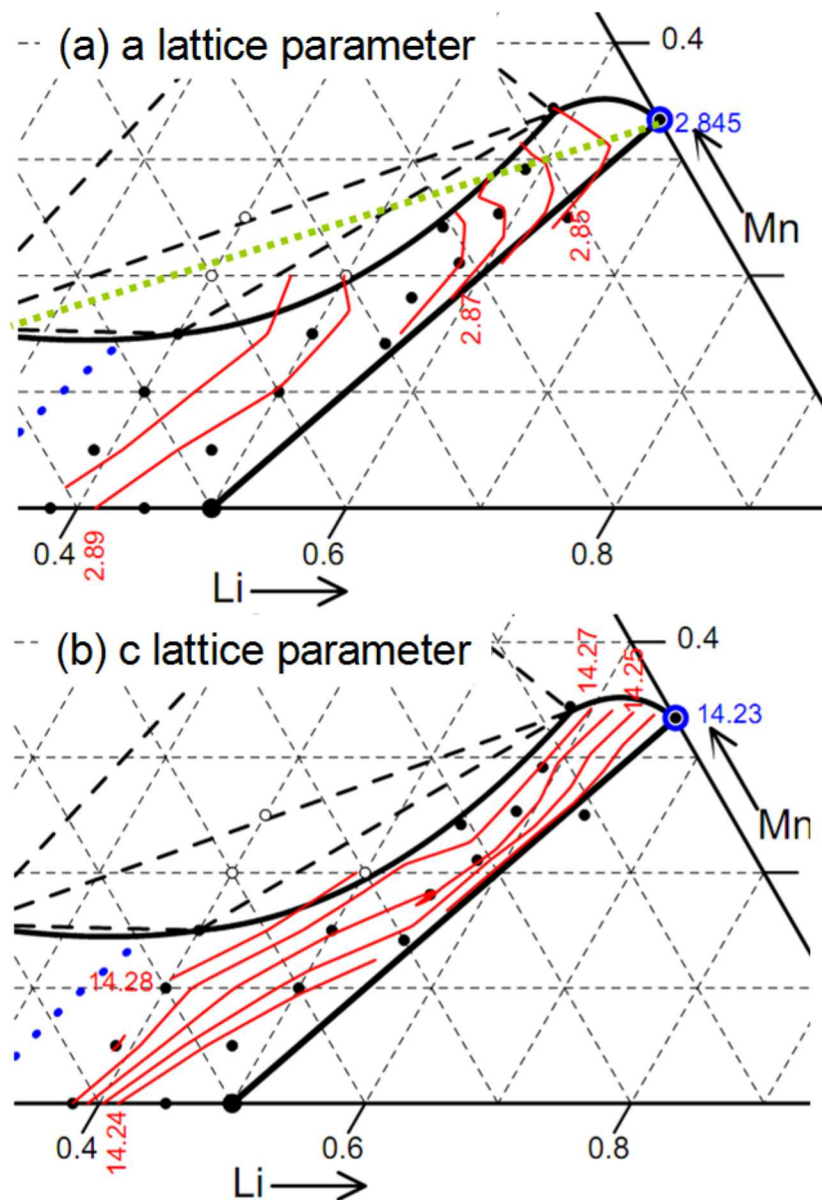


Figure 6.2: Contour plots of the  $a$  and  $c$  lattice parameters obtained by fitting all regular cooled layered structures made in oxygen as hexagonal structures. The green dotted line in (a) is the constant oxidation number line for layered structures with  $\text{Ni}^{2+}$  and  $\text{Mn}^{4+}$ . Filled points represent single-phase samples while open symbols represent multiple-phase samples.

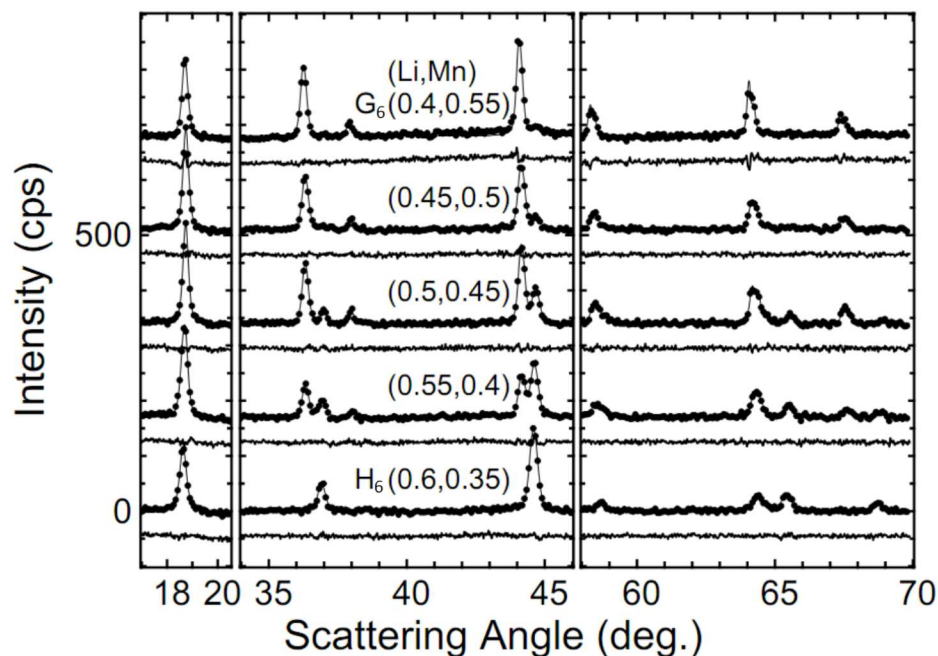


Figure 6.3: XRD scans of quenched samples in the co-existence region showing both layered and spinel structures near the Li-Mn line. The compositions of samples  $H_6$  and  $G_6$  are indicated in Figure 6.5.

### 6.3 Two-Phase Layered-Spinel Region

Figures 6.3 and 6.4 (right) show XRD scans near the Li-Mn edge of the Gibbs triangle, at compositions indicated in Figure 6.5 where the spinel and layered phases co-exist. The  $H_6$  sample at (0.6, 0.35) is single-phase consistent with the boundary that will be established in Section 6.8. All other samples show both spinel and layered peaks which are all well described by the two-phase fits. The scattering angle range 43-46°, emphasized in Figure 6.4 (right) clearly shows the relative amounts of the two phases, and this region will be of use in illustrating the phases present throughout this study.

Figure 6.6 shows the values of the lattice parameters obtained for quenched samples heated in oxygen in the co-existence region as a function of the distance between each point and the SM line shown in Figure 6.5. These graphs were used to determine the tie-lines. The results are consistent with tie-lines first fanning out from  $\text{Li}_2\text{MnO}_3$  ( $a = 2.8438 \pm 0.0006 \text{ \AA}$ ,  $c = 14.231 \pm 0.007 \text{ \AA}$  for a quenched combinatorial sample). The point (0.5, 0.45) is the sample with the most nickel that was found with lattice

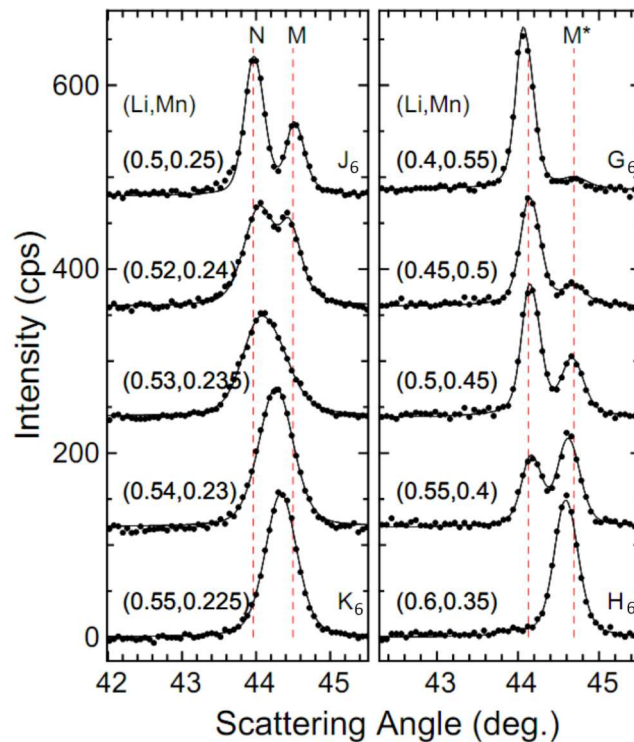


Figure 6.4: XRD scans of quenched samples in the layered-layered (left) and layered-spinel (right) co-existence regions.  $J_6$ ,  $K_6$ ,  $G_6$ , and  $H_6$  are indicated in Figure 6.5.  $M^*$  represents  $\text{Li}_2\text{MnO}_3$  and the unlabeled dashed line is a guide for the eye near the spinel peak.  $N$  and  $M$  correspond to two corners of the three-phase regions.

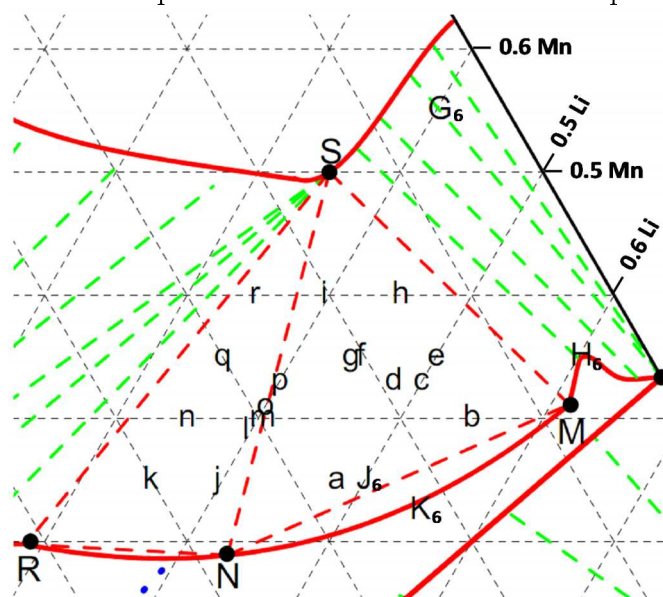


Figure 6.5: A partial phase diagram indicating compositions used in Figures 6.4, 6.7, 6.10 and 6.11.

parameters consistent with  $\text{Li}_2\text{MnO}_3$ , thus this was used to establish the end of the fanning out region. Further from the Li-Mn edge, the tie-lines move in such a way that both endpoints change, resulting in all three lattice parameters changing nearly linearly in this region in Figure 6.6. Since the tie-line through (0.5, 0.45) is nearly parallel to the SM line, it is reasonable to assume that the tie-lines continue to run parallel to the SM line and this is how they were drawn in Figure 5.2.

The lever rule was used, as described previously in Section 2.4, for the quenched samples in order to help determine the single-phase boundary of the layered region between the M-layered phase and  $\text{Li}_2\text{MnO}_3$ . Figure 6.1 (b) shows the points generated by this method as well as the positions of samples as determined by atomic absorption. Clearly, these observations are nearing the precision limits of the elemental analysis, but nonetheless the boundary generated in Section 6.8 to fit the points obtained by the lever rule is consistent with all but one of these data points and this one anomalous point is within uncertainty of the boundary.

#### 6.4 Two-Phase Layered-Layered Region

Figures 6.4 (left) and 6.7 show XRD scans of quenched samples lying between points  $J_6$  and  $K_6$  in Figure 6.5. The top two scans clearly show multiple phases present based on the region near  $44^\circ$ . The top sample is at the composition of  $\text{LiNi}_{0.5}\text{Mn}_{0.5}\text{O}_2$  and appears to be on the tie-line between the M and N points, consistent with the phase diagram in Figure 6.5. The reader is reminded that these are measurements for samples heated in oxygen and quenched. This left only one scan, (0.52, 0.24), in the two-phase region below the N - M line and this was insufficient to generate tie-lines. It should be kept in mind that the region between the N - M line and the upper layered boundary was composed of layered-layered composites.

The bottom two scans of Figure 6.4 (left) both appear to be single-phase. The one that is difficult to identify is the sample at (0.53, 0.235) where severe broadening was seen but two peaks cannot yet be distinguished. This suggests that two phases were present in this sample, and this was supported by the fact that the extra peak seen in the scan at (0.52, 0.24) appeared on the side where there is an asymmetry to the broad peak in (0.53, 0.235). The boundary was therefore placed at (0.535, 0.2325),

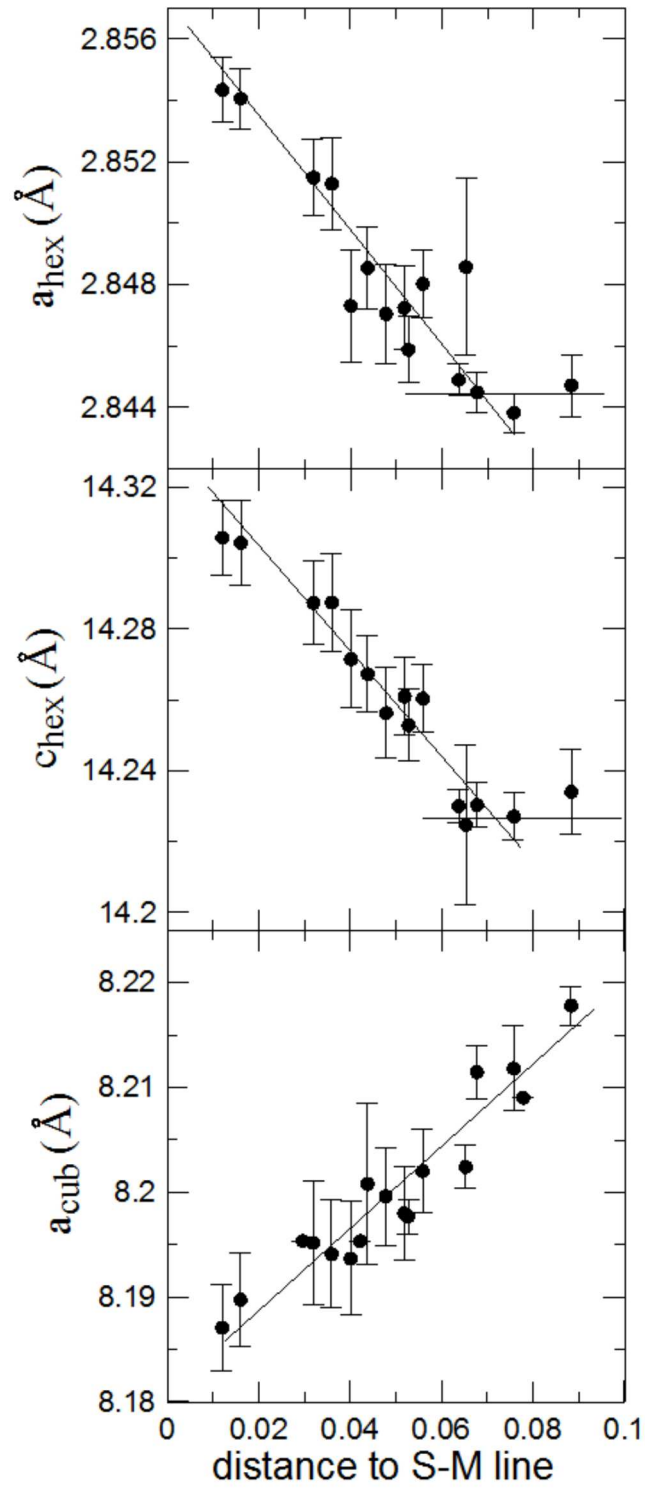


Figure 6.6: Lattice parameters obtained in the layered-spinel co-existence region as a function of the distance to the S-M line. The spinel lattice parameter is  $a_{cub}$  while the layered lattice parameters are  $a_{hex}$  and  $c_{hex}$ . The lines are guides for the eye.

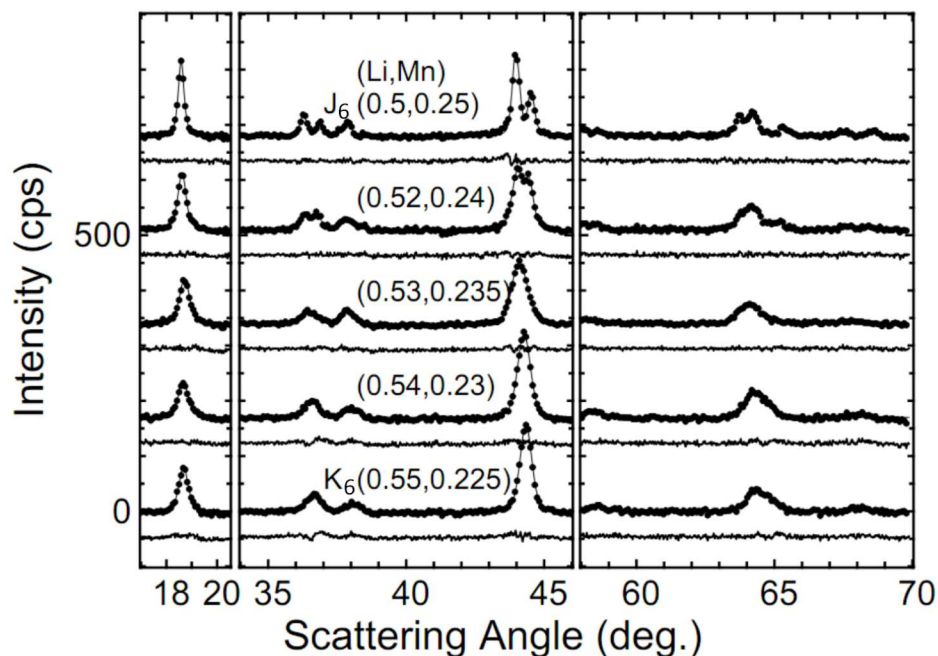


Figure 6.7: XRD scans in the two-phase region below the NM line obtained for quenched samples. Compositions of samples J<sub>6</sub> and K<sub>6</sub> are indicated on Figure 6.5.

halfway between the single and two-phase samples. Despite this analysis, the exact position of this boundary should still be considered in question to within about 0.01 in lithium content.

In samples cooled at the regular rate the XRD patterns look similar to that seen when quenched except for the one synthesized at point J<sub>6</sub> which shows evidence of the R phase as well as the N and M phases. This behaviour will be discussed further in Section 6.7.

### 6.5 The R, N, S and M phases

Figure 6.5 shows two three-phase regions side-by-side between the spinel and layered single-phase regions when samples were heated in oxygen and quenched. The two regions were the NSM and NSR triangles. R was an ordered rocksalt structure, S was a spinel structure and N and M were both layered structures (labels were chosen to represent nickel-rich or manganese-rich layered structures to distinguish them). The large array of samples shown in Figure 5.1(b) made it possible to identify samples

near each corner by matching lattice parameters to those obtained with the three-phase fits. Figures 6.8 and 6.9 (left) show XRD scans of quenched samples near the R, S, N and M corners. Fitting these patterns allowed the determination of the lattice parameters included in Table 6.1 and their coordinates in the Gibbs triangle are listed in Table 6.2. In the scattering angle range 43-46°, each of the four single-phase samples have a single peak without  $K_{\alpha_{1,2}}$  peak splitting. As such, this region is ideal to illustrate the phases present in the three-phase regions.

Bulk quenched samples synthesized at each of the R, N and M corners using the one-pot synthesis (Section 2.1.2) were scanned with the JD-2000 diffractometer. Table 6.3 shows the results of Rietveld refinement. The R phase only has 10 % vacancies such that the average Mn oxidation state is 3.6+, assuming that nickel is in the 2+ state. The density of this R phase sample was found to be  $5.4447 \pm 0.0090$  g/mL using a helium pycnometer and this value corresponds to  $8.8 \pm 2.0$  % vacancies on the 4b sites, in good agreement with the XRD results. In the previous chapter, an ordered rocksalt structure synthesized in oxygen and cooled at the regular rate was found to have approximately 30 % vacancies on the 4b sites and Mn in the 4+ state. These results suggest that the structure of this phase changed during slow cooling and further study is required to understand this fully.

The N-layered phase had a hexagonal structure with significant disorder in both the lithium and transition metal layers such that there was a 30 % nickel occupation on the lithium layers. By contrast, the M-layered phase was far more ordered with very little nickel on the lithium layers. XRD scans of this structure also show superlattice peaks in the range 20-35° consistent with ordering on  $\sqrt{3} \times \sqrt{3}$  lattices in the transition metal (TM) layers. Although the compositions of the TM layers were not in the 1:2 ratio needed for this ordering, it was quite close. As such, if one  $\sqrt{3} \times \sqrt{3}$  lattice was randomly occupied with 0.708Li and 0.292Ni while the other two contained 1.866Mn and 0.134Ni, the resulting scattering contrast would be sufficient to give rise to the weak ordering peaks seen here, consistent with the reasoning of Lu et al. [46] The ordering peaks should therefore not necessarily be interpreted as the presence of  $\text{Li}_2\text{MnO}_3$  and the sample may yet be single-phase as suggested here.



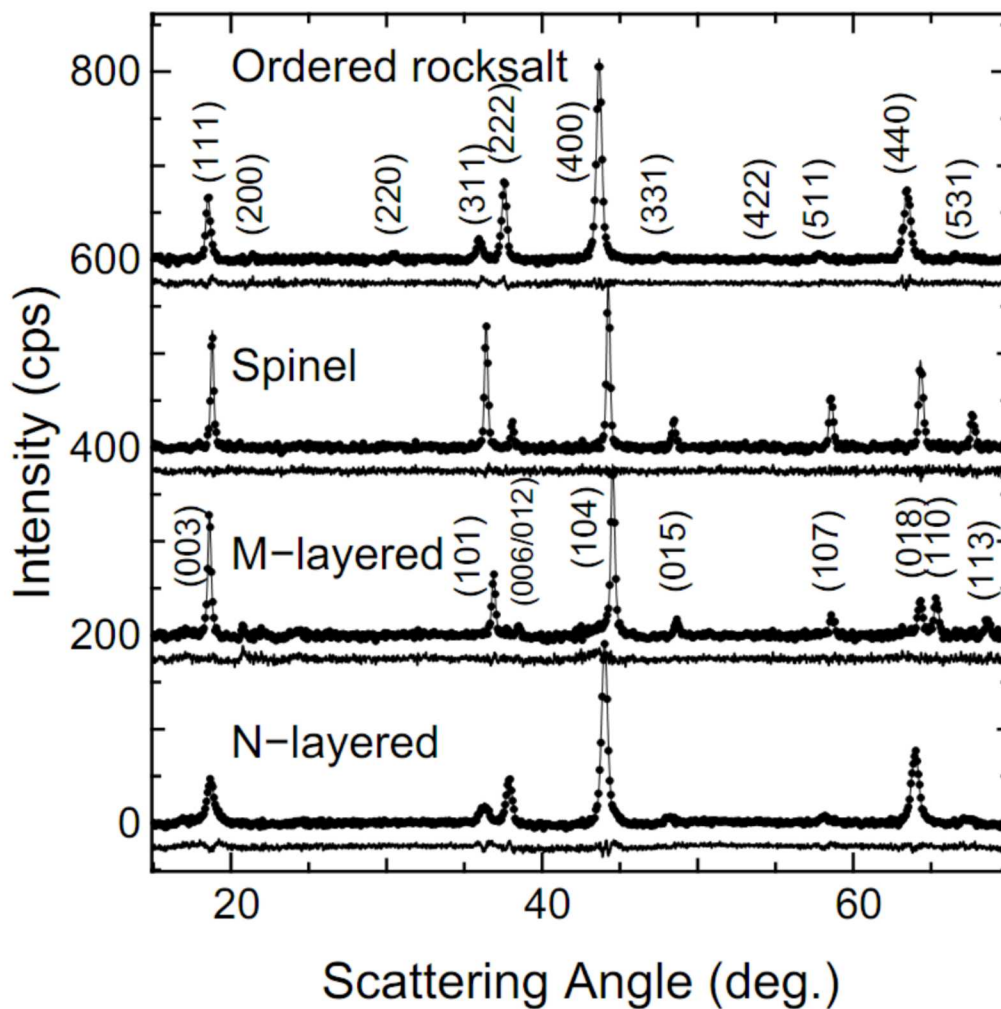


Figure 6.8: XRD patterns of the four samples found at the corners of the three-phase regions for samples heated in oxygen and quenched. The peak indices are indicated based on JCPDS #89-4619 for the ordered rocksalt phase and #52-0457 for the layered phases. The spinel peaks have the same indices as the ordered rocksalt; though there are no (200), (331), (422) reflections in the spinel structures and the (220) peak is weak. The M-layered structure is indexed to a hexagonal structure as discussed in the text. The N-layered peaks have the same indices, though the (018) and (110) peaks are not separated.

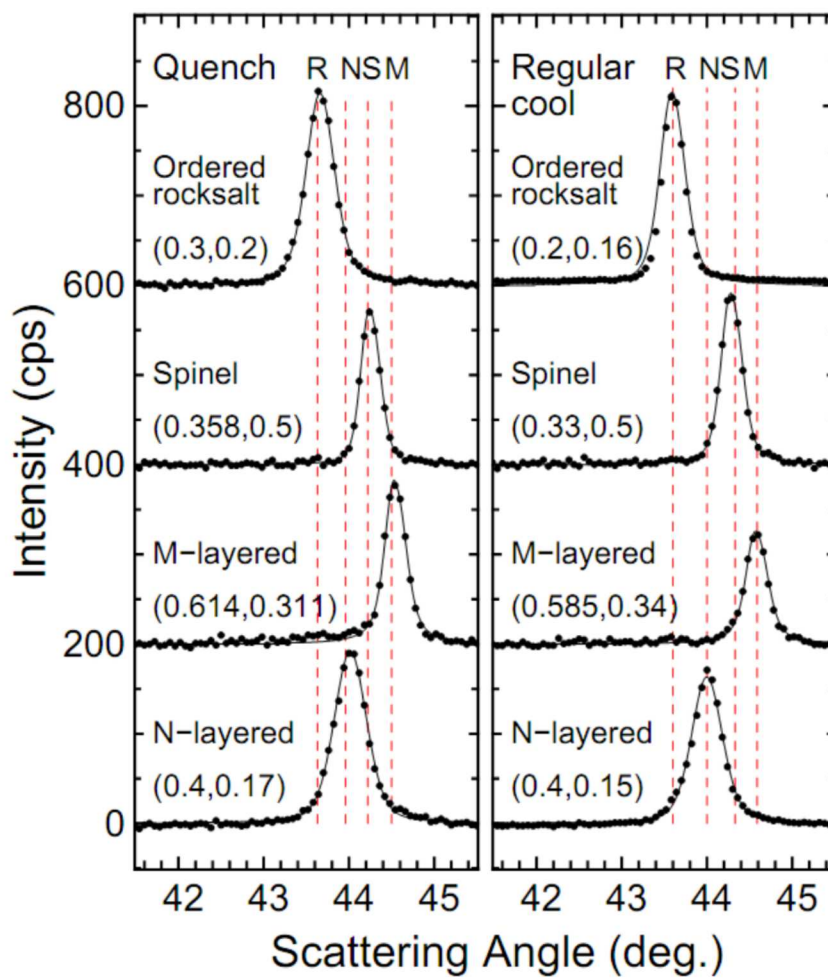


Figure 6.9: XRD patterns generated at the four corners of the three-phase regions obtained by quenching (left) and regular cooling (right). The coordinates are (Li, Mn) where Li is the lithium metal fraction and Mn is the manganese metal fraction.

Table 6.1: The lattice parameters obtained for the single-phase corners of the three-phase regions as well as the average values obtained in the three-phase regions and the standard deviations ( $\sigma$ ). All values are in Å. The uncertainty for the average lattice parameters is calculated as  $\sigma/\sqrt{N}$  where N is the number of samples.

	Rocksalt		Spinel		N-layered		M-layered	
	$a$	$\sigma$	$a$	$\sigma$	$a$	$\sigma$	$a$	$\sigma$
					$c$		$c$	
Quench:								
Single phase	8.284(2)		8.187(1)		2.909(1)		2.8543(6)	
					14.32(1)		14.291(6)	
SNM (26 fits)			8.1867(9)	0.0044	2.9025(6)	0.0033	2.8553(2)	0.00093
					14.347(2)	0.010	14.303(2)	0.002
RSN (12 fits)	8.284(3)	0.0097	8.182(2)	0.0070	2.902(2)	0.0053		
					14.322(5)	0.017		
Slow cool:								
Single phase	8.295(2)		8.173(1)		2.907(1)		2.8516(8)	
					14.30(1)		14.277(8)	
MRS (6 fits)	8.297(2)	0.0052	8.169(1)	0.0018			2.8502(5)	0.0012
							14.280(6)	0.013
MRN (12 fits)	8.294(2)	0.0080			2.9013(4)	0.00014	2.854(2)	0.0072
					14.312(4)	0.012	14.25(1)	0.032

Table 6.2: The coordinates of the four corners of the three-phase regions. All points are (Li, Mn).

	Rocksalt	Spinel	N-layered	M-layered
Quench:				
Single-phase	(0.3,0.2)	(0.36,0.5)	(0.4,0.17)	(0.61,0.31)
Lever rule	(0.29,0.20)	(0.36,0.5)	(0.43,0.19)	(0.61,0.31)
Slow cool:				
Single-phase	(0.22,0.16)*	(0.33,0.5)	(0.4,0.15)	(0.58,0.34)

\* This point lies midway between the 8.29 Å and 8.30 Å contour lines on the boundary of the ordered rocksalt region in Figure 5.10.

Although the ordering seen in the M sample is expected to be coupled with monoclinic distortions in the hexagonal lattice, the fact that a high-quality fit was obtained for a hexagonal structure shows that the extent of monoclinic distortion was small and it was completely masked by the peak broadening due to the diffractometer. The fact that the oxygen occupancy converges to a value above 100 % implies that there are metal site vacancies in the M-layered structure. Both of these issues will be resolved in Chapter 8.

## 6.6 Three-Phase Regions, Quenched

Figure 6.10 shows a number of XRD scans obtained within the three-phase regions of quenched samples. The patterns were complex with a number of overlapping peaks. The whole pattern fits were obtained as linear combinations of the four fits generated for the single-phase R, N, S and M samples in the previous section. The key feature of the fitting algorithm was that peak widths were never adjusted such that overlapping peaks could not be described by broadening the peaks of a particular phase. Instead the lattice parameters and phase intensities were allowed to be adjusted. The lattice constants of the three co-existing phases were virtually invariant for all the fits in the three-phase regions as expected. Figure 6.11 shows the 43 - 46° scattering angle range for a number of samples. All samples in the left column show primarily N, S, and M peaks while those in the right column show that N, S and R peaks dominate. In all samples, the relative intensities of the peaks were qualitatively consistent with that

Table 6.3: Rietveld results for bulk samples synthesized at the R, M and N corners by heating in oxygen for 5 h and quenching to room temperature. Occupations and positions of each site are shown, as well as lattice parameters in Å.

R (Fm3m)		N (R-3m)		M (R-3m)*	
$a = 8.2829(4)$		$a = 2.916(1)$		$a = 2.8574(5)$	
		$c = 14.324(6)$		$c = 14.289(4)$	
4a:	4.0 Mn	3a:	0.499 Li	3a:	0.708 Li
4b:	3.272 Li		1.134 Mn		1.866 Mn
	0.328 Ni		1.367 Ni	3a:	0.426 Ni
	0.4 □				
8c:	8 O	3b:	2.105 Li	3b:	2.976 Li
24d:	6.084 Li		0.895 Ni		0.024 Ni
	2.176 Mn				
	15.74 Ni	6c:	5.588 O	6c:	6.253 O
24e:	24 O		(0.2564,0,0)		(0.2579,0,0)
	(0.2378,0,0)				
$R_B =$	1.99 %		1.86 %		2.92 %

\* This ignores the superlattice peaks which can be indexed to the C2/m space group.

expected from Figure 6.5. Although the intensities of the peaks changed significantly, their positions were nearly constant throughout Figure 6.11, consistent with three-phase regions. The fits were obtained using three phases only so that sections of the XRD patterns where the fits were below the data revealed where trace amounts of the fourth phase was present. For example, Figure 6.5 shows that point f should be made up of N, S and M phases only, but Figure 6.11 shows a small peak corresponding to the R phase. This is consistent with trace conversion occurring during cooling as will be discussed in the next section. This conversion can be attributed to imperfect quenching such that the equilibrium conditions at 800°C were not maintained during cooling.

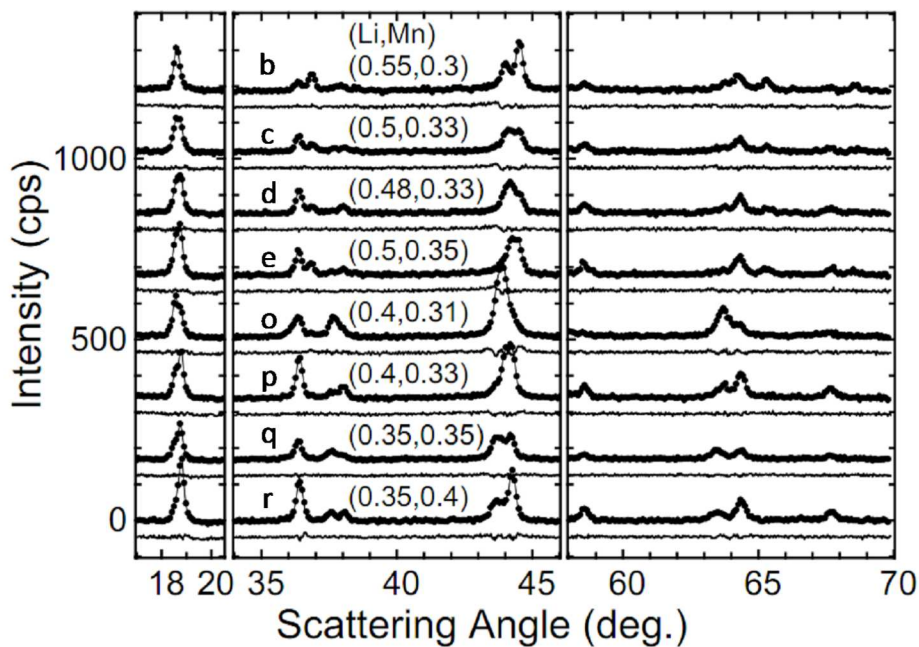


Figure 6.10: XRD scans of samples in the three-phase regions obtained by quenching. The fits are included as well as difference plots below each scan. The labels (b, c, d...) match those used in Figure 6.5.

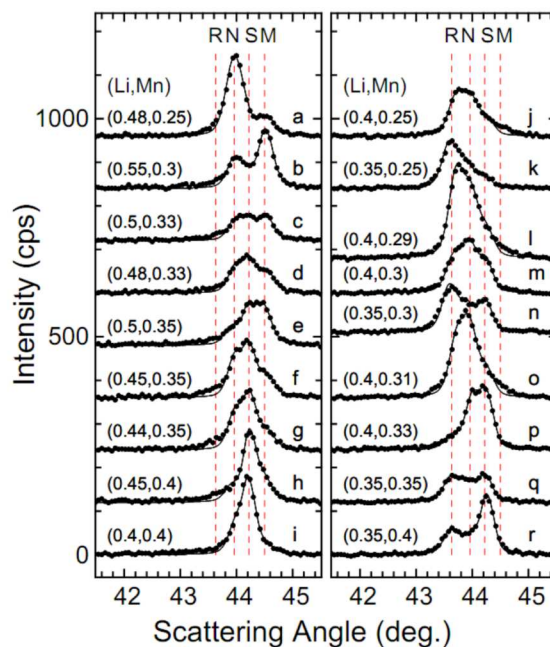


Figure 6.11: Partial XRD scans of samples in the three-phase regions obtained by quenching. Left: samples in the NSM triangle. Right: samples in the NSR triangle. The labels (a, b, c...) match those used in Figure 6.5.

The fitted lattice parameters show no trends with composition in the three-phase regions and the standard deviations shown in Table 6.1 are small. The values of the lattice parameters show good agreement with the values obtained for the single-phase samples at the corners. In all cases, the standard deviations are on the order of 0.1 % of the lattice parameter and therefore small enough to imply that the lattice parameters remain constant (this condition was determined in the previous chapter). This supports the claim that the NSM and NSR triangles are in fact three-phase regions.

Fitting the three-phase scans also allowed for the use of the lever rule to determine the tie-lines lying at the outer edges of the three-phase regions. The method was similar to that used in two-phase regions wherein phase fractions were calculated from fitted peak areas in the co-existence and single-phase regions. Precise values for the peak areas of the four corners were obtained from the fits shown in Figure 6.8. The sequence used to generate the tie-lines at the outer edges of the three-phase regions began by using the S corner as the pivot point for the lever rule in order to define the RN and NM lines. Figure 6.12 shows this use of the lever rule with black lines joining a three-phase sample in red to the calculated point on the RN or NM line in black. The intersection of these two lines gave the N point which was then used as the pivot in order to determine the SR and SM lines. These lines allowed the identification of the R and M corners. Finally, the R and M corners were used as pivots to define the MS line. The intersections of the MS, RS and NS lines were then used to verify the original choice of corner S. Figure 6.12 shows the results of using the lever rule to generate the boundaries and identify the locations of the corners. Many of the three-phase points could be used to generate all three boundaries, however some were found to be either too close or too far from the boundary to give accurate results. Despite this limitation, there are sufficient points to tightly constrain each boundary and therefore yield precise coordinates for the four corners. Table 6.2 shows that the coordinates of the four corners agree well with those obtained by searching for single-phase samples with lattice parameters matching those obtained in the three-phase regions.

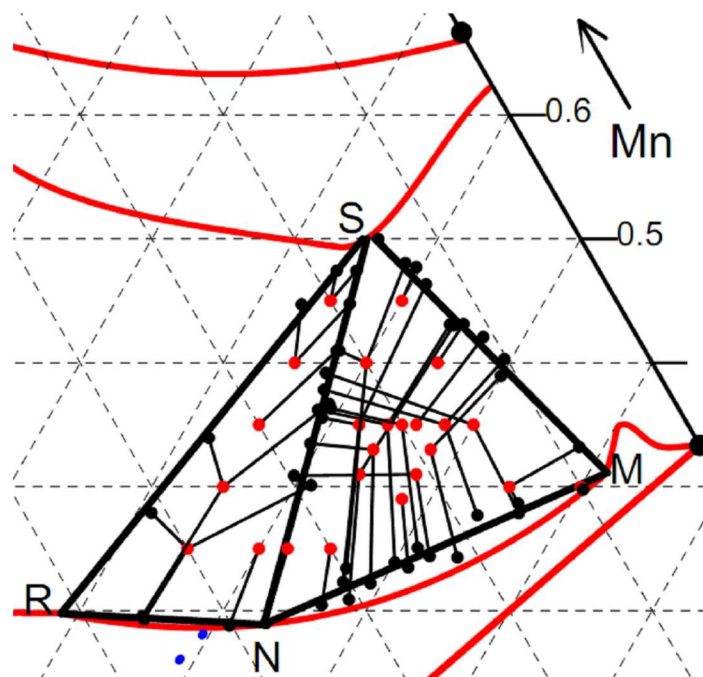


Figure 6.12: A partial phase diagram focusing on the three-phase regions for quenched samples. Samples represented by the red points show three-phases and they are connected to points on the tie-lines as calculated with the lever rule.

These results show that the phase compositions observed in the regions are consistent with the three-phase regions shown in Figure 5.2 (a), 6.5 and 6.12. However, imperfect quenching did result in trace contamination with a fourth phase being present in some samples.

### 6.7 Three-Phase Regions, Slow Cooled

The transformations during slow cooling are complex, and all samples in the three-phase regions change dramatically. Figure 6.13 shows partial XRD scans obtained by quenching, regular cooling (about  $8^{\circ}\text{C}/\text{min}$ ) and slow cooling ( $1^{\circ}\text{C}/\text{min}$ ). The compositions of the samples in the left panel are equally spaced along a line joining  $A_6$  and  $B_6$  in Figure 6.14 while the right panel represents samples equally spaced between points  $C_6$  and  $D_6$ . All quenched samples were consistent with Figure 6.12 (i.e. they have the expected amounts of R, N, S and M phases). For all samples along the  $A_6 - B_6$  and  $C_6 - D_6$  lines, the fraction of N-layered phase diminished as cooling



time increased. Although a small amount of N remained in some samples when slow cooled, it appears that all of these samples were tending towards having R, S and M phases only; consistent with XRD scans found in the literature for regular cooled samples [14].

Figure 6.9 (right) shows the XRD scans of regular-cooled single-phase samples identified near the four corners, which have moved relative to their positions in the quenched samples. Table 6.1 shows the fitted lattice parameters for these samples and Table 6.2 shows their locations within the Gibbs triangle. Figure 6.15 shows XRD scans and fits of a few samples obtained by regular cooling which appeared to have finished conversion (i.e. with only three peaks present in the region 43-46°). The fits clearly are poorer quality than those obtained for quenched samples, consistent with the fact that there was still significant amounts of the fourth phase present, and the fits included three phases only. Figure 6.16 shows the 43-46° region of XRD patterns from a variety of samples located as shown in Figure 6.17. The data suggests that at some temperature during cooling the equilibrium diagram is made up of the following three-phase regions: MRS and MRN. It is of interest that conversion occurred more rapidly in the region near the SM line where the change primarily involved the replacement of the N phase with the R structure.

The complex phase transformations occurring in the three-phase regions were seen once before in the literature by Hinuma et al. [56] as shown in Section 1.4.3. The sample synthesized at the composition of  $\text{LiNi}_{0.5}\text{Mn}_{0.5}\text{O}_2$  by ion-exchange, which the authors suggested results in a slight lithium deficiency. Extra peaks appeared after annealing at 600°C. Zooming in on the scattering angle region of 43-46° in the XRD scans (Figure 8a in Ref. [56]) shows a curve qualitatively similar to scan d from Figure 6.16 obtained here. This shows that the annealing step resulted in a phase diagram where the sample was positioned within the MRN triangle as obtained here by slow cooling in oxygen. Assuming that their sample was indeed lithium deficient, the results of Hinuma et al. are consistent with the phase diagrams presented here.

Figure 6.18 shows SEM images for three samples of interest as well as the corresponding XRD scans near 44°. Image (c) of a sample at composition (0.5, 0.2) shows small particles consistent with the peak broadening seen in the XRD patterns. The

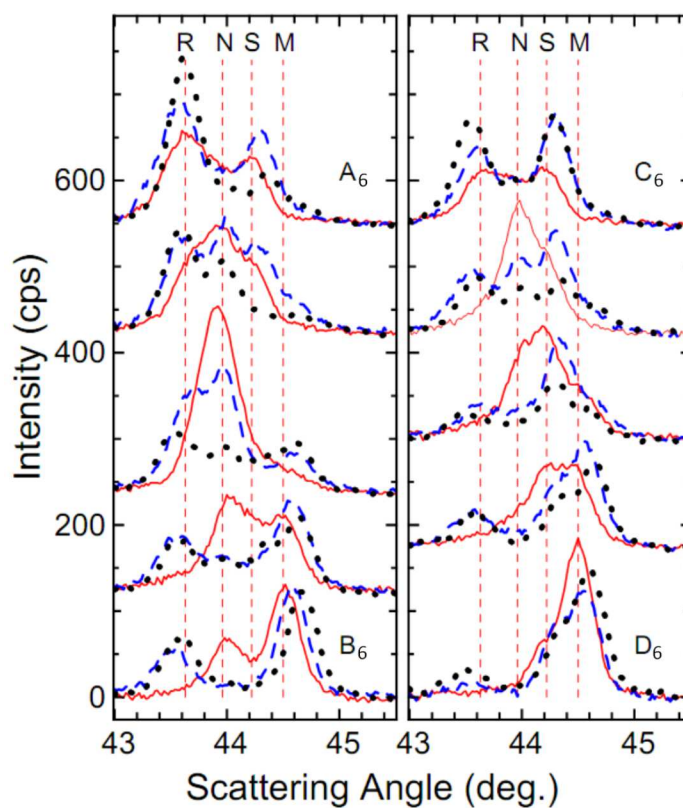


Figure 6.13: XRD scans obtained in oxygen by quenching (red-solid), regular cooling (blue-dashed), and slow cooling (black dotted). The vertical red dashed lines indicate the positions of the peaks obtained by quenching.

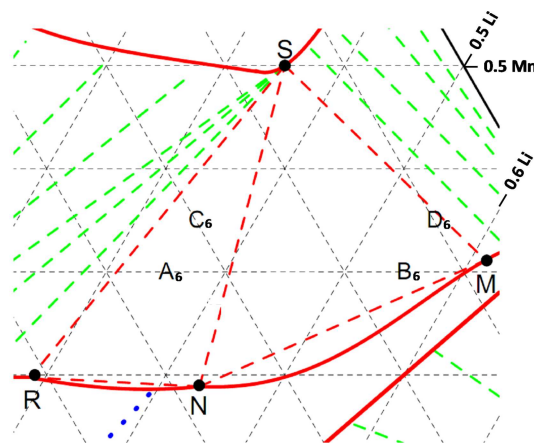


Figure 6.14: A partial phase diagram with useful composition labels used throughout this chapter.

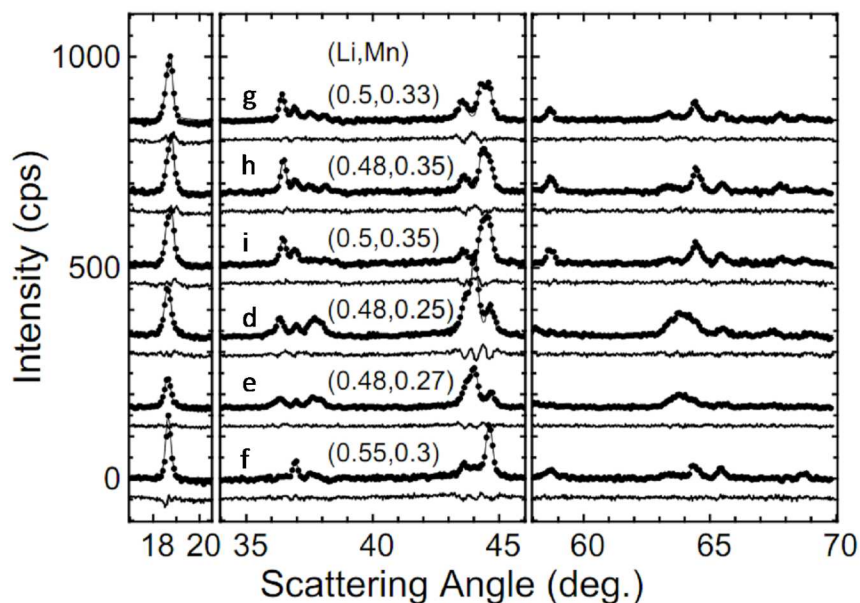


Figure 6.15: XRD scans of samples in three-phase regions obtained by regular cooling with fits and difference plots below each scan. The labels (d, e, f...) match those used in Figure 6.17.

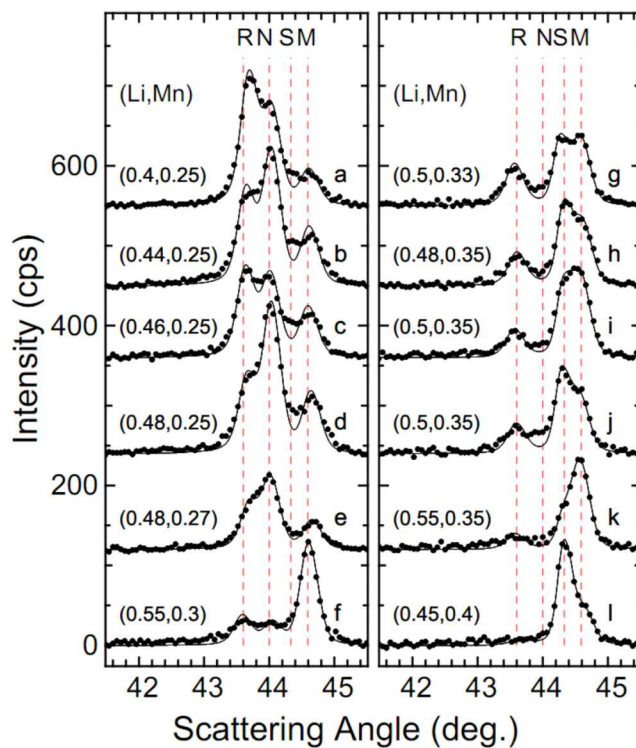


Figure 6.16: Partial XRD patterns obtained in the three-phase regions by regular cooling. The labels (a, b, c...) match those used in Figure 6.17.

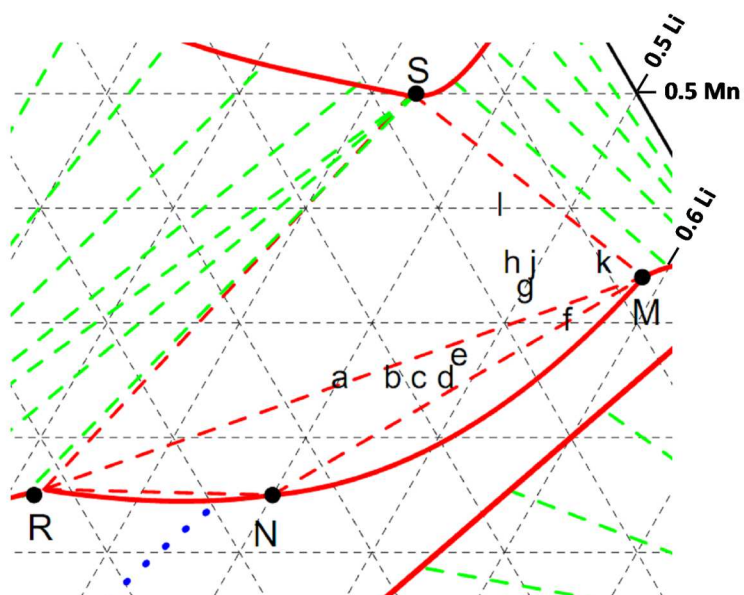


Figure 6.17: A partial phase diagram showing compositions used in Figures 6.15 and 6.16.

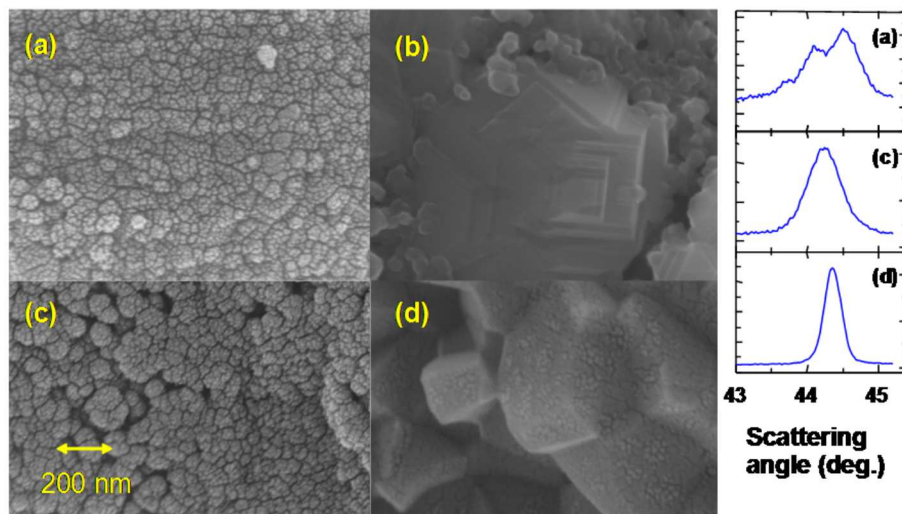


Figure 6.18: Left: SEM images taken by Ramesh Shunmugasundaram of three combinatorial samples made in oxygen with regular cooling: (a) and (b) are two images of a sample with  $(\text{Li}, \text{Mn}) = (0.5, 0.25)$ , (c)  $(0.5, 0.20)$  near the layered boundary and (d) is a sample dispensed at  $(0.5, 0.05)$ . Right: XRD scans of the three samples in the region near  $44^\circ$ .

sample imaged in (a) showed three phases in the XRD pattern consistent with the R, N and M phases discussed here. The SEM image of this also showed similar particles to those seen in (c), but a second image (b) of the (0.5, 0.25) sample showed that there are also a few large particles showing 90° crystal faces. These large particles may have been the ordered rocksalt, since being few in number and quite large would account for the small relatively sharp rocksalt peak in the XRD pattern. Such large ordered rocksalt particles would also be consistent with the fact that the ordered rocksalt phase grew rapidly during slow cooling of samples in the three-phase regions. Although more study is required here, the SEM images do appear to support the observations made based on the XRD patterns.

## 6.8 The Upper Boundary of the Layered Region

The upper boundary of the layered region was not easy to determine due to the three-phase regions. The lever rule in the three-phase regions only yielded three points on the layered boundary: R, M and N and this could only be done for quenched samples since the slow cooled samples never reached equilibrium. For the regular cooled samples, the boundary was made using a polynomial function through five points: the R, M, and N corners,  $\text{Li}_2\text{MnO}_3$  (which was on the boundary as determined in Section 6.3), and the single-phase point found on the edge of the layered-layered co-existence region (Section 6.4). Since only five points were used, the precision of this line is limited, particularly in the region below the R-N line where no samples were synthesized in the small two-phase region that must exist below the three-phase NSR region. It should also be noted that in the three-phase regions equilibrium is not reached during regular cooling so this could be the case in the layered-spinel two-phase region as well, making the layered boundary obtained by slow cooling particularly difficult to identify. Nonetheless, the boundary shown in Figure 5.2 (b) and 6.1 (a) is in good agreement with the data at hand.

Figure 6.1 (b) shows that for quenched samples the region near  $\text{Li}_2\text{MnO}_3$  shows a sharper “bump” than that seen for slow cooled materials. The points generated in Section 6.3 using the lever rule were used in addition to the five points mentioned here. The narrow “bump” seems strange in contrast to the rest of the boundaries

which are smooth broad curves. Again this feature is based on a relatively small number of data points and the quenching required about a minute suggesting that the high temperature structure may not have been frozen in. As such, more data was required to conclude that this feature was in fact the equilibrium boundary at 800°C. This region will therefore be examined in more detail in Chapter 8. The phase diagram shown in Figure 5.2 (a) is in agreement with all quenched samples synthesized with the combinatorial robot. It is also worth noting that the boundaries of the single-phase regions were obtained by fitting polynomials to a relatively small number of points. The curvature at some points may therefore not be perfect, but the boundaries are consistent with all experimental data.

## 6.9 Conclusions Regarding Combinatorial Studies of Li-Mn-Ni-O Materials

The phase diagrams obtained for quenched samples show that in both three-phase regions all samples contain some of the N and S phases, while during slow cooling they convert to structures containing at least some R and M phases. Though the thermodynamics of this are complex, a qualitative understanding can be achieved by considering the results of the Rietveld refinement. The R and M phases were collectively more ordered than the N and S phases (the N phase in particular showed considerable disorder in the hexagonal layers). This would suggest that the R and M phases have lower combined internal energies and lower combined entropies than the combination of the N and S phases. Since the structure of the three-phase regions at high temperature is driven by entropy, the N and S phases are present in all points in the regions. Upon slow cooling, a temperature is reached where internal energy becomes more important and there is still sufficient thermal energy for atomic transport such that the R and M phases begin to appear in all samples. Further study is required to have a better understanding of the thermodynamics and kinetics of these phase transformations.

The results obtained here along the lithium rich line between  $\text{LiNi}_{0.5}\text{Mn}_{0.5}\text{O}_2$  and  $\text{Li}_2\text{MnO}_3$  also require discussion. This composition line is not a solid solution over its entire length when synthesized in oxygen. This would suggest that the broadening

seen in XRD patterns by Jo et al. [55] was due to multiple phases. Furthermore, the region near  $43.5^\circ$  in the XRD spectra published by Jo et al. shows that there may be trace amounts of ordered rocksalt present, which means that this sample obtained with a slow cooling rate contained three phases, consistent with the phase diagram produced here.

Furthermore, the layered boundary moved upwards in the Gibbs triangle when heated to higher temperatures (i.e. quenched), especially near the N-layered corner. At  $800^\circ\text{C}$  in oxygen, a layered material synthesized at the composition of  $\text{LiNi}_{0.5}\text{Mn}_{0.5}\text{O}_2$  is not stable but instead phase separates into two layered structures: the N and M phases. As the boundary moves up (either with temperature or in air) the endpoints of the tie-line on which the sample lies will approach each other and ultimately become a single-phase sample. Inversely, during cooling the boundary moves down such that a single-phase sample near the upper boundary of the layered region phase separates into two layered structures during slow cooling. As suggested from the work in the Li-Co-Mn-O system in Chapter 4, these conditions would give rise to layered-layered nano-composites. However, the endpoints of this co-existence are not  $\text{Li}_2\text{MnO}_3$  and  $\text{LiNi}_{0.5}\text{Mn}_{0.5}\text{O}_4$  as assumed by many authors [44]. The tie-lines obtained here never extend to  $\text{Li}_2\text{MnO}_3$  and they include points to the left of  $\text{LiNi}_{0.5}\text{Mn}_{0.5}\text{O}_2$  in the Gibbs triangle. Therefore, the so-called  $\text{LiNi}_{0.5}\text{Mn}_{0.5}\text{O}_2$ - $\text{Li}_2\text{MnO}_3$  nano-phase separation promoted by many authors needs to be adapted given the actual endpoints of the co-existence. The layered-layered region does not include the lithium-rich materials at all at higher temperatures as the single-phase boundary sweeps upwards in the triangle though. This will be discussed in the next chapter. It is also relevant that the unit cell volumes of the M and N-layered phases differ by approximately 4.0 %; which is relatively large compared to that observed in Chapter 4 and would most likely result in fracturing of the lattice. This prediction is supported by the SEM images here where very small particles are seen in the samples with two layered structures and larger particles in the single phase layered sample. Thus, the region where nano-scale domains would be found is further restricted to some portion of the layered-layered region. Clearly, further study is needed to truly understand the short-range ordering in such samples and any sample near the boundary of the layered region where XRD

peak broadening is seen. In particular, the consequences of these nano-domains on the lithium layer must be evaluated given that one of the layered structures in the nano-composites must be quite close in composition to the N-layered structure which was found to contain a high fraction of nickel on the lithium layer. Clustering of nickel on the lithium layer during cooling would interfere significantly with lithium extraction during electrochemical cycling. This will be explored in Chapter 9 for materials near  $\text{LiNi}_{0.5}\text{Mn}_{0.5}\text{O}_4$ .

This chapter should be of particular benefit to researchers working on composite electrode materials in the Li-Mn-Ni-O system. The phase diagrams produced here are consistent with all published XRD patterns found in the literature for samples in the co-existence region between the spinel and layered regions. At this point in time, it is unclear what dominates the properties of composite electrodes and in particular how the respective phases affect each other during cycling. Having a phase diagram should now make it possible to perform systematic studies of spinel-layered composite electrodes to better understand how the properties of a composite relate to those of its component phases.



## Chapter 7

### Investigations of Bulk Li-Mn-Ni-O Samples to Confirm the Combinatorial Studies

Data in this chapter are reprinted from Refs. [13] and [85] with permission from the American Chemical Society and the Electrochemical Society.

#### 7.1 Motivation

Figure 7.1 shows isothermal sections of the Li-Mn-Ni-O phase diagrams obtained for the milligram-scale combinatorial samples heated in oxygen, the supporting evidence for which was presented in the last two chapters. Points  $A_7$  and  $B_7$  refer to compositions studied here in order to confirm that the results of the combinatorial work are relevant to bulk samples, and to help identify how the phase diagrams change for bulk samples. The single phase regions in the combinatorial studies were larger than previously suspected with an expanded layered region that encompassed areas both above and below the Li-rich layered line joining  $\text{Li}_2\text{MnO}_3$  to  $\text{LiNi}_{0.5}\text{Mn}_{0.5}\text{O}_2$ . This has significant consequences both in terms of re-interpreting published data and obtaining a better overall understanding of the electrochemistry of these materials. Some of these consequences will be explored in this chapter by studying bulk samples synthesized at the compositions listed in Table 7.1.

A sample made at point  $A_7$  in Figure 7.1 should be primarily made up of the N and S phases when quenched and convert to R and M during slow cooling. Rhines referred to such a transformation as a ternary four-phase equilibrium [86], though it is of note that oxygen content is changing here such that it is a more complicated transformation than those considered by Rhines. Nonetheless, he predicted that such a point would be present between two three-phase regions transforming during cooling as seen in Chapter 6. Such a point transforming reversibly would be sufficient to demonstrate that the three-phase regions exist and transform in the same manner

Table 7.1: Metal molar fractions for samples discussed in the text. For samples A<sub>7</sub>, A<sub>7</sub>' and B<sub>7</sub>, all heated in oxygen, the composition is as-dispensed, while for C<sub>7</sub>-G<sub>7</sub>, heated in air, the compositions shown were obtained with elemental analysis for the regular cooled samples. The values for the M, N, R, and S samples are for synthesis in oxygen from Chapters 5 and 6.

Sample	Li	Mn	Ni
A <sub>7</sub>	0.425	0.255	0.32
A <sub>7</sub> '	0.41	0.24	0.35
B <sub>7</sub>	0.45	0.3	0.25
C <sub>7</sub>	0.330	0.335	0.335
D <sub>7</sub>	0.367	0.317	0.317
E <sub>7</sub>	0.441	0.280	0.279
F <sub>7</sub>	0.450	0.276	0.274
G <sub>7</sub>	0.495	0.253	0.252
Quench			
M	0.61	0.31	0.08
N	0.40	0.17	0.43
R	0.29	0.20	0.51
S	0.36	0.50	0.14
Slow cool			
M	0.58	0.34	0.08
N	0.40	0.15	0.45
R	0.22	0.16	0.62
S	0.33	0.50	0.17

as found in the combinatorial studies. One objective of this chapter is to demonstrate that such a point does exist for bulk samples synthesized in either air or oxygen.

It is important to confirm that the combinatorial results hold up well when synthesis of bulk samples is done in a tank reactor. In this chapter, a few preliminary results obtained by Aaron Rowe will be included in order to discuss how boundaries change for bulk samples, particularly those heated to higher temperatures.

Finally, to determine the impact of the structures on the electrochemistry of the positive electrodes, coin cells of the M, N and R phases were made. These samples were the same quenched bulk samples heated in oxygen used in Chapter 6 to perform Rietveld refinements.

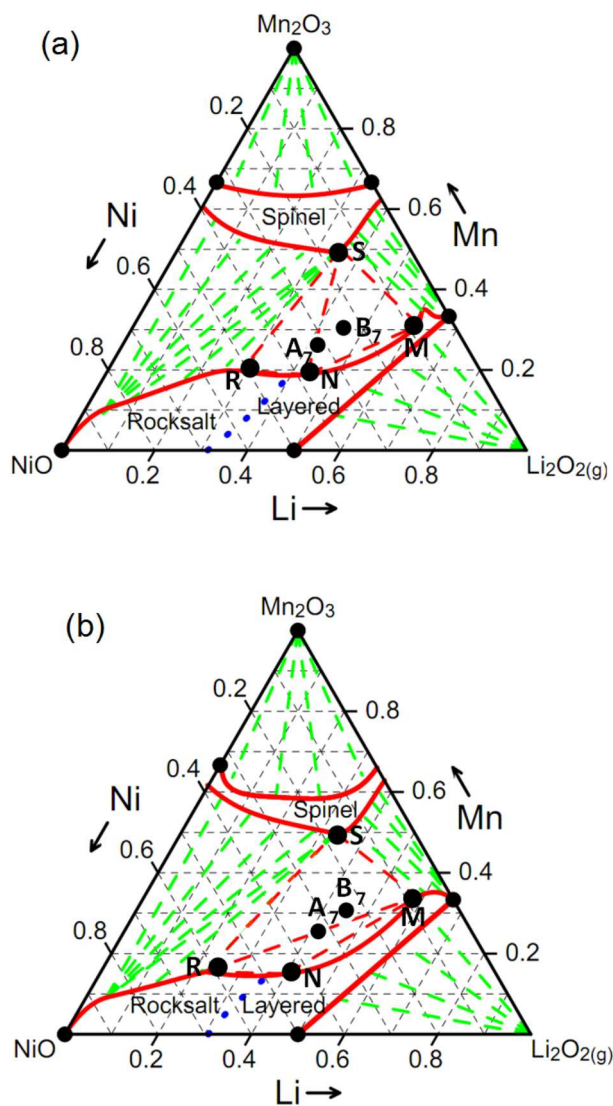


Figure 7.1: The pseudo-ternary phase diagrams obtained for the Li-Ni-Mn-O system for combinatorial samples obtained by quenching (a), and slow cooling (b). Red lines represent boundaries to single-phase regions, green dashed lines are tie-lines, red dashed lines are tie-lines bounding three-phase regions and the blue dotted line is the phase transition between cubic and layered rocksalt structures. There is a red tie-line joining R and N, however the two-phase region is so small that it cannot be distinguished from the layered boundary on the scale shown here. Points S, M, N and R refer to the corners of the 3-phase regions and move with synthesis conditions. Points  $A_7$  and  $B_7$  are two compositions referred to in the text.

## 7.2 Experimental Design

Bulk samples M, N, R, A<sub>7</sub>, A<sub>7</sub>' and B<sub>7</sub> were made using the one-pot synthesis approach described in Section 2.1.2. Sample A<sub>7</sub>' is not shown in Figure 7.1 as it is very near to A<sub>7</sub>, only a little closer to the nickel corner. The M, N and R materials were heated in oxygen to 800°C for 5 h before quenching. Coin cells were made with these materials as outlined in Section 2.5. Cells were cycled at a rate of 10 mA/g. The first two cycles were over the range 2.5 - 4.6 V, followed by ten cycles from 2 to 5 V. Finally the M material was tested for long-term cycling after the twelve preliminary cycles mentioned here. The long-term cycling was performed over the range 2 - 4.8 V.

The A<sub>7</sub>, A<sub>7</sub>' and B<sub>7</sub> samples were heated under various conditions discussed in the results section and characterized with XRD using the JD-2000 diffractometer.

Bulk samples C<sub>7</sub> - G<sub>7</sub> were made by the tank reactor method (Section 2.1.2) and characterized with XRD by Aaron Rowe. These samples were heated to either 800 or 900°C for 12 hours in air and then either quenched or regular cooled. The XRD scattering from these samples was then measured in either the JD-2000 or the D-5000 diffractometers.

## 7.3 Structural Results

Figure 7.2 shows X-ray diffraction (XRD) scans from bulk samples made at the composition A<sub>7</sub> given in Table 7.1 and shown in Figure 7.1. These scans demonstrate that the four-phase transformation does occur. Here, the progression of the phase transformation can be seen in the area of the R peak near 43.6° which grows steadily from scan (a) towards scan (e). The quenched samples, (a) and (b), show how rapidly the R phase grows with a significant amount present when quenched on a steel plate and none when liquid nitrogen was used. This rapid growth is consistent with the SEM images from the previous chapter showing a small number of large cubic crystallites in a sample containing the N, M and R phases. Scan (f) in Figure 7.2 shows that N replaced R when the slow cooled sample was re-heated and quenched; consistent with the transformation being reversed when heated back to high temperature. However, there were still remnants of the R phase here suggesting that some lithium

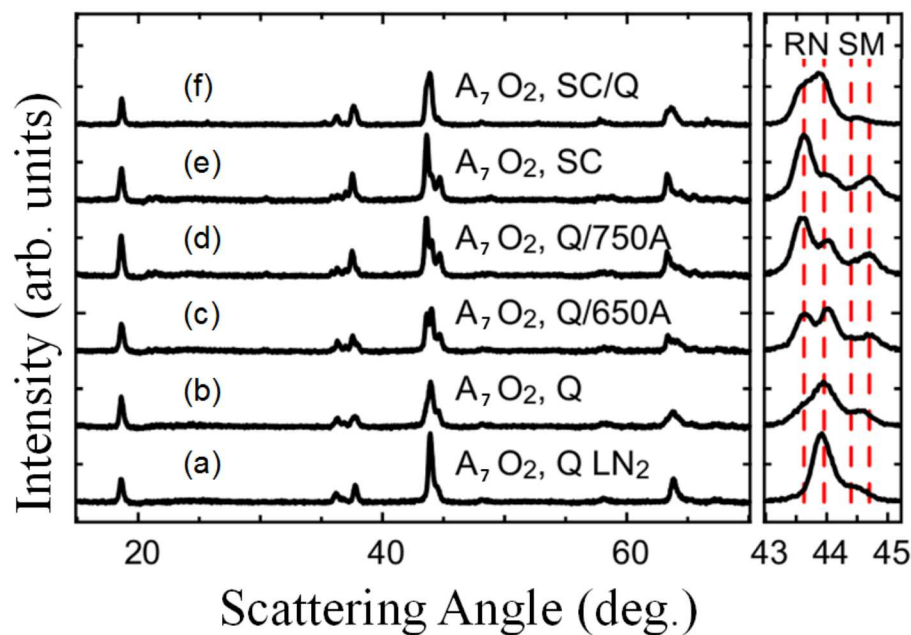


Figure 7.2: XRD patterns obtained for bulk sample  $A_7$  in the Li-Mn-Ni oxide system heated to  $800^\circ\text{C}$ . Composition  $A_7$  is indicated in Figure 7.1. The right frame focuses on the XRD peaks near  $44^\circ$  where the four phases have one peak each. The red dashed lines represent the positions of the N, R, S and M peaks when slow cooled after heating in oxygen. SC denotes samples slow cooled at  $1^\circ\text{C}/\text{min}$ , Q stands for quenching on steel while Q LN2 refers to quenching in liquid nitrogen, and SC/Q indicates a slow cooled sample that was reheated to  $800^\circ\text{C}$  and quenched. Q/650A and Q/750A were quenched samples that were annealed at  $650^\circ\text{C}$  and  $750^\circ\text{C}$  respectively for 5 h before quenching back to room temperature.

had been lost during the extended heating, moving point  $A_7$  away from the lithium corner and into the RNS three-phase region or, once again, quenching on steel was not fast enough to prevent phase transformations entirely.

Figure 7.3 shows XRD scans of bulk samples at two compositions,  $A_7'$  and  $B_7$ , given in Table 7.1 and  $B_7$  is also shown in Figure 7.1. In oxygen, the quenched bulk sample at  $A_7'$  (Figure 7.3) appears to be made up of the N phase only (though there may be traces of the S phase as well). This scan of a bulk sample quenched in oxygen suggests that the layered boundary has moved upwards compared to that seen in the combinatorial samples such that  $A_7'$  lies near to the layered boundary. Upon slow cooling in oxygen, however, at least three phases are present in the bulk

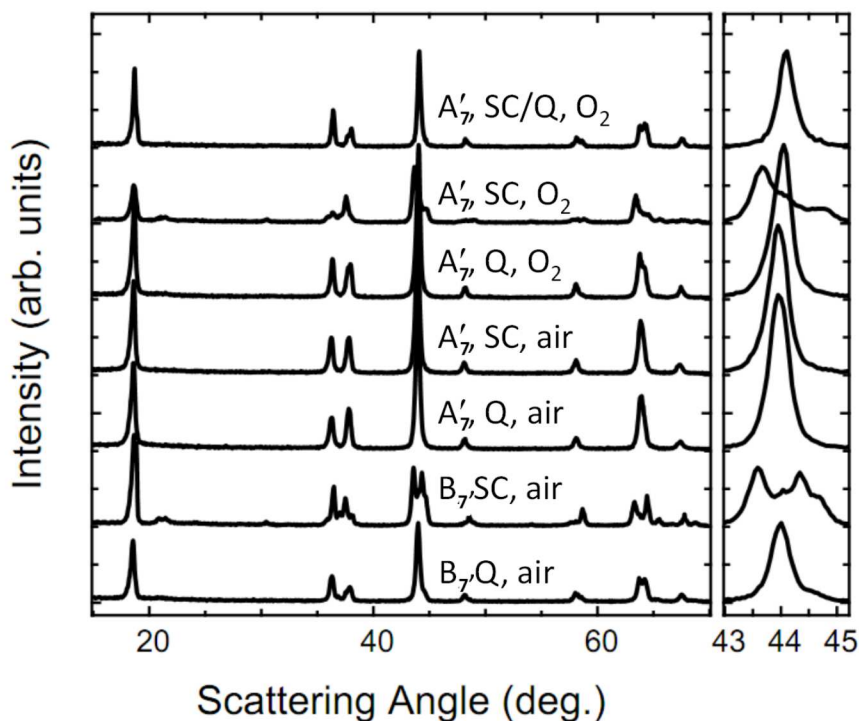


Figure 7.3: XRD scans of samples made at compositions  $A_7'$  and  $B_7$ , indicated in Table 7.1. An expanded view of the peaks near  $44^\circ$  is included in the right panel. Q indicates quenched while SC refers to slow cooling ( $1^\circ\text{C}/\text{min}$ ) and SC/Q denotes a slow cooled sample after being re-heated to  $800^\circ\text{C}$  and quenched.

sample at  $A_7'$  consistent with the expected R, N and M phases. This behaviour is consistent with the boundary moving down during slow cooling such that the sample is now in the RMN three-phase region shown in Figure 7.1. The sample that was then re-heated and quenched shows that this phase change was completely reversible demonstrating that the layered boundary moved back up upon heating. Bulk samples of  $A_7$  and  $A_7'$  together therefore show that the four-phase equilibrium exists and the transformations during cooling are reversible.

By contrast, both scans of sample  $A_7'$  obtained in air appeared to consist of a single phase in Figure 7.3. This is consistent with the boundary having moved even higher in air. To confirm that the co-existence regions do exist in air, quenched and slow-cooled bulk samples at composition  $B_7$  were prepared. Figure 7.3 shows that the quenched sample shows at least two phases (N and M with perhaps S causing an asymmetry in the N peak) consistent with the NMS triangle expected for quenched samples.

Upon slow cooling, the XRD scan showed that conversion towards R, S and M was taking place but some N phase remained implying that equilibrium was not reached and four peaks were seen in the XRD pattern. These few bulk samples show that although the boundaries move quite dramatically depending on synthesis conditions, the phase diagram shows the same features as those seen in the combinatorial studies. Hence, the current study should help considerably in interpreting data collected under various synthesis conditions.

Figure 7.4 shows preliminary results obtained for the tank reactor bulk samples made in air at 800°C along with the boundaries obtained in oxygen in the combinatorial studies. These results are included here to show how the layered boundary moves upwards as oxygen partial pressure decreases, particularly for quenched samples. The behaviour near the Li-Mn line (where a sharp bump was obtained in oxygen) will be discussed in detail in the next chapter. Again the boundary was found to move downwards during slow cooling consistent with oxygen content increasing in the samples thereby favouring the spinel phases.

Figure 7.5 shows the results for bulk samples in the Li-Mn-Ni-O system heated to 900°C in air. These conditions are similar to those used in commercial synthesis of positive electrodes. The phase diagram is similar to that obtained with the combinatorial samples in oxygen though the solid-solution boundaries shift with the decrease in oxygen partial pressure and increase in temperature. The XRD patterns in the range 43-46° show the phase transformations taking place during cooling. Samples C<sub>7</sub> - G<sub>7</sub> were all single-phase when quenched while samples C<sub>7</sub> - F<sub>7</sub> showed multiple phases when cooled more slowly. Sample E<sub>7</sub> showed four phases when regular cooled, again suggesting that conversion to the three new phases did not reach completion so that equilibrium was not reached at intermediate cooling rates. The two peaks seen in the quenched C<sub>7</sub> and D<sub>7</sub> samples correspond to the  $K\alpha_{1,2}$  splitting visible due to large crystallites giving sharp peaks and do not indicate phase separation. The XRD results were used to create the approximate boundaries shown in Figure 7.5. The upward movement of the layered boundary with temperature can be attributed to the reaction equilibrium favouring the layered phase over the spinel phase that contains more oxygen per metal atom. This again occurs as the high entropy of the

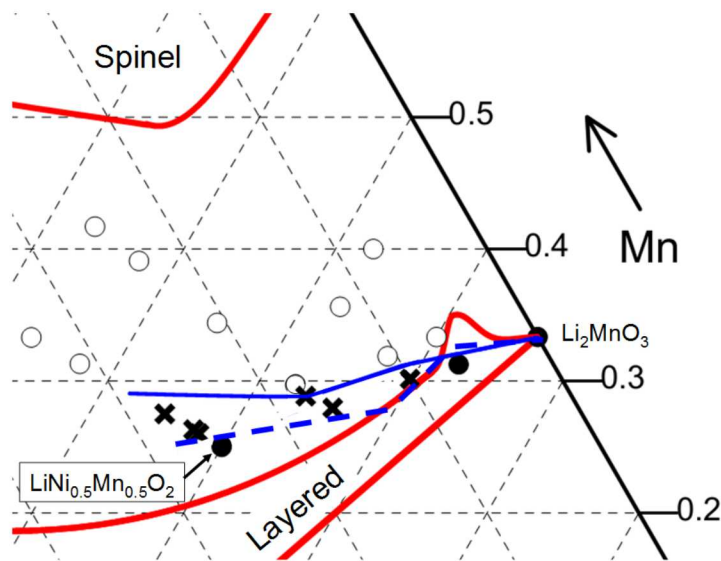


Figure 7.4: The single-phase boundaries obtained in this study for quenched combinatorial samples heated in oxygen (solid red lines). The points were obtained by visual inspection of XRD scans of bulk samples synthesized in air; the open circles represent multi-phase samples for both quenched and regular cooled conditions, the closed circles are single-phase for both, and the x symbols correspond to single-phase quenched samples that phase separate during regular cooling. The blue solid line is a rough estimate of the boundary in air for quenched samples based on these data points, while the blue dashed line is for regular cooling. Further work to completely determine the phase boundaries in air is currently being done by Aaron Rowe.

oxygen gas wins out at elevated temperatures. The improved performance of the Li-rich materials synthesized at high temperature [3, 87] may therefore simply be due to the samples remaining single-phase thereby avoiding the layered-layered co-existence region. This will be examined in detail in Chapter 9.

Furthermore, the layered region extends quite low in the Gibbs triangle compared to solid-solutions known prior to this thesis (Figure 1.8(b) in the introduction). This implies that some published results must be re-examined. For example, a sample reported by Ohzuku et al. [53] (blue point in Figure 7.5) had a very high capacity and is reported as being  $\text{LiNi}_{0.5}\text{Mn}_{0.5}\text{O}_2$  which is very near point  $G_7$ . However, the contour plots were used along with the published lattice parameter values of  $a = 2.883 \text{ \AA}$  and  $c = 14.269 \text{ \AA}$  to position this sample on the phase diagram in Figure 7.5. This result suggests that the sample lost very little of the 25% excess lithium used



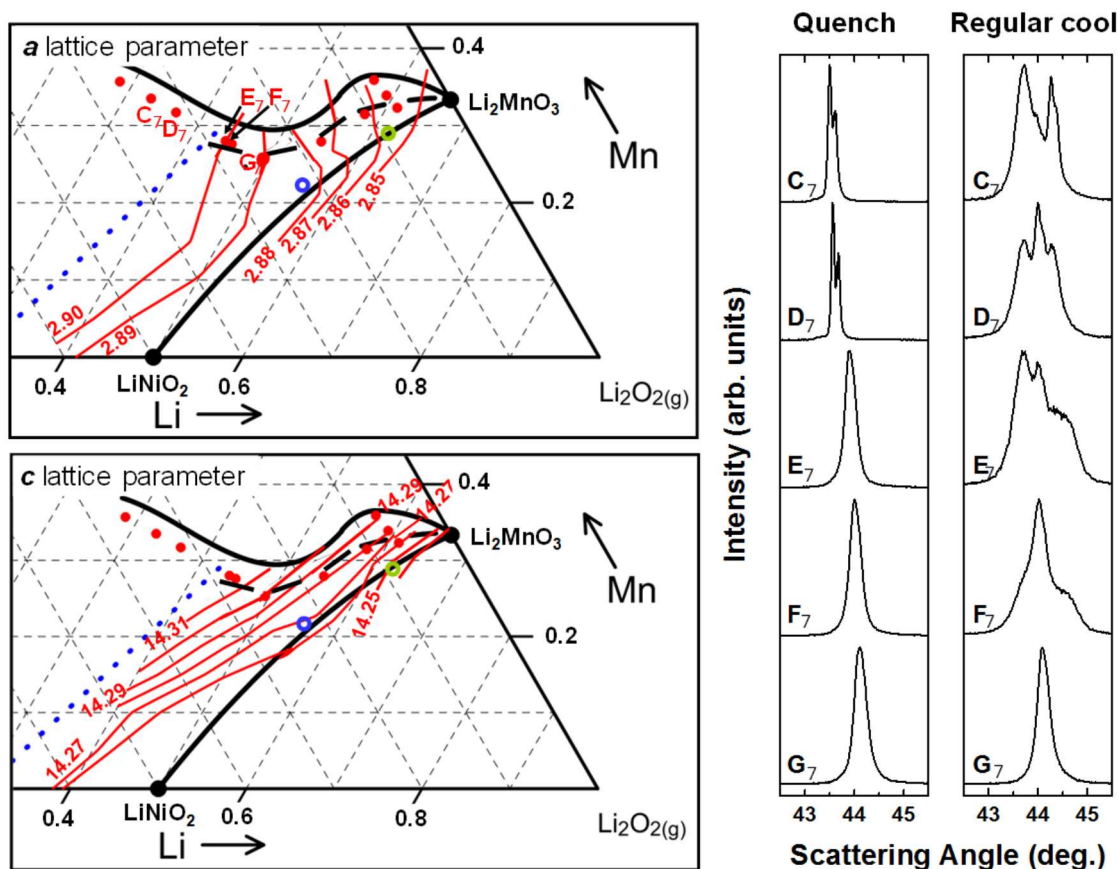


Figure 7.5: A partial Li-Mn-Ni oxide phase diagram for bulk samples synthesized in air at 900°C. The thick solid black lines are estimates to the boundaries of the layered region when quenched, the dashed black line is the upper boundary when slow cooled, and the blue dotted line is the cubic to layered phase transition. The contour plots shown as thin red lines for the lattice parameters were obtained using both combinatorial samples (not shown, from Chapter 6) and bulk samples (red points); all plotted compositions were determined by elemental analysis (with an uncertainty of about 0.02 in molar fraction).

during synthesis such that the material was in fact a lithium-rich layered material and thus its improved electrochemistry over other published  $\text{LiNi}_{0.5}\text{Mn}_{0.5}\text{O}_2$  samples can be attributed to the extra lithium after nickel oxidation. Similarly, the open green symbol in Figure 7.5 represents a sample from Ref. [52] that was reported to lie on the Li-rich line joining  $\text{Li}_2\text{MnO}_3$  to  $\text{LiNi}_{0.5}\text{Mn}_{0.5}\text{O}_2$ . This point was positioned using the published lattice parameter,  $a = 2.860 \text{ \AA}$  and  $c = 14.246 \text{ \AA}$ , again suggesting that it too was below the Li-rich line such that not all of the 5% excess lithium was

lost during synthesis. These two points were used to sketch the curved line joining  $\text{LiNiO}_2$  to  $\text{Li}_2\text{MnO}_3$ . The electrochemistry of single-phase layered materials below the lithium-rich layered line must be carefully studied and elemental analysis is required to confirm final compositions of samples in this region of the Gibbs triangle.

#### 7.4 Electrochemistry of the R, M and N Phases

Figure 7.6 shows the electrochemical data obtained for the three new materials: N, M and R made using the one-pot synthesis approach and heated to  $800^\circ\text{C}$  in oxygen for 5 h before being quenched. The only material with promising electrochemical properties was the M-layered phase. This is not surprising since the XRD patterns in Chapter 6 showed this material to be a highly ordered lithium-rich material. While some of the lithium was removed by oxidizing the nickel from 2+ to 4+ up to 4.45 V [3], the remaining lithium was removed at about 4.5 V via the high voltage plateau discussed in the introduction. This plateau has long been thought to involve lithium being removed along with oxygen gas via the so-called oxygen release process [3, 18]. This process would leave the oxidation states of the transition metals unchanged such that the manganese could then be reduced from its initial 4+ state during the next discharge, thereby activating it. More recently, Koga et al. [16] and Sathiya et al. [17] have demonstrated oxygen participation in the redox process in some lithium-rich oxides; a process that is accompanied with a phase transformation. Koga demonstrated that Li-Co-Mn-Ni-O layered materials with excess lithium convert to a two-phase material after the high voltage plateau, and this was attributed to the shell of particles losing oxygen while the core did not, such that much of the high voltage plateau can be attributed to oxygen redox in the core of the particles. Fell et al. [88] recently found this two-phase behaviour in  $\text{Li}_{1.2}\text{Ni}_{0.2}\text{Mn}_{0.6}\text{O}_2$  and used Rietveld refinement to determine that one of the phases was oxygen deficient while the other was not. At this moment, it is therefore unclear how much oxygen is lost and how much oxygen redox takes place in the M material discussed here during the high voltage plateau and remains an important question to answer. Regardless of the on-going debate about the nature of the high-voltage plateau, both the nickel redox and the high voltage plateau can be seen as peaks in the  $dQ/dV$  curve during the first charge of the

M material in Figure 7.6 The new peak appearing at 3.1 V in the second cycle was consistent with manganese redox. After the cycles shown in Figure 7.6, the M phase was tested between 2 - 4.8 V to test its long-term cycling performance. The long-term cycling capacities were 245.0 mAh/g during charge and 236.5 mAh/g during discharge initially, and 244.2 mAh/g and 237.4 mAh/g respectively 40 cycles later, demonstrating stable cycling.

By contrast to the highly ordered M-layered phase, the N-layered structure has a disordered lithium layer with 30 % nickel occupation that apparently prevents some lithium from diffusing out of the material since only 50 % of the 201 mAh/g total theoretical capacity was obtained during the first charge shown in Figure 7.6. The capacity also faded rapidly such that this material is not attractive for Li-ion batteries. The cubic rocksalt phase, R, did have some ordering of lithium, manganese and metal site vacancies on the cubic lattice as discussed in Chapters 5 and 6. Nonetheless, a capacity of only 20 mAh/g was achieved on first charge even though the theoretical capacity was 138 mAh/g, demonstrating that most lithium diffusion paths were blocked or severely hindered.

A consequence of the poor performance of the N and R phases is that synthesis conditions and compositions that give rise to these phases must be avoided. This limits the region of interest for layered-spinel composite electrodes to the area to the right of the M-S line in Figure 7.1 (b), with the M-S line being of particular interest since both the M and S phases are decent electrode materials. Furthermore, since the R phase appears in both three-phase regions during slow cooling, the effect of quenching on composite electrodes must be studied. The knowledge gained about the phase diagram also affects core-shell materials [89], where understanding the equilibrium phases is necessary to determine whether or not ion mobility at a given temperature is sufficient to destroy the desired core-shell structure.

The poor performance of the N-phase also impacts the so-called layered-layered nano-composites that have long been searched for along the Li-rich layered line with inconclusive results [45, 47]. The phase diagram suggests that samples showing this short range phase separation should appear elsewhere in the triangle, namely in the

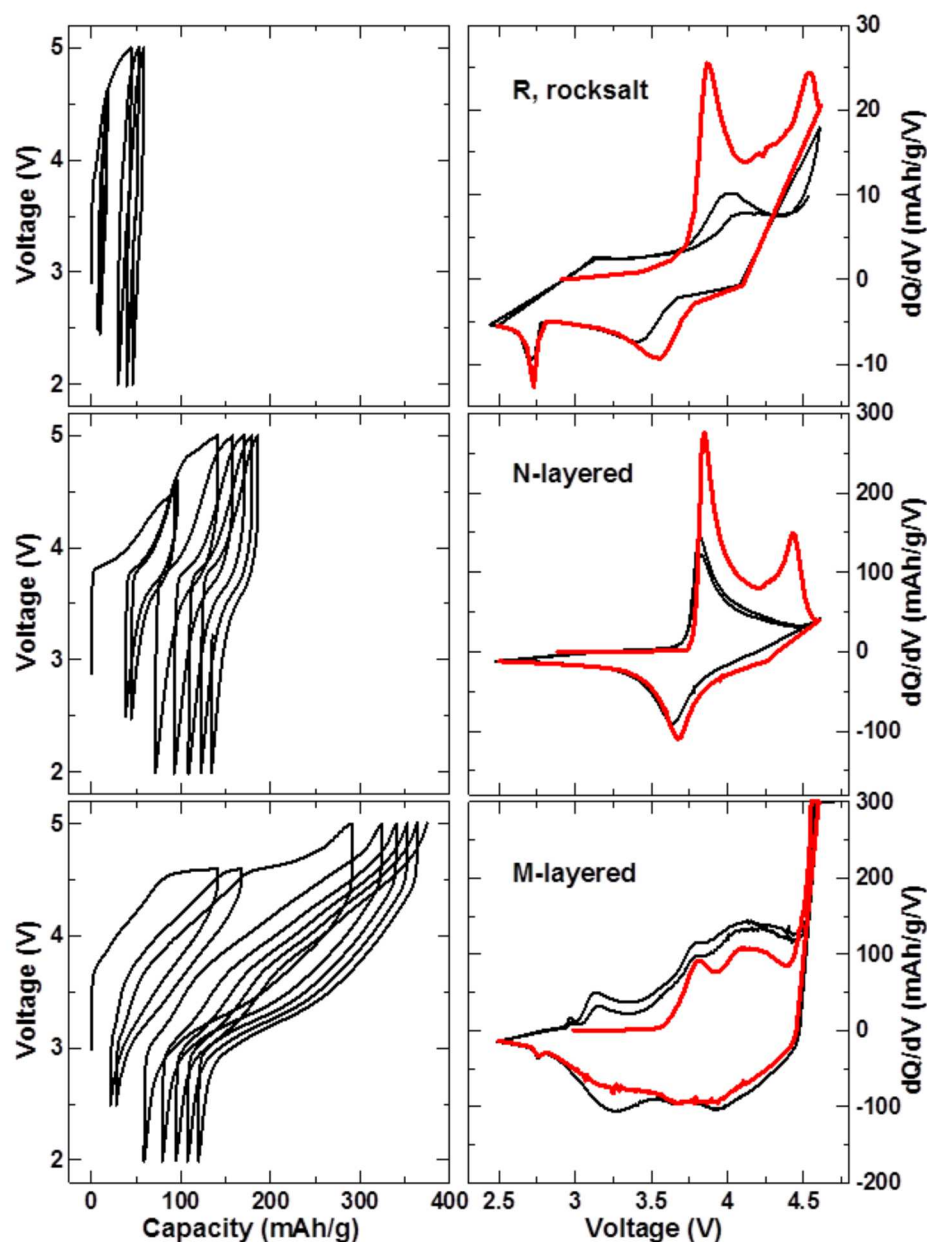


Figure 7.6: Electrochemical data of half-cells made from the M, N and R materials obtained by heating in oxygen at 800°C and quenching to room temperature. The cells were first cycled between 2.5 - 4.6 V for 2 cycles (shown in all panels, with the first cycle shown as a thick red line in the  $dQ/dV$  plots), then between 2 - 5 V for ten cycles (for clarity, only a few of these are included in the voltage versus capacity plots). All measurements were performed at a constant specific current of 10 mA/g such that the M-layered material was cycled at a rate of approximately  $C/24$  (i.e. 24 hours to charge or discharge).

region directly above point  $G_7$  in Figure 7.5. During slow cooling, the upper boundary of the layered region moves downwards. This implies that the layered-layered region also moves downwards as the M and N points move. A sample made near the composition of  $\text{LiNi}_{0.5}\text{Mn}_{0.5}\text{O}_2$  (point  $G_7$ ) would be single-phase if quenched from high temperature and would transform towards a layered-layered composite when regular cooled. The endpoints of the phase separation would lie along the boundary between N and M. Since the N phase contains a large amount of nickel on the lithium layer, the formation of nano-composites in this composition space would involve the clustering of nickel on the lithium layer which could interfere with lithium diffusion. This well-known composition,  $\text{LiNi}_{0.5}\text{Mn}_{0.5}\text{O}_2$ , therefore warrants further study and will be discussed from this new point of view in Chapter 9.

## 7.5 Conclusions Based on Bulk Li-Mn-Ni-O Samples

The key features in the Li-Mn-Ni-O pseudo-ternary phase diagrams, as determined using combinatorial samples, were confirmed with bulk samples synthesized under various conditions via two different synthesis routes. The four-phase equilibrium was observed and transformations were found to be reversible, thereby confirming that two-three phase regions exist and transform during slow cooling. The primary importance of this work is a better understanding of how the phase boundaries and co-existence regions transform when cooled at rates typically used commercially. It is also important to recognize that a small amount of transformation occurred even for samples quenched on a copper or steel plate. These changes cannot be avoided entirely without quenching in liquid nitrogen or avoiding the compositions where the transformations occur. Understanding the phase diagrams should have a significant impact on research focused on composite electrodes in the Li-Mn-Ni-O system since this work identified the compositions and conditions required to obtain layered-layered nano-composites and layered-spinel composites.

The lattice parameter contour plots developed here also showed that some samples made with excess lithium retain most of the excess even after heating to high temperatures. Elemental analysis on a sample in the layered region is therefore mandatory in order to be confident of the composition of the final product.

## Chapter 8

### Layered Materials with Metal Site Vacancies

Data in this chapter are reprinted from Ref. [90] with permission from the American Chemical Society.

#### 8.1 Motivation for the Study of Samples near $\text{Li}_2\text{MnO}_3$

In the Li-Mn-Ni-O system, studies of the lithium-rich layered materials have generally been limited to the composition line between  $\text{Li}_2\text{MnO}_3$  and  $\text{LiNi}_{0.5}\text{Mn}_{0.5}\text{O}_2$  (referred to here as “stoichiometric lithium-rich”) where reversible cycling above 250 mAh/g has been achieved [3, 4, 44]. These materials take the O3-type structure with lithium layers containing a small amount of nickel, and transition metal (TM) layers being made up of manganese, nickel and some lithium. The oxidation states of nickel and manganese are typically 2+ and 4+ in these structures [91]. In the previous chapters, it was found that the solid-solution layered structures can be made with either more or less lithium than the stoichiometric lithium rich line.

Figure 8.1 shows the phase diagram obtained by quenching combinatorial samples in oxygen. Also shown are composition lines obtained by keeping nickel and manganese oxidation numbers constant. This diagram shows that all spinel samples are consistent with  $\text{Ni}^{2+}$  and  $\text{Mn}^{3,4+}$ . The rocksalt/layered lines show that the majority of samples in this region have  $\text{Mn}^{4+}$  with  $\text{Ni}^{2,3+}$ . That excess lithium can be added to the stoichiometric lithium-rich materials while keeping the structures single-phase has been well known for some time and has been used extensively to make high capacity materials [52, 53]. These structures can be understood as being identical to the usual Li-rich materials with some of the nickel oxidized to 3+ during synthesis; which is quite feasible given that  $\text{LiNiO}_2$  can be made under the same conditions. However, there are two exceptions in Figure 8.2 where layered materials cannot be made without reducing some manganese to 3+ or having metal site vacancies: the

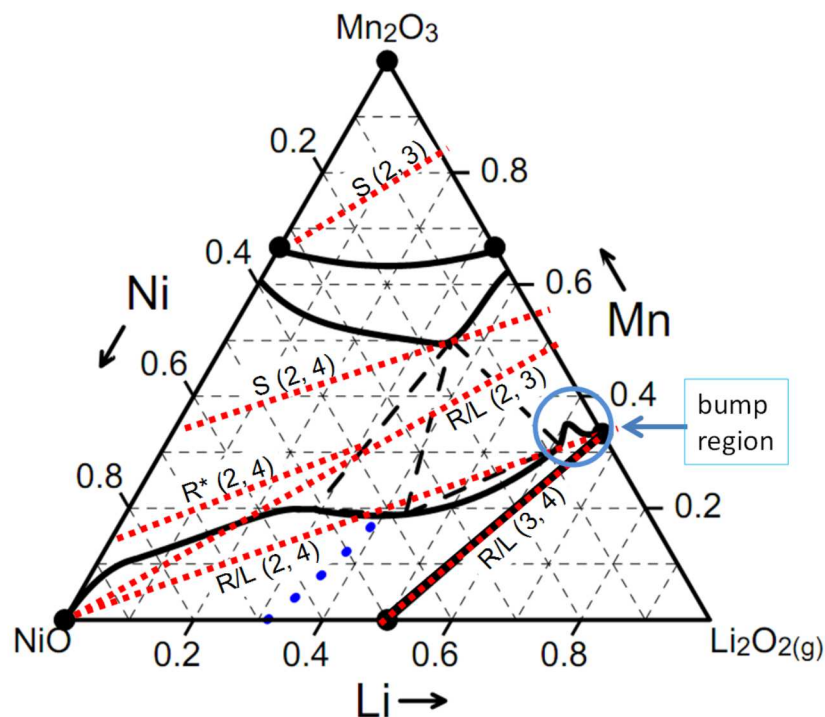


Figure 8.1: The phase diagram obtained in oxygen by quenching. The red dotted lines represent constant oxidation number lines, S refers to spinel compositions  $\text{Li}_x\text{Mn}_y\text{Ni}_{3-x-y}\text{O}_4$ , R/L denotes rocksalt or layered structures  $\text{Li}_x\text{Mn}_y\text{Ni}_{2-x-y}\text{O}_2$  and R\* denotes ordered rocksalt structures with unoccupied 4b sites. The coordinates used to label the lines are: (Ni oxidation number, Mn oxidation number).

“bump” region near the Li-Mn line (to be discussed here) and the top of the ordered rocksalt region. Structures in the ordered rocksalt region have already been shown to contain metal site vacancies which allow a higher manganese oxidation state (perhaps even keeping it in the 4+ state), as discussed in Chapters 5 and 6. However, for the bump region, the ambiguity remains: there may be metal site vacancies and/or some manganese reduced to 3+. This ambiguity requires further study and will be resolved in this chapter.

Figure 8.2 shows an approximate phase diagram of samples made in air at  $900^\circ\text{C}$  and then quenched, included in the previous chapter. Again, in the combinatorial studies, the single-phase material in the bump region with the most lithium deficiency had the metallic molar composition:  $\text{Li}_{0.6}\text{Mn}_{0.35}\text{Ni}_{0.05}$ . The two models considered

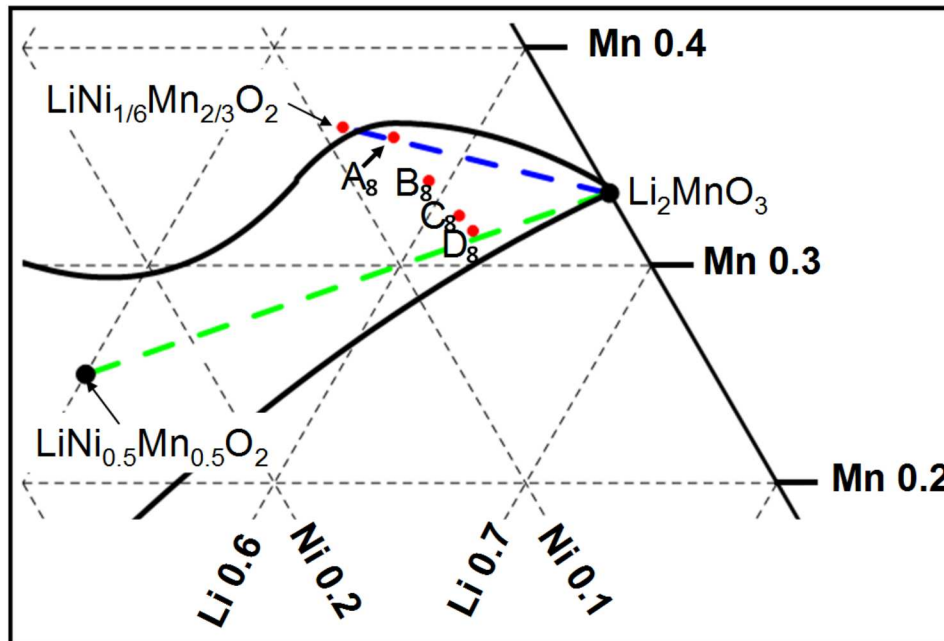


Figure 8.2: A partial phase diagram for bulk samples quenched from 900°C, with compositions indicated for samples discussed throughout this chapter. The black boundaries are estimates to the boundaries of the layered region, while the blue dashed line is the composition line with sufficient vacancies to have  $\text{Ni}^{2+}$ ,  $\text{Mn}^{4+}$  and  $2/3$  of TM filled with  $\text{Mn}^{4+}$  corresponding to the solid-solution series  $\text{Li}[\text{Li}_{1/3-x}\text{Ni}_{x/2}\square_{x/2}\text{Mn}_{2/3}]\text{O}_2$  with  $0 \leq x \leq 1/3$ . The green dashed line is the stoichiometric lithium rich line discussed in the text.

here (metal site vacancies or  $\text{Mn}^{3+}$ ) would predict the following two compositions:  $\text{Li}[\text{Li}_{0.136}\text{Ni}^{2+}_{0.146}\text{Mn}^{3+}_{0.154}\text{Mn}^{4+}_{0.564}]\text{O}_2$  or  $\text{Li}[\text{Li}_{0.057}\text{Ni}^{2+}_{0.136}\square_{0.139}\text{Mn}^{4+}_{0.668}]\text{O}_2$ . The main objective of this chapter is to determine which of these two models is correct. Given that the vacancy model predicts that 6.95 % of the metal sites remain vacant, density measurements as well as redox titrations are accurate enough to distinguish between the two models.

In the combinatorial study, the compositions at which one can expect layered-layered materials to appear were identified. It is of interest that the bump region discussed here never underwent such a phase separation. Instead, the upper section of the bump phase separated into layered-spinel composites with the region near the stoichiometric lithium rich line remaining single phase. To better understand why this is the case, this chapter includes a Monte Carlo simulation of a material in this



bump region. The details of this simulation are given in Section 2.12.

## 8.2 Experimental Design

Samples A<sub>8</sub>-D<sub>8</sub>, indicated in Figure 8.2, were synthesized by Aaron Rowe using the tank reactor method and were heated to 900°C for 12 hours before quenching between copper plates.

Li<sub>2</sub>MnO<sub>3</sub> was made by John Camardese as a reference material for this study by solid state synthesis. Lithium carbonate, with 10 % excess, was mixed with manganese oxyhydroxide (MnOOH, Chemetals) and heated to 1000°C for 48 hours.

A sample of Li[Ni<sub>1/6</sub>□<sub>1/6</sub>Mn<sub>2/3</sub>]O<sub>2</sub> (approximately 2 g) was made using the one-pot synthesis method described in Section 2.1.2. The sample was heated for 5 h in air at 900°C and then quenched by transferring it onto a copper plate.

For samples A<sub>8</sub>-D<sub>8</sub> and Li[Ni<sub>1/6</sub>□<sub>1/6</sub>Mn<sub>2/3</sub>]O<sub>2</sub>, ICP was used as elemental analysis to determine the actual metal molar fractions after heating. The X-ray scattering from all samples was measured in a Siemens D-5000 diffractometer. The resulting scans were then analyzed using Rietveld refinement. The refined value for the occupation of the oxygen sites converged to above 100 % such that it was used to calculate the vacancy content on the metal sites.

The true density of the samples was measured using a helium pycnometer. With values for lattice parameters and elemental analysis, the density of the samples were used to calculate the occupancy of the metal sites directly. This gave sufficiently precise results since the measured sample density was as much as 6.3 % lower than the crystallographic density.

Redox titrations, as described in Section 2.9, were performed in order to determine the average oxidation states of manganese and nickel. Finally, with elemental analysis results, the average oxidation states were used to calculate the vacancy concentrations assuming all oxygen was in the (2-) state.

To confirm the results of the redox titrations, the manganese K-edge XANES spectra of samples A<sub>8</sub>-D<sub>8</sub>, Li<sub>2</sub>MnO<sub>3</sub> and Mn<sub>2</sub>O<sub>3</sub> were collected by Paul Duchesne.

Electrochemical tests were carried out on the Li[Ni<sub>1/6</sub>□<sub>1/6</sub>Mn<sub>2/3</sub>]O<sub>2</sub> sample using a standard 2325 coin cell design as described in Section 2.5.

Finally, the Monte Carlo simulation discussed in Section 2.12 was used to illustrate the structures of interest and to better understand the experimental results. All compositions used in the simulations were consistent with the elemental analysis results, though the calculations assumed no nickel on the lithium layer such that only the transition metal layers needed to be considered. The results from Chapter 4 suggested that  $\beta_T = 1$  corresponds to a temperature where phase separation takes place. This temperature was experimentally determined to be below 800°C for Li-Co-Mn-O materials. In the previous chapter, such transformations were found to occur at or below 750°C in the Li-Ni-Mn-O system at certain compositions. Here, this same Monte Carlo simulation was used to explore the two possible structures at the top of the bump (point A<sub>8</sub> in Figure 8.2) as well as a sample lower in the layered region (point D<sub>8</sub>) in order to better understand why materials in the bump region do not form layered-layered composites.

### 8.3 Monte Carlo Results

Figure 8.3 shows the results of the Monte Carlo simulation for the two possible structures at the composition of the top of the bump: (Li, Mn, Ni) = (0.6, 0.35, 0.05). The two models are: (a) some manganese is in the 3+ state and (b) there are metal site vacancies. For simplicity, the vacancies were all assumed to be on the transition metal layer. However, if some vacancies were on the lithium layer the results of the Monte Carlo simulation would not change significantly since the roles of lithium and vacancies on the transition metal layers appear to be identical. Clearly, the presence of vacancies helps stabilize the structure, with manganese forming 2/3 of the transition metal layer. Without vacancies, manganese (III) had a tendency to cluster suggesting that such a structure would not form a solid solution particularly after slow cooling. The presence of vacancies in the model promoted a solid solution with random occupation of lithium, nickel and vacancies on one  $\sqrt{3} \times \sqrt{3}$  superlattice while only manganese occupied the other two superlattices. This structure suggests that the ordering peaks in the XRD should be sharp for this material. The fact that this composition never phase separated into two layered structures during the Monte Carlo simulation is consistent with experimental results where a sample near

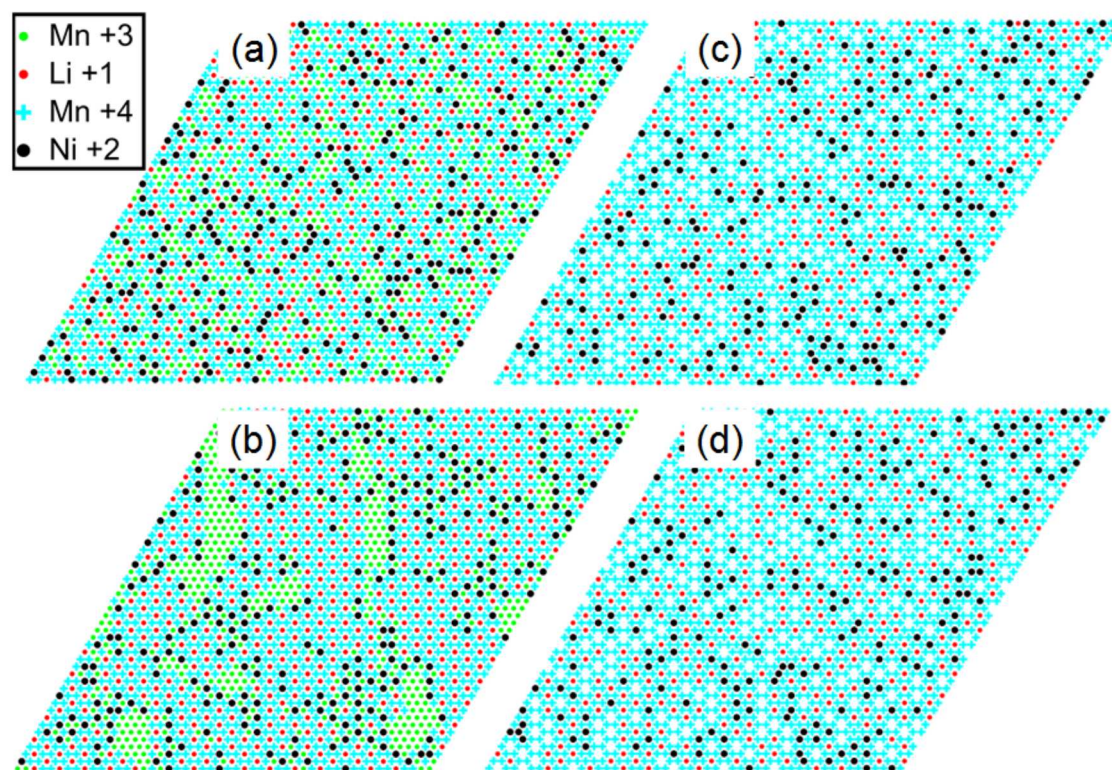


Figure 8.3: Monte Carlo results of sample  $\text{Li}_{0.6}\text{Mn}_{0.35}\text{Ni}_{0.05}$ : the composition at the top of the “bump” from the combinatorial studies, as shown in Figure 8.2. Two possible structures are included: (a-b)  $\text{Mn}^{3+}$  is present and (c-d) metal site vacancies (white areas) exist in sufficient concentrations to maintain  $\text{Mn}^{4+}$ . The diagrams shown were obtained at high temperature with  $\beta_T = 0.5$  for a, c and a temperature 10 times lower with  $\beta_T = 5.0$  in b, d.

the top of the bump phase separated into layered-spinel composites. Since the Monte Carlo simulation does not allow for tetrahedral sites, a transformation involving spinel structures is not possible with the simple model used here.

#### 8.4 Vacancy Measurements

Figure 8.4 shows the XRD patterns obtained for samples  $A_8 - D_8$  and  $\text{Li}_2\text{MnO}_3$  along with fits obtained using Rietveld refinement assuming a layered R-3m structure. For sample  $A_8$ , the difference plot shows significant errors particularly near the (104) peak, so the scan was refined again assuming a monoclinic structure with the C/2m

space group. Figure 8.5 (b) shows this region in more detail and clearly shows that monoclinic distortions have resulted in an asymmetry in the R-3m (104) peak such that a high quality fit can only be obtained using the monoclinic phase. The monoclinic fit yielded  $9.3 \pm 2.5$  % vacancies; the larger uncertainty arising as it becomes difficult to constrain the extra parameters available in the monoclinic fit. Still, this value is consistent with the other vacancy measurements for sample A<sub>8</sub> discussed below. Furthermore, the lattice parameters were  $a = 4.953(1)$  Å,  $b = 8.574(2)$  Å,  $c = 5.050(1)$  Å, and  $\beta = 109.33(2)^\circ$ . The value for  $\beta$  is slightly larger than the value of  $109.1^\circ$  for a hexagonal lattice, thereby confirming that monoclinic distortions existed in this material, they were relatively small and were comparable to that seen in Li<sub>2</sub>MnO<sub>3</sub> [25].

In order to confirm that the highly ordered structure seen in the Monte Carlo simulation is the stable phase found experimentally, the fraction of metal sites which are vacant have been determined for samples A<sub>8</sub>-D<sub>8</sub> three different ways using Rietveld refinement, density measurements, and average metal oxidation state. Table 8.1 shows the results for the elemental analysis while Table 8.2 shows the results for the vacancy fraction measurements. The uncertainty in the density is a statistical error in the mean of multiple values. The only measure of absolute error presented here is the small error of 0.014 g/mL found for Li<sub>2</sub>MnO<sub>3</sub>, which is expected to have no vacancies. The calculated vacancy concentrations for Li<sub>2</sub>MnO<sub>3</sub> show the precision of the methods used with both density measurements and the redox titration giving values very close to 0 % vacancies. For samples A<sub>8</sub>-D<sub>8</sub>, the agreement between the three approaches is generally excellent. The average value of 6.9 % with a standard deviation of 0.07 % for sample A<sub>8</sub> agrees with the expected 6.9 % required to keep all manganese in the 4+ state as discussed in Section 8.1. This helps confirm the structure generated with the Monte Carlo simulation where the 2/3 manganese occupation of sites on the T.M. layer allows for ordering of manganese and the formation of a solid solution on the remaining 1/3 of sites.

The results of the redox titrations show that manganese consistently had an oxidation state of 4+ in these materials. This is in contrast to recent results published by Simonin et al. [49] who report an average manganese oxidation state of 3.75 in

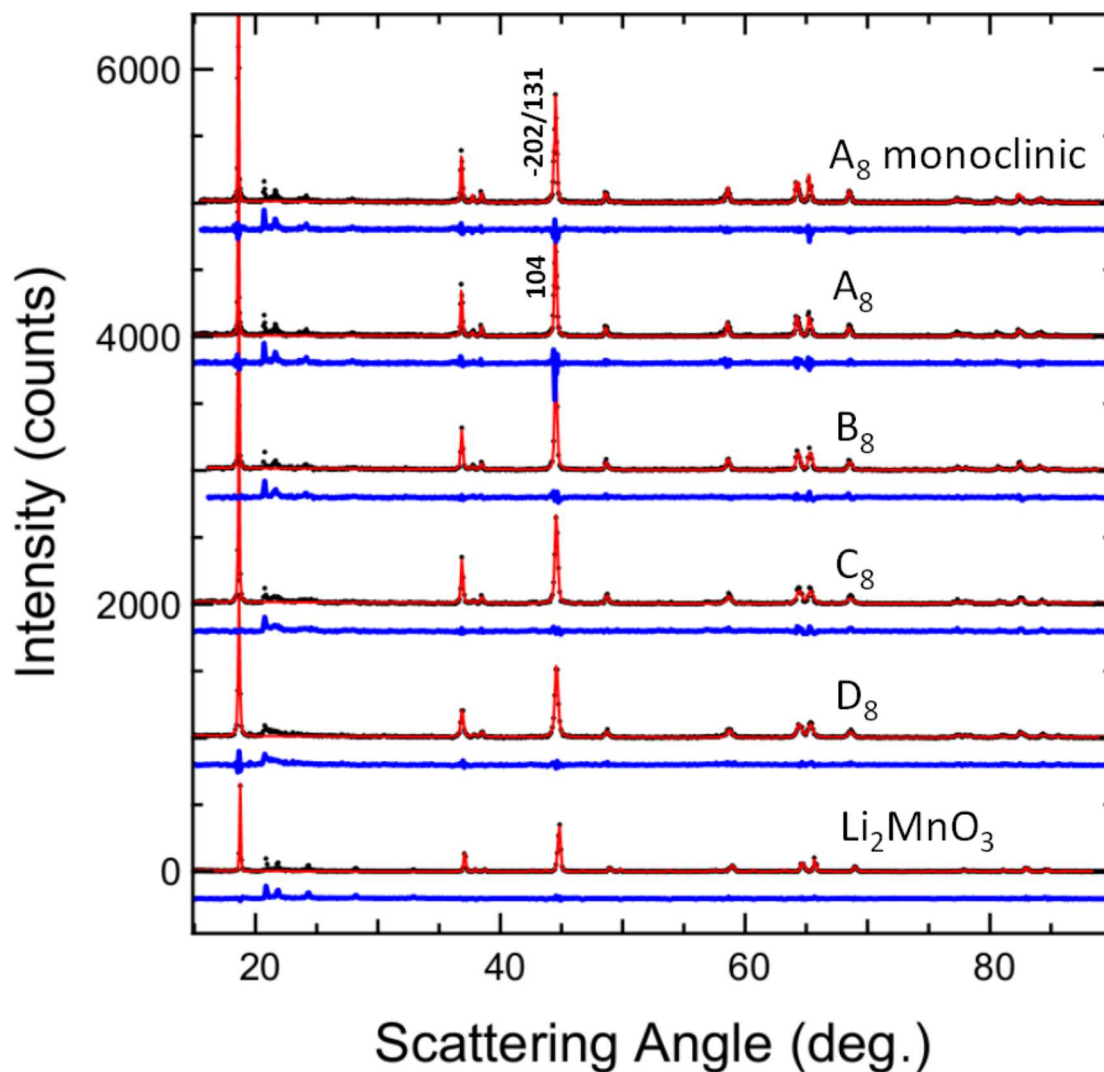


Figure 8.4: XRD scans with fits obtained with Rietveld refinement (red) and difference plots (blue). All are fit as layered, except for the top scan which is fit as  $C/2m$  (monoclinic). Scans are offset vertically for clarity.

a lithium-rich layered oxide. Figure 8.6 shows the Mn K-edge XANES spectra for samples  $A_8$ - $D_8$  as well as  $Mn_2O_3$  and  $Li_2MnO_3$  which were used as references for  $Mn^{3+}$  and  $Mn^{4+}$  respectively. The leading edge for each of the samples  $A_8$ - $D_8$  were extremely close to that of  $Li_2MnO_3$  in relation to  $Mn_2O_3$ . This confirms the results of the redox titration.

Figure 8.5 (a) shows that the superlattice ordering peaks get sharper from sample

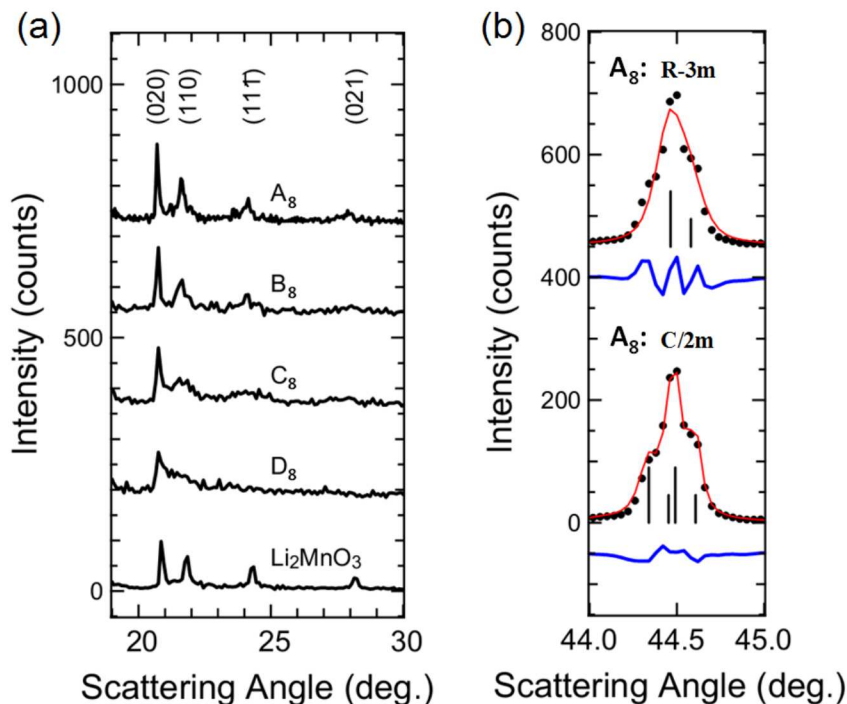


Figure 8.5: (a) XRD patterns in the region where superlattice peaks appear. (b) Peak near  $44.5^\circ$  degrees in sample  $A_8$  fit as both layered (top) and monoclinic (bottom) with scattering angle steps of  $0.02^\circ$ . Vertical lines in R-3m (top) correspond to  $K\alpha_1$  and  $K\alpha_2$  for the (104) peak, and to the (-202) and (131) peaks for C/2m (bottom).

Table 8.1: Metal molar fractions for samples  $A_8$ - $D_8$  and  $\text{Li}_2\text{MnO}_3$  discussed in this chapter. For  $\text{Li}_2\text{MnO}_3$  the expected composition is shown, while for  $A_8$ - $D_8$  the actual compositions obtained by elemental analysis are shown.

Sample	Li	Mn	Ni
$A_8$	0.568	0.359	0.073
$B_8$	0.592	0.339	0.069
$C_8$	0.612	0.323	0.065
$D_8$	0.621	0.316	0.063
$\text{Li}_2\text{MnO}_3$	0.666	0.333	0

$D_8$  to  $A_8$  (i.e. compositions moving upwards in the bump region). The superlattice peaks of sample  $A_8$  were, in fact, as sharp as those of  $\text{Li}_2\text{MnO}_3$  even though the latter was heated for far longer at a higher temperature. The superlattice peaks therefore support the claim that the vacancies allow for ordering of manganese on

Table 8.2: Results for Rietveld refinement, pycnometry, and redox titrations.

Property	A <sub>8</sub>	B <sub>8</sub>	C <sub>8</sub>	D <sub>8</sub>	Li <sub>2</sub> MnO <sub>3</sub> <sup>†</sup>
XRD					
<i>a</i> (Å)	2.8582(1)	2.8558(2)	2.8542(2)	2.8536(2)	<i>a</i> = 4.9318(3)
<i>c</i> (Å)	14.298(1)	14.283(2)	14.255(3)	14.253(3)	<i>b</i> = 8.5375(5) <i>c</i> = 5.0299(3) <i>β</i> = 109.32(1) <sup>°</sup>
Ni <sub>Li</sub> (%)	3.1(3)	2.1(2)	2.3(2)	2.7(2)	—
vacancies (%)	6.9(1.8)	8.1(1.3)	2.7(1.3)	1.0(1.5)	—
Pycnometry					
density (g/mL)	4.138(14)	4.089(9)	4.0884(12)	4.051(7)	3.868(7)
vacancies (%)	7.0(5)	5.2(4)	2.2(5)	2.0(5)	0.6(3)
Redox titration					
Mn	3.99(1)	3.98(1)	4.00	4.00	3.99(1)
Ni*	2.00	2.00	2.05(5)	2.20(5)	—
vacancies (%)	6.82(16)	3.81(16)	1.83(15)	1.17(15)	0.17(17)

\* The average nickel oxidation state was assumed to be 2.0 unless the manganese value was measured to be greater than 4.0. In the later case, the manganese oxidation state was assumed to be 4.0 with the nickel state > 2.0.

† The Li<sub>2</sub>MnO<sub>3</sub> XRD scan was fit as monoclinic, ignoring peaks between 20-33° and the crystallographic density assuming no vacancies is 3.882 g/mL.

2/3 of the TM layer. For samples B<sub>8</sub>-D<sub>8</sub>, the vacancy fraction diminishes as lithium content increased but it never reached zero. Even sample D<sub>8</sub>, which was on the stoichiometric lithium-rich line, had at least 1% of the metal sites vacant.

It is also important to recognize that although the data provided here clearly demonstrates the existence of the metal site vacancies, the data here cannot be used to determine the locations of the vacancies. For example, the Rietveld refinement performed on the XRD scattering from sample A<sub>8</sub> resulted in quality factor values of  $R_B = 3.74\%$ ,  $R_P = 19.00\%$ ,  $R_{WP} = 5.31\%$  assuming vacancies were spread evenly between the lithium and TM layers, while  $R_B = 3.78\%$ ,  $R_P = 19.02\%$ ,  $R_{WP} = 5.33\%$  was obtained if vacancies were assumed to be on TM layers only. This small change in goodness of fit factors implies that X-ray diffraction cannot easily distinguish between a vacancy and a lithium atom. In fact, all experimental data here can only establish the average metal site occupations and not the locations of the vacancies, such that

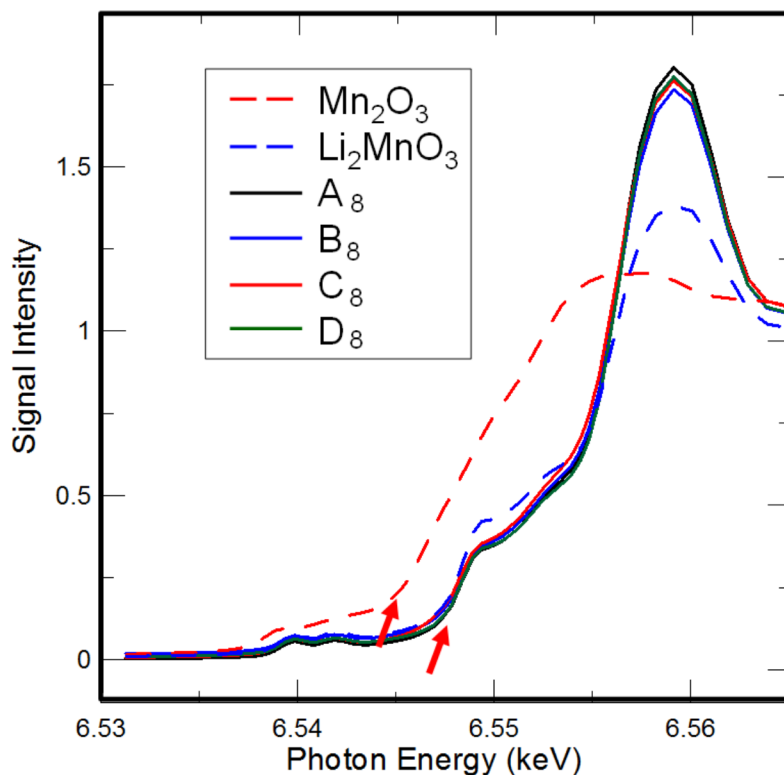


Figure 8.6: Mn K-edge XANES patterns collected for samples showing metal site vacancies, along with  $\text{Mn}_2\text{O}_3$  as a reference for  $\text{Mn}^{3+}$ , and  $\text{Li}_2\text{MnO}_3$  for  $\text{Mn}^{4+}$ . The red arrows indicate the positions of the absorption edge near 6.545 keV for  $\text{Mn}_2\text{O}_3$  and 6.548 keV for all other samples.

studies that are sensitive to lithium atoms, such as neutron scattering, are warranted in order to determine whether or not the vacancies are limited to the transition metal layer.

The local structure of sample  $\text{D}_8$ , which lies on the stoichiometric lithium-rich line, must now be reconsidered. Up to now, it has been assumed that structures on this composition line have  $\text{Ni}^{2+}$  and  $\text{Mn}^{4+}$  only. However, Table 8.2 shows that this is not the case: there is some  $\text{Ni}^{3+}$  as well as about 1% of the metal sites vacant. Figure 8.7 shows the results of a Monte Carlo simulation with the following composition on the TM layer:  $\text{Li}^{+}_{0.227}\text{Ni}^{2+}_{0.100}\square_{0.023}\text{Ni}^{3+}_{0.025}\text{Mn}^{4+}_{0.625}$ . At high temperatures ( $\beta_T = 0.5$ ), the simulation gave a structure very similar to that seen in Figure 8.3 with manganese occupying two superlattices; however, here  $\text{Ni}^{3+}$  substituted for manganese on these



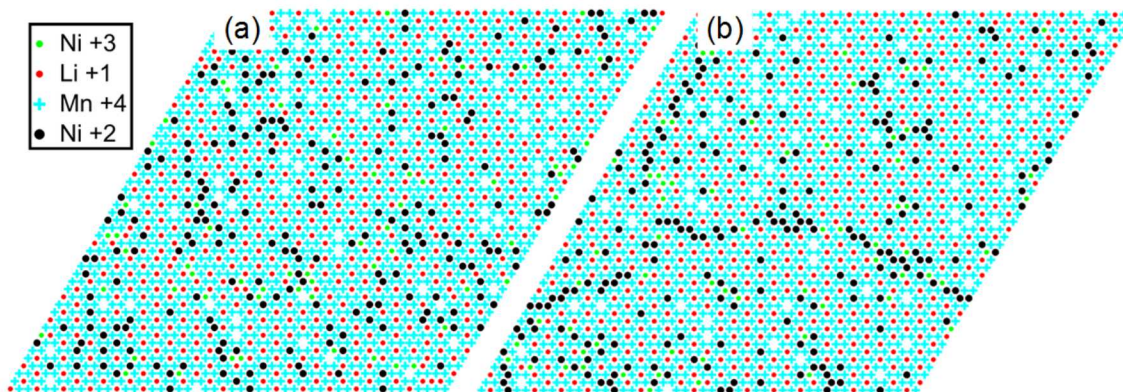


Figure 8.7: Results of a Monte Carlo simulation for sample  $D_8$  using the vacancy content and average nickel oxidation state from Table 8.1. The structures were obtained with  $\beta_T = 0.5$  (a) and  $\beta_T = 2.0$  (b).

sites. Together  $Mn^{4+}$  and  $Ni^{3+}$  occupy 65% of the TM layer thereby allowing them to very nearly occupy two  $\sqrt{3} \times \sqrt{3}$  lattices. It is also interesting to note that  $Ni^{2+}$  had a tendency to cluster in the simulation at lower temperature ( $\beta_T = 2$ , though this same structure was seen consistently for  $\beta_T > 1$ ). This clustering appears to give rise to nickel rich grain boundaries with the ordered vacancy-containing structure forming the bulk of the crystallite. In ab-initio calculations, Hinuma et al. [56] found that an arbitrary energy penalty on Ni-Ni nearest neighbour interactions was necessary to prevent clustering of nickel on the lithium layer in  $LiNi_{0.5}Mn_{0.5}O_2$ . The simple Monte Carlo simulation may simply be encountering the same issue and this clustering may not occur. Either way, experimental confirmation is necessary and the Monte Carlo simulation at the very least suggests that a stable phase exists at high temperature where  $Mn^{4+}$  and  $Ni^{3+}$  can order on two superlattices and a random occupation of Li,  $Ni^{2+}$  and vacancies exists on the third.

### 8.5 $Li[Ni_{1/6}\square_{1/6}Mn_{2/3}]O_2$

An important consequence of the stable phase at point  $A_8$  is that it suggests the existence of a solid-solution line linking  $Li_2MnO_3$  to  $A_8$ . This line would represent layered structures with manganese in the 4+ oxidation state occupying 2/3 of the transition metal layer sites:  $Li[Li_{1/3-x}Ni_{x/2}\square_{x/2}Mn_{2/3}]O_2$  with  $0 \leq x \leq 1/3$ . This solid solution

would terminate at the composition  $\text{Li}[\text{Ni}_{1/6}\square_{1/6}\text{Mn}_{2/3}]\text{O}_2$ , or in terms of metallic fractions:  $\text{Li}_{0.545}\text{Mn}_{0.364}\text{Ni}_{0.091}$ . This is in good agreement with  $\text{Li}_{0.542}\text{Mn}_{0.369}\text{Ni}_{0.089}$  obtained by chemical analysis for the sample made at this composition by heating at  $900^\circ\text{C}$  for 5 hours before quenching. Figure 8.8 shows the XRD pattern obtained for this sample, refined as hexagonal R-3m. The XRD pattern shows a trace amount of contaminant phase with a peak near  $44^\circ$  as seen in the difference plot. Based on the phase diagram in Figure 8.2, this contaminant is most likely a spinel phase. Despite this, the material is very nearly single phase and the results of the Rietveld refinement are:  $a = 2.8580(1) \text{ \AA}$ ,  $c = 14.311(2) \text{ \AA}$ ,  $9.0 \pm 1.6 \%$  metal site vacancies, and  $3.7 \%$  nickel occupation on the lithium layer. The  $a$  lattice parameter is very close to that of sample  $\text{A}_8$ , while the  $c$  lattice parameter is noticeably larger, consistent with the contour plots provided in the previous chapter. Furthermore, the expected vacancy content for  $\text{Li}[\text{Ni}_{1/6}\square_{1/6}\text{Mn}_{2/3}]\text{O}_2$  is  $9.09 \%$  in excellent agreement with the experimental value. It should be noted that with vacancies taken into account, this material is not lithium rich, lithium only occupies  $50 \%$  of the metal sites. The only lithium on the transition metal layer in this material comes about as a result of nickel disorder on the lithium layer; as is the case for other non Li-rich layered materials such as  $\text{Li}[\text{Ni}_{0.5}\text{Mn}_{0.5}]\text{O}_2$ .

Figure 8.9 shows electrochemical data obtained for the  $\text{Li}[\text{Ni}_{1/6}\square_{1/6}\text{Mn}_{2/3}]\text{O}_2$  sample cycled at  $10 \text{ mA/g}$  at  $30^\circ\text{C}$ . The usual features for Li-rich layered material can be seen in the  $dQ/dV$  plots such as the nickel redox up to about  $4.45 \text{ V}$  and the large irreversible peak referred to as the high voltage plateau just above  $4.5 \text{ V}$ . There is no sign of manganese  $3+/4+$  redox during the first cycle, again consistent with metal vacancies allowing for  $\text{Mn}^{4+}$  only in the starting material. However, with continued cycling the manganese redox peak near  $3.1 \text{ V}$  during discharge grew continuously. This transformation is typically attributed to conversion to spinel-like structures and results in a decrease in average voltage [92]. Since spinel structures have far more metal site vacancies in the transition metal layers than the layered structures, it is possible that the presence of vacancies on the TM layer in  $\text{Li}[\text{Ni}_{1/6}\square_{1/6}\text{Mn}_{2/3}]\text{O}_2$  promotes conversion to spinel at high voltage. Furthermore, despite showing the high voltage plateau typically associated with lithium rich oxides, this material is not

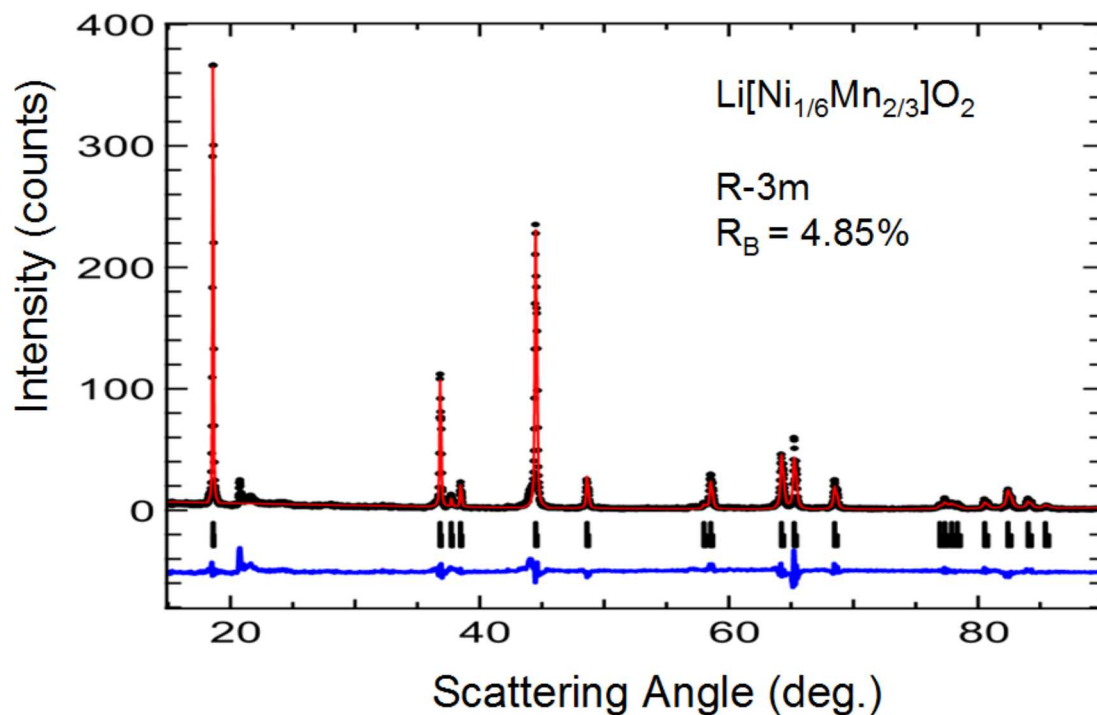


Figure 8.8: XRD pattern of  $\text{Li}[\text{Ni}_{1/6}\square_{1/6}\text{Mn}_{2/3}]\text{O}_2$  with the result of Rietveld refinement. Vertical lines are the calculated peak positions for  $K\alpha_1$  (full length) and  $K\alpha_2$  (half length).

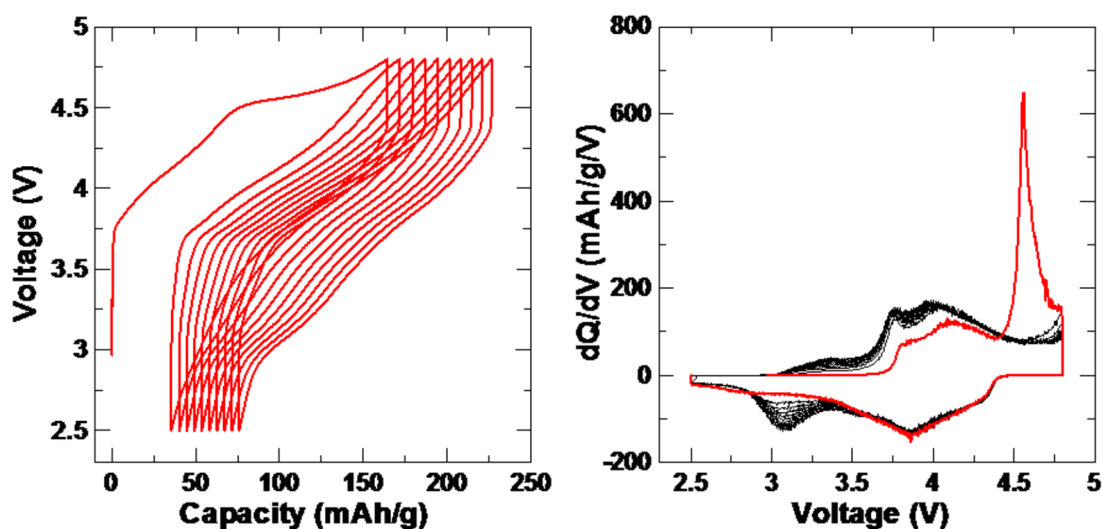


Figure 8.9: Voltage versus capacity and  $dQ/dV$  plots for  $\text{Li}[\text{Ni}_{1/6}\square_{1/6}\text{Mn}_{2/3}]\text{O}_2$  cycled at  $30^\circ\text{C}$  with a specific current of  $10\text{ mA/g}$ , or  $0.020\text{ mA/cm}^2$ . The red line in the  $dQ/dV$  curve represents the 1st cycle.

lithium rich: only half of the metal sites are occupied with lithium.

Figure 8.10 shows the capacity as a function of cycle number for two cells of  $\text{Li}[\text{Ni}_{1/6}\square_{1/6}\text{Mn}_{2/3}]\text{O}_2$ . The capacity for the material cycled at 10 mA/g at room temperature plateaus at about 150 mAh/g which is a small fraction of the theoretical capacity of 314 mAh/g assuming full lithium extraction. Higher capacities closer to the theoretical capacity can be achieved at slower rates and elevated temperatures. The maximum capacity obtained here was 250 mAh/g at 55 °C and a specific current of 5 mA/g. However, the capacity returned to about 150 mAh/g once the temperature and current were returned to 30°C and 10 mA/g. These results show that a high temperature formation cycle cannot be used to increase the capacity, which is not competitive with state-of-the-art lithium-rich materials.

## 8.6 Conclusions Regarding Metal Site Vacancies in Li-Mn-Ni-O

### Materials

Layered Li-Mn-Ni-O materials were analyzed in a region of the phase diagram where a strange bump was seen in the boundary of the layered region. These structures were found to contain a significant amount of metal site vacancies. The maximum vacancy content was found to result in highly ordered monoclinic structures where manganese occupies two of the  $\sqrt{3} \times \sqrt{3}$  superlattices on the transition metal layers while the third was randomly filled with nickel, lithium and vacancies. The resulting ordering predicted by a Monte Carlo simulation was consistent with the sharp ordering peaks seen in the XRD patterns. The vacancy concentrations were confirmed by Rietveld refinement, density measurements and redox titration; all of which were in good agreement. The role of the vacancies during electrochemical cycling, if there is one, remains unclear. The material with the greatest possible vacancy concentration,  $\text{Li}[\text{Ni}_{1/6}\square_{1/6}\text{Mn}_{2/3}]\text{O}_2$ , showed electrochemical behaviour consistent with lithium-rich layered materials, namely high irreversible capacity associated with the high voltage plateau and voltage fade associated with conversion to spinel. However, this material was not, in fact, lithium rich given that the vacancies result in lithium occupying only 50 % of metal sites. The vacancy results also demonstrated that there were roughly 1 % vacancies in a stoichiometric lithium-rich material lying along the line

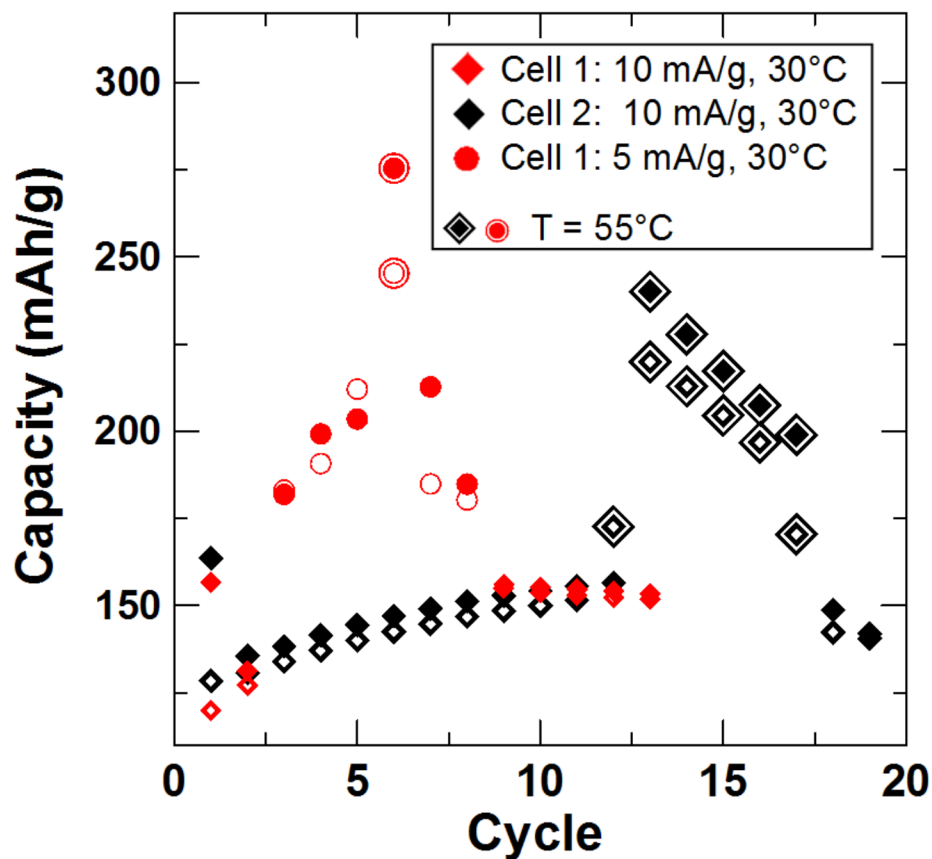


Figure 8.10: Capacity versus cycle number for  $\text{Li}[\text{Ni}_{1/6}\square_{1/6}\text{Mn}_{2/3}]\text{O}_2$ . All closed symbols shown in the legend represent charging, while the open symbols are discharge capacities.

from  $\text{Li}_2\text{MnO}_3$  and  $\text{LiNi}_{0.5}\text{Mn}_{0.5}\text{O}_2$ . The Monte Carlo simulation suggested that this allows  $\text{Ni}^{3+}$  to substitute for  $\text{Mn}^{4+}$  on two of the superlattices. This has never been recognized before and a complete understanding of the starting material is crucial to fully understand the complex electrochemical behaviour of the lithium-rich positive electrode materials. The exact shape of the other side of the bump (to the left of  $\text{Li}[\text{Ni}_{1/6}\square_{1/6}\text{Mn}_{2/3}]\text{O}_2$  in the Gibbs triangles) has not been determined. It is also unclear as to why the bump would be so sharp on both sides and this is worthwhile for further study.

## Chapter 9

### Materials Near the Layered Boundary

Data in this chapter are included in Ref. [93], to be submitted for publication to the Journal of the Electrochemical Society.

#### 9.1 Motivation for Studying $\text{LiNi}_{0.5}\text{Mn}_{0.5}\text{O}_2$

As previously discussed,  $\text{LiNi}_{0.5}\text{Mn}_{0.5}\text{O}_4$  lies near the upper boundary of the layered region. Figure 9.1 shows the phase boundaries of the layered region when heated in air to either 800 or 900°C as determined in previous chapters. The effect of synthesis atmosphere and cooling rate will be studied for two compositions in the current chapter, labeled  $A_9$  and  $B_9$ . The single-phase layered boundary moves downwards in the Gibbs triangle when samples are cooled more slowly such that sample  $A_9$ , which is single-phase if quenched, lies in the layered-layered two phase co-existence region when cooled more slowly. A higher oxygen partial pressure also lowers the upper layered boundary in the Gibbs triangle since more oxygen favours the spinel structures over the relatively oxygen-poor layered structures. Thus, for lower oxygen partial pressures sample  $A_9$  will lie very close to the layered boundary when regular cooled. The main objective of this chapter is to find conditions that produce a sample showing the first signs of layered-layered phase separation in order to study the consequences of this on the performance of the electrode material.

In the literature, there is considerable debate over whether or not lithium rich layered materials form solid solutions [3, 4, 47] or layered-layered nano-composites [44, 45]. In the combinatorial study, the compositions where one can expect layered-layered materials when synthesized in oxygen were determined. The fact that these materials can transform dramatically during slow cooling has been known for quite some time [12, 55]. Kang and Amine [12] observed that a single-phase sample of  $\text{Li}_{1.17}\text{Ni}_{0.25}\text{Mn}_{0.58}\text{O}_2$  had a first cycle capacity of 175 mAh/g when quenched and

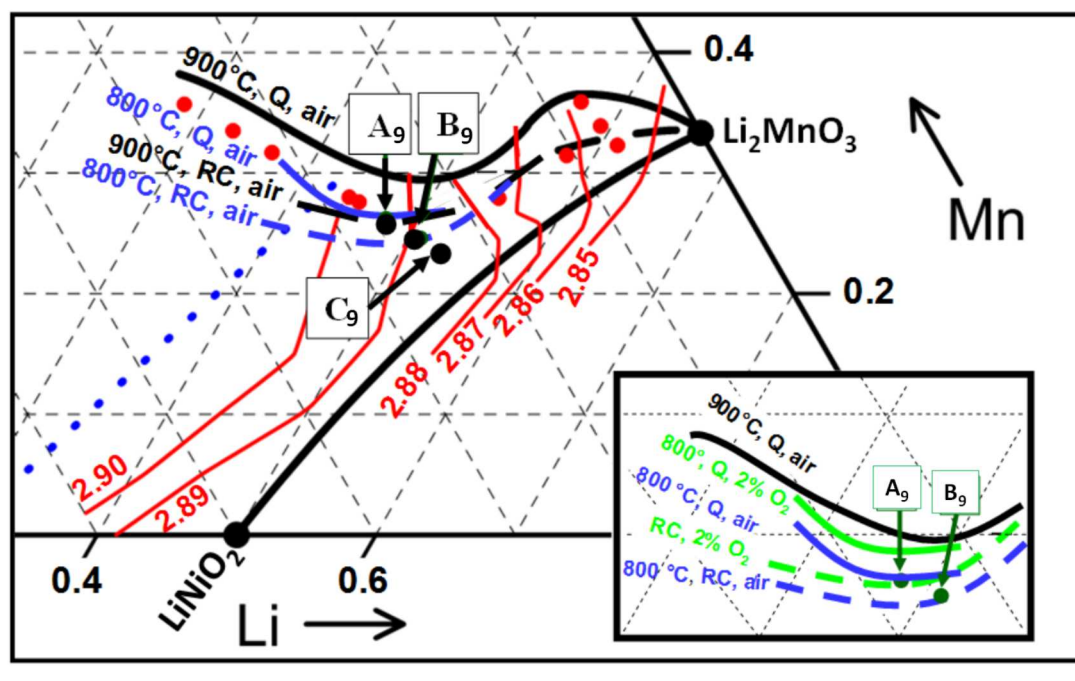


Figure 9.1: Partial phase diagram with contours for the  $a$  lattice parameter showing the boundaries of the single-phase layered region. The lower boundary is shown connecting  $\text{LiNiO}_2$  to  $\text{Li}_2\text{MnO}_3$  (no attempt was made to determine how this boundary changes with synthesis conditions since the current study focuses on compositions near the top of the layered region). The insert shows approximate upper boundaries of the layered region consistent with the current study. Points  $A_9$  and  $B_9$  were determined using elemental analysis and are referred to throughout the text. The red points are discussed in Chapter 7. The blue dotted line is the cubic to layered phase transition.

showed phase separation in the XRD pattern when slow cooled giving a first charge capacity as low as 55 mAh/g and never exceeding 85 mAh/g. It is difficult to identify the phases present based on the XRD shown in Ref. [12]. However, based on the phase diagrams from Chapters 5-7, their sample was made up of a monoclinic phase near M, a rocksalt phase and/or a layered phase near N. Nonetheless, the fact that such phase separation gives rise to such poor electrochemistry has been seen before, but the cause of this loss in capacity remains unclear and is the subject of this chapter.

Since there is a great deal of differing data in the literature for materials reported as  $\text{LiNi}_{0.5}\text{Mn}_{0.5}\text{O}_2$  this chapter will also help clarify why there has been such a wide

spread in results. Ohzuku et.al. first reported on this material and showed reversible cycling capacity of 150 mAh/g up to 4.3 V [87]. Lu et.al. [3] demonstrated that quenched samples cycled with a capacity of 140 mAh/g reversibly up to 4.4 V and 190 mAh/g up to 4.8 V with only 25 mAh/g irreversible capacity (IRC). These samples were made by co-precipitation with LiOH such that a small amount of excess lithium may have been present. The effect of excess lithium will be examined in detail here in the discussion of a set of  $\text{Li}_{1+x}[\text{Ni}_{0.5}\text{Mn}_{0.5}]_{1-x}\text{O}_2$  samples. An extreme example of this was obtained by Ohzuku et al. [53] who reported a sample of  $\text{LiNi}_{0.5}\text{Mn}_{0.5}\text{O}_2$  made with 25 % excess lithium that cycled 200 mAh/g stably up to 5.0 V with a larger IRC of 50 mAh/g. By contrast, Lin et al. [54] made  $\text{LiNi}_{0.5}\text{Mn}_{0.5}\text{O}_2$  without any excess lithium. The quenched sample had a first cycle discharge capacity of 175 mAh/g over the range 2.5 - 4.5 V and faded to 125 mAh/g after 50 cycles while a regular cooled sample showed stable cycling of 125 mAh/g over 30 cycles. Also, the XRD patterns of the samples from Lin et al. showed some ordering peaks in the range 20-30° in the regular cooled sample only. This is consistent with phase separation where one of the phases has ordering on the transition metal (TM) layer. However, the XRD patterns in the Lin paper are not sufficiently detailed to determine whether or not peak broadening was present in the regular cooled sample. Part of the current study therefore deals with reproducing this data in order to determine whether peak broadening is associated with this decrease in 1st cycle capacity.

It was also necessary to identify the features in the XRD patterns which are most sensitive to phase separation and then search for them carefully. In Chapter 4, in the Li-Co-Mn-O system, peak broadening at high angles ( $> 60^\circ$ ) in the XRD patterns was found to first indicate the formation of layered-layered composites and this corresponded to synthesis conditions where Wen et al. [23] found nano-composites. Upon slower cooling of the combinatorial samples described in Chapter 4, the broad peaks eventually resolved into two separate peaks corresponding to each layered phase such that the formation of nano-composites can be viewed as an incomplete phase separation into a layered-layered two-phase structure. To our knowledge, this was the first time that features in XRD patterns were correlated to nano-scale phase separation. Similar careful analysis of XRD patterns will be applied to samples in



the Li-Mn-Ni-O system here. Therefore, the condition used to identify the presence of nano-composites in the XRD pattern was a broadening of the high angle peaks. However, to distinguish this from micro-strain peak broadening a necessary condition to identify the formation of a nano-composite is that clear phase separation must be seen in the XRD if conditions are exaggerated (e.g. if cooling rates are slowed down further as done in Chapter 4 or if oxygen partial pressures are increased as used here).

## 9.2 Experimental Design

In order to obtain a sample showing this first signs of phase separation, the boundaries of the single-phase region were varied by changing the oxygen partial pressure during heating. Figure 9.1 shows the upper layered boundary under various conditions. The boundaries for samples heated in air were presented in previous chapters while the approximate boundaries for 2 % oxygen are based on the current study and so should only be considered accurate near compositions  $A_9$  and  $B_9$ . The boundary moves upwards as oxygen partial pressure decreases. Therefore, a sample made in pure oxygen at composition  $A_9$  will be multi-phase if quenched while the same composition in 2 % oxygen will be single-phase. As will be shown in the results section, the regular cooled sample made at composition  $A_9$  in 2 % oxygen showed the signs of being a layered-layered nano-composite. All samples made by the one-pot synthesis method at composition  $A_9$  were heated at a rate of 5°C/min up to 800°C and held there for 5 hours. The atmospheres used during heating were either air, or a flow of gas with either 2, 5.5 or 100 % oxygen content with the remainder being either nitrogen or argon gas. The samples were then either quenched or regular cooled. Samples at the composition  $B_9$  were made by Aaron Rowe and Eric McCalla using the tank reactor method. Samples were heated at 900°C for 12 hours before either quenching or regular cooling.

Electrochemical tests were carried out on some samples as described in Section 2.5. Two identical cells were made for each sample. All cycling was performed at a specific current of 10 mA/g. For samples  $A_9$  and  $B_9$  made by regular cooling after heating in the 2 % oxygen mixture, ICP was used as elemental analysis to determine the metal molar fractions of the final products (these values were used in generating

Figure 9.1). The X-ray diffraction patterns from all samples were measured in either a JD-2000 diffractometer or a Siemens D-5000 diffractometer. The resulting scans were then analyzed using Rietveld refinement.

A series of samples  $\text{Li}_{1+x}[\text{Ni}_{0.5}\text{Mn}_{0.5}]_{1-x}\text{O}_2$  was also synthesized at  $900^\circ\text{C}$  in air with regular cooling by Jing Li who performed all measurements on these samples. This composition line was previously studied by Myung et al. [65] over the range  $0 \leq x \leq 0.06$  and capacity was found to increase with  $x$  when cycled up to 4.6 V. Here, the wider composition range  $0 \leq x \leq 0.24$  was studied and the upper cutoff was 4.4 V in order to avoid the high voltage plateau [3]. Samples  $A_9$ ,  $B_9$  and  $C_9$  in Figure 9.1 have nominal compositions given by  $x = 0, 0.04$  and  $0.08$ , respectively. Samples with  $x = 0.12, 0.16, 0.20$  and  $0.24$  were also prepared.

Finally, to better understand the consequences of the layered-layered phase separation on the structure, a Monte Carlo simulation of a material of composition  $A_9$  in Figure 9.1 was performed. The details of this simulation are given in Section 2.12. The temperature scale was set by the parameter  $\beta_T$  and previous results suggest that  $\beta_T = 1$  corresponds to a temperature near and below  $800^\circ\text{C}$ , such that the value of  $\beta_T = 2$  used here is near  $250^\circ\text{C}$  and is therefore well below the critical temperature above which solid solutions are favoured due to a higher entropy. Two compositions were simulated:  $\text{Li}_{0.9}\text{Ni}_{0.1}[\text{Ni}_{0.4}\text{Mn}_{0.5}\text{Li}_{0.1}]\text{O}_2$  (stoichiometric  $\text{LiNi}_{0.5}\text{Mn}_{0.5}\text{O}_2$  with 10 % nickel on the lithium layer, consistent with Ref. [3]) and  $\text{Li}[\text{Ni}_{0.4}\text{Mn}_{0.5}\text{Li}_{0.1}]\text{O}_2$  simulated in order to determine the role played by nickel on the lithium layer. The fact that there was nickel on the lithium layer in the first simulation meant that the model required out-of-plane interactions. Therefore, two layers were simulated: one lithium layer and one TM layer. It was assumed that these two layers stack alternately and the only out-of-plane interactions included in the calculations were for nearest neighbours such that every atom had six in-plane and six out-of-plane nearest neighbour interactions. Periodic boundary conditions were used.

### 9.3 Structural Results

The results of the elemental analysis for composition  $A_9$  were  $\text{Li}_{0.48}\text{Ni}_{0.26}\text{Mn}_{0.26}$  and that point was positioned accordingly in Figure 9.1. This composition suggests the

material, if single phase, would be  $\text{Li}_{0.96}\text{Ni}_{0.52}\text{Mn}_{0.52}\text{O}_2$  assuming no metal/oxygen vacancies and can therefore be considered a slightly lithium-poor layered material. Figure 9.2 shows XRD scans of samples at composition  $A_9$  made under various conditions. The scan of the sample made in pure oxygen and regular cooled shows three phases (three peaks visible near  $44^\circ$ ) consistent with the R, N and M phases discussed at length in previous chapters. Since broadening of the Bragg peak near  $44^\circ$  is a clear indication of phase separation, the scans taken after synthesis in air and 5.5 % oxygen show clear signs that phase separation occurs during regular cooling. This is visible in the difference plots (calculated as the quenched pattern subtracted from the regular cooled one). The shape of the difference plots near  $44^\circ$  are consistent with broadening of the peak on both sides. By contrast, the sample made in 2 % oxygen showed no such peak broadening near  $44^\circ$ . The right panel of Figure 9.2 shows the region where superlattice peaks are expected if there is ordering on the transition metal layers. There are no peaks visible here for all quenched samples consistent with the disordered TM layer expected for  $\text{LiNi}_{0.5}\text{Mn}_{0.5}\text{O}_2$ . However, the regular cooled samples in 5.5 % oxygen, air and pure oxygen show small broad peaks near  $21^\circ$ . This is consistent with phase separation wherein one of the new phases is a layered material with ordering on the TM layer as seen in the M-layered phase in Chapter 6.

To more carefully quantify the changes taking place during cooling, the scans were fit using Rietveld refinement assuming a single hexagonal layered structure (R-3m space group). Table 9.1 shows the results of the refinement. For all three quenched samples made at composition  $A_9$ , the lattice parameters are consistent with previously presented contour plots (the  $a$  lattice parameter is shown in Figure 9.1, the  $c$  values can be found in Chapter 7). Table 9.1 also shows the widths of the calculated peaks at  $44$  and  $65^\circ$ . The extreme broadening seen in the 5.5 % oxygen and air samples suggests once again that these materials phase separated during regular cooling. By contrast, the 2 % oxygen regular cooled sample showed no peak broadening at  $44^\circ$  and moderate broadening of the higher angle peak, accompanied with a decrease in the  $c$  lattice parameter suggesting a broadening to the high angle side of peaks. The same behaviour was seen in regular-cooled samples of Li-Co-Mn-O under conditions where

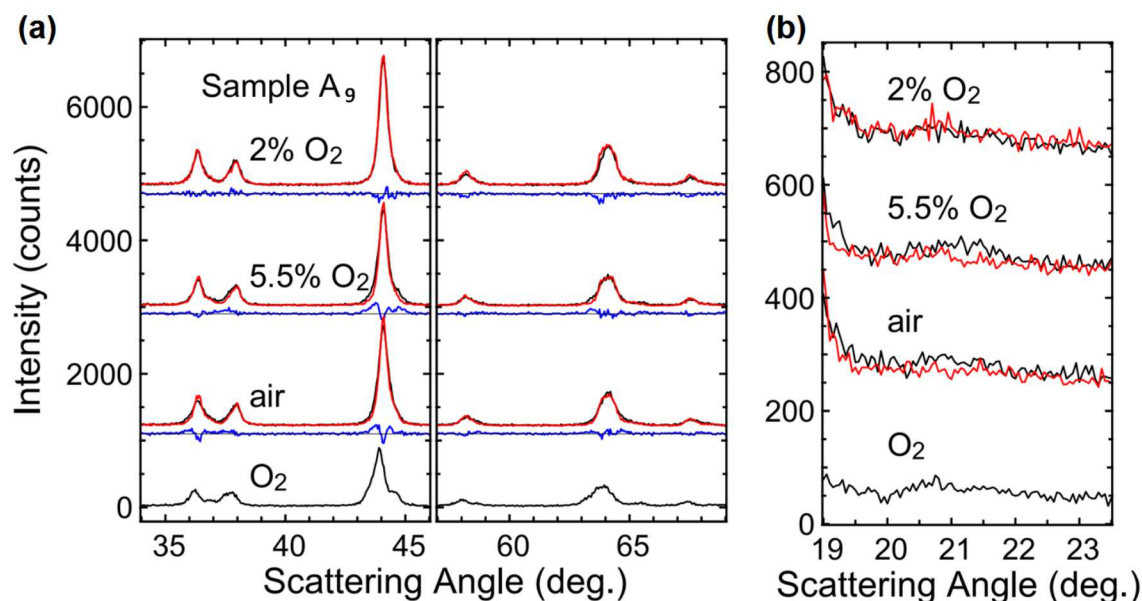


Figure 9.2: XRD scans of samples with composition  $A_9$  heated at  $800^\circ\text{C}$ . Black lines represent samples that were regular cooled, while red is for quenched samples. The difference plots in blue in the left panel represent the quenched scan subtracted from the regular cooled scan.

layered-layered nano-composites were seen (Chapter 4): a broadening of high angle peaks only and clear phase separation if conditions are exaggerated (i.e. the samples prepared under higher oxygen partial pressures showed clear phase separation here. The sample  $A_9$  heated in 2 % oxygen therefore shows the signs of forming a layered-layered composite on short length scales when regular cooled. The sample made in air and quenched also shows broadening at the higher angle peak only (though less so with a FWHM of 0.49) suggesting that in air the boundary for quenched samples is quite close to point  $A_9$ . This again suggests that the phase boundary was lower in the triangle as the oxygen partial pressure was increased such that the sample made in air may have already begun to phase separate on short length scales even when quenched. The Rietveld refinement results also show that the fraction of nickel on the lithium layer is slightly above 10 % consistent with previous studies [3]. It would be of high interest to study such samples with methods sensitive to short range ordering such as high resolution transmission electron microscopy in order to distinguish between phase separation over short distances and phase separation between two phases very

Table 9.1: XRD Rietveld refinement results for samples of composition  $A_9$  fit as single-phase layered. Q denotes quenched while RC represents regular cooled samples.

Synthesis	a (Å)	c (Å)	FWHM*		Ni <sub>Li</sub> (%) <sup>†</sup>
			44°	65°	
2 % O <sub>2</sub> / Q	2.8986(11)	14.312(4)	0.43	0.43	13
5.5 % O <sub>2</sub> / Q	2.8983(10)	14.315(4)	0.40	0.44	12
Air / Q	2.8968(14)	14.310(3)	0.43	0.49	13
2 % O <sub>2</sub> / RC	2.8986(11)	14.293(4)	0.44	0.52	11
5.5 % O <sub>2</sub> / RC	**	**	0.50	0.62	**
air / RC	**	**	0.52	0.63	**
100 % O <sub>2</sub> / RC	**	**	0.67	0.75	**

\* FWHM is the full width at half maximum of the calculated peaks, measured in degrees.

\*\* Values omitted as these samples contained multiple phases.

† Nickel occupation on the lithium layer.

close to each other on the phase diagram. In either case, the XRD patterns indicate that the layered samples at  $A_9$  all phase separate during regular cooling, with the sample made in 2 % O<sub>2</sub> showing the smallest signs of multiple phases.

For comparison, a regular cooled sample synthesized in 2 % oxygen at composition  $B_9$  was found to have the composition  $\text{Li}_{1.02}\text{Mn}_{0.50}\text{Ni}_{0.48}\text{O}_2$  according to elemental analysis and Rietveld refinement yielded  $a = 2.8891 \text{ \AA}$  and  $c = 14.296 \text{ \AA}$  again consistent with the contour plots shown in Figure 9.1 and Chapter 7. The XRD patterns for this sample showed no peak broadening after regular cooling and as such indicated that the sample stayed single-phase. The boundaries in Figure 9.1 were drawn to be consistent with all XRD results discussed in this thesis. The 2 % oxygen boundary is therefore approximate and should only be considered valid near the compositions  $A_9$  and  $B_9$  since the rest of the phase diagram has not been studied extensively under these conditions. Similarly, since it was difficult to precisely determine the position of the boundaries for the 800°C quenched samples, it was drawn going through point  $A_9$  given that a small amount of peak broadening was seen in the high angle peaks in this sample.

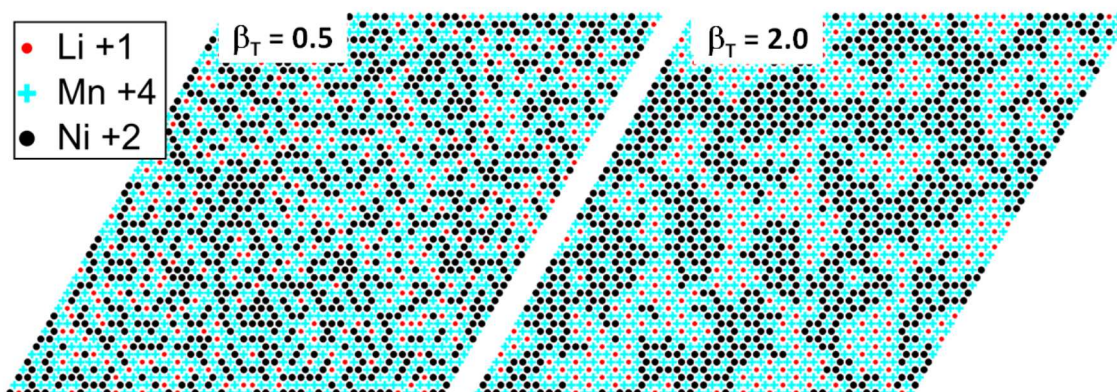


Figure 9.3: Monte Carlo simulation results for the transition metal layer with composition  $\text{Ni}_{0.4}\text{Mn}_{0.5}\text{Li}_{0.1}$  and no nickel on the lithium layer.

#### 9.4 Monte Carlo Simulation Results

Figure 9.3 shows the results of the Monte Carlo simulation for the composition  $\text{Li}[\text{Ni}_{0.4}\text{Mn}_{0.5}\text{Li}_{0.1}]\text{O}_2$  (i.e. no nickel present on the lithium layer). The results at  $\beta_T = 0.5$  (very high temperature) showed a solid solution where sites were randomly occupied except for lithium coordinating around Mn on the TM layer as has been well documented before. Upon cooling to  $\beta_T = 2.0$  ( $T \propto 1/\beta_T$ ), phase separation was evident with clusters of pure  $\text{LiMn}_2$  separated by regions with nickel and manganese only of approximate composition  $\text{Ni}_{0.5}\text{Mn}_{0.5}$ . This phase separation is promoted heavily in the literature [44, 45]. Figure 9.4, however, shows that phase separation is strongly hindered when nickel is present on the lithium layer. The  $\text{LiMn}_2$  clusters stayed much smaller and also contained some nickel. This Ni in the  $\text{LiMn}_2$  clusters is consistent with the phase diagram where co-existence includes a structure close to the M-layered material which contains a small amount of nickel on the transition metal layer. Allowing the simulation to run 10 times longer (labeled annealed) did promote phase separation somewhat though domains were still smaller than those seen in Figure 9.3 and there was still disorder in the domains.

Another significant feature seen in the Monte Carlo simulation results in Figure 9.4 was that in the regions of disordered  $\text{LiMn}_2$  on the TM layer, there was no nickel on the corresponding region in the lithium layer. This implies that nickel in the lithium layer is clustering to the regions of  $\text{Ni}_{0.5}\text{Mn}_{0.5}$  on the TM layers. Once again,

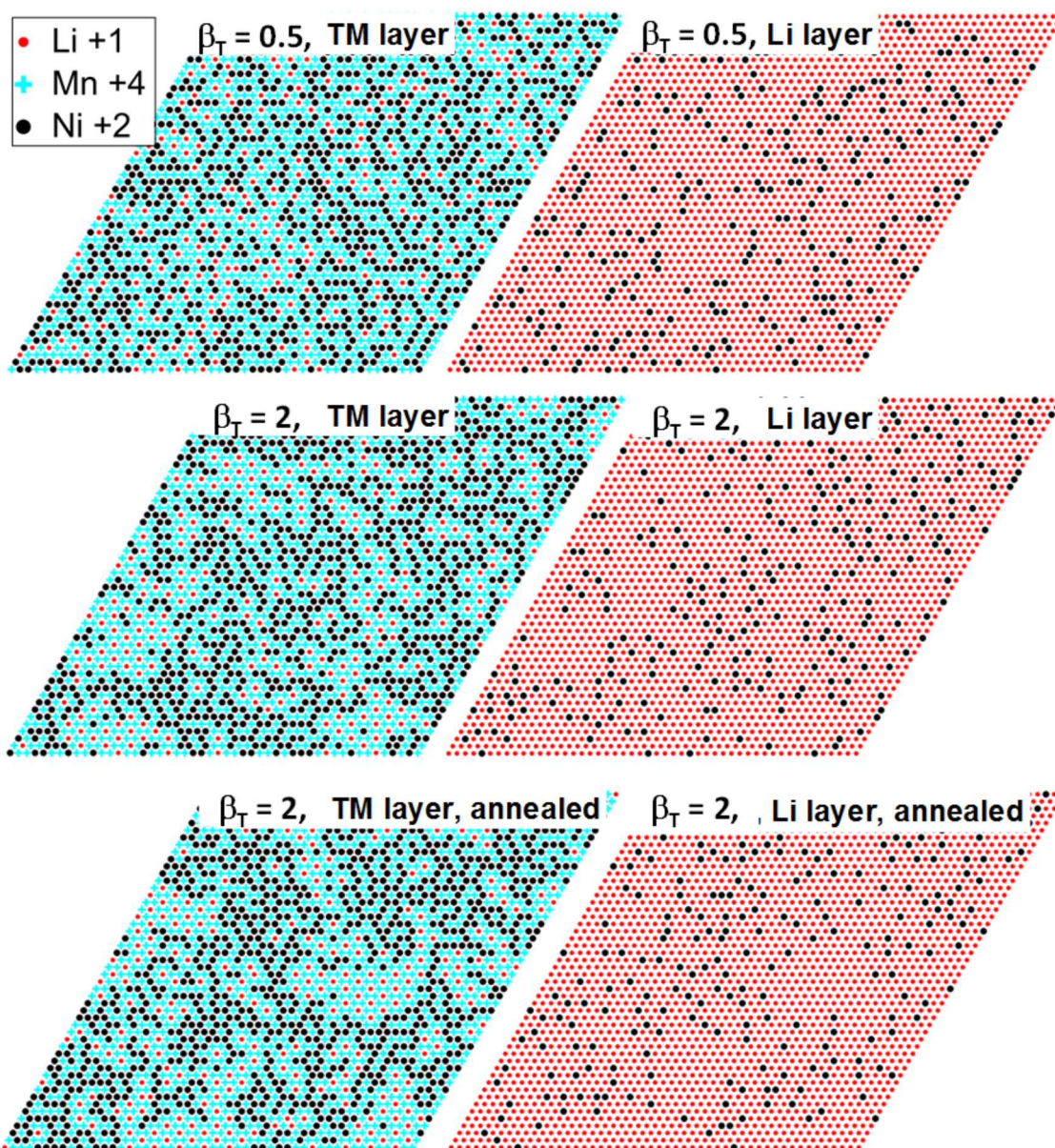


Figure 9.4: Monte Carlo simulation results of sample  $\text{LiNi}_{0.5}\text{Mn}_{0.5}\text{O}_2$  with 10 % nickel on the lithium layer. The TM layer had composition  $\text{Ni}_{0.4}\text{Mn}_{0.5}\text{Li}_{0.1}$ . Annealed indicates 10 times as many Monte Carlo cycles.

this feature is expected from the phase diagram given that the N phase has roughly 30 % nickel on the lithium layer while the M phase only contains approximately 2 % such that M-N phase separation would result in clustering of nickel on the lithium layers. Here, the endpoints lie along the M-N segment of the boundary such that some nickel clustering on the lithium layer is expected. These results suggest that the ordering of  $\text{LiMn}_2$  on the transition metal layer may drag lithium on the lithium layer. This effect is consistent with the tendency of lithium to coordinate around manganese though this coordination is now between two neighbouring layers. The consequence of lithium coordinating to manganese is that nickel must cluster on the lithium layer. This may create a severe hindrance to the diffusion of lithium in the lithium layer.

## 9.5 Electrochemical Measurements

Figure 9.5 shows the capacity versus cycle number for cells made from materials made under either 2 % oxygen or in air. The quenched and regular cooled materials at composition  $A_9$  made in air are consistent with those seen by Lin et al. in Ref. [54] with the quenched sample here showing a capacity of 150 mAh/g fading rapidly with cycling up to 4.4 V and the regular cooled sample cycling about 100 mAh/g. No efforts were made here to determine the changes taking place during cycling that give rise to this capacity fade and this question remains a significant one. The higher capacities (190 mAh/g up to 4.8 V and 150 mAh/g up to 4.4 V) seen for samples at composition  $B_9$  heated to 900°C and either quenched or regular cooled confirm the importance of staying within the single-phase region during cooling. These values are also consistent with those reported elsewhere [3, 87] for  $\text{LiNi}_{0.5}\text{Mn}_{0.5}\text{O}_2$  samples made with a small amount of excess lithium.

Of higher interest for the current study was the behaviour of the  $A_9$  samples made in 2 % oxygen. When the electrode material was quenched, the cell capacities for samples heated in 2 % oxygen were slightly higher than those made in air and show the same capacity fade with cycling. However, upon regular cooling the capacity dropped dramatically to be well below that of the material made in air, for both upper voltage cutoff limits of 4.4 and 4.8 V. This large drop in capacity took place even



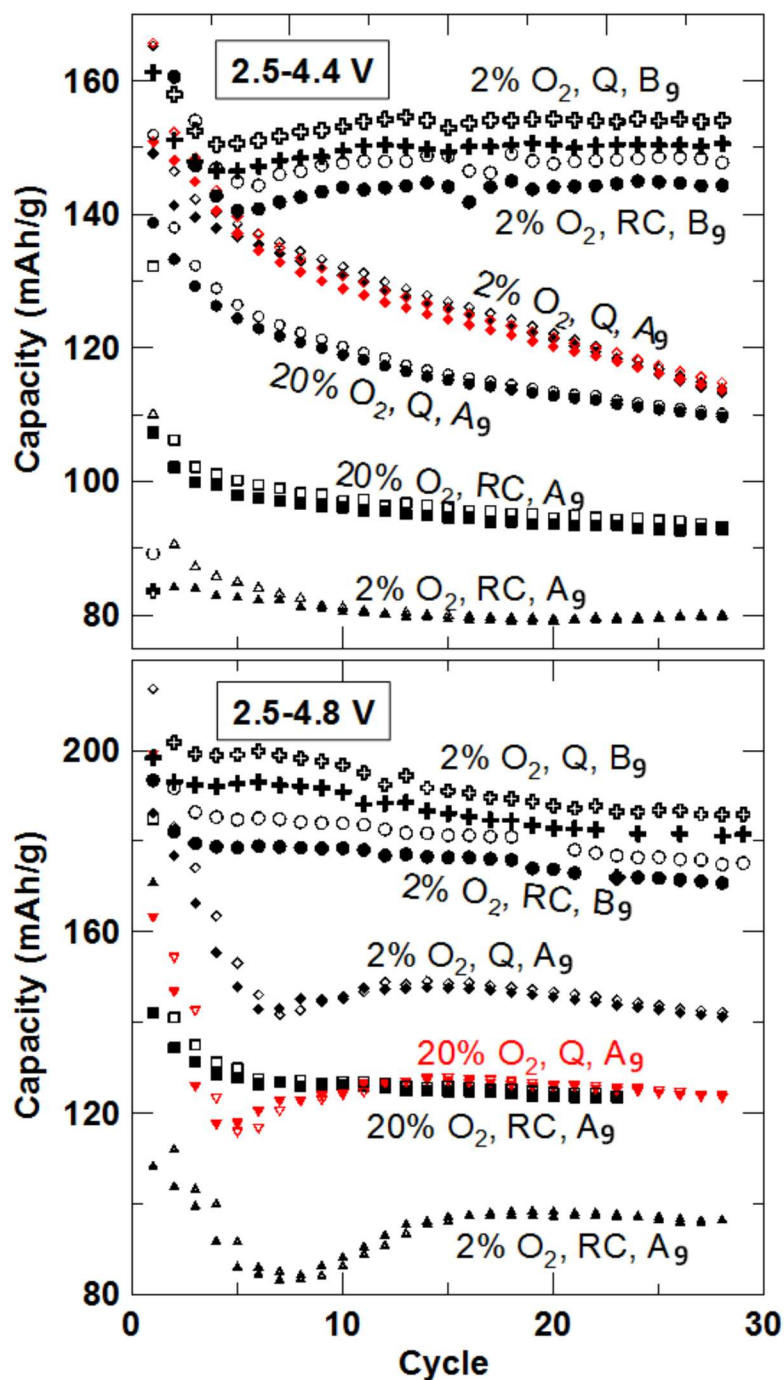


Figure 9.5: Capacity versus cycle number for samples A<sub>9</sub> heated to 800°C and B<sub>9</sub> heated to 900°C cycled at 10 mA/g. Q is for quenched samples, RC is for regular cooled, while 20% oxygen is for samples heated in air. In the top panel, twin cells are included for the 2 % oxygen sample when quenched in order to show the reproducibility.

though the 2 % oxygen samples showed the least sign of phase separation based on the XRD. This may be due to the clustering of nickel on the lithium layer on a single crystallite blocking lithium diffusion paths as would occur in a nano-scale composite material. Then, upon completing the phase separation, the materials made in air would have separate crystallites of each phase such that the more ordered phase would then cycle nicely explaining the higher capacities obtained in air when regular cooled even though phase separation was more evident in the XRD.

Figures 9.6 and 9.7 show the voltage vs capacity and  $dQ/dV$  vs voltage plots for these cells. The main feature in the  $dQ/dV$  plots was a peak near 3.75 V with some smaller peaks near 4.5 V corresponding to a small high voltage plateau in the capacity versus voltage plots. The most relevant features in the cells made from regular cooled  $A_9$  materials heated in 2 % oxygen were a large irreversible capacity when cycled up to 4.8 V and a significant impedance growth in both regular cooled materials. This impedance can be seen as a voltage difference between charge and discharge, which was noticeably larger in the regular cooled samples as compared to the quenched samples). This change was also seen in the samples made in air, though it was less severe, while the cells made from sample  $B_9$  showed no such impedance growth such that this can again be attributed to the presence of multiple-phases appearing during cooling.

### 9.6 $Li_{1+x}[Ni_{0.5}Mn_{0.5}]_{1-x}O_2$ Series with $0 \leq x \leq 0.24$

Figure 9.8 shows the region of the X-ray diffraction patterns near  $44^\circ$  for the composition line  $Li_{1+x}[Ni_{0.5}Mn_{0.5}]_{1-x}O_2$  with  $x = 0.0, 0.04$  and  $0.08$  made at  $900^\circ C$  in air and regular cooled. The samples have not been analyzed by elemental analysis but, based on the small amount of lithium-loss in the previous samples, these samples lie near points  $A_9, B_9$  and  $C_9$  in Figure 9.1. The sample with  $x = 0.00$  (point  $A_9$ ) shows evidence for the presence of a second phase, consistent with the XRD pattern expected for sample  $A_9$  heated to  $900^\circ C$  in air and regular cooled in Figure 9.1. The samples with  $x = 0.04$  and  $0.08$  do not show evidence of a second phase, although the peak width increases with  $x$ . The crystallite size and micro-strain may therefore depend on the composition,  $x$ . Table 9.2 summarizes the XRD results for the

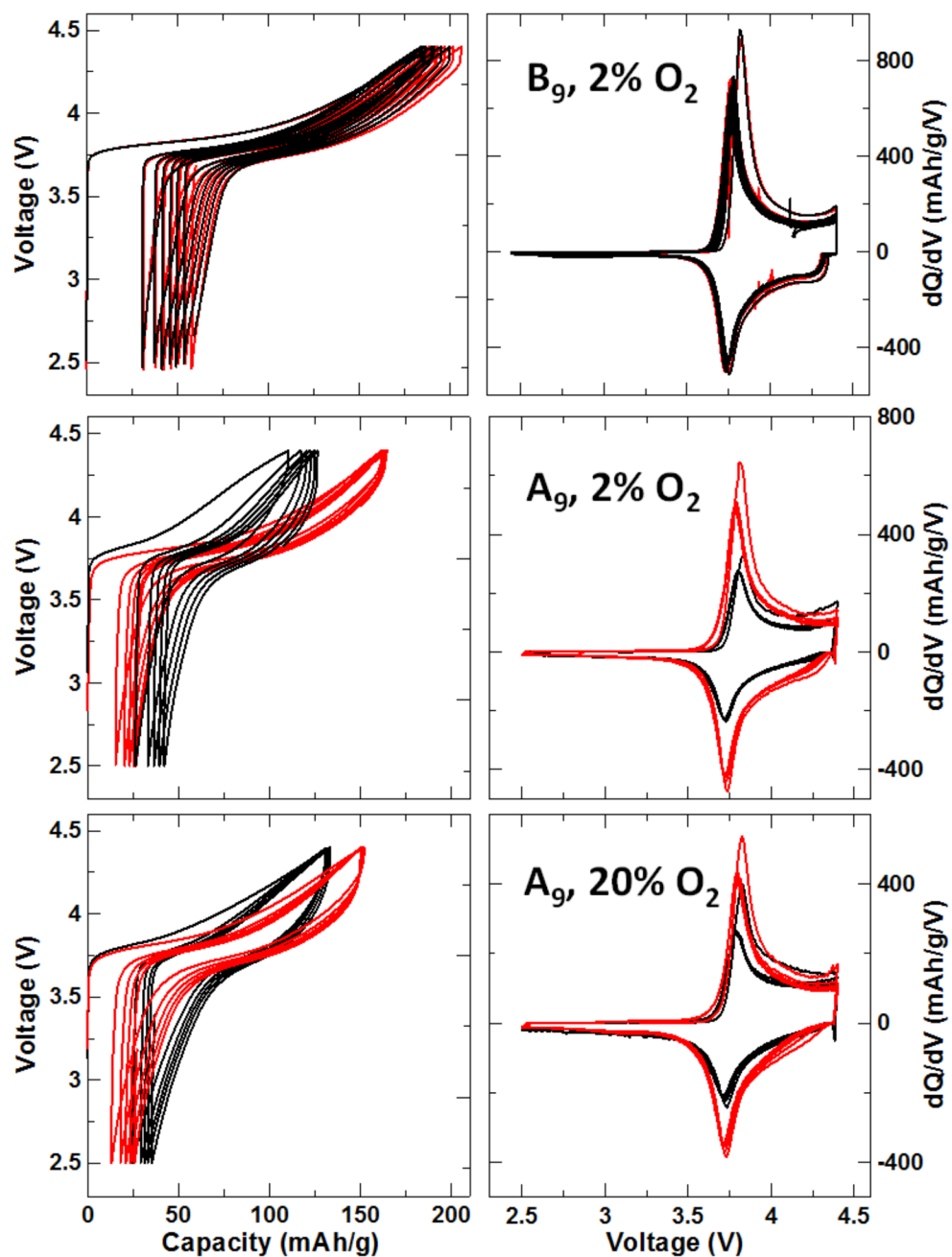


Figure 9.6: Voltage curves and  $dQ/dV$  for samples  $A_9$  and  $B_9$  cycled up to 4.4V. The red lines are for quenched samples, while the black are for regular cooled.

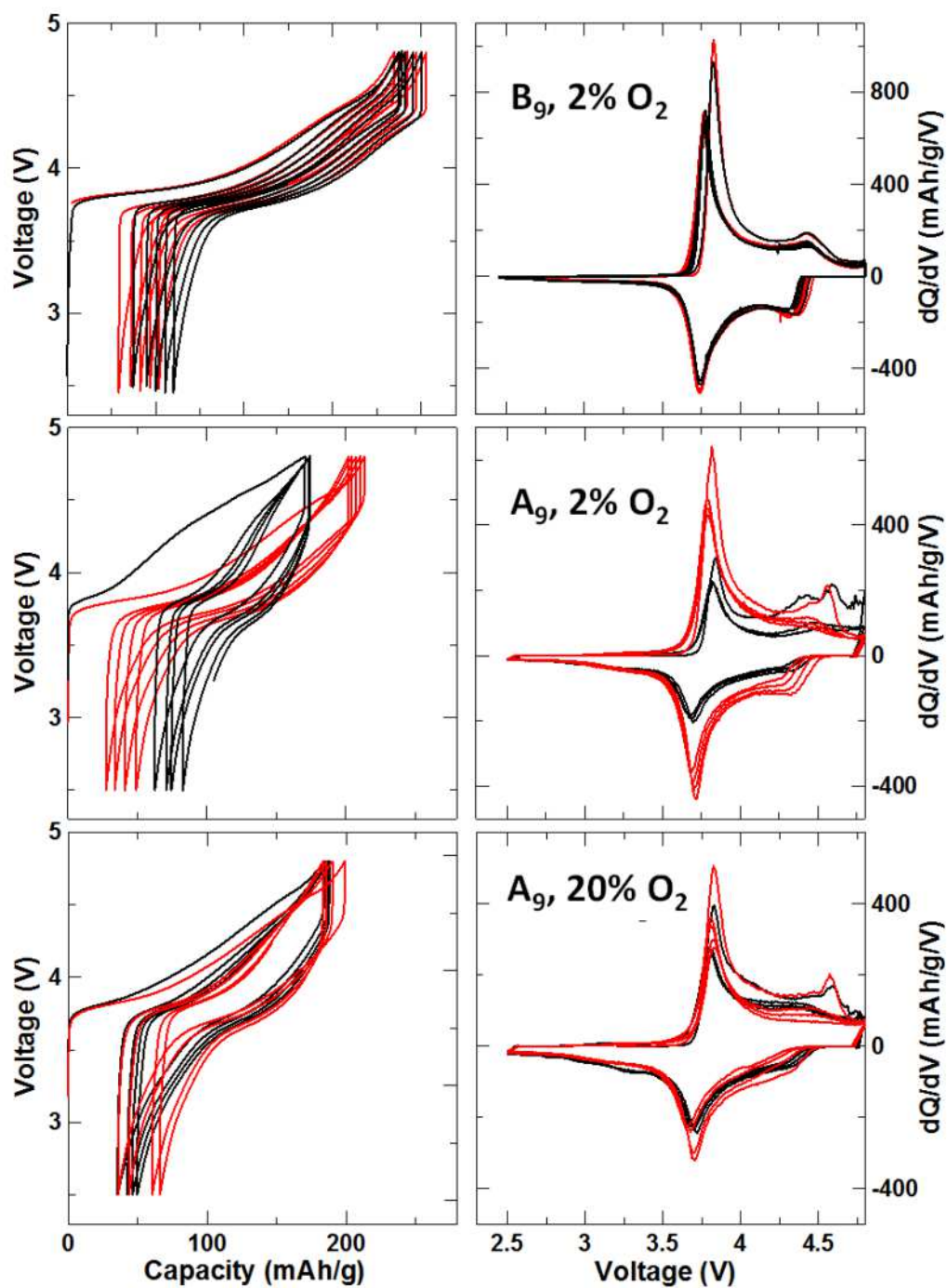


Figure 9.7: Voltage curves and  $dQ/dV$  for samples  $A_9$  and  $B_9$  cycled up to 4.8V. The red lines are for quenched samples, while the black are for regular cooled.

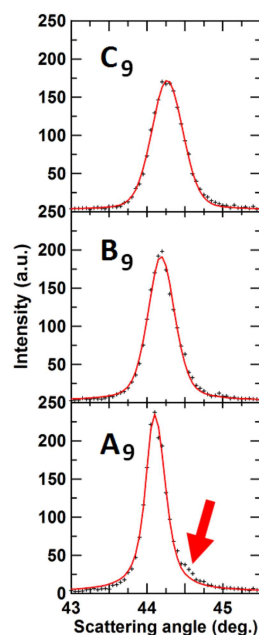


Figure 9.8: Partial XRD patterns for samples A<sub>9</sub> ( $x = 0.00$ ), B<sub>9</sub> ( $x = 0.04$ ) and C<sub>9</sub> ( $x = 0.08$ ) obtained as part of the composition series  $\text{Li}_{1+x}[\text{Ni}_{0.5}\text{Mn}_{0.5}]_{1-x}\text{O}_2$ . The arrow indicates the presence of a second peak in sample A<sub>9</sub>. The red lines are single-phase layered fits.

$\text{Li}_{1+x}[\text{Ni}_{0.5}\text{Mn}_{0.5}]_{1-x}\text{O}_2$  series with  $0 \leq x \leq 0.24$ . The XRD patterns therefore confirm that changing the value of  $x$  in this manner moved samples from outside the single phase region (sample A<sub>9</sub>,  $x = 0.0$ ), to within the single-phase region (samples B<sub>9</sub> and C<sub>9</sub>) and then outside the single-phase region, where excess  $\text{Li}_2\text{CO}_3$  was observed in the XRD patterns ( $x = 0.20$  and  $0.24$ ). Studies of these samples also allow the determination of the impact of the layered-layered phase separation as all samples were made under identical conditions.

Figure 9.9 shows the reversible specific capacity of the  $\text{Li}_{1+x}[\text{Ni}_{0.5}\text{Mn}_{0.5}]_{1-x}\text{O}_2$  samples during the first and fourth discharges. This figure shows that samples should be prepared as single-phase materials in order to deliver the highest capacity and that phase separation into layered-layered composites ( $x = 0$  in Figure 9.9) should be avoided. Figure 9.9 also shows that samples closest to the single-phase boundary have the highest capacity when cycled to 4.4 V. This illustrates the importance of a complete understanding of the phase diagram in order to avoid  $\text{Ni}^{3+}$  in the starting

Table 9.2: XRD Rietveld refinement results for samples along the composition line  $\text{Li}_{1+x}[\text{Ni}_{0.5}\text{Mn}_{0.5}]_{1-x}\text{O}_2$  with  $0 \leq x \leq 0.24$ . The capacity is the average first cycle discharge capacity for two twin cells cycled over the range 2.5 - 4.4 V at 10mA/g.

Sample	x	a ( $\pm 0.0004$ Å)	c ( $\pm 0.002$ Å)	Ni <sub>Li</sub> (%)	Single phase	Capacity (mAh/g)
$\text{LiNi}_{0.5}\text{Mn}_{0.5}\text{O}_2$	0.00	2.8944	14.311	10.0	No	129.7(7)
$\text{Li}_{1.04}\text{Ni}_{0.48}\text{Mn}_{0.48}\text{O}_2$	0.04	2.8890	14.307	9.0	Yes	160.3(5)
$\text{Li}_{1.08}\text{Ni}_{0.46}\text{Mn}_{0.46}\text{O}_2$	0.08	2.8816	14.293	7.4	Yes	149.9(7)
$\text{Li}_{1.12}\text{Ni}_{0.44}\text{Mn}_{0.44}\text{O}_2$	0.12	2.8765	14.279	5.0	Yes	142(1)
$\text{Li}_{1.16}\text{Ni}_{0.42}\text{Mn}_{0.42}\text{O}_2$	0.16	2.8704	14.255	3.7	Yes	134.3(5)
$\text{Li}_{1.20}\text{Ni}_{0.4}\text{Mn}_{0.4}\text{O}_2$	0.20	2.8678	14.250	2.2	No*	129.7(5)
$\text{Li}_{1.24}\text{Ni}_{0.38}\text{Mn}_{0.38}\text{O}_2$	0.24	2.8679	14.242	0.7	No*	121(2)

\* This co-existence is between the layered material and un-reacted  $\text{Li}_2\text{CO}_3$ .

material and to produce materials with the best electrochemical performance.

## 9.7 Conclusions Regarding Layered-Layered Nano-Composites

The structural changes taking place during regular cooling of materials with metallic compositions near that of  $\text{LiNi}_{0.5}\text{Mn}_{0.5}\text{O}_2$  were studied after heating under various oxygen partial pressures and were related to features in the phase diagram determined previously. Materials made with 5 % excess lithium (at point B<sub>9</sub> in Figure 9.1) were found to stay single-phase even when the regular cooling rate of 5-10°C/min was used. These single-phase layered materials showed good electrochemical performance with a reversible capacity of 180 mAh/g for the quenched sample and 170 mAh/g for the regular cooled sample when cycled up to 4.8 V. By contrast, under the same cycling conditions, samples without excess lithium (at point A<sub>9</sub> in Figure 9.1) made in 2 % oxygen had a capacity of 140 mAh/g when quenched and only 90 mAh/g when regular cooled. The changes in the XRD pattern for this A<sub>9</sub> sample were small with peak broadening only seen at high angle, consistent with the first sign of phase separation into layered-layered nano-composites. The dramatic loss in capacity seen in the sample made in 2 % oxygen at point A<sub>9</sub> can be attributed to nickel clustering on the lithium layer such that lithium islands form, many of which would be surrounded by the clustered nickel. This behaviour was expected from the phase diagram where

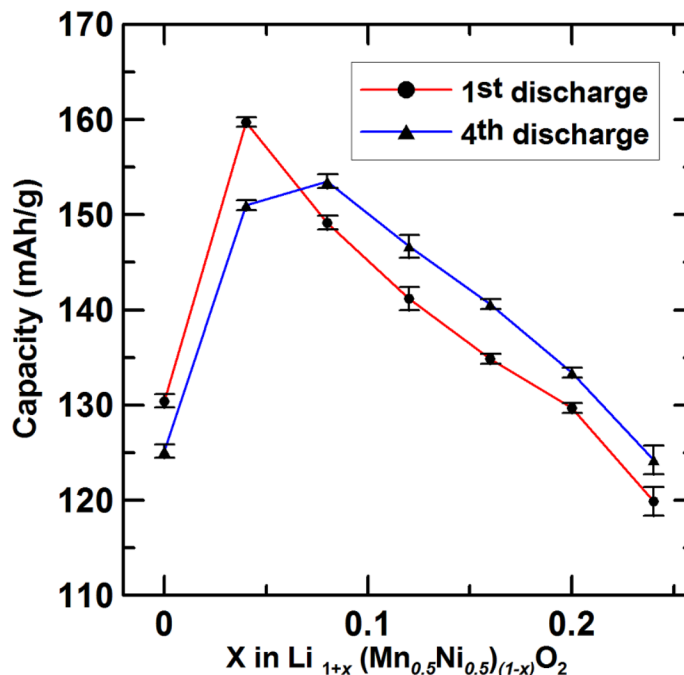


Figure 9.9: Discharge capacity as a function of nominal composition  $x$  in  $\text{Li}_{1+x}[\text{Ni}_{0.5}\text{Mn}_{0.5}]_{1-x}\text{O}_2$ . Cells were cycled over the range 2.5 - 4.4 V at 10 mA/g. The error bars represent the variation between two twin cells.

phase separation into a nickel rich and nickel poor phase was demonstrated in Chapter 6, and this clustering of nickel was also seen in a Monte Carlo simulation performed in this chapter.

Samples made in air, which showed greater signs of phase separation, had a smaller decrease in capacity when regular cooled, consistent with phase separation reaching completion such that whole crystallites of each phase exist and the more ordered layered material then de-lithiates more easily. Samples of  $\text{Li}_{1+x}[\text{Ni}_{0.5}\text{Mn}_{0.5}]_{1-x}\text{O}_2$  which were made in air at  $900^\circ\text{C}$  showed the highest capacity when they were single phase near the phase boundary. This work therefore shows the importance of precisely knowing where the samples lie in the phase diagram and carefully examining XRD peak shapes in order to detect the smallest signs of phase separation. It would now be of high value to collect short range information on materials near the layered boundary from techniques such as transmission electron microscopy in order to more

carefully determine the compositions where layered-layered composites form on the nano-scale and to correlate this to the results discussed here. It is important to realize that such electron microscopy experiments would need to be done with extreme care in order to avoid situations where apparent phase separation might be caused by electron beam heating.



## Chapter 10

### Conclusions and Future Works

#### 10.1 The Li-Co-Mn-Ni-O Pseudo-Quaternary System

Figure 10.1 shows the Li-Co-Mn-Ni-O pseudo-quaternary system with the Li-Co-Mn-O and Li-Mn-Ni-O faces shown, as determined with combinatorial samples quenched from 800°C. Some approximations were made to join the two faces since the Li-Co-Mn-O face was synthesized in air while the nickel containing samples were made in oxygen. Nonetheless, the two faces join quite well. The pyramid strongly suggests that both single-phase regions of importance for battery materials, spinel and layered, extend into the pyramid and form relatively large three dimensional shapes. On the Li-Co-Mn-O system, the layered region is restricted to a single line showing that cobalt is always synthesized in the 3+ state as it is in  $\text{LiCoO}_2$ . By contrast, nickel can be in the 2+ state as in NiO rocksalt or the 3+ state as in layered  $\text{LiNiO}_2$  such that a much larger and more complex layered region exists on the Li-Mn-Ni-O face. The spinel-layered co-existence region is also simpler in the Li-Co-Mn-O triangle with all tie-lines connecting to either the cobalt spinel,  $\text{Co}_3\text{O}_4$ , or the manganese layered material,  $\text{Li}_2\text{MnO}_3$ , while in the Li-Mn-Ni-O system there are two three-phase regions. The differences between the roles of cobalt and nickel should prove significant in upcoming combinatorial work in the Li-Co-Mn-Ni-O pseudo-quaternary system that is of extreme interest for battery materials as it includes commercial materials such as  $\text{Li}[\text{Ni}_{1/3}\text{Mn}_{1/3}\text{Co}_{1/3}]\text{O}_2$  [94] as well as promising spinel-layered core-shell materials [89] and lithium-rich layered materials [4].

One of the main findings in this work is that the boundaries of the single-phase region move dramatically with synthesis conditions. Most importantly, the layered single-phase regions become smaller when cooled more slowly, and this occurred in both faces of the pyramid. The consequences of this were discussed in detail throughout the thesis and will be summarized here by showing how this work helps resolve a

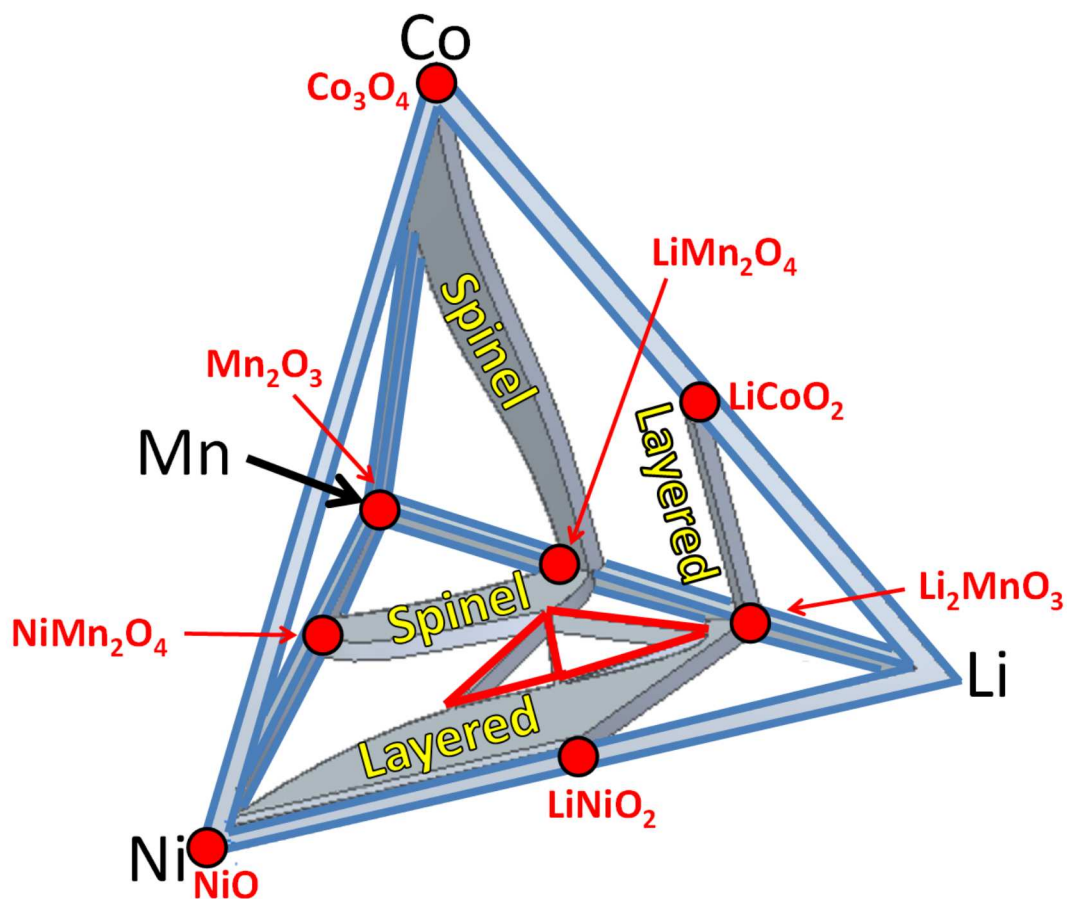


Figure 10.1: The Li-Co-Mn-Ni-O pseudo-quaternary system for samples heated to 800°C and quenched with single-phase regions identified. The red lines indicate boundaries of three-phase regions while the blue lines denote the axes.

number of points of confusion in the literature mentioned in Chapter 1. These were listed with roman numerals and will be repeated and addressed here with the same numerals in the next section.

## 10.2 Resolving Points of Confusion

I In the Li-Co-Mn-O system, Kim et al. [19] stated that the composition line joining  $\text{LiCoO}_2$  to  $\text{Li}_2\text{MnO}_3$  forms a solid-solution while Bareño et al. [24] determined that samples near the center of the line phase separate into layered-layered composites on

the 2-10 nm length scale. The combinatorial work described in Chapter 4 demonstrated that the line was a solid solution if quenched from at least 800°C, implying that at these temperatures the high entropy of the solid solutions result in the lowest free energies. However, upon extreme slow cooling, samples clearly phase separated near the center of the composition line. This showed that internal energy plays a greater role below 800°C and these results were confirmed with a Monte Carlo simulation. At intermediate cooling rates, XRD peaks broadened at compositions where phase separation was seen upon slow cooling. This broadening was attributed to the formation of layered-layered nano-composites as seen by Bareño. Thus, the center of the solid-solution phase separates into nano-composites during regular cooling.

**II** Bareño et al. [24] claimed that the phase separation along the  $\text{LiCoO}_2$  -  $\text{Li}_2\text{MnO}_3$  line involved the formation of  $\text{LiCoO}_2$  (Co on the TM layers) and  $\text{Li}_2\text{MnO}_3$  ( $\text{Li}_{1/3}\text{Mn}_{2/3}$  on the TM layers) domains. The combinatorial work showed that the phase separation does not occur over the whole composition line. Even at the slow cooling rate of 1°C/min the two domains were roughly 80 % Co, 20 %  $\text{Li}_{1/3}\text{Mn}_{2/3}$  and 20 % Co, 80 %  $\text{Li}_{1/3}\text{Mn}_{2/3}$ . This result suggests that although careful TEM studies can be useful in finding nano-composites, another method is required to determine the compositions of the domains present. It is also important to note that the phase separation can be avoided entirely by quenching or making materials at compositions near the end-members of the composition line.

**III** Lithium loss during synthesis is either viewed as  $\text{Li}_2\text{O}$  evaporation [31] or the formation of lithium peroxide vapour [32]. In the process of optimizing the combinatorial synthesis method, it was found that lithium loss occurred primarily by way of the formation of lithium peroxide or, at the very least, involved  $\text{Li}_2\text{O}$  reacting with oxygen. Samples heated in oxygen-free atmospheres showed solid lithium oxide in the XRD while samples heated in oxygen-containing atmospheres did not. This implies that  $\text{LiO}_2$  does not evaporate under the conditions used to make electrode materials, but rather it must react with oxygen in order to leave the sample.

**IV** A number of researchers have found a rocksalt contaminant in either spinel or layered-spinel materials in the Li-Mn-Ni-O system [35, 38, 39]. The composition and structure of this contaminant was under debate prior to the current thesis. The results

of the combinatorial study show that the contaminant, when slow cooled in oxygen, had metallic composition  $\text{Li}_{0.22}\text{Mn}_{0.16}\text{Ni}_{0.62}$  which lies well inside the Gibbs triangle and not on the Li-Ni line as previously believed. The structure of this material is a cubic rocksalt with a  $2 \times 2 \times 2$  superlattice with ordering of manganese on one site and lithium, nickel and vacancies on another.

**V** The  $\text{LiNi}_{0.5}\text{Mn}_{1.5}\text{O}_4$  spinel material phase separates in air forming the rocksalt material already mentioned and a spinel lying higher in the Gibbs triangle [35]. However,  $\text{LiNi}_{0.5}\text{Mn}_{0.5}\text{O}_4$  may also accommodate oxygen vacancies [40, 41]. It is difficult to distinguish these two processes in air because the sample is two-phase and both the phase separation and the formation of oxygen vacancies involve the loss of oxygen and an increase in lattice parameter. However, in oxygen, this composition is single-phase and the lattice parameter contour plots in Chapter 5 clearly show a larger lattice parameter for the quenched sample. This shows that the Li-Mn-Ni-O spinel materials do sustain oxygen vacancies at high temperature, whereas the Li-Mn-O spinels do not as the lattice parameters do not change dramatically here.

**VI** The lithium-rich layered line from  $\text{LiNi}_{0.5}\text{Mn}_{0.5}\text{O}_2$  to  $\text{Li}_2\text{MnO}_3$  was considered to be either solid solutions [3] or layered-layered nano-composites [44] in the literature. Once again, the results from this project showed that the structure of these materials is strongly affected by cooling rate. If quenched from above  $800^\circ\text{C}$  in air, the entire composition line is single-phase. If cooled more slowly, the samples near the  $\text{LiNi}_{0.5}\text{Mn}_{0.5}\text{O}_2$  end of the composition line phase separate into layered-layered nano-composites. If cooled even more slowly, these samples will form layered-layered composites or even layered-layered-rocksalt materials. In terms of electrochemistry, the layered-layered composites were found to have lower capacity and a higher impedance than single-phase samples synthesized with the same metallic composition. This poor performance of the layered-layered composites may be attributed to the fact that one of the layered materials must have more nickel on the lithium layer than  $\text{LiNi}_{0.5}\text{Mn}_{0.5}\text{O}_2$  (i.e. more than 10 %). When this nickel clusters during phase separation, lithium diffusion may be severely hindered. It is also of note that the material over which there has been the most debate,  $\text{Li}_{1.2}\text{Ni}_{0.2}\text{Mn}_{0.6}\text{O}_2$  [45, 47], is very near to the boundary of the layered region when regular cooled. As such, differing opinions as

to whether or not this material is single-phase may simply be due to slight differences in synthesis conditions and compositions.

**VII** Materials along the lithium-rich layered line from  $\text{LiNi}_{0.5}\text{Mn}_{0.5}\text{O}_2$  to  $\text{Li}_2\text{MnO}_3$  are generally considered to contain  $\text{Ni}^{2+}$  and  $\text{Mn}^{4+}$  [50, 51]. However, Simonin et al. [49] recently found that the magnetic moment in one such layered material was too low and this was attributed to some manganese being in the 3+ state. This material,  $\text{Li}_{1.2}\text{Ni}_{0.2}\text{Mn}_{0.6}\text{O}_2$ , is in the “bump” region in the layered material on the Li-Mn-Ni-O face in Figure 10.1. Materials in this part of the phase diagram were shown to contain metal site vacancies in Chapter 8. The presence of some vacancies could very well account for the lowering of the overall magnetic moment of the samples. XANES and redox titrations confirmed that manganese was in fact in the 4+ state in these materials. This work also demonstrated that there is a solid solution line from  $\text{Li}_2\text{MnO}_3$  to  $\text{Li}[\text{Ni}_{1/6}\square_{1/6}\text{Mn}_{2/3}]\text{O}_2$ . Along this line, the transition metal layers all have 2/3 manganese occupation allowing for ordering on two  $\sqrt{3} \times \sqrt{3}$  superlattices. This gave rise to sharp superlattice peaks in the XRD patterns and the Monte Carlo simulation demonstrated that these structures do not phase separate into layered-layered composites.

**VIII** Some layered materials in the Li-Mn-Ni-O system lose a significant amount of lithium during synthesis. Typically, researchers counter this by adding a small amount of excess lithium and assume it is lost during synthesis (e.g. Refs. [52, 53]). However, the phase diagrams here show that most lithium-rich structures in the Li-Mn-Ni-O system can accommodate more lithium without phase separating. It can no longer be assumed that all excess lithium is lost during synthesis. Elemental analysis is therefore required to determine the composition of samples after heating. The contour plots generated in Chapter 7 can also be used to obtain approximate compositions. These contours show that as one adds excess lithium the  $c$  axis decreases rapidly, while the  $a$  axis is reduced more gradually. As such, it is vital to use both parameters in identifying final materials. Recognizing the actual compositions of the sample also helps explain differences in electrochemistry found in the literature. For example, Lin et al. [54] made a  $\text{LiNi}_{0.5}\text{Mn}_{0.5}\text{O}_2$  sample without excess lithium that showed a lower capacity than materials made by Lu et al. [3]. The samples made by Lu used

LiOH to cause co-precipitation of the mixed transition metal hydroxide precursor such that a small amount of excess lithium was inevitable. As such, the Lu sample was just within the layered region while the Lin sample was slightly outside. In the previous chapter, it was shown that this results in the single-phase material having a significantly higher capacity, consistent with the published results from Lu and Lin. A more extreme example of making  $\text{LiNi}_{0.5}\text{Mn}_{0.5}\text{O}_2$  with excess lithium was published by Ohzuku et al. [53]. The contour plots were used to demonstrate that this sample lost little of the excess lithium during synthesis and the electrochemical performance was therefore attributed to being a lithium-rich layered material.

Two articles show very strange XRD patterns for  $\text{LiNi}_{0.5}\text{Mn}_{0.5}\text{O}_2$ . **IX** The first was published by Jo et al. [55] and showed extreme peak broadening when regular cooled in oxygen. This was attributed to crystallites on the order of 14 nm. Here, it was shown that samples phase separate into layered-layered composites under such conditions. Therefore, the peak broadening seen by Jo was due to phase separation and not small crystallites since 14 nm is extremely small for having been heated for 3 h at 800°C. **X** The second strange result was obtained by Hinuma et al. [56] who found that a single-phase  $\text{LiNi}_{0.5}\text{Mn}_{0.5}\text{O}_2$  underwent a complex phase separation upon annealing at 600°C and a return to single-phase upon re-heating to 1000°C. The new phases appearing upon annealing were not identified in the original paper. The transformations can now be understood. The layered boundary is high in the Gibbs triangle at high temperature such that the initial material synthesized at 1000°C was single-phase. Upon annealing at 600°C the boundary was lower in the Gibbs triangle and the sample was then in the layered-layered-rocksalt three-phase region determined in Chapter 6. The XRD pattern of the 600°C annealed sample shown in the introduction is consistent with the R, N and M phases identified here. These transformations were also shown to be reversible in Chapter 7 explaining the return to single-phase upon re-heating to 1000°C.

**XI** Much work has been done in trying to develop layered-spinel composite electrodes in the Li-Mn-Ni-O system, but there was a poor understanding of the nature of the co-existence region. The work here shows that the layered-spinel region is small and ties to layered materials in the “bump” region discussed extensively in Chapter

8. Slow cooling in the layered-spinel two-phase region may result in the presence of some rocksalt material which grows rapidly as the three-phase regions transform. The rest of the co-existence region contains three-phase materials. Layered-layered-spinel materials can be made by quenching, though one of the layered materials is the disordered N phase discussed in Chapter 6. The N-material has poor electrochemistry and as such should be avoided. Kim et al. [95] have recently claimed to make a layered-layered-spinel material under regular cooling conditions. This cannot be done as rocksalt will always be present in the three-phase samples that are not quenched. Instead the materials made by Kim were near enough to the Li-Mn line to be layered-spinel composites.

### 10.3 Future Work

There are now a wide variety of studies that can be performed using the PixSys solution-processing robot to synthesize combinatorial positive electrode materials. The first opportunity for continued research in combinatorial positive electrode materials is to adapt the combinatorial electrochemical method used by Fleischauer [96] for negative electrode materials. The primary challenge here is that the combinatorial positive electrodes are synthesized as powders and cannot be readily made by sputtering. The project of adapting the 64 channel combinatorial electrochemistry method for powders made using the PixSys robot is underway. Having both structural and electrochemical information for the combinatorial samples would be very useful in the search for promising new electrode materials.

Even without the electrochemical information, there are now a number of composition spaces that are worth studying with XRD of combinatorial samples. The first is to map out the single-phase regions in the Li-Co-Mn-Ni-O system. The main challenge with respect to mapping out the entire pseudo-quaternary system involves the co-existence regions. Since the layered boundaries are surfaces, it will be extremely difficult to determine directions of tie-lines. Nonetheless, it should be possible to identify approximate boundaries using the visual inspection of XRD patterns in a very large array of samples spanning hundreds of compositions. Mapping out the single-phase regions in the entire pyramid is therefore the main objective for on-going

combinatorial work and this project has also already begun.

The robot can also be used to study any number of systems where a few single-phase structures of interest for positive electrode materials are already known. For example,  $\text{LiFePO}_4$  has been used commercially as a relatively high power electrode material [97] and many efforts have been made to substitute a variety of atoms for either the iron or the phosphorous [98–100]. Efforts are now being made to develop a  $\text{Li}_2\text{MSiO}_4$  material with  $\text{M} = (\text{Fe}, \text{Mn})$  in order to cycle two lithium ions per formula unit [101]. All these efforts can be helped significantly by complete phase diagrams. Likely compositions where two-lithium cycling is possible could then be identified and tested.

The combinatorial approach discussed at length here for lithium containing layered oxides could also be of use in sodium-ion battery research where commercially viable electrode systems are still under development. Promising sodium layered oxide materials with varying amounts of iron and manganese on the transition metal layer are being studied [102,103]. Making these materials with the combinatorial method is not trivial given that sodium loss during synthesis is more severe than lithium loss in layered materials. Assuming sodium loss can be reduced to a manageable level as was lithium loss in this thesis, a rapid screening of potential positive electrode materials for sodium-ion batteries could lead to new materials permitting sodium-ion batteries to become a viable alternative to lithium-ion batteries.

In terms of optimizing the search for promising positive electrode materials with the highest energy density, the current research strongly suggests that the best approach is to ensure that the samples lie within the single-phase layered region and in some cases they should be made as near as possible to the boundaries of these regions. The phase diagrams generated here should therefore be of significant value to Li-ion battery researchers. Two factors favouring the layered structures have been identified: increasing the synthesis temperature and lowering the oxygen partial pressure. Both of these conditions result in a larger single-phase layered region such that a greater range of compositions remain single-phase during regular cooling. There is therefore still a considerable amount of work that can be done in the Li-Mn-Ni-O pseudo-ternary system. Much of this requires synthesis of bulk samples in order to



perform a variety of tests to find the optimum compositions and synthesis conditions for lithium-rich layered oxides.

There are also opportunities to make interesting core-shell materials in the Li-Mn-Ni-O system. One challenge with core-shell particles has always been to maintain the core-shell structure while heating at sufficiently high temperatures to make the desired materials. The quenched phase diagram shows the equilibrium phases such that tie-lines show which core-shell materials are possible during extended heating periods at that particular temperature. This therefore allows for careful selection of compositions and heating temperature in order to maintain the desired co-existence. This challenging project is also underway. Furthermore, as the combinatorial project in the Gibbs pyramid progresses, there will be opportunities to study new materials meeting the criteria listed in the introduction, namely high energy density and as little cobalt as possible to minimize cost.

## Appendix A

### Copyright Agreements

Copies of all copyright agreements required for figures and tables reprinted with permission throughout the thesis are included here.



**Title:** Local structure and composition studies of  $\text{Li}_{1.2}\text{Ni}_{0.2}\text{Mn}_{0.6}\text{O}_2$  by analytical electron microscopy  
**Author:** C.H. Lei, J. Bareño, J.G. Wen, I. Petrov, S.-H. Kang, D.P. Abraham  
**Publication:** Journal of Power Sources  
**Publisher:** Elsevier  
**Date:** 15 March 2008  
Copyright © 2008, Elsevier

Logged in as:  
Eric McCalla  
Account #:  
3000695528

LOGOUT

#### Order Completed

Thank you very much for your order.

This is a License Agreement between Eric McCalla ("You") and Elsevier ("Elsevier"). The license consists of your order details, the terms and conditions provided by Elsevier, and the [payment terms and conditions](#).

[Get the printable license.](#)

License Number	3230860182779
License date	Sep 16, 2013
Licensed content publisher	Elsevier
Licensed content publication	Journal of Power Sources
Licensed content title	Local structure and composition studies of $\text{Li}_{1.2}\text{Ni}_{0.2}\text{Mn}_{0.6}\text{O}_2$ by analytical electron microscopy
Licensed content author	C.H. Lei, J. Bareño, J.G. Wen, I. Petrov, S.-H. Kang, D.P. Abraham
Licensed content date	15 March 2008
Licensed content volume number	178
Licensed content issue number	1
Number of pages	12
Type of Use	reuse in a thesis/dissertation
Portion	figures/tables/illustrations
Number of figures/tables/illustrations	1
Format	electronic
Are you the author of this Elsevier article?	No
Will you be translating?	No
Order reference number	
Title of your thesis/dissertation	Structural and Electrochemical Studies of the Li-Mn-Ni-O and Li-Co-Mn-O Pseudo-Ternary Systems
Expected completion date	Oct 2013
Estimated size (number of pages)	200
Elsevier VAT number	GB 494 6272 12

## License Details

This is a License Agreement between Eric McCalla ("You") and Elsevier ("Elsevier"). The license consists of your order details, the terms and conditions provided by Elsevier, and the [payment terms and conditions](#).

[Get the printable license.](#)

License Number	3230850895978
License date	Sep 16, 2013
Licensed content publisher	Elsevier
Licensed content publication	Electrochemistry Communications
Licensed content title	Electrochemical properties of $\text{Li}(\text{Li}_{1-x})_3\text{Co}_x\text{Mn}_{2-2x}\text{O}_2$ ( $0 < x < 1$ ) solid solutions prepared by poly-vinyl alcohol (PVA) method
Licensed content author	Jung-Min Kim, Syo Tsuruta, Naoki Kumagai
Licensed content date	January 2007
Licensed content volume number	9
Licensed content issue number	1
Number of pages	6
Type of Use	reuse in a thesis/dissertation
Portion	figures/tables/illustrations
Number of figures/tables/illustrations	1
Format	electronic
Are you the author of this Elsevier article?	No
Will you be translating?	No
Order reference number	None
Title of your thesis/dissertation	Structural and Electrochemical Studies of the $\text{Li-Mn-Ni-O}$ and $\text{Li-Co-Mn-O}$ Pseudo-Ternary Systems
Expected completion date	Oct 20 13
Estimated size (number of pages)	200
Elsevier VAT number	GB 494 6272 12



**ACS Publications** Title:  
High quality. High impact.

Long-Range and Local Structure  
in the Layered Oxide  
 $\text{Li}_{1.2}\text{Co}_{0.4}\text{Mn}_{0.4}\text{O}_2$

**Author:** J. Bareño, M. Balasubramanian,  
S. H. Kang, J. G. Wen, C. H. Lei,  
S. V. Pol, I. Petrov, and D. P.  
Abraham

Logged in as:  
Eric McCallb  
Account # :  
3000695528

[LOGOUT](#)

**Publication:** Chemistry of Materials  
**Publisher:** American Chemical Society  
**Date:** Apr 1, 2011  
Copyright © 2011, American Chemical Society

#### PERMISSION/LICENSE IS GRANTED FOR YOUR ORDER AT NO CHARGE

This type of permission/license, instead of the standard Terms & Conditions, is sent to you because no fee is being charged for your order. Please note the following:

- Permission is granted for your request in both print and electronic formats, and translations.
- If figures and/or tables were requested, they may be adapted or used in part.
- Please print this page for your records and send a copy of it to your publisher/graduate school.
- Appropriate credit for the requested material should be given as follows: "Reprinted (adapted) with permission from (COMPLETE REFERENCE CITATION). Copyright (YEAR) American Chemical Society." Insert appropriate information in place of the capitalized words.
- One-time permission is granted only for the use specified in your request. No additional uses are granted (such as derivative works or other editions). For any other uses, please submit a new request.



**Title:** Structural study of  $\text{Li}_2\text{MnO}_3$  by electron microscopy  
**Author:** C. H. Lei  
**Publication:** Journal of Materials Science (full set)  
**Publisher:** Springer  
**Date:** Jan 1, 2009  
 Copyright © 2009, U.S. Department of Energy, Argonne National Laboratory

Logged in as:  
 Eric McCalla  
 Account #: 3000695528

LOGOUT

### Order Completed

Thank you very much for your order.

This is a License Agreement between Eric McCalla ("You") and Springer ("Springer"). The license consists of your order details, the terms and conditions provided by Springer, and the [payment terms and conditions](#).

[Get the printable license.](#)

License Number	3230860307422
License date	Sep 16, 2013
Licensed content publisher	Springer
Licensed content publication	Journal of Materials Science (full set)
Licensed content title	Structural study of $\text{Li}_2\text{MnO}_3$ by electron microscopy
Licensed content author	C. H. Lei
Licensed content date	Jan 1, 2009
Volume number	44
Issue number	20
Type of Use	Thesis/Dissertation
Portion	Figures
Author of this Springer article	No
Title of your thesis / dissertation	Structural and Electrochemical Studies of the Li-Mn-Ni-O and Li-Co-Mn-O Pseudo-Ternary Systems
Expected completion date	Oct 2013
Estimated size(pages)	200



**ACS Publications** Title:  
High quality. High impact.

Atomic Structure of a  
Lithium-Rich Layered Oxide  
Material for Lithium-Ion  
Batteries: Evidence of a Solid  
Solution

Logged in as:

Eric McCall

Account #:

3000695528

[LOGOUT](#)

**Author:** Karalee A. Jarvis, Zengqiang  
Deng, Lawrence F. Allard,  
Arumugam Manthiram, and  
Paulo J. Ferreira

**Publication:** Chemistry of Materials

**Publisher:** American Chemical Society

**Date:** Aug 1, 2011

Copyright © 2011, American Chemical Society

#### **PERMISSION/LICENSE IS GRANTED FOR YOUR ORDER AT NO CHARGE**

This type of permission/license, instead of the standard Terms & Conditions, is sent to you because no fee is being charged for your order. Please note the following:

- Permission is granted for your request in both print and electronic formats, and translations.
- If figures and/or tables were requested, they may be adapted or used in part.
- Please print this page for your records and send a copy of it to your publisher/graduate school.
- Appropriate credit for the requested material should be given as follows: "Reprinted (adapted) with permission from (COMPLETE REFERENCE CITATION). Copyright (YEAR) American Chemical Society." Insert appropriate information in place of the capitalized words.
- One-time permission is granted only for the use specified in your request. No additional uses are granted (such as derivative works or other editions). For any other uses, please submit a new request.



**ACS Publications**  
High quality. High impact.

**Title:** Phase Transitions in the  
LiNi<sub>0.5</sub>Mn<sub>0.5</sub>O<sub>2</sub> System with  
Temperature  
**Author:** Yoyo Hinuma, Ying S.  
Meng, Kisuk Kang, and,  
and Gerbrand Ceder\*

Logged in as:  
Eric McCallb  
Account # :  
3000695528

[LOGOUT](#)

**Publication:** Chemistry of Materials  
**Publisher:** American Chemical Society  
**Date:** Apr 1, 2007

Copyright © 2007, American Chemical Society

#### PERMISSION/LICENSE IS GRANTED FOR YOUR ORDER AT NO CHARGE

This type of permission/license, instead of the standard Terms & Conditions, is sent to you because no fee is being charged for your order. Please note the following:

- Permission is granted for your request in both print and electronic formats, and translations.
- If figures and/or tables were requested, they may be adapted or used in part.
- Please print this page for your records and send a copy of it to your publisher/graduate school.
- Appropriate credit for the requested material should be given as follows: "Reprinted (adapted) with permission from (COMPLETE REFERENCE CITATION). Copyright (YEAR) American Chemical Society." Insert appropriate information in place of the capitalized words.
- One-time permission is granted only for the use specified in your request. No additional uses are granted (such as derivative works or other editions). For any other uses, please submit a new request.



**ACS Publications**  
High quality. High impact.

**Title:** Lack of Cation Clustering in  
Li[NixLi1/3-2x/3Mn2/3-x/3]O2  
( $0 < x \leq 1/2$ ) and Li[CrxLi(1-x)/3Mn(2-2x)/3]O2 ( $0 < x < 1$ )

**Author:** Zhonghua Lu, Zhaohui Chen,  
and, and J. R. Dahn\*

**Publication:** Chemistry of Materials

**Publisher:** American Chemical Society

**Date:** Aug 1, 2003

Copyright © 2003, American Chemical Society

Logged in as:

Eric McCallb

Account #:

3000695528

[LOGOUT](#)

#### PERMISSION/LICENSE IS GRANTED FOR YOUR ORDER AT NO CHARGE

This type of permission/license, instead of the standard Terms & Conditions, is sent to you because no fee is being charged for your order. Please note the following:

- Permission is granted for your request in both print and electronic formats, and translations.
- If figures and/or tables were requested, they may be adapted or used in part.
- Please print this page for your records and send a copy of it to your publisher/graduate school.
- Appropriate credit for the requested material should be given as follows: "Reprinted (adapted) with permission from (COMPLETE REFERENCE CITATION). Copyright (YEAR) American Chemical Society." Insert appropriate information in place of the capitalized words.
- One-time permission is granted only for the use specified in your request. No additional uses are granted (such as derivative works or other editions). For any other uses, please submit a new request.





**Title:** Analytical electron microscopy of Li<sub>1.2</sub>Co<sub>0.4</sub>Mn<sub>0.4</sub>O<sub>2</sub> for lithium-ion batteries

**Author:** J.G. Wen, J. Bareño, C.H. Lei, S.H. Kang, M. Balasubramanian, I. Petrov, D.P. Abraham

Logged in as:  
Eric McCalla  
Account #: 3000695528

LOGOUT

**Publication:** Solid State Ionics  
**Publisher:** Elsevier  
**Date:** 3 February 2011  
Copyright © 2011, Elsevier

### Order Completed

Thank you very much for your order.

This is a License Agreement between Eric McCalla ("You") and Elsevier ("Elsevier"). The license consists of your order details, the terms and conditions provided by Elsevier, and the [payment terms and conditions](#).

### [Get the printable license.](#)

License Number	3230851103860
License date	Sep 16, 2013
Licensed content publisher	Elsevier
Licensed content publication	Solid State Ionics
Licensed content title	Analytical electron microscopy of Li <sub>1.2</sub> Co <sub>0.4</sub> Mn <sub>0.4</sub> O <sub>2</sub> for lithium-ion batteries
Licensed content author	J.G. Wen, J. Bareño, C.H. Lei, S.H. Kang, M. Balasubramanian, I. Petrov, D.P. Abraham
Licensed content date	3 February 2011
Licensed content volume number	182
Licensed content issue number	1
Number of pages	10
Type of Use	reuse in a thesis/dissertation
Portion	figures/tables/illustrations
Number of figures/tables/illustrations	1
Format	electronic
Are you the author of this Elsevier article?	No
Will you be translating?	No
Order reference number	
Title of your thesis/dissertation	Structural and Electrochemical Studies of the Li-Mn-Ni-O and Li-Co-Mn-O Pseudo-Ternary Systems
Expected completion date	Oct 2013
Estimated size (number of pages)	200
Elsevier VAT number	GB 494 6272 12



**ACS Publications** Title:  
High quality. High impact.

Synthesis of  $\text{Li}[(\text{Ni}_{0.5}\text{Mn}_{0.5})_{1-x}\text{Li}_x]\text{O}_2$  by Emulsion Drying Method and Impact of Excess Li on Structural and Electrochemical Properties

**Author:** Seung-Taek Myung et al.

**Publication:** Chemistry of Materials

**Publisher:** American Chemical Society

**Date:** Mar 1, 2006

Copyright © 2006, American Chemical Society

Logged in as:

Eric McCallb

Account #:

3000695528

[LOGOUT](#)

#### **PERMISSION/LICENSE IS GRANTED FOR YOUR ORDER AT NO CHARGE**

This type of permission/license, instead of the standard Terms & Conditions, is sent to you because no fee is being charged for your order. Please note the following:

- Permission is granted for your request in both print and electronic formats, and translations.
- If figures and/or tables were requested, they may be adapted or used in part.
- Please print this page for your records and send a copy of it to your publisher/graduate school.
- Appropriate credit for the requested material should be given as follows: "Reprinted (adapted) with permission from (COMPLETE REFERENCE CITATION). Copyright (YEAR) American Chemical Society." Insert appropriate information in place of the capitalized words.
- One-time permission is granted only for the use specified in your request. No additional uses are granted (such as derivative works or other editions). For any other uses, please submit a new request.

### Request for Permission to Reproduce or Re-Publish ECS Material

Please fax this form to: The Electrochemical Society (ECS), Attn: Permissions Requests, 1.609.730.0629.  
You may also e-mail your request to: [copyright@electrochem.org](mailto:copyright@electrochem.org). Include all the information as required on this form. Please allow 3-7 days for your request to be processed.

I am preparing a (choose one):  paper  chapter  book  thesis

entitled: Structural and Electrochemical studies of the Li-Mn-Ni-O and Li-Co-Mn-O pse.

to be published by: Dalhousie University

in an upcoming publication entitled: \_\_\_\_\_

ternary  
system!

I request permission to use the following material in the publication noted above, and request nonexclusive rights for all subsequent editions and in all foreign language translations for distribution throughout the world.

**Description of material to be used**—Indicate what material you wish to use (figures, tables, text, etc.) and give the full bibliographic reference for the source publication. You may attach a separate list, organized by ECS title.

~~One figure from each of:~~

Cabana et al. J. Electrochem Soc vol 156, p A730 (2009)

and - Fig. 2

~~Marks et al. J. Electrochem Soc. vol 158, p A51~~

~~(2011)~~ All figures & tables JES 160(8) A1134-A1138 (2013)

Signature: \_\_\_\_\_

Date: Sept 15, 2013

Name: Eric McCalla

Address: \_\_\_\_\_

Telephone: \_\_\_\_\_

Fax: \_\_\_\_\_

E-mail: eric\_mccalla@yahoo.ca

Permission is granted to reproduce the above-referenced material. Please acknowledge the author(s) and publication data of the original material, and include the words: "Reproduced by permission of The Electrochemical Society."

Sept. 23, 2013  
Date

\_\_\_\_\_  
Ann F. Goedkoop, Director of Publications



**Title:** Lithium loss mechanisms during synthesis of layered  $\text{Li}_x\text{Ni}_2-x\text{O}_2$  for lithium ion batteries

**Author:** E. McCalla, G.H. Carey, J.R. Dahn

**Publication:** Solid State Ionics

**Publisher:** Elsevier

**Date:** Jul 6, 2012

Copyright © 2012, Elsevier

Logged in as:  
Eric McCalla  
Account #: 3000695528

LOGOUT

### Order Completed

Thank you very much for your order.

This is a License Agreement between Eric McCalla ("You") and Elsevier ("Elsevier") The license consists of your order details, the terms and conditions provided by Elsevier, and the [payment terms and conditions](#).

License number	Reference confirmation email for license number
License date	Sep 12, 2013
Licensed content publisher	Elsevier
Licensed content publication	Solid State Ionics
Licensed content title	Lithium loss mechanisms during synthesis of layered $\text{Li}_x\text{Ni}_2-x\text{O}_2$ for lithium ion batteries
Licensed content author	E. McCalla, G.H. Carey, J.R. Dahn
Licensed content date	6 July 2012
Licensed content volume number	219
Number of pages	9
Type of Use	reuse in a thesis/dissertation
Portion	figures/tables/illustrations
Number of figures/tables/illustrations	All
Actual number of figures/tables/illustrations	11
Format	electronic
Are you the author of this Elsevier article?	Yes
Will you be translating?	No
Order reference number	
Title of your thesis/dissertation	Structural and Electrochemical Studies of the Li-Mn-Ni-O and Li-Co-Mn-O Pseudo-Ternary Systems
Expected completion date	Oct 2013
Elsevier VAT number	GB 494 6272 12



**ACS Publications** Title:  
High quality. High impact.

Formation of Layered-Layered  
Composites in the Li-Co-Mn  
Oxide Pseudoternary System  
during Slow Cooling

Logged in as:  
Eric McCalla  
Account #: 3000695528

**Author:** E. McCalla, C. M. Lowartz, C. R.  
Brown, and J. R. Dahn

LOGOUT

**Publication:** Chemistry of Materials

**Publisher:** American Chemical Society

**Date:** Mar 1, 2013

Copyright © 2013, American Chemical Society

#### PERMISSION/LICENSE IS GRANTED FOR YOUR ORDER AT NO CHARGE

This type of permission/license, instead of the standard Terms & Conditions, is sent to you because no fee is being charged for your order. Please note the following:

- Permission is granted for your request in both print and electronic formats, and translations.
- If figures and/or tables were requested, they may be adapted or used in part.
- Please print this page for your records and send a copy of it to your publisher/graduate school.
- Appropriate credit for the requested material should be given as follows: "Reprinted (adapted) with permission from (COMPLETE REFERENCE CITATION). Copyright (YEAR) American Chemical Society." Insert appropriate information in place of the capitalized words.
- One-time permission is granted only for the use specified in your request. No additional uses are granted (such as derivative works or other editions). For any other uses, please submit a new request.



**Title:** The spinel and cubic rocksalt solid-solutions in the Li-Mn-Ni oxide pseudo-ternary system  
**Author:** E. McCalla, J.R. Dahn  
**Publication:** Solid State Ionics  
**Publisher:** Elsevier  
**Date:** Jul 1, 2013  
 Copyright © 2013, Elsevier

Logged in as:  
 Eric McCalla  
 Account #: 3000695528

LOGOUT

## Order Completed

Thank you very much for your order.

This is a License Agreement between Eric McCalla ("You") and Elsevier ("Elsevier") The license consists of your order details, the terms and conditions provided by Elsevier, and the [payment terms and conditions](#).

License number	Reference confirmation email for license number
License date	Sep 12, 2013
Licensed content publisher	Elsevier
Licensed content publication	Solid State Ionics
Licensed content title	The spinel and cubic rocksalt solid-solutions in the Li-Mn-Ni oxide pseudo-ternary system
Licensed content author	E. McCalla, J.R. Dahn
Licensed content date	1 July 2013
Licensed content volume number	242
Number of pages	9
Type of Use	reuse in a thesis/dissertation
Portion	figures/tables/illustrations
Number of figures/tables/illustrations	All
Actual number of figures/tables/illustrations	17
Format	electronic
Are you the author of this Elsevier article?	Yes
Will you be translating?	No
Order reference number	
Title of your thesis/dissertation	Structural and Electrochemical Studies of the Li-Mn-Ni-O and Li-Co-Mn-O Pseudo-Ternary Systems
Expected completion date	Oct 2013
Elsevier VAT number	GB 494 6272 12



**ACS Publications** Title:  
High quality. High impact.

Structural Study of the Li-Mn-Ni  
Oxide Pseudoternary System of  
Interest for Positive Electrodes  
of Li-Ion Batteries

Logged in as:

Eric McCalla

Account #:  
3000695528

**Author:** E. McCalla, A. W. Rowe, R.  
Shunmugasundaram, and J. R.  
Dahn

LOGOUT

**Publication:** Chemistry of Materials

**Publisher:** American Chemical Society

**Date:** Mar 1, 2013

Copyright © 2013, American Chemical Society

#### PERMISSION/LICENSE IS GRANTED FOR YOUR ORDER AT NO CHARGE

This type of permission/license, instead of the standard Terms & Conditions, is sent to you because no fee is being charged for your order. Please note the following:

- Permission is granted for your request in both print and electronic formats, and translations.
- If figures and/or tables were requested, they may be adapted or used in part.
- Please print this page for your records and send a copy of it to your publisher/graduate school.
- Appropriate credit for the requested material should be given as follows: "Reprinted (adapted) with permission from (COMPLETE REFERENCE CITATION). Copyright (YEAR) American Chemical Society." Insert appropriate information in place of the capitalized words.
- One-time permission is granted only for the use specified in your request. No additional uses are granted (such as derivative works or other editions). For any other uses, please submit a new request.



**ACS Publications** Title:  
High quality. High impact.

The Role of Metal Site Vacancies  
in Promoting Li-Mn-Ni-O  
Layered Solid Solutions

**Author:** E. McCalla, A. W. Rowe, J.  
Camardese, and J. R. Dahn

**Publication:** Chemistry of Materials

**Publisher:** American Chemical Society

**Date:** Jul 1, 2013

Copyright © 2013, American Chemical Society

Logged in as:

Eric McCalla

Account #:

3000695528

[LOGOUT](#)

#### **PERMISSION/LICENSE IS GRANTED FOR YOUR ORDER AT NO CHARGE**

This type of permission/license, instead of the standard Terms & Conditions, is sent to you because no fee is being charged for your order. Please note the following:

- Permission is granted for your request in both print and electronic formats, and translations.
- If figures and/or tables were requested, they may be adapted or used in part.
- Please print this page for your records and send a copy of it to your publisher/graduate school.
- Appropriate credit for the requested material should be given as follows: "Reprinted (adapted) with permission from (COMPLETE REFERENCE CITATION). Copyright (YEAR) American Chemical Society." Insert appropriate information in place of the capitalized words.
- One-time permission is granted only for the use specified in your request. No additional uses are granted (such as derivative works or other editions). For any other uses, please submit a new request.



## Bibliography

- [1] B. Franklin, *Poor Richard 1734, An Almanack*. Philadelphia: B. Franklin, 1734.
- [2] J. R. Dahn and G. M. Ehrlich, *Handbook of Batteries, third edition, chapter 35*. New York: McGraw-Hill, 2002.
- [3] Z. Lu, L. Y. Beaulieu, R. A. Donabarger, C. L. Thomas, and J. R. Dahn, "Synthesis, structure, and electrochemical behavior of  $\text{Li}[\text{Ni}_x\text{Li}_{1/3-2x/3}\text{Mn}_{2/3-x/3}]\text{O}_2$ ," *Journal of The Electrochemical Society*, vol. 149, no. 6, pp. A778–A791, 2002.
- [4] H. Koga, L. Croguennec, P. Mannessiez, M. Ménétrier, F. Weill, L. Bourgeois, M. Duttine, E. Suard, and C. Delmas, " $\text{Li}_{1.20}\text{Mn}_{0.54}\text{Co}_{0.13}\text{Ni}_{0.13}\text{O}_2$  with different particle sizes as attractive positive electrode materials for lithium-ion batteries: insights into their structure," *The Journal of Physical Chemistry C*, vol. 116, no. 25, pp. 13 497–13 506, 2012.
- [5] Y. Cho, Y. S. Lee, S. A. Park, Y. Lee, and J. Cho, " $\text{LiNi}_{0.8}\text{Co}_{0.15}\text{Al}_{0.05}\text{O}_2$  cathode materials prepared by  $\text{TiO}_2$  nanoparticle coatings on  $\text{Ni}_{0.8}\text{Co}_{0.15}\text{Al}_{0.05}(\text{OH})_2$  precursors," *Electrochimica Acta*, vol. 56, no. 1, pp. 333–339, 2010.
- [6] D. D. MacNeil, Z. Lu, and J. R. Dahn, "Structure and electrochemistry of  $\text{Li}[\text{Ni}_x\text{Co}_{1-2x}\text{Mn}_x]\text{O}_2$  ( $0 \leq x \leq 1/2$ )," *Journal of The Electrochemical Society*, vol. 149, no. 10, pp. A1332–A1336, 2002.
- [7] Y. Gao and J. R. Dahn, "The high temperature phase diagram of  $\text{Li}_{1+x}\text{Mn}_{2-x}\text{O}_4$  and its implications," *Journal of The Electrochemical Society*, vol. 143, no. 6, pp. 1783–1788, 1996.
- [8] T. Takada, H. Hayakawa, E. Akiba, F. Izumi, and B. C. Chakoumakos, "Novel synthesis process and structure refinements of  $\text{Li}_4\text{Mn}_5\text{O}_{12}$  for rechargeable lithium batteries," *Journal of Power Sources*, vol. 68, no. 2, pp. 613–617, 1997.
- [9] J. M. Paulsen and J. R. Dahn, "Phase diagram of Li-Mn-O spinel in air," *Chemistry of Materials*, vol. 11, no. 11, pp. 3065–3079, 1999.
- [10] Z. Lu, D. D. MacNeil, and J. R. Dahn, "Layered  $\text{Li}[\text{Ni}_x\text{Co}_{1-2x}\text{Mn}_x]\text{O}_2$  cathode materials for lithium-ion batteries," *Electrochemical and Solid-State Letters*, vol. 4, no. 12, pp. A200–A203, 2001.
- [11] G. H. Carey and J. R. Dahn, "Combinatorial synthesis of mixed transition metal oxides for lithium-ion batteries," *ACS Combinatorial Science*, vol. 13, no. 2, pp. 186–189, 2011.

- [12] S.-H. Kang and K. Amine, "Synthesis and electrochemical properties of layer-structured  $0.5 \text{Li}(\text{Ni}_{0.5}\text{Mn}_{0.5})\text{O}_2$ - $0.5 \text{Li}(\text{Li}_{1/3}\text{Mn}_{2/3})\text{O}_2$  solid mixture," *Journal of Power sources*, vol. 124, no. 2, pp. 533–537, 2003.
- [13] E. McCalla, A. W. Rowe, R. Shunmugasundaram, and J. R. Dahn, "Structural study of the Li–Mn–Ni oxide pseudoternary system of interest for positive electrodes of Li-ion batteries," *Chemistry of Materials*, vol. 25, no. 6, pp. 989–999, 2013.
- [14] J. Cabana, S.-H. Kang, C. S. Johnson, M. M. Thackeray, and C. P. Grey, "Structural and electrochemical characterization of composite layered-spinel electrodes containing Ni and Mn for Li-ion batteries," *Journal of the Electrochemical Society*, vol. 156, no. 9, pp. A730–A736, 2009.
- [15] S.-H. Park, S.-H. Kang, C. S. Johnson, K. Amine, and M. M. Thackeray, "Lithium–manganese–nickel-oxide electrodes with integrated layered–spinel structures for lithium batteries," *Electrochemistry Communications*, vol. 9, no. 2, pp. 262–268, 2007.
- [16] H. Koga, L. Croguennec, M. Ménétrier, P. Mannesiez, F. Weill, and C. Delmas, "Different oxygen redox participation for bulk and surface: a possible global explanation for the cycling mechanism of  $\text{Li}_{1.20}\text{Mn}_{0.54}\text{Co}_{0.13}\text{Ni}_{0.13}\text{O}_2$ ," *Journal of Power Sources*, 2013.
- [17] M. Sathiya, K. Ramesha, G. Rouse, D. Foix, D. Gonbeau, A. Prakash, M. Doublet, K. Hemalatha, and J. M. Tarascon, "High performance  $\text{Li}_2\text{Ru}_{1-y}\text{Mn}_y\text{O}_3$  ( $0.2 \leq y \leq 0.8$ ) cathode materials for rechargeable lithium-ion batteries: Their understanding," *Chemistry of Materials*, vol. 25, no. 7, pp. 1121–1131, 2013.
- [18] A. R. Armstrong, M. Holzappel, P. Novák, C. S. Johnson, S. H. Kang, M. M. Thackeray, and P. G. Bruce, "Demonstrating oxygen loss and associated structural reorganization in the lithium battery cathode  $\text{Li}[\text{Ni}_{0.2}\text{Li}_{0.2}\text{Mn}_{0.6}]\text{O}_2$ ," *Journal of the American Chemical Society*, vol. 128, no. 26, pp. 8694–8698, 2006.
- [19] J.-M. Kim, S. Tsuruta, and N. Kumagai, "Electrochemical properties of  $\text{Li}(\text{Li}_{(1-x)/3}\text{Co}_x\text{Mn}_{(2-2x)/3})\text{O}_2$  ( $0 \leq x \leq 1$ ) solid solutions prepared by poly-vinyl alcohol (PVA) method," *Electrochemistry Communications*, vol. 9, no. 1, pp. 103–108, 2007.
- [20] H. Kawai, M. Nagata, H. Kageyama, H. Tukamoto, and A. R. West, "5 V lithium cathodes based on spinel solid solutions  $\text{Li}_2\text{Co}_{1+x}\text{Mn}_{3-x}\text{O}_8$ :  $-1 \leq x \leq 1$ ," *Electrochimica Acta*, vol. 45, no. 1, pp. 315–327, 1999.
- [21] J. M. Amarilla, J. L. M. De Vidales, and R. M. Rojas, "Electrochemical characteristics of cobalt-doped  $\text{LiCo}_y\text{Mn}_{2-y}\text{O}_4$  ( $0 \leq y \leq 0.66$ ) spinels synthesized at low temperature from  $\text{Co}_x\text{Mn}_{3-x}\text{O}_4$  precursors," *Solid State Ionics*, vol. 127, no. 1-2, pp. 73–81, 2000.

- [22] L. Guohua, H. Ikuta, T. Uchida, and M. Wakihara, "The spinel phases  $\text{LiM}_y\text{Mn}_{2-y}\text{O}_4$  (M= Co, Cr, Ni) as the cathode for rechargeable lithium batteries," *Journal of the Electrochemical Society*, vol. 143, no. 1, pp. 178–182, 1996.
- [23] J. G. Wen, J. Bareño, C. H. Lei, S. H. Kang, M. Balasubramanian, I. Petrov, and D. P. Abraham, "Analytical electron microscopy of  $\text{Li}_{1.2}\text{Co}_{0.4}\text{Mn}_{0.4}\text{O}_2$  for lithium-ion batteries," *Solid State Ionics*, vol. 182, no. 1, pp. 98–107, 2011.
- [24] J. Bareño, M. Balasubramanian, S. H. Kang, J. G. Wen, C. H. Lei, S. V. Pol, I. Petrov, and D. P. Abraham, "Long-Range and local structure in the layered oxide  $\text{Li}_{1.2}\text{Co}_{0.4}\text{Mn}_{0.4}\text{O}_2$ ," *Chemistry of Materials*, vol. 23, no. 8, pp. 2039–2050, 2011.
- [25] J. Bréger, M. Jiang, N. Dupré, Y. S. Meng, Y. Shao-Horn, G. Ceder, and C. P. Grey, "High-resolution X-ray diffraction, DIFFaX, NMR and first principles study of disorder in the  $\text{Li}_2\text{MnO}_3\text{-Li}[\text{Ni}_{1/2}\text{Mn}_{1/2}]\text{O}_2$  solid solution," *Journal of Solid State Chemistry*, vol. 178, no. 9, pp. 2575–2585, 2005.
- [26] H. P. Klug and L. E. Alexander, *X-Ray Diffraction Procedures*. New York: John Wiley and Sons, 1974.
- [27] Y. S. Meng, Y. W. Wu, B. J. Hwang, Y. Li, and G. Ceder, "Combining ab initio computation with experiments for designing new electrode materials for advanced lithium batteries:  $\text{LiNi}_{1/3}\text{Fe}_{1/6}\text{Co}_{1/6}\text{Mn}_{1/3}\text{O}_2$ ," *Journal of The Electrochemical Society*, vol. 151, no. 8, pp. A1134–A1140, 2004.
- [28] S. Ping Ong, L. Wang, B. Kang, and G. Ceder, "Li- Fe- P-  $\text{O}_2$  phase diagram from first principles calculations," *Chemistry of Materials*, vol. 20, no. 5, pp. 1798–1807, 2008.
- [29] A. Jain, G. Hautier, C. J. Moore, S. Ping Ong, C. C. Fischer, T. Mueller, K. A. Persson, and G. Ceder, "A high-throughput infrastructure for density functional theory calculations," *Computational Materials Science*, vol. 50, no. 8, pp. 2295–2310, 2011.
- [30] S. P. Ong, A. Jain, G. Hautier, M. Kocher, S. Cholia, D. Gunter, D. Bailey, K. Skinner, K. Persson, and G. Ceder, <http://materialsproject.org>, 2011.
- [31] E. Antolini, "Hexagonal-to-cubic phase transition by  $\text{Li}_2\text{O}$  evaporation from ordered  $\text{Li}_x\text{Ni}_{1-x}\text{O}$  solid solution," *Physica Status Solidi (A)*, vol. 173, no. 2, pp. 357–364, 1999.
- [32] T. Sata, "High-temperature vaporization of  $\text{Li}_2\text{O}$  component from solid solution  $\text{Li}_x\text{Ni}_{1-x}\text{O}$  in air," *Ceramics International*, vol. 24, no. 1, pp. 53–59, 1998.

- [33] J. R. Dahn, U. von Sacken, and C. A. Michal, "Structure and electrochemistry of  $\text{Li}_{1\pm y}\text{NiO}_2$  and a new  $\text{Li}_2\text{NiO}_2$  phase with the  $\text{Ni}(\text{OH})_2$  structure," *Solid State Ionics*, vol. 44, no. 1, pp. 87–97, 1990.
- [34] R. Moshtev, P. Zlatilova, V. Manev, and K. Tagawa, "Synthesis of  $\text{LiNiO}_2$  in air atmosphere: X-ray diffraction characterization and electrochemical investigation," *Journal of Power Sources*, vol. 62, no. 1, pp. 59–66, 1996.
- [35] Q. Zhong, A. Bonakdarpour, M. Zhang, Y. Gao, and J. R. Dahn, "Synthesis and electrochemistry of  $\text{LiNi}_x\text{Mn}_{2-x}\text{O}_4$ ," *Journal of The Electrochemical Society*, vol. 144, no. 1, pp. 205–213, 1997.
- [36] H. Kobayashi, H. Sakaebe, H. Kageyama, K. Tatsumi, Y. Arachi, and T. Kamiyama, "Changes in the structure and physical properties of the solid solution  $\text{LiNi}_{1-x}\text{Mn}_x\text{O}_2$  with variation in its composition," *Journal of Materials Chemistry*, vol. 13, no. 3, pp. 590–595, 2003.
- [37] W. Li, J. N. Reimers, and J. R. Dahn, "Crystal structure of  $\text{Li}_x\text{Ni}_{2-x}\text{O}_2$  and a lattice-gas model for the order-disorder transition," *Physical Review B*, vol. 46, no. 6, pp. 3236–3246, 1992.
- [38] L.-W. Ma, B.-Z. Chen, X.-C. Shi, W. Zhang, and X.-Y. Yang, "Structure and stability of Li-Mn-Ni composite oxides as lithium ion sieve precursors in acidic medium," *Journal of Central South University of Technology*, vol. 18, pp. 314–318, 2011.
- [39] J. Cabana, M. Casas-Cabanas, F. O. Omenya, N. A. Chernova, D. Zeng, M. S. Whittingham, and C. P. Grey, "Composition-structure relationships in the Li-ion battery electrode material  $\text{LiNi}_{0.5}\text{Mn}_{1.5}\text{O}_4$ ," *Chemistry of Materials*, vol. 24, no. 15, pp. 2952–2964, 2012.
- [40] S. H. Park, S. W. Oh, S. H. Kang, I. Belharouak, K. Amine, and Y. K. Sun, "Comparative study of different crystallographic structure of  $\text{LiNi}_{0.5}\text{Mn}_{1.5}\text{O}_{4-\delta}$  cathodes with wide operation voltage (2.0-5.0 v)," *Electrochimica Acta*, vol. 52, no. 25, pp. 7226–7230, 2007.
- [41] Y. Idemoto, H. Narai, and N. Koura, "Crystal structure and cathode performance dependence on oxygen content of  $\text{LiMn}_{1.5}\text{Ni}_{0.5}\text{O}_4$  as a cathode material for secondary lithium batteries," *Journal of Power Sources*, vol. 119, pp. 125–129, 2003.
- [42] S. T. Myung, S. Komaba, N. Kumagai, H. Yashiro, H. T. Chung, and T. H. Cho, "Nano-crystalline  $\text{LiNi}_{0.5}\text{Mn}_{1.5}\text{O}_4$  synthesized by emulsion drying method," *Electrochimica Acta*, vol. 47, no. 15, pp. 2543–2549, 2002.

- [43] Y. Meng, G. Ceder, C. Grey, W.-S. Yoon, M. Jiang, J. Breger, and Y. Shao-Horn, "Cation ordering in layered O3  $\text{Li}[\text{Ni}_x\text{Li}_{1/3-2x/3}\text{Mn}_{2/3-x/3}]\text{O}_2$  ( $0 \leq x \leq 1/2$ ) compounds," *Chemistry of Materials*, vol. 17, no. 9, pp. 2386–2394, 2005.
- [44] M. M. Thackeray, C. S. Johnson, J. T. Vaughey, N. Li, and S. A. Hackney, "Advances in manganese-oxide composite electrodes for lithium-ion batteries," *Journal of Materials Chemistry*, vol. 15, no. 23, pp. 2257–2267, 2005.
- [45] C. H. Lei, J. Bareño, J. G. Wen, I. Petrov, S. H. Kang, and D. P. Abraham, "Local structure and composition studies of  $\text{Li}_{1.2}\text{Ni}_{0.2}\text{Mn}_{0.6}\text{O}_2$  by analytical electron microscopy," *Journal of Power Sources*, vol. 178, no. 1, pp. 422–433, 2008.
- [46] Z. Lu, Z. Chen, and J. R. Dahn, "Lack of cation clustering in  $\text{Li}[\text{Ni}_x\text{Li}_{1/3-2x/3}\text{Mn}_{2/3-x/3}]\text{O}_2$  ( $0 \leq x \leq 1/2$ ) and  $\text{Li}[\text{Cr}_x\text{Li}_{(1-x)/3}\text{Mn}_{(2-2x)/3}]\text{O}_2$  ( $0 \leq x \leq 1$ )," *Chemistry of Materials*, vol. 15, no. 16, pp. 3214–3220, 2003.
- [47] K. A. Jarvis, Z. Deng, L. F. Allard, A. Manthiram, and P. J. Ferreira, "Atomic structure of a lithium-rich layered oxide material for lithium-ion batteries: Evidence of a solid solution," *Chemistry of Materials*, vol. 23, no. 16, pp. 3614–3621, 2011.
- [48] C. H. Lei, J. G. Wen, M. Sardela, J. Bareño, I. Petrov, S. H. Kang, and D. P. Abraham, "Structural study of  $\text{Li}_2\text{MnO}_3$  by electron microscopy," *Journal of Materials Science*, vol. 44, no. 20, pp. 5579–5587, 2009.
- [49] L. Simonin, J.-F. Colin, V. Ranieri, E. Canévet, J.-F. Martin, C. Bourbon, C. Baehtz, P. Strobel, L. Daniel, and S. Patoux, "In situ investigations of a Li-rich Mn–Ni layered oxide for Li-ion batteries," *Journal of Materials Chemistry*, vol. 22, no. 22, pp. 11 316–11 322, 2012.
- [50] S. Hy, W. N. Su, J. M. Chen, and B. J. Hwang, "Soft x-ray absorption spectroscopic and raman studies on  $\text{Li}_{1.2}\text{Ni}_{0.2}\text{Mn}_{0.6}\text{O}_2$  for lithium-ion batteries," *The Journal of Physical Chemistry C*, vol. 116, no. 48, pp. 25 242–25 247, 2012.
- [51] M. Jiang, B. Key, Y. S. Meng, and C. P. Grey, "Electrochemical and structural study of the layered, Li-excess lithium-ion battery electrode material  $\text{Li}[\text{Li}_{1/9}\text{Ni}_{1/3}\text{Mn}_{5/9}]\text{O}_2$ ," *Chemistry of Materials*, vol. 21, no. 13, pp. 2733–2745, 2009.
- [52] A. van Bommel, L. J. Krause, and J. R. Dahn, "Investigation of the irreversible capacity loss in the lithium-rich oxide  $\text{Li}[\text{Li}_{1/5}\text{Ni}_{1/5}\text{Mn}_{3/5}]\text{O}_2$ ," *Journal of The Electrochemical Society*, vol. 158, no. 6, pp. A731–A735, 2011.
- [53] T. Ohzuku, M. Nagayama, K. Tsuji, and K. Ariyoshi, "High-capacity lithium insertion materials of lithium nickel manganese oxides for advanced lithium-ion batteries: toward rechargeable capacity more than 300 mA hg<sup>-1</sup>," *Journal of Materials Chemistry*, vol. 21, no. 27, pp. 10 179–10 188, 2011.

- [54] H. Lin, J. Zheng, and Y. Yang, "The effects of quenching treatment and  $\text{AlF}_3$  coating on  $\text{LiNi}_{0.5}\text{Mn}_{0.5}\text{O}_2$  cathode materials for lithium-ion battery," *Materials Chemistry and Physics*, vol. 119, no. 3, pp. 519–523, 2010.
- [55] E. B. Jo, S. H. Ju, H. C. Jang, and Y. C. Kang, "The properties of Li-Ni-Mn-O powders prepared by spray pyrolysis," *Journal of Ceramic Processing Research*, vol. 8, no. 5, pp. 352–355, 2007.
- [56] Y. Hinuma, Y. S. Meng, K. Kang, and G. Ceder, "Phase transitions in the  $\text{LiNi}_{0.5}\text{Mn}_{0.5}\text{O}_2$  system with temperature," *Chemistry of Materials*, vol. 19, no. 7, pp. 1790–1800, 2007.
- [57] I. Belharouak, G. M. Koenig Jr, J. Ma, D. P. Wang, and K. Amine, "Identification of  $\text{LiNi}_{0.5}\text{Mn}_{1.5}\text{O}_4$  spinel in layered manganese enriched electrode materials," *Electrochemistry Communications*, vol. 13, no. 3, pp. 232–236, 2011.
- [58] H. Deng, I. Belharouak, R. E. Cook, H. Wu, Y.-K. Sun, and K. Amine, "Nanostructured lithium nickel manganese oxides for lithium-ion batteries," *Journal of The Electrochemical Society*, vol. 157, no. 4, pp. A447–A452, 2010.
- [59] A. van Bommel and J. R. Dahn, "Analysis of the growth mechanism of coprecipitated spherical and dense nickel, manganese, and cobalt-containing hydroxides in the presence of aqueous ammonia," *Chemistry of Materials*, vol. 21, no. 8, pp. 1500–1503, 2009.
- [60] P. R. Bevington, *Data Reduction and Error Analysis for the Physical Sciences*. New York: McGraw Hill, 1969.
- [61] B. E. Warren, *X-Ray Diffraction, second edition*. New York: Dover Publications Inc., 1990.
- [62] S. K. Chatterjee and S. P. S. Gupta, "An integral breadth analysis for particle size and strain determinations in cold-worked fcc alloys," *Journal of Physics D: Applied Physics*, vol. 5, no. 3, pp. 609–612, 1972.
- [63] V. Berbenni, V. Massarotti, D. Capsoni, R. Riccardi, A. Marini, and E. Antolini, "Structural and microstructural study of the formation of the solid solution  $\text{Li}_x\text{Ni}_{1-x}\text{O}$ ," *Solid State Ionics*, vol. 48, no. 1, pp. 101–111, 1991.
- [64] T. Marks, S. Trussler, A. J. Smith, D. Xiong, and J. R. Dahn, "A guide to Li-ion coin-cell electrode making for academic researchers," *Journal of the Electrochemical Society*, vol. 158, no. 1, pp. A51–A57, 2011.
- [65] S. T. Myung, S. Komaba, K. Kurihara, K. Hosoya, N. Kumagai, Y. K. Sun, I. Nakai, M. Yonemura, and T. Kamiyama, "Synthesis of  $\text{Li}[(\text{Ni}_{0.5}\text{Mn}_{0.5})_{1-x}\text{Li}_x]\text{O}_2$  by emulsion drying method and impact of excess Li

- on structural and electrochemical properties,” *Chemistry of Materials*, vol. 18, no. 6, pp. 1658–1666, 2006.
- [66] N. Metropolis, A. W. Rosenbluth, M. N. Rosenbluth, A. H. Teller, and E. Teller, “Equation of state calculations by fast computing machines,” *The Journal of Chemical Physics*, vol. 21, p. 1087, 1953.
- [67] E. McCalla, G. H. Carey, and J. R. Dahn, “Lithium loss mechanisms during synthesis of layered  $\text{Li}_x\text{Ni}_{2-x}\text{O}_2$  for lithium ion batteries,” *Solid State Ionics*, vol. 219, pp. 11–19, 2012.
- [68] G. R. Gavalas, S. Edelstein, M. Flytzani-Stephanopoulos, and T. A. Weston, “Alkali-alumina sorbents for high-temperature removal of  $\text{SO}_2$ ,” *AIChE journal*, vol. 33, no. 2, pp. 258–266, 1987.
- [69] S. M. Lala, L. A. Montoro, and J. M. Rosolen, “ $\text{LiCoO}_2$  sub-microns particles obtained from micro-precipitation in molten stearic acid,” *Journal of Power Sources*, vol. 124, no. 1, pp. 118–123, 2003.
- [70] A. R. Naghash and J. Y. Lee, “Preparation of spinel lithium manganese oxide by aqueous co-precipitation,” *Journal of Power Sources*, vol. 85, no. 2, pp. 284–293, 2000.
- [71] E. Antolini, “Lithium loss kinetics from polycrystalline  $\text{Li}_x\text{Ni}_{1-x}\text{O}$  at high temperatures,” *Journal of Materials Chemistry*, vol. 8, no. 12, pp. 2783–2786, 1998.
- [72] J. B. Goodenough, D. G. Wickham, and W. J. Croft, “Some magnetic and crystallographic properties of the system  $\text{Li}_x^+\text{Ni}_{1-2x}^{++}\text{Ni}_x^{+++}\text{O}$ ,” *Journal of Physics and Chemistry of Solids*, vol. 5, no. 1, pp. 107–116, 1958.
- [73] R. Gunawan and D. Zhang, “Thermal stability and kinetics of decomposition of ammonium nitrate in the presence of pyrite,” *Journal of Hazardous Materials*, vol. 165, no. 1, pp. 751–758, 2009.
- [74] R. D. Vold and G. S. Hattiangdi, “Characterization of heavy metal soaps by X-ray diffraction,” *Industrial & Engineering Chemistry*, vol. 41, no. 10, pp. 2311–2320, 1949.
- [75] V. Berbenni and A. Marini, “Thermogravimetry and X-ray diffraction study of the thermal decomposition processes in  $\text{Li}_2\text{CO}_3$ – $\text{MnCO}_3$  mixtures,” *Journal of Analytical and Applied Pyrolysis*, vol. 62, no. 1, pp. 45–62, 2002.
- [76] E. McCalla, C. M. Lowartz, C. R. Brown, and J. R. Dahn, “Formation of layered-layered composites in the Li-Co-Mn oxide pseudoternary system during slow cooling,” *Chemistry of Materials*, vol. 25, no. 6, pp. 912–918, 2013.

- [77] C. R. Brown, E. McCalla, and J. R. Dahn, "Analysis of the cubic spinel region of the Li-Co-Mn oxide pseudo-ternary system," *accepted by Solid State Ionics*, 2013.
- [78] S. Levasseur, M. Menetrier, E. Suard, and C. Delmas, "Evidence for structural defects in non-stoichiometric HT-LiCoO<sub>2</sub>: electrochemical, electronic properties and <sup>7</sup>Li NMR studies," *Solid State Ionics*, vol. 128, no. 1, pp. 11–24, 2000.
- [79] Y. Sun, Y. Shiosaki, Y. Xia, and H. Noguchi, "The preparation and electrochemical performance of solid solutions LiCoO<sub>2</sub>-Li<sub>2</sub>MnO<sub>3</sub> as cathode materials for lithium ion batteries," *Journal of Power Sources*, vol. 159, no. 2, pp. 1353–1359, 2006.
- [80] A. Van der Ven, M. K. Aydinol, G. Ceder, G. Kresse, and J. Hafner, "First-principles investigation of phase stability in Li<sub>x</sub>CoO<sub>2</sub>," *Physical Review B*, vol. 58, no. 6, p. 2975, 1998.
- [81] E. McCalla and J. R. Dahn, "The spinel and cubic rocksalt solid-solutions in the Li-Mn-Ni oxide pseudo-ternary system," *Solid State Ionics*, vol. 242, pp. 1–9, 2013.
- [82] J. S. Kasper and J. S. Prener, "The crystal structure of Mg<sub>6</sub>MnO<sub>8</sub>," *Acta Crystallographica*, vol. 7, no. 3, pp. 246–248, 1954.
- [83] G. W. Brindley, "The effect of grain or particle size on X-ray reflections from mixed powders and alloys, considered in relation to the quantitative determination of crystalline substances by X-ray methods," *Philosophical Magazine*, vol. 36, no. 256, pp. 347–369, 1945.
- [84] B. J. Neudecker, R. A. Zuhr, B. S. Kwak, J. B. Bates, and J. D. Robertson, "Lithium manganese nickel oxides Li<sub>x</sub>(Mn<sub>y</sub>Ni<sub>1-y</sub>)<sub>2-x</sub>O<sub>2</sub> i. synthesis and characterization of thin films and bulk phases," *Journal of the Electrochemical Society*, vol. 145, no. 12, pp. 4148–4159, 1998.
- [85] E. McCalla, A. W. Rowe, C. R. Brown, L. R. P. Hacquebard, and J. R. Dahn, "How phase transformations during cooling affect Li-Mn-Ni-O positive electrodes in lithium ion batteries," *Journal of The Electrochemical Society*, vol. 160, no. 8, pp. A1134–A1138, 2013.
- [86] F. N. Rhines, *Phase Diagrams in Metallurgy*. New York: McGraw-Hill., 1956.
- [87] T. Ohzuku, and Y. Makimura, "Layered lithium insertion material of LiNi<sub>1/2</sub>Mn<sub>1/2</sub>O<sub>2</sub>: a possible alternative to LiCoO<sub>2</sub> for advanced lithium-ion batteries," *Chemistry Letters*, vol. 30, no. 8, pp. 744–745, 2001.



- [88] C. R. Fell, D. Qian, K. J. Carroll, M. Chi, J. L. Jones, and Y. S. Meng, "Correlation between oxygen vacancy, microstrain, and cation distribution in lithium-excess layered oxides during the first electrochemical cycle," *Chemistry of Materials*, vol. 25, no. 9, pp. 1621–1629, 2013.
- [89] Y. Cho, S. Lee, Y. Lee, T. Hong, and J. Cho, "Spinel-layered core-shell cathode materials for Li-ion batteries," *Advanced Energy Materials*, vol. 1, no. 5, pp. 821–828, 2011.
- [90] E. McCalla, A. W. Rowe, J. Camardese, and J. R. Dahn, "The role of metal site vacancies in promoting Li-Mn-Ni-O layered solid-solutions," *Chemistry of Materials*, vol. 25, no. 13, pp. 2716–2721, 2013.
- [91] C. S. Johnson, J.-S. Kim, A. J. Kropf, A. J. Kahaian, J. T. Vaughey, L. M. Fransson, K. Edström, and M. M. Thackeray, "Structural characterization of layered  $\text{Li}_x\text{Ni}_{0.5}\text{Mn}_{0.5}\text{O}_2$  ( $0 \leq x \leq 2$ ) oxide electrodes for Li batteries," *Chemistry of Materials*, vol. 15, no. 12, pp. 2313–2322, 2003.
- [92] M. Gu, I. Belharouak, J. Zheng, H. Wu, J. Xiao, A. Genc, K. Amine, S. Thethathan, D. R. Baer, and J. G. Zhang, "Formation of the spinel phase in the layered composite cathode used in Li-ion batteries," *ACS Nano*, vol. 7, no. 1, pp. 760–767, 2012.
- [93] E. McCalla, J. Li, A. W. Rowe, and J. R. Dahn, "The negative impact of layered-layered composites on the electrochemistry of Li-Mn-Ni-O positive electrodes for lithium-ion batteries," *submitted to the Journal of The Electrochemical Society*, 2013.
- [94] T. Ohzuku and Y. Makimura, "Layered lithium insertion material of  $\text{LiCo}_{1/3}\text{Ni}_{1/3}\text{Mn}_{1/3}\text{O}_2$  for lithium-ion batteries," *Chemistry Letters*, vol. 30, no. 7, pp. 642–643, 2001.
- [95] D. Kim, G. Sandi, J. R. Croy, K. G. Gallagher, S.-H. Kang, E. Lee, M. D. Slater, C. S. Johnson, and M. M. Thackeray, "Composite 'layered-layered-spinel' cathode structures for lithium-ion batteries," *Journal of The Electrochemical Society*, vol. 160, no. 1, pp. A31–A38, 2013.
- [96] M. Fleischauer and J. Dahn, "Combinatorial investigations of the Si-Al-Mn system for Li-ion battery applications," *Journal of The Electrochemical Society*, vol. 151, no. 8, pp. A1216–A1221, 2004.
- [97] P. Marks, "Dawn of motorsport's electric dream," *New Scientist*, vol. 211, no. 2831, pp. 26–27, 2011.
- [98] N. Jayaprakash, N. Kalaiselvi, and P. Periasamy, "Synthesis and characterization of  $\text{LiM}_X\text{Fe}_{1-X}\text{PO}_4$  ( $M = \text{Cu}, \text{Sn}; X = 0.02$ ) cathodes—a study on the effect

- of cation substitution in  $\text{LiFePO}_4$  material,” *International Journal of Electrochemical Sciences*, vol. 3, pp. 476–488, 2008.
- [99] H.-Y. Hu, W.-H. Qiu, F.-X. Li, H.-L. Zhao, and B.-Y. Wang, “Influence of the Mg-substitution on electrochemical performances of  $\text{LiFePO}_4$ ,” *Chinese Journal of Power Sources*, vol. 30, no. 1, p. 18, 2006.
- [100] J. Hong, C. S. Wang, X. Chen, S. Upreti, and M. S. Whittingham, “Vanadium modified  $\text{LiFePO}_4$  cathode for Li-ion batteries,” *Electrochemical and Solid-State Letters*, vol. 12, no. 2, pp. A33–A38, 2009.
- [101] D. Rangappa, K. D. Murukanahally, T. Tomai, A. Unemoto, and I. Honma, “Ultrathin nanosheets of  $\text{Li}_2\text{MSiO}_4$  (M= Fe, Mn) as high-capacity Li-ion battery electrode,” *Nano Letters*, vol. 12, no. 3, pp. 1146–1151, 2012.
- [102] N. Yabuuchi, M. Kajiyama, J. Iwatate, H. Nishikawa, S. Hitomi, R. Okuyama, R. Usui, Y. Yamada, and S. Komaba, “P2-type  $\text{Na}_x[\text{Fe}_{1/2}\text{Mn}_{1/2}]\text{O}_2$  made from earth-abundant elements for rechargeable na batteries,” *Nature Materials*, vol. 11, no. 6, pp. 512–517, 2012.
- [103] J. Thorne, R. Dunlap, and M. Obrovac, “Structure and electrochemistry of  $\text{Na}_x\text{Fe}_x\text{Mn}_{1-x}\text{O}_2$  ( $1.0 \leq x \leq 0.5$ ) for Na-ion battery positive electrodes,” *Journal of The Electrochemical Society*, vol. 160, no. 2, pp. A361–A367, 2013.